2013

Interplay Between Inhibited Transport and Reaction in Nanoporous Materials

David Ackerman
Iowa State University

Recommended Citation

Ackerman, David, "Interplay Between Inhibited Transport and Reaction in Nanoporous Materials" (2013). *Graduate Theses and Dissertations*. 13448.
https://lib.dr.iastate.edu/etd/13448

Interplay between inhibited transport and reaction in nanoporous materials

by

David Michael Ackerman

A thesis submitted to the graduate faculty

in partial fulfillment of the requirements for the degree of

DOCTOR OF PHILOSOPHY

Major: Physical Chemistry

Program of Study Committee:
James W. Evans, Co-Major Professor
Mark S. Gordon, Co-Major Professor
David Hoffman
Michael Tringides
Javier Vela

Iowa State University

Ames, Iowa

2013

TABLE OF CONTENTS

ABSTRACT

This work presents a detailed formulation of reaction and diffusion dynamics of molecules in confined pores such as mesoporous silica and zeolites. A general reaction-diffusion model and discrete Monte Carlo simulations are presented. Both transient and steady state behavior is covered. Failure of previous mean-field models for these systems is explained and discussed. A coarse-grained, generalized hydrodynamic model is developed that accurately captures the interplay between reaction and restricted transport in these systems. This method incorporates the non-uniform chemical diffusion behavior present in finite pores with multi-component diffusion. Two methods of calculating these diffusion values are developed: a random walk based approach and a driven diffusion model based on an extension of Fick's law.

The effects of reaction, diffusion, pore length, and catalytic site distribution are investigated. In addition to strictly single file motion, quasi-single file diffusion is incorporated into the model to match a range of experimental systems. The connection between these experimental systems and model parameters is made through Langevin dynamics modeling of particles in confined pores.

CHAPTER 1. GENERAL INTRODUCTION

1 Introduction

Dynamics of particles within confined systems has been of interest with recent focuses on mesoscale structures such as mesoporous silica, nanotubes, and zeolites. The dynamics of motion within these particles is strongly affected by the confined nature of the systems. As these dynamics form an important part of the behavior in catalytic system, an accurate treatment of them is important to understanding system behavior. Experimental studies are limited in their ability to determine the composition within the pore. A theoretical approach can address this. It can also model actual experiments to help explain results by giving a better understanding of the small scale motion involved.

The pores in these types of systems often have widths with a diameter on the order of the size of one or two molecules. The narrowness of the pore can result in a single file motion which prevents molecules from passing. The limitations of this motion make simple diffusional analysis difficult and so the behavior is not well understood. Simple theoretical treatments such as a mean-field approximation of the steady state concentrations fail dramatically in this case because they do not retain the single file restriction that is a critical component of the system.

The majority of this thesis is the development of a theory and simulation model of the reaction-diffusion behavior in confined pores. Both a kinetic Monte Carlo (KMC) simulation framework and a hydrodynamic theory are discussed. A generalized hydrodynamic (g-hydro) model for reaction and diffusion was created to address shortcoming in mean field type approaches. The g-hydro model utilizes KMC diffusion data to accurately model transport throughout the pore. The transient and steady state behavior predicted by the g-hydro model was validated by comparison with KMC simulations. Both models are general to a wide range of cases, but include parameters that can be tailored to specific systems. While the single file behavior is of key interest, this work also addresses the case where molecules have a limited ability to pass each other.

As a strong motivation for this work is existing experimental studies of catalysis in pores, it valuable to connect the general parameters in KMC and g-hydro to specific experimental systems. In particular, catalytic yields have been shown to depend on pore sizes. This is due to a relaxation of the single file nature of the system which alters the dynamic. A Langevin dynamics study was performed to connect the degree of passing with the size of the pore as well as the size and shape of the molecules. This allows an important connection between the general model described here and actual experimental systems.

This work was performed at the Ames Laboratory under contract number DE-AC02-07CH11358 with the U. S. Department of Energy. The document number assigned to this thesis is IS-T 3106.

2 Thesis Organization

The remainder of this chapter outlines the layout of the thesis, describes how the chapters are connected, and explains my role in the work in the chapters taken from published papers. Chapters not published elsewhere are predominantly my work except where noted otherwise.

Chapter 2 is a paper[1] published in The Journal of Chemical Physics which discusses the initial work of developing the discrete and continuum model of a reaction, $A \rightarrow B$, in linear nanopores. It presents results for both steady state and transient behavior in pores with different configurations of catalytic sites. My role was creation of the discrete simulation model and generation of results as well as the the early development of the hydrodynamic model. This chapter lays out the basic system description and initial modeling, both of which are expanded on later.

Next, chapter 3 is modified from a paper[2] published in American Chemical Society Catalysis. The original paper is divided roughly into two sections. One section addresses the single file model described above with extensions to a multistage conversion model $A \rightarrow B \rightarrow C$. It also gives a more detailed description of the time evolution of the concentration profile. My role in this part was the development of the model and simulation results used in the paper as well as the selection of cases for comparison between the hydrodynamic and kinetic Monte Carlo models. The second part involved polymerization reactions within a confined pore. This part has been omitted from the thesis as I was not involved in that work.

A modification of the model to include passing is presented in chapter 4, which was published[3] in the Materials Research Society Proceedings. It also expands the comparison of catalytic site distribution. My role was again the Monte Carlo simulation and modeling work within the paper.

Chapter 5 is a paper[4] published in Physical Review Letters which adapts the hydrodynamic model to a generalized hydrodynamic model. This new model incorporates the non uniform tracer diffusion coefficients generated from the kinetic Monte Carlo simulations. My role in this work was the development and running of the random walk simulation used to generate the diffusion coefficients that are central to the generalized model.

An alternate approach for calculating diffusion coefficients is given in Chapter 6. This driven diffusion model utilizes Fick's law and concentration gradients to produce diffusion coefficients instead of the random walk based approach developed in the previous chapter.

Chapter 7 is a paper[5] published in The Journal of Chemical Physics that expands on the basic pore model to include the effect of varying the interaction of the pore with the product, adding reversible reactions, and creating enhanced reactivity. My role in this was generating the kinetic Monte Carlo data needed for the diffusion coefficients. In addition, it involved addressing a number of subtle behaviors that manifest with the change in model.

The initial Langevin dynamics treatment of passing is given in chapter 8. This work quantifies passing behavior within the pore by modeling in more detail the motion that leads to passing. From this, a connection is formed between the local, small scale dynamics of a pair of particles and the passing rates used in the previous studies. This is an early step in linking the generic simulations above with specific systems by applying some physical meaning to the passing rates. This work treats particles as circles and spheres as a simplified way of analyzing the behavior shown in the Langevin dynamics method.

Expanding on the case of circles and spheres, chapter 9 addresses the more general case where particles are no longer restricted to spheres and circles. This breaks the rotational symmetry, adding in Langevin rotations not present in the earlier work. A general method is given and results are presented for dimers and spheres.

The two appendices included are work related to dynamics and structure. Appendix I is a paper[6] published in Multiscale Modeling and Simulation. It lays out a comprehensive treatment of boundary conditions on vicinal Si surfaces. The model development and simulation in the work was done by me.

Appendix II investigates the structure of amorphous silicon ring systems. These systems are similar to the mesoporous Si particles containing pores. A system of modeling and counting ring correlations was developed which could yield insight into mechanical properties of such systems.

References

1) Ackerman, D. M.; Wang, J.; Wendel, J. H.; Liu, D.-J.; Pruski, M.; Evans, J.W. J. Chem. Phys. **2011**, 134, 114107.

2) Liu, D.-J.; Wang, J.; Ackerman, D. M.; Slowing, I. I.; Pruski, M.; Chen, H.-T.; Lin, V. S.-Y.; Evans, J. W. ACS Catalysis **2011**, 1, 751-763.

3) Wang, J.; Ackerman, D. M.; Kandel, K.; Slowing, I. I.; Pruski, M.; Evans, J. W. Mater. Res. Soc. Symp. Proc. **2012**, 1423.

4) Ackerman, D. M.; Wang J.; Evans, J. W. Physical Review Letters **2012**, 108, 228301.

5) Wang, J.; Ackerman, D. M.; Lin, V. S.-Y.; Pruski, M.; Evans, J. W. J. Chem. Phys. **2013**, 138, 134705.

6) Ackerman, D. M.; Evans, J. W. Multiscale Model. Simul. **2011**, 9, 59-88.

CHAPTER 2. CATALYTIC CONVERSION REACTIONS MEDIATED BY SINGLE-FILE DIFFUSION IN LINEAR NANOPORES: HYDRODYNAMIC VERSUS STOCHASTIC BEHAVIOR

David M. Ackerman,[1,2] Jing Wang,[1,3] Joseph H. Wendel,[1] Da-Jiang Liu,[1] Marek Pruski,[1]
and James W. Evans[1,3,4]

A paper published in *The Journal of Chemical Physics*

[1]Ames Laboratory – USDOE, and Departments of [2]Chemistry, [3]Mathematics,
and [4]Physics & Astronomy, Iowa State University, Ames Iowa 50011

Abstract

We analyze the spatiotemporal behavior of species concentrations in a diffusion-mediated conversion reaction which occurs at catalytic sites within linear pores of nanometer diameter. Diffusion within the pores is subject to a strict single-file (no passing) constraint. Both transient and steady-state behavior is precisely characterized by Kinetic Monte Carlo simulations of a spatially discrete lattice-gas model for this reaction-diffusion process considering various distributions of catalytic sites. Exact hierarchical master equations can also be developed for this model. Their analysis, after application of a mean-field type truncation approximations, produces discrete reaction-diffusion type equations (mf-RDE). For slowly varying concentrations, we further develop coarse-grained continuum hydrodynamic reaction-diffusion equations (h-RDE) incorporating a precise treatment of single-file diffusion in this multi-species system. The h-RDE successfully describe non-trivial aspects of transient behavior, in contrast to the mf-RDE, and also correctly capture unreactive steady-state behavior in the pore interior. However, steady-state reactivity, which is localized near the pore ends when those regions are catalytic, is controlled by fluctuations not incorporated into the hydrodynamic treatment. The mf-RDE partly capture these fluctuation effects, but cannot describe scaling behavior of the reactivity.

1 Introduction

Diffusion-mediated reaction processes have traditionally been modeled with mean-field reaction-diffusion equations (RDE) [1,2]. These RDE include a conventional treatment of chemical kinetics which ignores spatial correlations between reactants, and also a simple description of diffusion typically with constant Fickian diffusion coefficients. This approach has been effectively applied to heterogeneous catalysis on extended surfaces, where reactant species reside at a periodic array of adsorption sites on the nanoscale, and complex spatial concentration patterns can develop on the micron scale [3]. Actually, for such catalytic surface reactions, it has been recognized that mean-field kinetics has limitations due to non-random reactant distributions. However, there has been less appreciation of the complexity of diffusion in mixed reactant adlayers. This complexity arises even in simple lattice-gas reaction models with no interactions between reactants on different adsorption sites (but exclusion of multiple occupancy of sites) [4]. There are further complications in the treatment of diffusion in these mixed systems when one accounts for interactions between reactants [5].

In contrast, the non-trivial nature of diffusion is well-recognized for transport and possible reaction in so-called single-file systems. Such mesoporous (or more accurately nanoporous) systems are realized by materials incorporating arrays of linear pores which are sufficiently narrow that molecules cannot pass each other inside the pores. This no-passing feature results in anomalous tracer diffusion [6-8]. To assess the interplay between such anomalous transport and reaction, there have been several studies of a basic conversion reaction model and its variants [9-15]. In this basic model, the reactant, A, adsorbs at the end of pore, converts to product, B, at catalytic sites within the pore, and both reactants and products can exit the pore.

In an early study considering possibly reversible conversion reactions, Tsikoyiannis and Wei [9] developed hierarchical rate equations for a general class of lattice-gas (LG) models. They analyzed behavior for the canonical irreversible reaction model $A \rightarrow B$ with all sites catalytic by Kinetic Monte Carlo (KMC) simulation and compared results against predictions from first-order mean-field and second-order pair truncation approximations of the hierarchy [9]. The model was revisited by Okino *et al.* [10] who refined the pair or doublet truncation approximation and analyzed behavior of the reversible $A \leftrightarrow B$ as well as irreversible $A \rightarrow B$ conversion reaction.

Kärger and coworkers [11-13] examined model behavior via KMC simulation and included the possibility of attractive interactions between participating molecules. Finally, Nedea *et al.* [14,15], also considered behavior of the canonical irreversible reaction model A→B without interactions, exploiting both KMC simulation and truncation of hierarchical rate equations. They further considered behavior for different distributions of catalytic sites within the pore, and also analyzed non-trivial limiting behavior for rapid diffusion (but with finite exchange rates at the pore ends). These studies have focused primarily on elucidating steady-state reactivity.

While the anomalous aspects of tracer diffusion in single-file systems are well characterized, the behavior of chemical diffusion, which is of particular relevance for reaction-diffusion phenomena, is less completely characterized. It has been recognized that Onsager's classic theory of transport can be applied to assess chemical diffusion fluxes in multi-species systems with and without single-file constraints [16,17]. Also, some of the above studies of single-file conversion reactions have described the corresponding discrete RDE, but only based on approximate mean-field treatments [9,14]. However, what has not been exploited is the existence of exact results for diffusion fluxes in multi-species lattice-gas models with site exclusion and species-independent hop rates and interactions [18]. One can apply these results to single-file systems. One goal here is to use these exact results to assess the consequences of single-file diffusion for the transient behavior in conversion reactions, a relatively unexplored issue. We will also analyze behavior for various distributions of catalytic sites within the pore. In addition, regarding steady-state behavior, we will assess fundamental scaling behavior of quantities related to reactivity as a function of key model parameters.

In Sec.2, we specify in detail the single-file conversion reaction model, the associated hierarchical rate equations and mean-field-type RDE (mf-RDE), and discuss basic model properties. Then, in Sec.3, we formulate a treatment for the "hydrodynamic regime" where the evolution of slowly varying species concentrations might be described by continuum hydrodynamic RDE (h-RDE). Both steady-state and transient behavior is described in Sec.4 for a "canonical" conversion reaction model where all sites within the pore are catalytic. Behavior where either the peripheral or the central sites are catalytic is described in Sec.5. Finally, we offer some comments on more general models, and present conclusions in Sec.6.

2 Reaction-Diffusion Model: Prescription and Basic Properties

The model considered in this study was developed previously to describe the diffusion-mediated catalytic conversion of a reactant to a product (A→B) inside linear pores which are sufficiently narrow as to allow only single-file diffusion [9-15]. To treat the spatial aspects of this process, the model incorporates the feature that both reactants and products inside the pore reside at the sites of a linear lattice. The introduction of a discrete spatial structure should not affect the basic aspects of model behavior, at least for concentration profiles varying smoothly over several lattice constants. Such LG modeling also greatly facilitates both analytic investigation and simulation. The key mechanistic steps in the model are: adsorption of “external” (ext) reactant species A at terminal sites (t) of the pore provided that these sites are unoccupied or empty, E; subsequent diffusion of A within the pore by hopping to nearest-neighbor (NN) empty sites; conversion reaction A→B at catalytic sites (c) within the pore. The product, B, also undergoes diffusion by hopping to NN empty sites, and both the reactant and product undergo desorption from terminal sites (t) of the pore. Thus, to summarize, the mechanistic steps of the reaction are:

$$A(ext) + E_t \rightarrow A_t \text{ (adsorption)}; A_n + E_{n+1} \leftrightarrow E_n + A_{n+1} \text{ (diffusion)}; A_t \rightarrow A(ext) + E_t \text{ (desorption)}$$

$$A_c \rightarrow B_c \text{ (reaction)}; B_n + E_{n+1} \leftrightarrow E_n + B_{n+1} \text{ (diffusion)}; B_t \rightarrow B(ext) + E_t \text{ (desorption)}$$

where we label the sites in the pore by n=1, 2,…, L (for pore length L). Thus, the terminal sites t are n=1 and n=L. The catalytic sites may constitute all sites or various subsets of sites within the pore, as described below. Total reactivity (i.e., the total production rate of B), R^B_{tot}, is simply proportional to the total amount of A within the catalytic regions of the pore. The system geometry and these mechanistic steps are also illustrated in Fig.1.

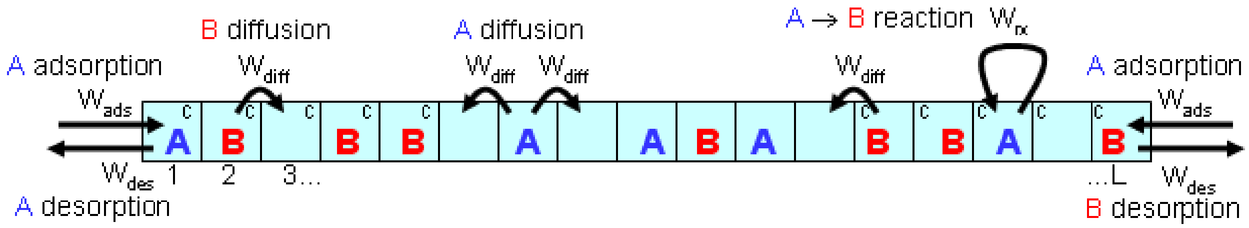

Figure 1: Schematic of a catalytic conversion reaction A→B in a single-file system. Catalytic sites (c) are located near the pore ends in this illustration. The configuration shown represents the transient regime. See Sec.5.

Rates for the various processes described above will be denoted by $W^A_{ads} = W_{ads}$ for adsorption of A, W^K_{des} for desorption of species K = A or B; W^K_{diff} for hopping of species K to NN empty sites, and W_{rx} for A → B conversion. An exact analytical description of such stochastic Markov processes is provided by the *master equation* for the evolution of probabilities of various configurations for the entire system [19]. Often this are written in *hierarchical form*. Here, we use $<K_n>$ to denote the probability or ensemble averaged concentration for species K at site n, $<K_nE_{n+1}>$ for the probability that K is at site n and for site n+1 to be empty (E), etc.. Then, the lowest order-equations describe the probabilities that individual sites are occupied by various species. When *all* sites are catalytic, one has that

$$d/dt <A_1> = W_{ads}<E_1> - W^A_{des}<A_1> -W_{rx}<A_1> - J_A^{1>2}, \quad (1a)$$

$$d/dt <B_1> = - W^B_{des}<B_1> +W_{rx}<A_1> - J_B^{1>2}, \quad (1b)$$

$$d/dt <A_n> = -W_{rx}<A_n> - J_A^{n>n+1} + J_A^{n-1>n}, \text{ for } 1<n<L, \text{ and} \quad (1c)$$

$$d/dt <B_n> = +W_{rx}<A_n> - J_B^{n>n+1} + J_B^{n-1>n}, \text{ for } 1<n<L, \quad (1d)$$

and similar equations for the terminal site n=L to those for n=1. In these equations,

$$J_K^{n>n+1} = W^K_{diff} [<K_nE_{n+1}> - <E_nK_{n+1}>], \quad (2)$$

denotes the *net* diffusive flux of K = A or B from n to n+1 (i.e., the difference between the flux from n to n+1 and that from n+1 to n). The total reactivity is given by $R^B_{tot} = W_{rx} \Sigma_{n=c}<A_n>$, where the sum is over all catalytic sites (i.e., over the entire pore in the above example).

These equations (1) are coupled to probabilities for various configurations of pairs of sites. Equations for pair probabilities couple to those for various triples, etc., thus generating a hierarchy. Pair, triplet, etc., probabilities are not trivially related to single-site probabilities due to the presence of spatial correlations. In these models, correlations derive from the interplay of adsorption-desorption and diffusion with reaction. Implementing a simple mean-field (MF) factorization approximation, $<K_nE_{n+1}> \approx <K_n><E_{n+1}>$, etc., produces a closed set of discrete mf-RDE's for single site concentrations, $<A_n>$ and $<B_n>$ noting that $<A_n> + <B_n> + <E_n> =1$.

A more accurate pair approximation retains pair quantities like $<K_nE_{n+1}>$, but factorizes triplet quantities, e.g., $<K_nM_{n+1}N_{n+2}> \approx <K_nM_{n+1}><M_{n+1}N_{n+2}>/<M_{n+1}>$, with K, M, N = A, B, or E.

This generates a closed set of equations for single site quantities, $<A_n>$ and $<B_n>$, together with the pair quantities, $<A_nA_{n+1}>$, $<A_nB_{n+1}>$, $<B_nA_{n+1}>$, and $<B_nB_{n+1}>$. See, e.g., [9,10,14]. Note that there exist various exact relations determined by conservation of probability, i.e., $<A_nB_{n+1}> + <A_nA_{n+1}> + <A_nE_{n+1}> = <A_n>$, allowing one to determine $<A_nE_{n+1}>$ from the set of the six selected quantities above. Higher-order approximations are also possible retaining probabilities of configurations of strings of n>2 sites, although the gain in accuracy with increasing order, n, may be slow [20].

A precise determination of model behavior is obtained by standard KMC simulation implementing processes with probabilities proportional to their rates. More specialized simulation algorithms may be applied to assess behavior in limiting regimes [15].

Following previous studies [10,12,14,15], to reduce the number of parameters in the model and also to induce some special features of model behavior, we will primarily consider the case where desorption rates and diffusion rates for both species are equal, i.e., $W^K_{des} = W_{des}$ and $W^K_{diff} = W_{diff}$, for K = A and B. There is an important consequence of this rate choice. Suppose one does not discriminate between the identity of particles, but only considers whether sites are empty, E, or filled, X=A+B (i.e., if one just considers the total concentration at various sites). Then, the dynamics corresponds to a pure adsorption-desorption-diffusion process for particles X with no reaction. Correspondingly, from (1), one obtains the *exact* equations

$$d/dt <X_1> = W_{ads}<E_1> - W_{des}<X_1> - J_X^{1>2}, \tag{3a}$$

$$d/dt <X_n> = - J_X^{n>n+1} + J_X^{n-1>n}, \text{ and} \tag{3b}$$

$$d/dt <X_L> = W_{ads}<E_L> - W_{des}<X_L> + J_X^{L-1>L}, \tag{3c}$$

$$\text{where } J_K^{n>n+1} = W_{diff} [<X_nE_{n+1}> - <E_nX_{n+1}>] = W_{diff} [<X_n> - <X_{n+1}>]. \tag{4}$$

The exact relation corresponding to the last equality in (4) expressing $J_K^{n>n+1}$ in terms of single-site quantities amounts to an exact reduction of a many (X) particle problem to a single-particle problem. This feature was first noted by Kutner for an infinite lattice [21]. Extension of this reduction to semi-infinite and finite lattices has also been recognized previously [14,22]. Thus, the evolution of $<X_n>$ is described exactly by standard discrete diffusion equations (3b), augmented by adsorption and desorption terms at the end sites in (3a,b). The equations are closed noting that $<E_n> = 1 - <X_n>$.

It is thus straightforward to visualize the evolution of the total concentration starting from an empty pore. The total concentration will first build up near the ends of the pore, then spread by diffusion to the interior, and finally achieve a spatially uniform steady-state. Since there is no reaction in the dynamics of particles X, the steady-state corresponds to a conventional *grand canonical equilibrium state* with activity $z = W_{ads}/W_{des}$ [23]. Furthermore, since there are no interactions between particles X in this model, they are randomly distributed (i.e., there are no spatial correlations) in this trivial equilibrium state. The equilibrium concentration at each site satisfies $<X_n>_{eq} = X_{eq} = z/(1+z) = W_{ads}/(W_{ads}+W_{des})$ (cf. [9,15]). As an aside, we note that while the equilibrium steady-state is free of spatial correlations just considering the distribution of filled sites, X, such correlations do develop during filling of the pore. Remarkably, an exact closed set of equations can be obtained for pair probabilities, $<X_nX_{n+m}>$, or associated correlations, as these decouple from triplet correlations [24]. Likewise, an exact closed set of equations can be obtained for the triplet correlations which decouple from the quartet correlations, etc. The nature of this decoupling is analogous to that described for (4).

In our analyses below, we will choose $W_{ads} + W_{des} =1$ which sets the time-scale. We will present results only for: (i) $W_{ads} = 0.2$, $W_{des} = 0.8$ [low loading]; (ii) $W_{ads} = 0.8$ (or 0.9), $W_{des} = 0.2$ (or 0.1) [high loading]. Single-file effects are stronger for high loading. Parameters W_{rx} and W_{diff} will either have suitably-selected fixed values when comparing predictions of various treatments, or will be systematically varied in scaling studies. Note that well-defined limiting behavior is found in the regimes where: (a) $W_{ads}+W_{des}$ (with fixed $z = W_{ads}/W_{des}$) far exceeds W_{rx} and W_{diff} [12], so that reaction is not limited by adsorption and desorption at the ends at the pore; (b) W_{diff} far exceeds all other parameters. In contrast to typical reaction-diffusion systems where concentrations become uniform in this limit, non-trivial behavior is found in this single-file system [15]; (c) W_{diff} is far smaller than other parameters, so then only the terminal sites have a non-zero population of A in the steady-state [25].

3 Hydrodynamic Regime and Reaction-Diffusion Equations

In discrete LG reaction-diffusion systems, it is common to consider behavior in the "hydrodynamic regime" of substantial diffusion (on the time scale of other adsorption-desorption and reaction processes) and slowly varying particle concentrations (on the length scale of lattice constants) [4,5,26]. Within this framework, one might describe behavior by continuum hydrodynamic reaction-diffusion equations (h-RDE) after coarse-graining the discrete spatial variable to a continuous variable. Specifically, for linear lattices, one sets x = na, where n is the lattice site label and "a" is the lattice constant. (As an aside, it is often convenient to set a=1 in the following.) Then, species concentrations per unit length become functions of a continuous variable $K(x=na) \approx a^{-1} \langle K_n \rangle$, where we leave implicit the t-dependence. To develop h-RDE, one needs an appropriate description of collective or chemical diffusion in this multi-species lattice-gas system [4,5,16,17,26] incorporating the single-file nature of diffusion.

Before addressing this major challenge, we comment on the much simpler task of describing the behavior of the coarse-grained total particle concentration per unit length, $X(x=na) \approx a^{-1} \langle X_n \rangle$, in the hydrodynamic regime. As noted in Sec.2, the dynamics of this concentration profile is described by a reaction-free discrete diffusion equation. If J_X denotes the corresponding diffusion flux, then in the hydrodynamic regime, one has that

$$\partial/\partial t\ X(x) = -\partial/\partial x\ J_X \text{ with } J_X = -D_X\ \partial/\partial x\ X(x) \text{ and } D_X = a^2 W_{diff}\ . \qquad (5)$$

The feature that the chemical diffusion coefficient, D_X, is independent of concentration is well known for this single-component problem [21]. Thus, the single-file nature of the system does not reveal itself when considering chemical diffusion for a single species X. Equation (5) is augmented with the appropriate Robin boundary conditions $\pm J_X = aW_{ads}(X_m - X) - aW_{des}X$ at the pore ends, a relation derived from a steady-state form of (1a). Here, $X_m = 1/a$ is the maximum concentration per unit length.

For the case where all sites are catalytic, the h-RDE in our conversion reaction model for individual species concentrations, A(x) for A, and B(x) for B (leaving implicit the t-dependence), have the form

$$\partial/\partial t\ A(x) = -W_{rx}\ A(x) - \partial/\partial x\ J_A \text{ and } \partial/\partial t\ B(x) = +W_{rx}\ A(x) - \partial/\partial x\ J_B. \qquad (6)$$

where $X(x) = A(x)+B(x)$. If sites within the pore are catalytic only in specific (e.g., peripheral) regions, then the reaction terms appear only for those locations. Description of the diffusion fluxes, J_A and J_B, for species A and B, respectively, is non-trivial in mixed lattice-gases even in the absence of interactions beyond site exclusion. The appropriate Robin boundary conditions for (6) at the pore ends have the form $\pm J_A = aW_{ads}(X_m - X) - aW_{des}A$, and $\pm J_B = -aW_{des}B$.

Onsager's transport theory ensures that the diffusive flux of A has the form [4,5,16,17,26]

$$J_A = - D_{A,A}\, \partial/\partial x\, A(x) - D_{A,B}\, \partial/\partial x\, B(x), \qquad (7)$$

where in general the diffusion coefficients $D_{A,K}$ depend on species concentrations. Thus, the flux J_A is induced by gradients in both <A> and <B>. A similar expression applies for the flux, J_B, of B. The four diffusion coefficients, $D_{K,K'}$, with K, K´ = A or B, can be conveniently collected into a 2x2 diffusion tensor $\underline{\underline{D}}$. Onsager's theory [16,17,26] further shows that this tensor involves both a thermodynamic "inverse compressibility" factor and a kinetic "conductivity" factor [27].

3.A. Exact hydrodynamic diffusion fluxes

As indicated above, there is a general appreciation that in principle the components of $\underline{\underline{D}}$ can be determined using the statistical mechanical formulation of Onsager theory. However, what has not been exploited is the existence of an exact result for the case of a multi-species lattice-gas with no interactions beyond site exclusion and for equal hop rates, W_{diff} [4,18,26]. For one-dimensional (1D) systems with single-file diffusion, one has the simple and intuitive *exact form*

$$J_A = -D_X\, [A(x)X(x)^{-1}]\, \partial/\partial x\, X(x), \quad J_B = -D_X\, [B(x)X(x)^{-1}]\, \partial/\partial x\, X(x). \qquad (8)$$

In obtaining (8) from more general results [18,26], we have exploited the feature that the tracer diffusion coefficient vanishes for 1D single-file systems. See Appendix A.

There is an important consequence of the form (8) of the diffusion fluxes for the steady-states of the h-RDE. From (8), it is clear that fluxes J_A and J_B vanish for states with uniform total concentration, $X(x)$ = constant, irrespective of whether there are gradients in individual species concentrations. This reflects the lack of intermixing in single-file systems. Since the steady-state of the reaction model is characterized by constant $X(x) = a^{-1} X_{eq} = a^{-1} W_{ads}/(W_{ads}+W_{des})$, J_A and J_B

must *vanish* for long times. Consequently, in this regime, concentrations interior to the pore change only due to reaction. As a result, any A is converted to B in regions with catalytic sites, so that <A>=0 and <B> = X_{eq} in the steady-state in such regions. For example, if all sites are catalytic, then the steady-state is completely unreactive in the hydrodynamic picture. In the actual model with all sites catalytic, reactivity does actually persist near pore ends in the steady state, but only due to fluctuations absent in the hydrodynamic treatment.

In the transient regime, as noted above, the evolution of $\langle X_n \rangle$ or X(x) is simply described by the non-reactive diffusion problem. A gradient develops as particles diffuse into the pore, and thus the diffusion fluxes J_A and J_B in (8) are non-zero and always in the direction towards the center of the pore. We will show that the correct description of diffusion in hydrodynamic RDE does capture key aspects of transient behavior. For such comparisons KMC simulation results, we utilize discrete hydrodynamic RDE which incorporate a discrete version of (8) as described in Appendix B.

3.B. Mean-field diffusion fluxes

In contrast to the above hydrodynamic treatment, a mean-field (MF) treatment of chemical diffusion fluxes yields the distinct form

$$J_A(MF) = -D_X\,[1 - B(x)X_m^{-1}]\,\partial/\partial x\,A(x) - D_X\,[A(x)X_m^{-1}]\,\partial/\partial x\,B(x), \qquad (9)$$

and an analogous expression applies for J_B^{MF}. Again X_m=1/a is the maximum concentration per unit length. This previously utilized result [16,17,28] can be obtained from Onsager theory accounting for the known thermodynamics of a non-interacting lattice-gas, but also incorporating a crude approximation for species conductivity [27]. However, it is instructive to note that an alternative simple kinetic derivation of the MF result (9) is also possible [14,29]: one simply applies the MF factorization to $J_A^{n>n+1}$ and $J_B^{n>n+1}$ in (1c,d) and recasts the results in terms of continuous derivatives for slowly varying concentrations.

Clearly, this MF form of the diffusion fluxes which applies for any lattice dimension fails to capture the single-file nature of diffusion, and thus also fails to capture aspects of the correct hydrodynamic behavior. For example, the form (9) allows non-zero diffusion fluxes for constant

X, and this can produce artificially enhanced intermixing of A and B. Specifically, one has that

$$J_K(MF) \rightarrow -D_X(1-X_{eq})\, \partial/\partial x\, K(x) \text{ when } X \rightarrow a^{-1} X_{eq} \text{ (steady-state)} \quad \text{for } K = A \text{ or } B. \tag{10}$$

The MF form also allows diffusion of species away from the center of the pore. Severe failure can be anticipated in the regime of large W_{diff} where the MF formulation predicts complete intermixing [14,15], but the actual single-file nature of diffusion prohibits such behavior.

For comparison with results of KMC simulation for both transient and steady-state behavior, we will implement the mf-RDE associated with the MF truncation approximation to (1). These constitute the natural discrete version of (9). See Appendix B. In addition, we will implement discrete mf-RDE associated with the pair approximation which might be regarded as providing a refined treatment of diffusion. (As an aside, it is non-trivial to extract continuum h-RDE for the pair-approximation [30].) We shall see that both the MF and pair approximations do capture some aspects of fluctuation effects near the end of the pore in contrast to the hydrodynamic treatment.

4 Canonical Model: All Sites Catalytic

4.A. Steady-state behavior

Fig. 2 shows a “typical” example of the evolution of concentration profiles towards the steady-state for the parameter choice W_{ads}=0.2, W_{des}=0.8, W_{rx}=1, W_{diff}=1, and pore length L=30. Precise results of KMC simulations in Fig.2a are compared against those from various approximate analytic formulations in Fig.2b-d. The mean-field and pair approximation are quite effective in capturing behavior near the pore end as noted previously [9,10,14]. These approximations and the hydrodynamic treatment all describe effectively exactly evolution in the interior of the pore where there is just one species (B). Note that the A-concentration profile reaches a non-trivial steady-state form (with significant population only on the four sites closest to the pore end) long before the steady-state of the entire system is reached (for which $\langle X_n \rangle$=0.2). This can be anticipated since all that is required for development of steady-state

$\langle A_n \rangle$ is sufficient diffusion into the pore end so that $\langle X_n \rangle$ is close to its steady state value at sites near the pore end. Filling of the interior of the pore by species B occurs on a slower time scale. Simulation with the same rate parameters but for longer pores produces essentially identical steady-state $\langle A_n \rangle$ distribution, but just take longer for the interior of the pore to fill with B.

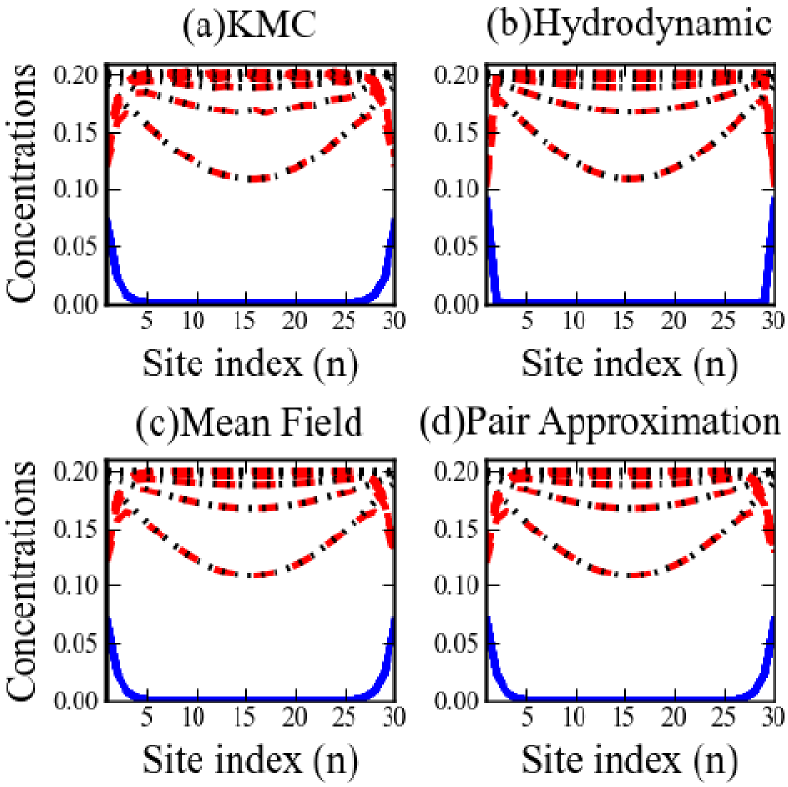

Figure 2: Evolution of concentration profiles to the steady-state in a pore with all sites reactive: A (blue solid lines); B (red dashed lines); X=A+B (black dotted lines). This format is used in subsequent figures. Parameters are $W_{ads} = 0.2$, $W_{des} = 0.8$, $W_{rx} = 1$, $W_{diff} = 1$, and $L = 30$. Time increments are $\Delta t = 100$. (a) KMC results averaged over 2.5×10^5 simulations; (b) hydrodynamic, (c) MF, and (d) pair approximation results. The B-concentration increases with time.

As noted above, hydrodynamic analysis predicts that in the steady-state, the central region will contain just B and no A, so that $\langle B_n \rangle = W_{ads}/(W_{ads}+W_{des}) \approx X_{eq}$ and $\langle A_n \rangle \approx 0$. Only the end sites have significant A population in our discrete formulation. Thus, the non-zero population of A near the pore ends observed in simulations can be associated with fluctuation effects not included in the hydrodynamic formulation. Since the reactivity of the system is determined by the population of A in the pore, these fluctuations are entirely responsible for the steady-state reactivity.

This motivates more detailed analysis of the dependence of this steady-state $<A_n>$ concentration profile on model parameters. Steady-state profiles appear to have an exponential form,

$$<A_n> \approx c\cdot r^n = c\cdot\exp(-\lambda n) = c\cdot\exp(-n/L_{p1}), \text{ at least for larger } n < L/2. \tag{11}$$

In (11), $\lambda = -\ln r$ is the decay rate, and $L_{p1}=1/\lambda$ is a measure of the penetration depth of A into the pore. In our analysis of KMC data below, we do find deviations from simple exponential decay for smaller n, most clearly in cases where L_{p1} is large (so decay is slow). The behavior (11) also implies that the production rate, R_B^{tot}, should converge exponentially to a finite value with increasing pore length. We note that another natural measure a penetration depth, L_p, at least in the regime where L_p is large is $L_{p2} = \Sigma_{n<L/2} <A_n>/<A_1>$. Yet another alternative is $L_{p3} = -1/\ln(1-1/L_{p2})$, which would correspond exactly to L_{p1} for perfect exponential decay where $<A_n> = <A_1> r^{n-1}$.

First, we examine the *dependence on reaction rate*, W_{rx}, of steady-state penetration depth L_p (considering all of L_{p1}, L_{p2}, and L_{p3}). We set $W_{diff} =1$ and vary W_{rx} from 1 to 10^{-3} for a system of size L=100. The lower the reaction rate, the greater the extent of penetration of A into the pore, and the greater L_p. Fig.3a-b show concentration profiles for $W_{ads}=0.8$ and $W_{des}=0.2$ for various W_{rx}. Analysis of this data and analogous data for $W_{ads}=0.2$ and $W_{des}=0.8$ to extract L_p versus W_{rx} is shown in Fig.3c-d. One finds that L_p increases with decreasing W_{rx} much more slowly than $(W_{rx})^{-1/2}$. Instead, we suggest that $L_p \sim (W_{rx})^{-1/4}$, as $W_{rx} \to 0$, corresponding to asymptotically linear behavior in Fig.3c-d for large abscissa. This behavior might be anticipated from the postulate that L_p should reflect the root-mean-square displacement for single-file diffusion on a time-scale corresponding to the reaction time, $\tau_{rx} = 1/W_{rx.}$ This implies that $(L_p)^4 \sim \tau_{rx}$ and thus that $L_p \sim (W_{rx})^{-1/4}$. This result for L_p immediately yields scaling of the total reactivity per pore as $R^B{}_{tot} \sim W_{rx}\, L_p \sim (W_{rx})^{3/4}$.

Second, we examine the *dependence on diffusion rate*, W_{diff}, of steady-state behavior. For a conventional reaction-diffusion system, increase of hopping rates ultimately produces spatial uniformity of species concentrations due to “efficient stirring” corresponding to $L_p \to \infty$. One also achieves randomization of configurations in the absence of interactions [4,30]. A special feature of the single-file system being considered here [14,15] is the existence of non-trivial spatially non-uniform limiting behavior as $W_{diff} \to \infty$ (but retaining finite W_{ads}, W_{des}, and W_{rx}) [31]. One obtains a well-defined limiting concentration profile with finite penetration depth, $L_p(W_{diff} \to \infty) < \infty$, in this regime. More detailed analysis of steady-state concentration profiles for increasing W_{diff} suggests that $L_{p1} \sim L_{p1}(W_{diff} \to \infty) + c(W_{diff})^{-1/4}$. See Fig.4. Limiting values of $L_{p1}(W_{diff} \to \infty)$ was obtained from a tailored simulation algorithm (cf. [15]). Separate analysis indicates that L_{p2} and L_{p3} are fairly insensitive to W_{diff}.

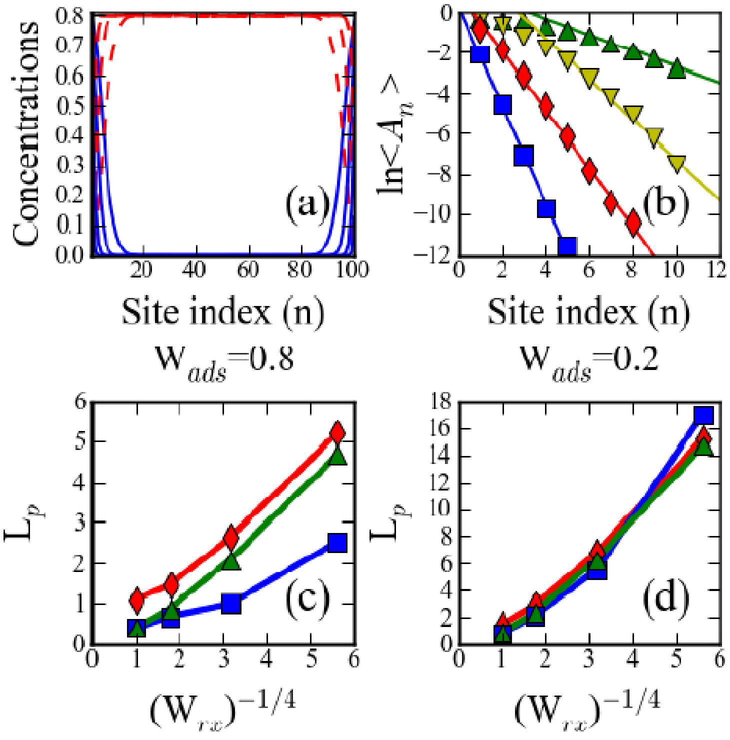

Figure 3: Steady-state behavior for a mesopore with all sites catalytic. (a) Concentration profiles for $W_{ads}=0.8$, $W_{des}=0.2$, and $W_{diff}=1$, with $L=100$ for $W_{rx}=1$, 0.1, 0.01, and 0.001; (b) ln $<A_n>$ versus $n<<L/2$ for the data in (a); data for smaller W_{rx} has greater penetration in (a) and smaller slopes in (b); L_p versus $(W_{rx})^{-1/4}$ with $W_{diff}=1$ for: (c) $W_{ads}=0.8$, $W_{des}=0.2$; and for (d) $W_{ads}=0.2$, $W_{des}=0.8$. Squares, diamonds, and triangles denote L_{p1}, L_{p2}, and L_{p3}, respectively.

Table 1: Tabulation of L_p-values from KMC simulations, and the MF and pair-approximations, for the cases analyzed in Fig.3.

	W_{ads} = 0.8 and W_{des} = 0.2					W_{ads} =0.2 and W_{des} = 0.8			
W_{rx}	1	0.1	0.01	0.001		1	0.1	0.01	0.001
L_{p1}(KMC)	0.41	0.69	1.00	2.56		0.88	2.13	5.56	16.7
L_{p2}(KMC)	1.10	1.47	2.64	5.21		1.47	2.92	6.77	15.2
L_{p3}(KMC)	0.42	0.88	2.10	4.69		0.87	2.39	6.25	14.7
$L_{p1,3}$(MF)	0.520	1.44	4.48	14.1		0.937	2.84	8.95	28.29
L_{p2}(MF)	1.17	2.00	5.00	14.7		1.53	3.37	9.46	27.78
L_{p1}(pair)	0.432	1.23	2.92	9.26		0.882	2.59	8.11	27.89
L_{p2}(pair)	1.11	1.79	3.47	9.77		1.48	3.12	8.61	27.84
L_{p3}(pair)	0.433	1.23	2.94	9.26		0.882	2.59	8.10	27.33

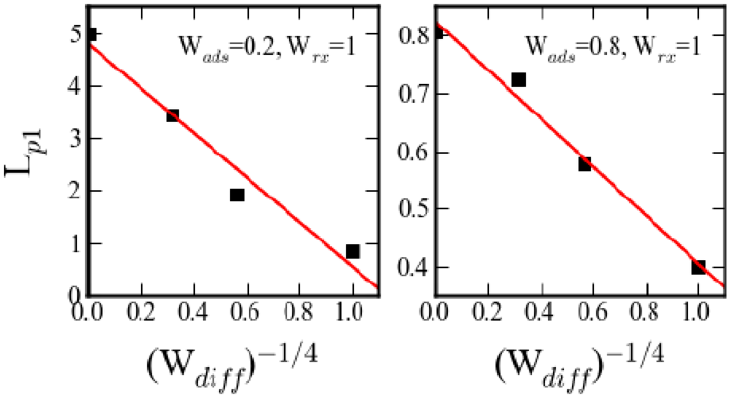

Figure 4: Dependence of L_{p1} on W_{diff} (but retaining fixed finite values of W_{ads}, W_{des}, and W_{rx}) demonstrating the nature of the convergence to $L_{p1}(W_{diff} \rightarrow \infty)$ as $W_{diff} \rightarrow \infty$.

Next, we consider the *predictions of MF-type analytic treatments* regarding the above behavior. The simplest MF approximation exhibits precise exponential decay for long pores. This behavior, noted previously [14], is a result of the feature that $\langle E_n \rangle = 1 - \langle X_n \rangle$ is constant, which in turn allows reduction of the steady-state form of (1c) to a *linear* coupled set of equations. Setting $\varepsilon = W_{rx}/W_{diff}$ and $X_{eq} = W_{ads}/(W_{ads}+W_{des})$, then seeking a solution to these linear equations of the form $\langle A_n \rangle \propto r^n$ yields for r the quadratic equation (cf. [14])

$$(1-X_{eq})(r + r^{-1} - 2) = \varepsilon. \qquad (12)$$

Consequently, one has that $\delta = 1 - r \sim (1-X_{eq})^{-1/2}\,\varepsilon^{1/2}$, for small ε, so that (cf. [14])

$$L_{p1}(MF) \sim \delta^{-1} \sim (1-X_{eq})^{1/2}\,(W_{rx})^{-1/2}(W_{diff})^{1/2},\ \text{for}\ W_{rx} \rightarrow 0\ \text{or}\ W_{diff} \rightarrow \infty. \qquad (13)$$

The result (13) can be obtained more directly from the continuum MF formulation [32]. This result reveals a fundamental failure of the MF treatment to describe asymptotic behavior of L_p. The failure to describe scaling as $W_{rx} \rightarrow 0$ or $W_{diff} \rightarrow \infty$ reflects an inability to capture single-file aspects of diffusion. Since concentration profiles become spatially uniform within the MF approximation as $W_{diff} \rightarrow \infty$, this enables simple direct analysis of MF behavior, e.g., showing that MF reactivity converges like 1/L rather than exponentially as $L \rightarrow \infty$. See Appendix C.

It is instructive to assess the predictions of the higher-order pair approximation for the behavior of the penetration length, L_p. The complex non-linear form of pair equations [14] excludes exact exponential decay. However, there should be asymptotic exponential decay $\langle A_n \rangle \sim \exp(-n/L_{p1})$ for large $n < L/2$. In the steady-state, one has the relations $\langle A_n \rangle + \langle B_n \rangle = X_{eq}$ and $\langle B_nB_{n+1} \rangle + \langle B_nA_{n+1} \rangle + \langle A_nB_{n+1} \rangle + \langle A_nA_{n+1} \rangle = (X_{eq})^2$. Since one expects that $\langle A_nA_{n+1} \rangle$ decreases more quickly than $\langle A_n \rangle$, $\langle A_nB_{n+1} \rangle$, or $\langle B_{n-1}A_n \rangle$ for increasing n, it follows that one can just analyze equations for the latter quantities. Anticipating solutions of the form $\langle A_n \rangle \approx c \cdot r^n$, $\langle A_nB_{n+1} \rangle \approx c \cdot \beta \cdot r^n$, and $\langle B_{n-1}A_n \rangle \approx c \cdot \gamma \cdot r^n$ and substituting into the rate equations for the pair approximation yields three coupled equations

$$(1-\beta)(r-1) + (1-\gamma)(r^{-1}-1) = \varepsilon,\quad (1-\gamma)(\gamma^{-1}X_{eq})(r^{-1}+1) - (1-X_{eq}) - (1-\beta) = \varepsilon,$$
$$\text{and}\ (1-\beta)(\beta^{-1}X_{eq})(r+1) - (1-X_{eq}) - (1-\gamma) = \varepsilon. \qquad (14)$$

Seeking solutions for small ε and $\delta = 1-r$ with $\beta \approx X_{eq} + B\delta$ and $\gamma \approx X_{eq} + C\delta$ yields $C = -B = X_{eq}(1-X_{eq})(2+X_{eq})^{-1}$ [33] and

$$L_{p1}(\text{pair}) \sim \delta^{-1} \sim (2-X_{eq})^{1/2}(2+X_{eq})^{-1/2}L_p(MF)\ ,\ \text{for large}\ L_{p1}. \qquad (15)$$

Thus, L_{p1}(pair) is smaller than L_{p1}(MF) and closer to the exact L_{p1}, but still has the incorrect asymptotic functional form as $W_{rx} \rightarrow 0$ or $W_{diff} \rightarrow \infty$.

4.B. Transient behavior

In this subsection, we characterize the evolution of concentration profiles during filling of a very long (semi-infinite) pore with an emphasis on scaling behavior for increasing time, t. Recall that the total concentration satisfies a standard discrete diffusion equation which reduces to the conventional continuum equation in the hydrodynamic regime. Thus, it follows that this profile has the “classic” scaling form

$$\langle X_n(t)\rangle \approx \langle X(t=\infty)\rangle\, F(n/(W_{diff}\, t)^{1/2}), \text{ for } n<L/2, \text{ where } F(y) = \mathrm{erfc}(y/2), \tag{16}$$

where erfc is the complementary error function [34]. Thus, concentration profiles collapse onto a single curve for increasing t after rescaling the n-axis by $(W_{diff}\ t)^{1/2}$. However, when considering the individual species A and B, the system is dominated by B for increasing time due to reaction (when keeping all parameters fixed). After rescaling the spatial variable, one obtains $\langle B_n\rangle \sim \langle X_n\rangle$ and $\langle A_n\rangle \sim 0$. To achieve non-trivial scaling profiles with significant populations of both species inside the pore, it is natural to reduce the reaction rate as time is increased so that $W_{rx}t$ remains constant. More precisely, we seek scaling solutions for the individual species concentrations of the form

$$\langle A_n(t)\rangle \approx \langle X(t=\infty)\rangle\, F^A(n/(W_{diff}\, t)^{1/2}, W_{rx}t) \text{ and} \tag{17a}$$

$$\langle B_n(t)\rangle \approx \langle X(t=\infty)\rangle\, F^B(n/(W_{diff}\, t)^{1/2}, W_{rx}t), \tag{17b}$$

for $n<L/2$, where $F^A + F^B = F$. Support for the existence of such solutions comes from substitution of these forms into the hydrodynamic reaction-diffusion equations of Sec.3. One then obtains a closed coupled pair of partial differential equations for the scaling functions $F^{A,B}(y, u)$. The specific form of the equations depends on the choice of diffusion fluxes (e.g., hydrodynamic versus MF), as do the solutions $F^{A,B}$. See Appendix D.

From the earlier discussion of hydrodynamic versus fluctuation effects, one might anticipate the following: (i) The MF and pair approximations should capture exact KMC behavior better for shorter times when most particles are relatively close to the pore opening. In this regime, behavior is more influenced by fluctuations. (ii) The hydrodynamic treatment should provide a better description of exact KMC behavior for longer times where the concentration profiles varies smoothly over many lattice constants. Indeed, this is the case as shown in Fig.5. For the selected parameters, the peak $\langle A_n\rangle$-concentration of around 0.08 in the MF and pair approximations for smaller times (larger W_{rx}) matches KMC results, but these approximations retain this value for longer times. In contrast, the peak in hydrodynamic treatment increases to about 0.13-0.14 for longer times (smaller W_{rx}) in good agreement with long-time KMC results. This peak is far above the converged MF and pair approximation value of 0.08.

5 Peripheral or Central Catalytic Sites

5.A. Peripheral catalytic sites

Here, we consider situations where contiguous strings of sites at each end of the pore are catalytic, but sites in the central region are not. One can imagine this type of distribution might result where catalytic sites are created by grafting after formation of a meso- or nano-porous material and where diffusion into the pores is inhibited. (An alternative co-condensation process for mesoporous silica materials tends to produce a more uniform distribution of catalytic sites [35].) An example of the results of KMC simulations for evolution to the steady-state is shown in Fig.6. The parameter choices is $W_{ads} = 0.8$, $W_{des} =0.2$, $W_{rx} =0.017$, and $W_{diff} =10$ for a pore of length L=100 with 20 catalytic sites at each end.

Characterization of behavior in this system is most appropriately divided into two regimes (provided that the reaction rate is not too large). In the *first transient regime* of “pore filling”, a significant amount of A may avoid reaction in the peripheral catalytic regions and diffuse into the central non-catalytic region, i.e., A will successfully *run the gauntlet* passing catalytic sites without conversion. After the pore has filled so that the total concentration $<X_n> \sim X_{eq}$ is roughly constant, one expects a peak in the concentration of A (i.e., a “blob” of A) in the center of the pore, and strongly decreasing A concentrations approaching and entering the peripheral regions from the center of the pore. Indeed, in a hydrodynamic treatment, one achieves a stationary state with a frozen blob of A in the central non-catalytic region of the pore, and the peripheral catalytic regions occupied only by B and completely devoid of A. (Note that this hydrodynamic steady-state is not unique, the specific form of the frozen A-distribution in the central region will depend on the initial conditions.) However, this is *not* a true steady-state of the stochastic model, although it might be regarded as a metastable state.

Fluctuations at the end of the pore ensure that the A-concentration profile always has a local maximum at this location which does not diminish for long times (contrasting the hydrodynamic

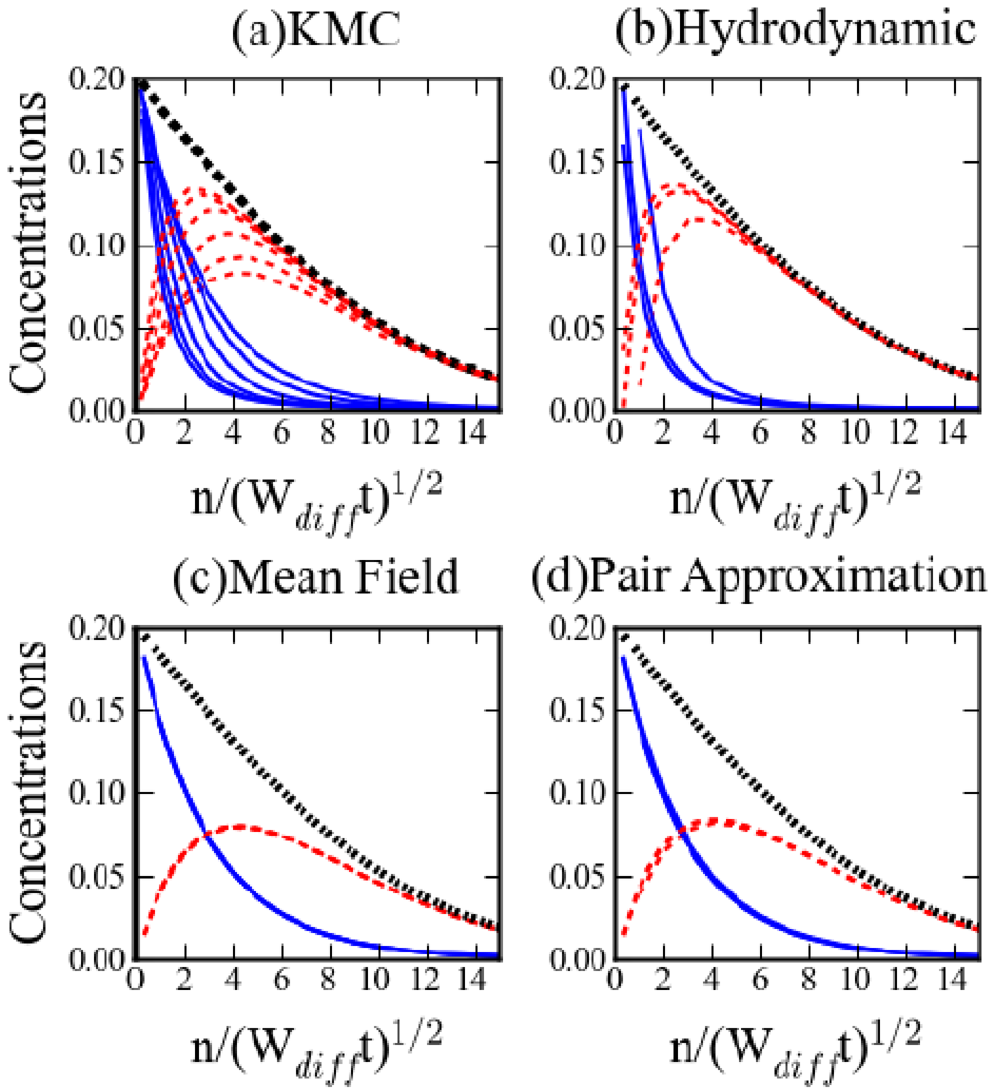

Figure 5: Diffusion into an initially empty semi-infinite pore with all sites catalytic. Parameters are: W_{ads}=0.2, W_{des}=0.8, W_{diff} = 1, and W_{rx} t = 4 (ensuring comparable amounts of A and B in the pore). Rescaled concentration profiles for: (a) KMC simulation; (b) hydrodynamic; (c) MF; and (d) pair approximations. KMC results are shown for W_{rx} = 0.1, 0.01,… and 0.000001 (6 cases), where convergence to the limiting profile shapes is very slow. Convergence is fast for the MF and pair approximations (by W_{rx}~0.01), and moderate for the hydrodynamic treatment (by W_{rx} ~ 0.001 where data is shown for W_{rx} = 0.1, 0.01, and 0.001).

description). In fact, part of the concentration profile is very similar to that for pore with all sites reactive (and with the same rate parameters).

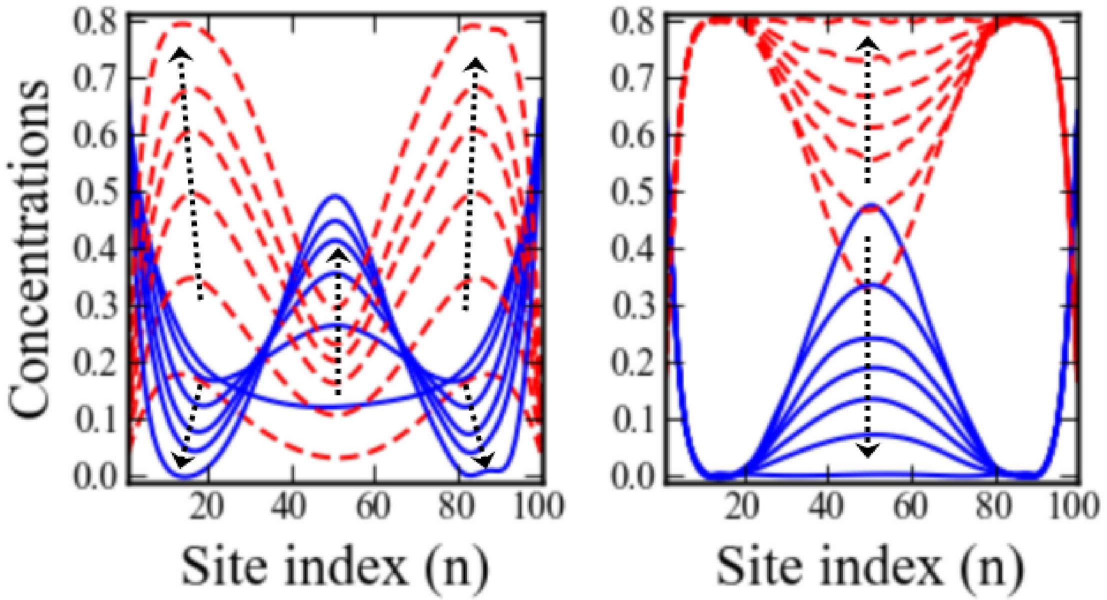

Figure 6: KMC results for the complete evolution of species concentrations for a pore of length L=100 with 20 catalytic sites at each end. Parameters are W_{ads} = 0.8, W_{des} =0.2, W_{rx} =0.017, and W_{diff} =10. The left frame shows the transient pore-filling regime for time increments of 60 up to t=600 where the peak $<A_{50}>$ is growing significantly to reach a maximum. The following "metastable regime" has little change over ~10^3 time units. The right frame shows slow late-stage evolution for times t = 1000, 5000, 10000, 14000, 20000, and 100000 where $<A_{50}>$ decreases below its maximum. The steady-state (with $<A_n>\approx 0$ in the central region) is reached after ~10^5 time units. Black dotted arrows indicate evolution with increasing time.

However, more dramatically, in the *second late-stage regime*, fluctuation effects mean that the blob of A formed during the transient regime in the central non-catalytic region is not frozen. The entire blob can undergo anomalous diffusion, and is thus guaranteed to reach the peripheral catalytic regions. As a result, eventually essentially all of the A in this blob will be converted to B leading to the true steady-state with the central non-catalytic region, and indeed most of the interior of the pore, devoid of A. Indeed, the true steady-state for this case is very similar to that for the case where all sites are catalytic (with the same rate parameters). The reason is that for the case with all sites catalytic, it is only the end of the pore where one has conversion A→B in the steady state.

Fig.7 compares the predictions of the hydrodynamic treatment and other approximations with exact KMC simulations for a finite time selected to correspond to the *end of the first transient regime* in the KMC results. The parameter choices is W_{ads} = 0.8, W_{des} =0.2, W_{rx} =0.017, and W_{diff}

=10. Specifically, we choose the time t = 420 where the A-concentration at the center of the pore has roughly reached its maximum. In Fig.7, the concentration profile of the central A-blob in the KMC simulations is reasonably described by the hydrodynamic treatment. Small discrepancies presumably result from the feature that we have chosen a fairly small system, so fluctuation effects are still significant. In contrast, the MF and pair approximations fail to predict a significant peak in the concentration of A in central region. This is a consequence of the tendency of these approximations to allow artificially enhanced mixing of A and B. The pair approximation prediction is slightly closer to KMC behavior, reflecting the somewhat improved description of diffusion relative to MF.

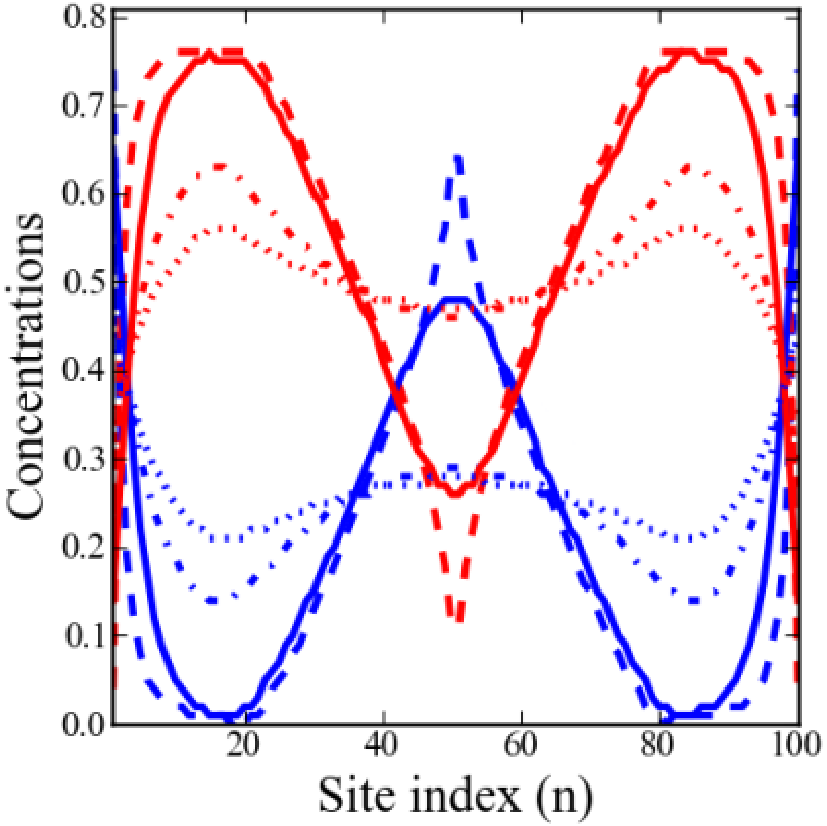

Figure 7: Behavior roughly at the end of the transient regime t = 420 for a pore of length L=100 with 20 peripheral catalytic sites at each end. Parameters are W_{ads} = 0.8, W_{des} =0.2, W_{rx} =0.017, and W_{diff} =10. Reactant A in the pore center has "run the gauntlet" through the peripheral catalytic regions. Results from: KMC (solid); hydrodynamic (dashed); pair (dot-dashed); MF (dotted).

In Fig.8, we show a series of snapshots from KMC simulations for fluctuation-dominated evolution in the *late-stage regime*. These fluctuations lead to diminution and removal of the significant A-concentration in the central non-reactive region of the pore. The diffusion of the A-blob within the non-catalytic region is clear, as well as its ultimate complete annihilation after several "collisions" with the peripheral catalytic region.

5.B. Central catalytic sites

Here, we consider situations where a contiguous string of sites in the center of the pore is catalytic, but sites in the peripheral regions are not. This geometry of catalytic sites has been considered in previous studies [14]. Towards the end of the *first transient stage* of pore filling, a central catalytic region with reactant A largely converted to product B has been created, with non-catalytic regions on both sides primarily occupied by reactant A. Then, in the *second late-stage regime*, the central catalytic region remains essentially exclusively populated by B, but the concentration of product B in the non-catalytic end regions increases and that of reactant A decreases to achieve the final steady-state form. The details of this fluctuation dominated process are described below. It should be noted that there is very low reactivity in the steady-state for this system (compared with a pore with all sites catalytic and the same parameters) since there is little population by A of the central catalytic region.

Fig.9 compares evolution in exact KMC simulations with the predictions of the hydrodynamic treatment and also the MF and pair approximations for a finite time selected to correspond roughly to the *end of the first transient regime*. In the hydrodynamic treatment, since diffusion fluxes are always towards the center of the pore, it is impossible to populate the non-catalytic end regions with B. Thus for long times in this treatment one has $\langle A_n \rangle \approx X_{eq}$ and $\langle B_n \rangle = 0$ in the non-catalytic end regions, and $\langle A_n \rangle \approx 0$ and $\langle B_n \rangle \approx X_{eq}$ in the central catalytic region. This is a steady-state in the hydrodynamic treatment, which might be described as a metastable state for the stochastic model. In fact, this simple hydrodynamic picture describes quite well the KMC results, deviations being due to fluctuations. In contrast, the MF and pair approximations predict a B-population in the non-catalytic end regions which is far too high. This is again a consequence of the tendency of these approximations to allow artificially enhanced mixing of A and B. The pair approximation prediction is slightly closer to KMC behavior, again reflecting the somewhat improved description of diffusion relative to MF.

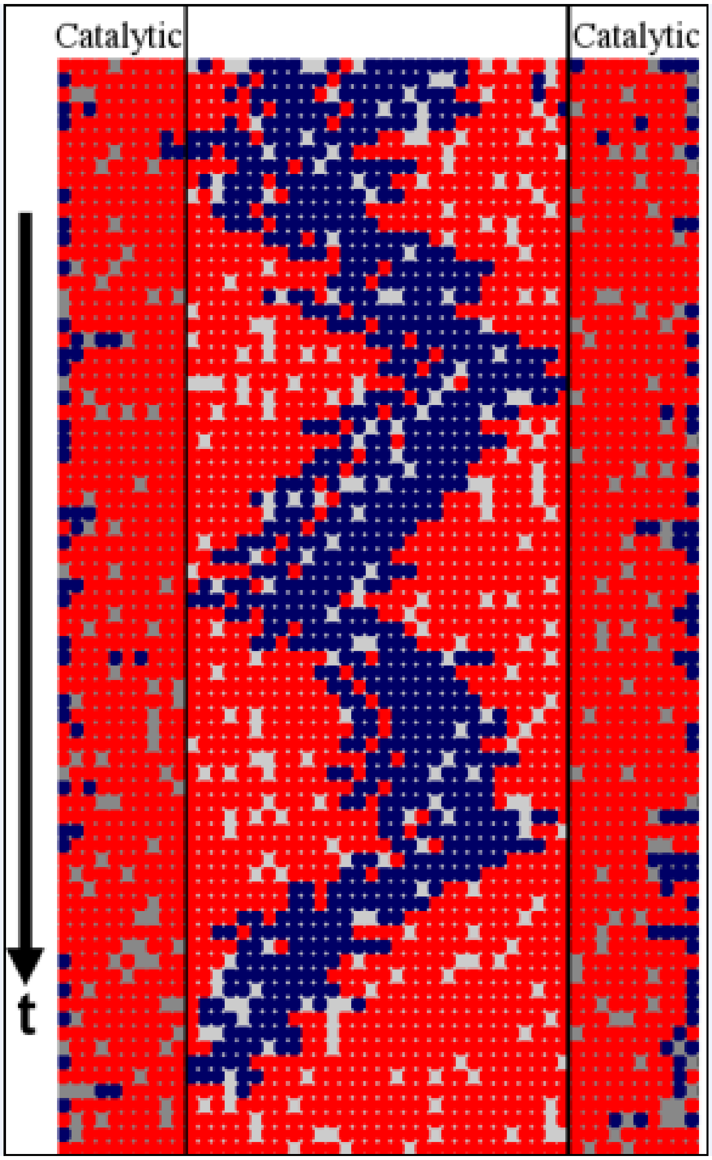

Figure 8: Later-stage evolution in a pore of length L=50 with 10 catalytic sites (gray) on each end catalytic. Dark blue circles are reactant A. Lighter red circles are product B. Sequence of images separated by 42 time units from a single KMC simulation run. Parameters are W_{ads}=0.1, W_{des}=0.9, W_{rx}=0.08, and W_{diff}=100. The central A-blob diffuses to the peripheral catalytic regions ultimately being converted to product. Higher X_{eq}=0.9 makes the A-blob more visible.

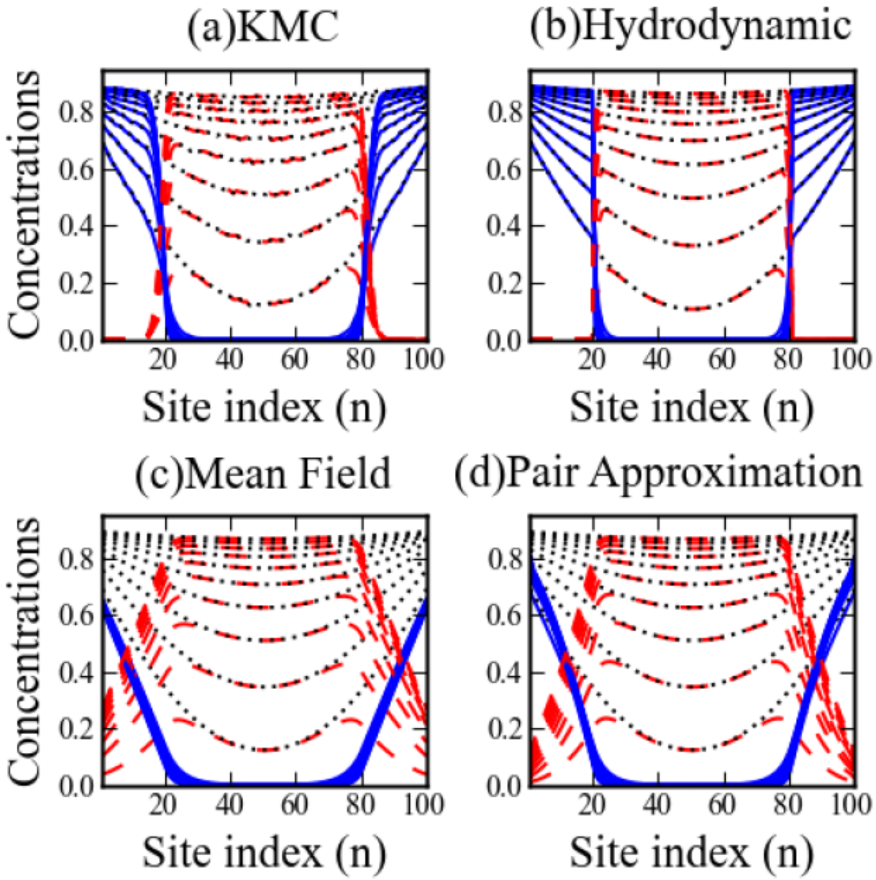

Figure 9: KMC of concentration profile evolution for the central 60 sites catalytic in a pore of length L=100. Parameters are W_{rx} = 0.33, W_{diff} = 10, and for (a) W_{ads} = 0.1, W_{des} = 0.9; (b) W_{ads} = 0.9, W_{ads} = 0.1. Time increments are 50 and the final time is t=500.

Fig. 10 shows KMC results for more complete evolution to the reactive steady-state. This occurs quite quickly for X_{eq}=0.1 (left frame). But for the case with X_{eq}=0.9 (right frame), this evolution is much slower. In either case, one finds the development of quasi-linear concentration profiles in non-catalytic end regions. Note that the MF treatment predicts linear concentration profiles in the non-catalytic end regions. This result follows from (10) noting that the steady-state J_K(MF) must be constant in these regions which yields the relation ∂/∂x K(x) = constant for K = A or B. Further insight into this behavior comes from the analysis immediately following.

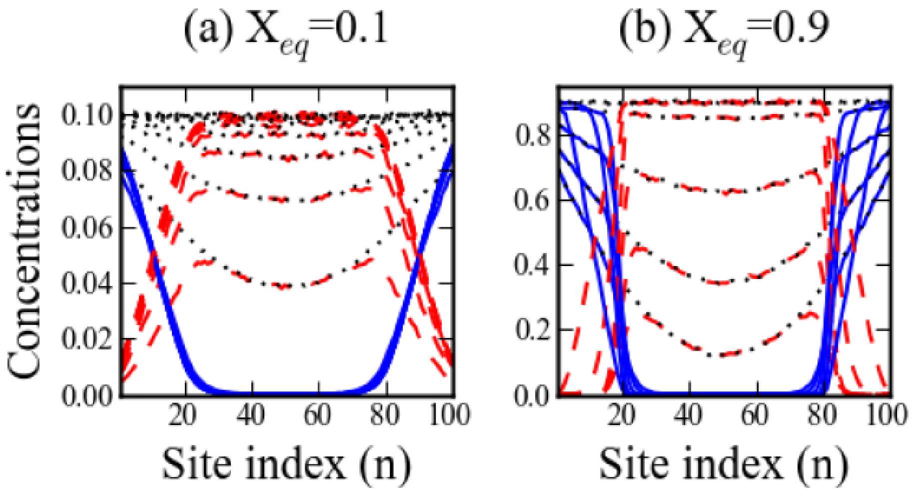

Figure 10: KMC results for the complete evolution of species concentrations for the central 60 sites catalytic in a pore of length L=100 with W_{rx} = 0.33 and W_{diff} = 10 for two cases. (a) W_{ads} = 0.1, W_{des} = 0.9 (so X_{eq}=0.1) with time-evolution in increments of 100, so the steady-state is achieved quickly by t ~700; (b) W_{ads} = 0.9, W_{ads} = 0.1 (so X_{eq}=0.9) and profiles are shown at times t=50, 100, 200, 500, 1500, 15000. Thus in (b), the steady-state is achieved slowly, where $\langle A_n \rangle$ again finally achieves a quasi-linear steady-state variation in the end non-catalytic regions.

In Fig.11, we show a series of snapshots from KMC simulations for fluctuation-dominated evolution in the *late-stage regime* for a case similar to Fig.9 where X_{eq}=0.9. These fluctuations lead to the development of a significant B-population in the peripheral non-catalytic regions of the pore (while the central catalytic region remains essentially exclusively populated by B). The simplest case is where the reaction rate W_{rx} is fairly large. Then, in any single realization of the reaction system, there is relatively little intermixing of the A and B species, i.e., the peripheral regions are essentially all A and the central region is essentially all B. (There is strictly no intermixing in the limit $W_{rx} \to \infty$.) Thus, evolution in this regime simply involves the interface between A- and B-regions undergoing an (anomalous) random walk within the non-catalytic end regions, where this random walk is effectively subject to reflecting boundary conditions. When the interface and thus A species attempts to move into the central catalytic region, those A are quickly converted to B, so the interface effectively cannot pass into the catalytic region and eventually meanders back into the non-catalytic region. When the interface and thus the B species reach the end of the pore, they can desorb and are replaced by adsorbing A species, so that the interface eventually wanders back toward the center of the pore. Thus, the quasi-linear steady-state concentrations in non-catalytic region shown in Fig.9, and also in previous studies [14], correspond to an ergodic-like time-average over the interface position.

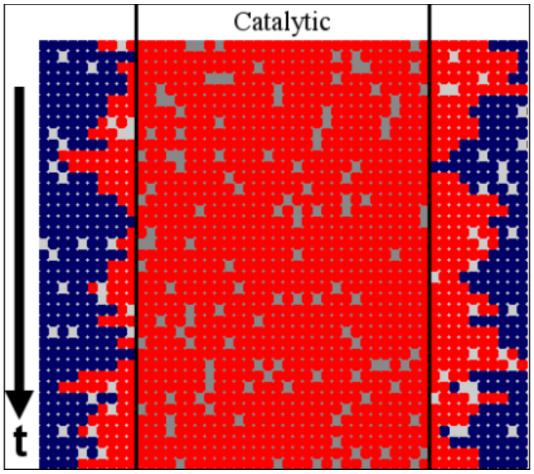

Figure 11: Later-stage evolution in a pore of length L=50 with the 30 central catalytic sites (gray). Dark blue circles are reactant A. Lighter red circles are product B. Sequence of images separated by 300 time units from a single KMC simulation run. Parameters are $W_{ads} = 0.9$, $W_{des} = 0.1$, $W_{rx} = 0.6$, and $W_{diff} = 3$. The interface between A- and B-dominated regions diffuses within the non-catalytic end regions. Higher $X_{eq}=0.9$ makes the interface more visible.

6 Generalizations and Conclusions

There are many instructive generalizations of the above model and analyses. Here, we briefly comment on a few of these. It is natural to consider *other distributions of catalytic sites* not necessarily involving contiguous strings of such site. Simple examples would be periodic or spatially homogeneous random distributions. For a conventional reaction-diffusion system (without single-file diffusion), a coarse-grained continuum description of the form (6) would simply reduce the reaction rate by a factor proportional to the local density of catalytic sites. However, in single-file systems with steady-state reactivity localized at the end of the pore, this procedure might not be effective unless the penetration depth is very large.

Other natural generalizations include the introduction of *unequal hop rates* for reactant and product species in the absence of interactions between species. Then, the behavior of the non-equilibrium steady-state will be more complex, but key features induced by single-file diffusion persist [36]. One could also introduce *interactions* between these species where all rates must be chosen to satisfy detailed-balance [13]. For simplicity, one might choose the strength of the interactions and also the adsorption-desorption rates to be species-independent (cf. [13]). Then, just focusing on whether sites are occupied by particles X=A+B, the steady-state is a conventional grand canonical equilibrium state with a uniform total particle density away from the pore ends. In the hydrodynamic regime, the chemical diffusion fluxes must still vanish in this steady-state as a consequence of the single-file nature of diffusion [36]. Thus, just as for our simpler model, one can conclude that catalytic regions inside the pore will be unreactive (as all reactant A will be converted to product), and that steady-state reactivity will be controlled by fluctuations [36].

Yet another class of generalizations of the above process include sequential conversion reactions $A \rightarrow B \rightarrow C \rightarrow . . .$ or parallel conversion reactions $A \rightarrow B$, $A \rightarrow C$, etc., at catalytic sites. For simplicity, consider the special choice of rates, $W^{K}_{des} = W_{des}$ and $W^{K}_{diff} = W_{diff}$, for all species types, K. Again, if one does not discriminate between the identity of particles, but only considers whether sites are empty, E, or filled, X=A+B+. . ., then evolution of X is described by a standard discrete diffusion equation. Furthermore, significantly, the exact hydrodynamic treatment of diffusion for the two-species case readily generalizes to treat this more complex case (cf. [37]). Thus, effective analysis of transient behavior should be possible with appropriate h-RDE, and again we expect steady-state reactivity to be controlled by fluctuation effects [36].

In summary, the transient and steady-state behavior of single-file conversion reaction systems displays some general features. Transient evolution of concentration profiles is effectively described by hydrodynamic RDE which properly incorporate the single-file nature of diffusion. However, steady-state reactivity is controlled by fluctuation effects not incorporated in the hydrodynamic treatment. MF-type treatments can capture some aspects of this steady-state behavior, but not scaling properties for extreme choices of reaction and diffusion rates.

Acknowledgments

This work was supported by the Division of Chemical Sciences (Basic Energy Sciences), U.S. Department of Energy (USDOE) through the Ames Laboratory PCTC, Chemical Physics, and Catalysis projects, and also a SULI project. Ames Laboratory is operated for the USDOE by Iowa State University under Contract No. DE-AC02-07CH11358.

Appendix A: Exact Hydrodynamic Diffusion Fluxes

Consider a two-component lattice-gas where species A and B have equal hop rates, W_{diff}, to NN empty sites, and there are no interactions beyond site exclusion. Set $D_X = a^2 W_{diff}$. Then, for hyper-cubic lattice of any dimension, the diffusion flux for species A in the hydrodynamic regime of slowly varying concentrations has the exact form [4,18,26]

$$\begin{aligned} J_A &= -D_X\, X^{-1}[A + B\, F_{tr}(X)]\, \nabla A - D_X\, X^{-1} A\, [1 - F_{tr}(X)]\, \nabla B \\ &= -D_X\, [A X^{-1}]\, \nabla X - D_X\, F_{tr}(X)\, X^{-1}\, [B\, \nabla A - A\, \nabla B], \end{aligned} \qquad (18)$$

with an analogous expression for J_B. Here, A, B and X=A+B represent concentrations per unit length, and ∇ denotes the spatial gradient. The quantity F_{tr} represents the tracer diffusion coefficient for a tagged particle with hop rate of unity within a dense single-component lattice-gas on the hyper-cubic lattice of concentration X. Generalizations have been explored for the case of unequal hop rates of A and B [4,38].

For an infinite 1D lattice, J_A is a scalar, $\nabla = \partial/\partial x$, and $F_{tr} = 0$, recovering the result (8). F_{tr} vanishes since diffusion is anomalous in 1D, the root-mean-square displacement of the tagged particle increasing like $t^{1/4}$ rather than $t^{1/2}$ [6-8]. It is instructive to note that the MF form of the diffusion fluxes (9) is recovered by choosing $F_{tr} = (1 - X/X_m)$. This offers the possibility of developing a hybrid expression for the diffusion fluxes capturing both aspects of the MF description near the pore ends and the hydrodynamic description in the pore interior [36].

Appendix B: Discrete Forms of Diffusion Fluxes

For comparison of KMC results sometimes for relatively short pores with predictions based on a hydrodynamic treatment of diffusion, we naturally incorporate an appropriate discrete version, $J_K^{n>n+1}$, of the hydrodynamic diffusion fluxes (8) into the discrete RDE's (1). We have utilized discrete forms

$$J_K^{n>n+1} = -W_{diff}\, P_K^{n,n+1}\, \Delta<X_n> \text{ with } \Delta<X_n> = <X_{n+1}>-<X_n> \text{ for K=A or B,} \tag{19}$$

with $P_K^{n,n+1} = 1$ if $<X_n><X_{n+1}> = 0$. For $<X_n><X_{n+1}> \neq 0$, one standard choice would set

$$P_K^{n,n+1} = ½\,(<K_n>/<X_n> + <K_{n+1}>/<X_{n+1}>). \tag{20}$$

However, other reasonable choices have the form $P_K^{n,n+1} = <K_{n,n+1}>/<X_{n,n+1}>$ where $<K_{n,n+1}> = ½\,(<K_n>+<K_{n+1}>)$, or $2<K_n><K_{n+1}>/(<K_n>+<K_{n+1}>)]$, or $\surd<K_n>\surd<K_{n+1}>$. Analysis of evolution typically finds only small differences between results from these different choices.

One case requiring special treatment is where just the central sites are catalytic. Then, there is a sharp boundary between a central region with finite population of B and peripheral regions devoid of B (in a continuum treatment). Choice (20) produces a substantial B-flux from the site just outside to that just inside the catalytic region, producing an unphysical negative B-concentration for the former. The same behavior occurs to varying degrees in the other choices. However, in our analysis, we eliminate this problem by setting to zero the B-flux between these two sites (and identifying the A-flux with the total particle flux).

As an aside, for the continuum MF diffusion flux (9), a standard numerical PDE treatment would implement various discretizations, e.g., analogous to (20). However, our analysis starting with the discrete master equations and applying a factorization approximation suggests the natural form

$$J_A^{n>n+1}(\mathrm{MF}) = -W_{diff}\,[(1-<B_n>)\Delta<A_n> + <A_n>\Delta<B_n>]. \tag{21}$$

Appendix C: Mean-field Behavior as $W_{diff}\to\infty$

The MF prediction for $W_{diff}\to\infty$ of spatially uniform concentration profiles enables simple analysis of the MF steady-state. Summing all of the equations for $<A_n>$ implies

$$\begin{aligned}0 &= d/dt\,(\Sigma_n <A_n>)\\ &= W_{ads}(<E_1>+<E_L>) - W_{des}(<A_1>+<A_L>) - W_{rx}\,(\Sigma_n <A_n>) + (\Sigma_n J_A^{n>n+1}=0),\end{aligned} \tag{22}$$

where $\Sigma_n J_A^{n>n+1}=0$ by symmetry. Consequently, using spatial homogeneity yields

$$\langle A_n\rangle|_{MF} = 2W_{ads}\, E_{eq}/(2W_{des} + LW_{rx}) \sim 1/L \text{ where } E_{eq} = W_{des}/(W_{ads}+W_{des}). \tag{23}$$

and $\langle A_n\rangle|_{MF} + \langle B_n\rangle\,|_{MF} = X_{eq}=1-E_{eq}$. Thus, the MF total reactivity, $R_{tot}^{MF} = W_{rx}L\langle A_n\rangle|_{MF}$, converges like 1/L, as $L\rightarrow\infty$, rather than displaying the correct exponential convergence.

Appendix D: Scaling Forms for Pore Filling

For the total concentration X(x,t), substitution of the form $X(x,t) \approx F(x/(D_x t)^{1/2})$ into the standard diffusion equation yields

$$-½\, yF'(y) = F''(y), \tag{24}$$

which is satisfied by the “classic” erfc solution. Next, consider the scaling forms $A(x,t) \approx F^A(x/(D_x t)^{1/2}, W_{rx}t)$ and $B(x,t) \approx F^B(x/(D_x t)^{1/2}, W_{rx}t)$ for the concentrations of A and B. Substitution into the hydrodynamic RDE yields

$$-½\, y\, F^A{}_1(y,u) + uF^A{}_2(y,u) = -\, uF^A(y,u) + K(F^A, F^B), \text{ and} \tag{25a}$$

$$-½\, y\, F^B{}_1(y,u) + uF^B{}_2(y,u) = +\, uF^B(y,u) + K(F^B, F^A), \tag{25b}$$

where the subscripts 1(2) denote partial differentiation with respect to the first (second) variable y (u). The “diffusion terms” K have the form

$$K(F^A, F^B) = [1-F^B]F^A{}_{11} + F^AF^B{}_{11} \text{ (MF), and} \tag{26a}$$

$$K(F^A, F^B) = F^A{}_1F^B{}_1/F - F^A\, (F)^{-2}\, (F_1)^2 + F^A\, (F)^{-1}\, F_{11} \text{ (exact hydrodynamic).} \tag{26b}$$

References

1) G. Nicolis and I. Prigogine, *Self-organization in Non-equilibrium Systems* (Wiley, New York, 1977).

2) A.S. Mikhailov, *Foundations of Synergetics I* (Springer, Berlin, 1990)

3) R. Imbihl and G. Ertl, Chem. Rev. **95**, 697 (1995).

4) J.W. Evans, D.-J. Liu, and M. Tammaro, Chaos **12**, 131 (2002).

5) D.-J. Liu and J.W. Evans, Surf. Sci. **603**, 1706 (2009) (Ertl Nobel issue).

6) A.L. Hodgkin and R.D. Keynes, J. Physiol. (London) **128**, 61 (1955).

7) T.E. Harris, J. Appl. Prob. **2**, 323 (1965).

8) P.A. Fedders, Phys. Rev. B, **16**, 1393 (1977).

9) J.G. Tsikoyiannis and J.E. Wei, Chem. Eng. Sci, **46**, 233 (1991).

10) M.S. Okino, R.Q. Snurr, H.H. Kung, J.E. Ochs, and M.L. Mavrovouniotis, J. Chem. Phys. **111**, 2210 (1999).

11) J. Kärger, M. Petzold, H. Pfieffer, S. Ernst, and J. Weitkamp, J. Catal. **136**, 283 (1992).

12) C. Rodenbeck, J. Kärger, and K. Hahn, J. Catal. **157**, 656 (1995).

13) C. Rodenbeck, J. Kärger, and K. Hahn, Phys. Rev. E **55**, 5697 (1997).

14) S.V Nedea, A.P.J. Jansen, J.J. Lukkien, and P.A.J. Hilbers, Phys. Rev. E **65**, 066701 (2002); **66**, 066705 (2002).

15) S.V Nedea, A.P.J. Jansen, J.J. Lukkien, and P.A.J. Hilbers, Phys. Rev. E **67**, 046707 (2003).

16) R. Krishna, T.J.H. Vlugt, and B. Smit, Chem. Eng. Sci.**54**, 1751 (1999).

17) D. Paschek and R. Krishna, Phys. Chem. Chem. Phys. **3**, 3185 (2001).

18) J. Quastel, Commun. Pure Appl. Math. **45**, 623 (1992).

19) N.G. Van Kampen, *Stochastic Processes in Physics and Chemistry* (North Holland, Amsterdam, 1981).

20) J.W. Evans, Rev. Mod. Phys. **65**, 1281 (1993).

21) R. Kutner, Phys. Lett. **81A**, 239 (1981)

22) J.W. Evans, Phys. Rev. B **41**, 2158 (1990).

23) T.L. Hill, *Introduction to Statistical Thermodynamics* (Addison-Wesley, Reading, 1960).

24) J.W. Evans and D.K. Hoffman, Phys. Rev. B **30**, 2704 (1984).

25) For W_{diff} <<1, the steady-state $\langle A_n \rangle \approx 0$ except for n=1 and L. Solving (1a) yields $\langle A_1 \rangle$ =

p_A<X_1> with p_A=W_{des}/(W_{des}+W_{rx}), and <B_1> = p_B<X_1> with $p_A + p_B = 1$.

26) H. Spohn, *Large Scale Dynamics in Interacting Particle Systems* (Springer, Berlin, 1991).

27) Onsager theory writes $J_K = - \Sigma_M \sigma_{K,M} \partial/x\, \mu_M$ where μ_M is the chemical potential for species M, and $\sigma_{K,M}$ are components of the conductivity tensor. Without interactions, one has that $\mu_K = (k_BT) \ln[\langle K\rangle(1-\langle X\rangle)^{-1}]$. The MF approximation sets $\sigma_{K,M} \propto (k_BT)^{-1}\langle K\rangle(1-\langle X\rangle)\delta_{K,M}$.

28) V.P. Zhdanov, Surf. Sci. **194**, 1 (1988).

29) J.W. Evans, J. Chem. Phys. **97**, 572 (1992).

30) See X. Guo, Y. De Decker, and J.W. Evans, Phys. Rev. E **82**, 021121 (2010). h-RDE have been extracted for pair approximations in simple single-species reaction diffusion models. However, for this two species model, there are additional challenges related to the asymptotic convergence of continuum quantities $a^{-1} \langle A_nB_{n+1}\rangle \sim [AB](x)$ and $a^{-1} \langle B_nA_{n+1}\rangle \sim [BA](x)$.

31) There is partial randomization of configurations as $W_{diff} \rightarrow \infty$ [15]: configurations with the same number of particles and sequence of particle types have equal probability.

32) In the steady state, one has $W_{rx}\, A(x) = -\partial/\partial x\, J_A = D_X(1-X_{eq})\, \partial 2/\partial x^2\, A(x)$ from (6) and (10), solution of which immediately reveals the exponentially decaying solutions.

33) The result C>0 and B<0 is consistent with the expectation that $\langle A_nB_{n+1}\rangle$ exceeds $\langle B_{n-1}A_n\rangle$ given a higher B concentration further into the pore.

34) J. Crank, *Mathematics of Diffusion* (Oxford University Press, Oxford, 1956).

35) S. Huh, J.W. Wiench, J.-C. Yoo, M. Pruski, and V.S.-Y. Lin, Chem. Mater. **15**, 4247 (2003).

36) D.-J. Liu, J. Wang, D.M. Ackerman, M. Pruski, H.-T. Chen, V.S.-Y. Lin, and J.W. Evans, ACS Catalysis, submitted (2011). (Victor S.-Y. Lin Memorial Issue).

37) M. Tammaro and J.W. Evans, J. Chem. Phys. **108**, 7805 (1998).

38) K.W. Kehr, K. Binder, and S.M. Reulein, Phys. Rev. B **39**, 4891 (1989).

CHAPTER 3. INTERPLAY BETWEEN ANOMALOUS TRANSPORT AND CATALYTIC REACTION KINETICS IN SINGLE-FILE NANOPOROUS SYSTEMS

Da-Jiang Liu,[1] Jing Wang,[1,2] David M. Ackerman,[1,3] Igor I. Slowing,[1] Marek Pruski,[1] Hung-Ting Chen,[1] Victor S.-Y. Lin,[1,3] and James W. Evans[1,2,4]

Modified from a paper published in *American Chemical Society Catalysis*

[1]Ames Laboratory – USDOE, and Departments of [2]Mathematics, [3]Chemistry,
and [4]Physics & Astronomy, Iowa State University, Ames Iowa 50011

Abstract

Functionalized nanoporous materials have broad utility for catalysis applications. However, the kinetics of catalytic reaction processes in these systems can be strongly impacted by the anomalous transport. The most extreme case corresponds to single-file diffusion for narrow pores in which species cannot pass each other. For conversion reactions with a single-file constraint, traditional mean-field-type reaction-diffusion equations fail to capture the initial evolution of concentration profiles, and they cannot describe the scaling behavior of steady-state reactivity. Hydrodynamic reaction-diffusion equations accounting for the single-file aspects of chemical diffusion can describe such initial evolution, but additional refinements are needed to incorporate fluctuation effects controlling, e.g., steady-state reactivity localized near pore openings.

1 Introduction

Advances in the synthesis of functionalized porous materials, either microporous zeolites (aluminosilicates) or mesoporous silica nanoparticles (MSN), have provided significant opportunities for development of new catalytic systems [1-4]. Pore diameters for zeolites are in the range of 1-2 nm [1] and those for MSN range from 2-10 nm [2]. Our focus is on the regime of small pore diameters no larger than ~2 nm. We note that the effective diameter for pores in MSN can be even smaller than the nominal ~2 nm minimum after functionalization with catalytic sites. Clearly, small pore diameters provide mechanism for selectivity. However, it is also the case that diffusive transport within such pores can be severely restricted. In the extreme case, transport within one-dimensional (1D) linear pores corresponds to so-called single-file diffusion where molecules cannot pass each other. Naturally, there have been extensive studies of transport in single-file systems, often emphasizing the anomalous nature of tracer- or self-diffusion [5,6]. This anomaly is reflected in a sub-linear increase with time in mean-square displacement of a specific “tagged” particle [7,8]. Such behavior contrasts the linear increase for conventional diffusion. However, of additional interest for catalysis, and the focus of this contribution, is the *interplay* between this type of anomalous transport and the catalytic reaction kinetics.

The above examples constitute special class from amongst general reaction-diffusion processes, which are traditionally described by mean-field *reaction-diffusion equations* (RDE) [9,10]. These RDE include a conventional mean-field treatment of chemical kinetics which ignores spatial correlations in the reactant distribution. These RDE typically also include a simplified treatment of chemical diffusion with constant Fickian diffusion coefficients and independent transport of different species. Note that chemical or collective diffusion describes the diffusion flux induced by concentration gradients [11] and is distinct from tracer diffusion mentioned above. We remark that heterogeneous catalytic reactions on two-dimensional (2D) surfaces have been effectively treated by mean-field RDE [12]. However, it is well recognized that interactions between chemisorbed reactants can produce islanding or ordering, and thus non-mean-field kinetics [13]. The complexities of diffusion in mixed reactant adlayers are less appreciated [14]. Nonetheless, such complications can be appropriately treated by realistic atomistic-level modeling [15,16].

In contrast, for 1D nanoporous reaction-diffusion systems, there is a broad appreciation of complexities of diffusion as well as analysis of certain aspects of chemical (as well as tracer) diffusion [6,17,18]. There has also been some development of approximate RDE for simple catalytic reaction models [19-21]. One might anticipate that the restricted nature of transport in these systems (as well as interactions between reactants) could induce spatial correlations in the reactant distributions, and thus deviations from mean-field reaction kinetics. The nature of the reaction kinetics, and also the interplay with chemical diffusion, have been explored in some simulation studies [19-25]. However, such analyses are limited and the current understanding is far from complete. Thus, the goal of this contribution is to provide a perspective on recent developments and also to contribute new results in the analysis of catalytic conversion and polymerization reactions in nanoporous single-file systems.

Conversion reactions (A → B) in 1D nanoporous systems with single-file diffusion have been the subject of the most extensive analyses [19-26]. It should be emphasized that for systems with inhibited passing or a strict single-file constraint, the key factor impacting reactivity is the extent to which reactants and products A and B can pass each other. The influence on reactivity of the extent of passing of reactants A with each other, and products B with each other, is relatively minor. One general expectation emerging already from earlier studies of a generic A → B conversion model with single-file diffusion [24] is that reactivity is localized near the pore openings. Various single-file conversion reactions have been considered in zeolites, including a detailed study of Pd-catalyzed neopentane conversion [25]. Our motivation here comes from studies of various conversion reactions, such as Beckman rearrangement [27,28], in functionalized MSNs with narrow pores. In some cases, the effective diameter of the pores is reduced below 2 nm by functionalization with the catalytic group. Then, larger reactant and product species cannot pass, at least not without difficulty due to the need for orientational alignment with each other and with the pore axis. We are also interested in more general catalytic transformations involving two reactants (A+A´ → B) subject to inhibited passing or a strict single-file constraint for A and B. These processes can be analyzed using the simpler A → B conversion models provided that A´ is sufficiently small so that it can readily pass both A and B, and provided that A´ is present in excess. Examples of this type might the nucleophilic catalytic reactions in MSNs functionalized with the bulky dialkylaminopyridine (DMAP-MSN) [29], and the Diels-Alder reaction in urea or thiourea-functionalized MSN [30]. As discussed further below, of particular interest for our modeling of the effects of anomalous transport is a study of the conversion of p-nitrobenzaldehyde (PNB) to an aldol compound in amine-functionalized MSN where the dependence of reactivity on effective pore diameter has been quantified [31].

Fundamental questions for these conversion reactions still requiring resolution include:

(i) How does overall reactivity depend on basic parameters such as the intrinsic rate of reaction for reactant species in the vicinity of a catalytic site and on species mobility within the pore?

(ii) How does the propensity for passing of various reactant and product species within the pore (which depends strongly on pore diameter) affect the overall reactivity?

(iii) How does the distribution of catalytic sites affect overall reactivity, particularly catalytic functionalization restricted to near the pore openings versus uniformly throughout the entire pore?

(iv) To what extent can the evolution of concentration profiles and thus reactivity be described within a traditional deterministic mean-field-type RDE picture as opposed to being controlled by stochastic effects (e.g., fluctuations in numbers of adsorbing and desorbing species at the pore openings).

(v) Can shortcomings of traditional RDE approaches be overcome by refined treatments?

In this study, we consider simple $A \to B$ and sequential $A \to B \to C$ conversion reaction mechanisms, and provide new insights and modeling strategies addressing the above issues.

In Sec.2, we describe the conversion reaction models analyzed in this study, together with the hierarchical form of the associated exact master equations. In Sec.3, we present hydrodynamic RDE formulations for continuous coarse-grained versions of the models. Precise results from KMC simulations are compared with predictions from various analytic formulations in Sec.4. Conclusions are provided in Sec.5.

2 Conversion Reactions: Models and Master Equations

2.A. Models

First, we describe a general class of models for the diffusion-mediated catalytic conversion of a reactant to a product ($A \to B$) inside narrow pores. Reactants and products are localized to sites of a 1D linear lattice traversing the pore, or more generally to sites on a ladder (see Fig.1). The separation between adjacent sites is given by the lattice constant “a” which is selected to be comparable to the reactant and product size (~1 nm). The simplest scenario for diffusion is that A and B hop to adjacent empty sites. This prescription corresponds to single-file diffusion with a strict no-passing constraint on the 1D linear lattice, but not on the ladder. One could allow positional exchange of adjacent A and B on the 1D linear lattice to relax the strict single-file constraint, noting that exchange of adjacent particles of the same type has no effect. (Allowing longer hops over other particles would also relax the constraint.) On the other hand, one could impose a nearest-neighbor (NN) exclusion constraint on the linear ladder which would enforce no-passing. One has considerable flexibility treating diffusive dynamics! The other mechanistic steps in the model are: adsorption of external reactant species A at terminal sites of the pore provided that these sites are unoccupied or empty (E); conversion A → B at catalytic sites (c) within the pore; and desorption of both the reactant, A, and product, B, from terminal sites of the pore. The catalytic sites may constitute all sites or various subsets of sites within the pore. These mechanistic steps and a configuration with catalytic sites just near the pore openings are also illustrated in Fig.1. The total reactivity (i.e., the total production rate of B) is proportional to the total amount of A within the catalytic regions of the pore. Sequential conversion reactions, e.g., A→B→C, could also be considered.

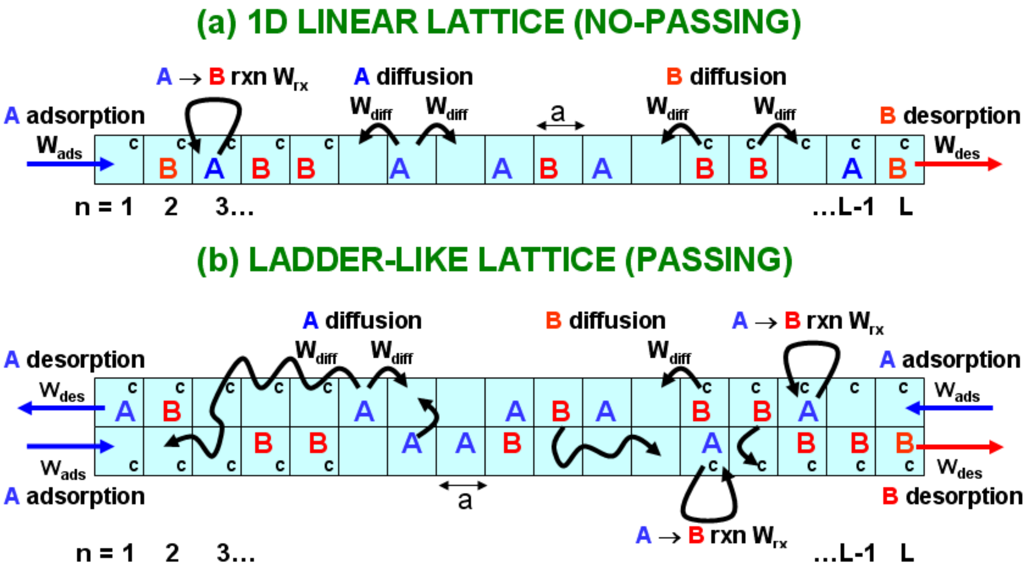

Figure 1: Schematic of the A→B conversion reaction (rxn) model with hopping only to NN empty sites within a pore described by: (a) a 1D linear lattice (no passing); (b) a ladder-like lattice (passing). Here, only sites near pore ends are catalytic "c", and desorption and hopping rates for A and B are equal; n labels sites in the direction along the pore axis.

2.B. Hierarchical master equations

We first formulate our model for a general sequential conversion reactions A→B→C→. . .

(including A→B as a special case) on a linear lattice. Sites in the pore are labeled by n=1, 2,…, L (for pore length L), so that the terminal sites are n=1 and n=L. Allowing only hopping to NN empty sites results in strict single-file diffusion, but this constraint is relaxed if one includes exchange of NN particles. Rates for the various processes will be denoted by: $W_{ads}(A) = W_{ads}$ for adsorption of A; $W_{des}(K)$ for desorption of species K=A, B,...; $W_{diff}(K)$ for hopping to NN empty sites for K; $W_{ex}(K|K')$ for exchange of NN K and K´; and $W_{rx}(A)$ for A→B conversion, etc.. An exact analytical description of such stochastic Markov processes is provided by the *master equations* for the evolution of probabilities of various configurations for the entire system [32]. Often these are written in *hierarchical form* [19-23]. Here, we use $<K_n>$ to denote the probability or ensemble averaged concentration for species K at site n, $<K_nE_{n+1}>$ for the probability that K is at site n and for site n+1 to be empty (E), etc.. Then, the lowest-order equations in the hierarchy describe the evolution of the probabilities for individual sites to be occupied by various species.

For just A→B conversion in the case where *all sites are catalytic*, one has that

$$d/dt <A_1> = W_{ads}<E_1> - W_{des}(A)<A_1> - W_{rx}(A)<A_1> - J_A^{1>2}, \tag{1a}$$

$$d/dt <B_1> = - W_{des}(B)<B_1> + W_{rx}(A)<A_1> - J_B^{1>2}, \tag{1b}$$

$$d/dt <A_n> = -W_{rx}(A)<A_n> - J_A^{n>n+1} + J_A^{n-1>n}, \text{ for } 1<n<L, \tag{1c}$$

$$d/dt <B_n> = +W_{rx}(A)<A_n> - J_B^{n>n+1} + J_B^{n-1>n}, \text{ for } 1<n<L, \tag{1d}$$

together with equations for the terminal site n=L similar to those for n=1. In these equations,

$$J_A^{n>n+1} = W_{diff}(A)[<A_nE_{n+1}> - <E_nA_{n+1}>] + W_{ex}(A|B)[<A_nB_{n+1}> - <B_nA_{n+1}>], \tag{2}$$

denotes the *net* flux of A from site n to n+1. The expression for $J_B^{n>n+1}$ is similar. The total rate of production of B is given by $R^B_{tot} = W_{rx}(A)\ \Sigma_{n=c}<A_n>$, where the sum is over all catalytic sites (i.e., over all sites in this example).

It is instructive to consider the special case where $W_{ex}(A|B) = W_{diff}(A)$, so that transport of A including passing of B is completely unhindered (in some sense the opposite of a strict single-file constraint). Then, it follows that (2) reduces exactly to $J_A^{n>n+1} = W_{diff}(A)\ [<A_n> - <A_{n+1}>]$. An analogous exact reduction of diffusion fluxes was demonstrated by Kutner [33] for a single-species system.

The equations (1) are coupled to probabilities for various configurations of site pairs. Equations for pair probabilities couple to those for triples, etc., thus generating a hierarchy. Pair, triplet, etc., probabilities are not simply related to single-site probabilities due to spatial correlations deriving from the reaction-diffusion process. A simple mean-field (MF) factorization approximation, $\langle K_nE_{n+1}\rangle \approx \langle K_n\rangle\langle E_{n+1}\rangle$, etc., produces a closed set of discrete reaction-diffusion equations (dRDE) for single-site concentrations, $\langle A_n\rangle$ and $\langle B_n\rangle$, noting that $\langle A_n\rangle + \langle B_n\rangle + \langle E_n\rangle = 1$. A higher-level pair approximation retains pair quantities like $\langle K_nE_{n+1}\rangle$, but factorizes triplet quantities, e.g., $\langle K_nM_{n+1}N_{n+2}\rangle \approx \langle K_nM_{n+1}\rangle\langle M_{n+1}N_{n+2}\rangle/\langle M_{n+1}\rangle$, with K, M, N = A, B, or E. This generates a closed set of equations for single-site quantities, $\langle A_n\rangle$ and $\langle B_n\rangle$, and the pair quantities, $\langle K_nM_{n+1}\rangle$, with K, M = A or B [19-23]. Such approximations should not be expected to accurately capture all features of single-file diffusion. It is straightforward to generalize the exact master equations and approximations to the case of more general sequential conversion reactions $A \to B \to C \to \ldots$

Similar to previous studies of the A → B reaction [20-23], we will explore this and the more general reaction $A \to B \to C$ for a parameter choice where the *desorption rates and diffusion rates are equal for all species*, i.e., $W_{des}(K) = W_{des}$ and $W_{diff}(K) = W_{diff}$, for K = A, B, and C. There is an important consequence of this rate choice. Suppose one does not discriminate between the identity of particles, but only considers whether sites are empty, E, or filled, X=A+B+…. Then, the particle dynamics corresponds to a pure adsorption-desorption-diffusion process for particles X with *no reaction*. Thus, the single-site concentrations, $\langle X_n\rangle$, satisfy a standard discrete diffusion equation with constant (concentration-independent) diffusion coefficient [20,22,33,34]. Since there is no reaction in the dynamics of particles X, the steady-state corresponds to a conventional Gibbsian grand canonical equilibrium state. Furthermore, since there are no interactions between particles X at different sites, they are randomly distributed in this equilibrium state (i.e., there are no spatial correlations). The equilibrium concentration at each site satisfies $\langle X_n\rangle_{eq} = X_{eq} = W_{ads}/(W_{ads}+W_{des})$ [19-22]. Below, we always choose $W_{ads} + W_{des} = 1$ which sets the time-scale.

3 Conversion Reactions: Hydrodynamic Regime

In discrete LG reaction-diffusion systems, it is common to consider behavior in the "hydrodynamic regime" where there is sufficient diffusion to produce slowly varying particle concentrations over several lattice constants [12,14,35]. This treatment applies to models where the particles are confined either to a linear lattice or to more general ladder-like lattices.

3.A. Hydrodynamic reaction-diffusion equations

In the hydrodynamic regime, behavior is described by continuum hydrodynamic reaction-diffusion equations (hRDE) after coarse-graining. Specifically, for linear or ladder lattices, one sets x = na, where n is the lattice site label in the direction along the pore. Then, species concentrations per unit length become functions of a continuous variable $K(x=na) \approx a^{-1} \langle K_n \rangle$ (leaving t-dependence implicit). Thus, $X_m=1/a$ corresponds to the maximum concentration per unit length. Below, we set a=1.

The hRDE in our A→B conversion reaction model with all sites catalytic for individual species concentrations, A(x) for A, and B(x) for B (leaving implicit the t-dependence), have the form

$$\partial/\partial t\, A(x) = -W_{rx}(A)\, A(x) - \partial/\partial x\, J_A, \tag{3a}$$

$$\partial/\partial t\, B(x) = +W_{rx}(A)\, A(x) - \partial/\partial x\, J_B. \tag{3b}$$

The total concentration satisfies X(x) = A(x)+B(x), and E(x) = 1-X(x) gives the concentration of empty sites. If sites within the pore are catalytic only in specific regions (e.g., the peripheral regions), then the reaction terms appear only for those locations. Boundary conditions for (3) at the pore ends reflect the adsorption-desorption dynamics [22]. Description of the diffusion fluxes, J_K, for K = A and B is non-trivial for this mixed lattice-gas, even in the absence of interactions beyond site-exclusion. However, Onsager transport theory [17,18,35] ensures that, e.g., the diffusive flux of A has the form

$$J_A = -\,D_{A,A}\, \partial/\partial x\, A(x) - D_{A,B}\, \partial/\partial x\, B(x), \tag{4}$$

where the diffusion coefficients $D_{A,K}$ generally depend on species concentrations. A similar expression applies for the flux, J_B, of B. One *simple case* allows exchange of A and B with $W_{ex}(A|B) = W_{diff}(A)$, i.e., unhindered transport of A including passing of B, as discussed in Sec.2B. Then, it follows that $D_{A,A} = a^2 W_{diff}(A)$ and $D_{A,B} = 0$, i.e., the presence of B does not interfere with the diffusion of A.

We will compare predictions of a discrete form of these RDE with results from KMC simulation. The appropriate discretization of the reaction kinetics is clear (e.g., from the exact master equations) [22], and that for the diffusion fluxes is mentioned below. The above formulation naturally extends to sequential conversion reactions, e.g., A → B → C.

3.B. Diffusion fluxes for species-independent hop rates

Here, we consider the case of non-interacting lattice-gases (with exclusion of multiple site occupancy) with two components A and B on linear or ladder lattices and with *equal hop rates* to NN empty sites, so that $W_{diff}(A) = W_{diff}(B) = W_{diff}$, and where exchange can be operative at rate $W_{ex} = W_{ex}(A|B)$. Then, in the hydrodynamic regime, one has that [35-38]

$$\begin{aligned} J_A &= -\, X(x)^{-1}[D_X\, A(x) + B(x)\, D_{tr}(X)]\, \partial/\partial x\, A(x) \\ &\quad - X(x)^{-1} A(x)\, [D_X - D_{tr}(X)]\, \partial/\partial x\, B(x) \\ &= -D_X\, [A(x) X(x)^{-1}]\, \partial/\partial x\, X(x) \\ &\quad - D_{tr}(X)\, X(x)^{-1}\, [B(x)\, \partial/\partial x\, A(x) - A(x)\, \partial/\partial x\, B(x)], \end{aligned} \tag{5}$$

with $D_X = a^2\, W_{diff}$ [39]. An analogous expression applies for J_B. $D_{tr} = D_{tr}(X)$ represents the tracer diffusion coefficient for a tagged particle within a dense single-component lattice-gas of concentration $X = X(x)$ with hop rate of W_{diff} to NN empty sites, and where all NN pairs of particles can exchange with rate W_{ex}. For systems with *no single-file constraint*, e.g., due to exchange with adjacent particles on a 1D linear lattice, or due to a ladder-like lattice model of pore structure, $D_{tr} = D_{tr}(X)$ is non-zero and depends in a non-trivial way with $X = X(x)$. It should decrease from D_X to 0 as X increases from 0 to 1. In the special case of unhindered exchange with $W_{ex} = W_{diff}$, one has that $D_{tr}(X) = D_X$ for all X. In this case, (5) reduces to $J_A = -D_X\, \partial/\partial x\, A(x)$ consistent with the analysis of this simple case in Sec.3A.

Next, we describe the form of these diffusion fluxes for a linear lattice constituting a strict *single-file system* for different choices of D_{tr}. In the *hydrodynamic limit for large systems*, one has the exact result $D_{tr}(X) = 0$. This is a consequence of the anomalous nature of the diffusion of a tagged particle. Then, (5) gives the *exact hydrodynamic (h) diffusion fluxes* [22]

$$J_K(h) = -D_X\,[K(x)/X(x)]\,\partial/\partial x\,X(x), \text{ for } K = A \text{ or } B. \tag{6}$$

This result follows directly from (5) and is also intuitively clear. The J_K must sum to the total diffusion flux which satisfies $J_X = -D_X\,\partial/\partial x\,X(x)$ for this non-interacting lattice-gas, and the individual fluxes are in proportion to the local species concentrations.

The *mean-field (MF) treatment* for a single-file system sets $D_{tr}(X) = D_X\,[1 – X]$ which yields chemical diffusion fluxes with the form

$$J_A(MF) = -D_X\,[1 - B(x)]\,\partial/\partial x\,A(x) - D_X\,A(x)\,\partial/\partial x\,B(x), \tag{7}$$

and an analogous expression applies for $J_B(MF)$. This result has been obtained previously by making simple MF-approximations for the conductivity in Onsager's transport theory [17,18,40], and also from coarse-graining of a MF approximation to the discrete hierarchical master equations [20,22,41]. This MF form (7) can produce artificially high diffusion fluxes relative to (6).

Finally, we introduce a *perturbed hydrodynamic (ph) treatment* for a single-file system which is intended to account for finite system size (i.e., finite pore length, L). We first note that the tracer diffusion for finite 1D systems of L sites with periodic boundary conditions satisfies $D_{tr} = D_{tr}(X, L) = X^{-1}[1–X]D_X/(L-1)$ where the concentration is restricted to $X = m/L$ for m particles in the system [42]. For finite open systems of L sites where transport is *not* limited by adsorption-desorption at the pore ends, we use the effective form

$$D_{tr}(X, L) \approx [1–X]D_X/[1 + X(L-1)]. \tag{8}$$

This choice is motivated by analogous expressions for D_{tr} applied in the analysis of membrane transport [43], and by noting that (8) recovers the desired results that $D_{tr} \rightarrow 0$ as $X \rightarrow 1$, and $D_{tr} \rightarrow D_X$ as $X \rightarrow 0$. The requirement that transport is not adsorption-desorption limited in our modeling will be met by restricting consideration to cases where $W_{ads} + W_{des} \geq W_{diff}$. In our perturbed hydrodynamic treatment, we incorporate the expression (8) into the general form (5) for $J_K = J_K(ph)$.

The steady-state of our model has a constant particle concentration, $X(x) = X_{eq} = W_{ads}/(W_{ads}+W_{des})$. Thus, for the case of a *single-file system* treated above, the *steady-state diffusion fluxes* have the form

$$J_K(h) \to 0,\ \ J_K(MF) \to -D_X(1-X_{eq})\, \partial/\partial x\, K(x), \text{ and } J_K(ph) \to -D_{tr}(X_{eq})\, \partial/\partial x\, K(x), \tag{9}$$

as $X(x) \to X_{eq}$ (constant). In the hydrodynamic treatment, this result implies that the pore is populated only by the product B if all sites are catalytic; the pore can have non-trivial frozen concentration distributions in regions with no catalytic sites. These artificial features are erased in the perturbed hydrodynamic treatment. One anticipates that the mean-field treatment results in artificially large diffusion fluxes in the steady-state.

As noted above, we will compare the predictions of discrete versions of various RDE with results of KMC simulation for both transient and steady-state behavior. To this end, one must implement a natural discrete version of the diffusion fluxes. For the MF approximation, this is automatically provided from the master equations, and for other cases we utilize choices described elsewhere [22].

4 Conversion Reactions: KMC and Analytic Results

4.A. All sites catalytic (A→B)

Here, we highlight the key features of steady-state behavior for our single-file A→B conversion reaction model, the shortcomings of popular mean-field treatments in describing this behavior, and the potentially far higher reactivity of systems with no single-file constraint. Our parameter choice is $W_{ads} = 0.8$, $W_{des} = 0.2$ (so $X_{eq} = 0.8$), $W_{diff} = 1$, with fairly low reaction rate $W_{rx} = W_{rx}(A) = 0.001$ which will amplify the above differences, for a pore of length L=100. To analyze behavior, it is instructive to introduce the concept of a penetration depth, L_p, for reactant A. In the steady-state, one typically finds a roughly exponential decay of the concentration $\langle A_n \rangle \sim \exp(-n/L_p)$ into the pore for $n \ll L/2$, with possible deviations for the first few sites n=1,2,…. [20,22]. Determination of L_p allows an assessment of steady-state reactivity since $R^B{}_{tot} \sim W_{rx}(A)\, L_p$. Fig.2a shows steady-state concentration profiles for single-file diffusion noting that $\langle X_n \rangle = \langle A_n \rangle + \langle B_n \rangle = X_{eq} = 0.8$ for all n. The small penetration for the exact KMC results (thickest line) with L_p(KMC) ≈ 2.6 reflects single-file effects where the center of the pore is devoid of reactant and thus does not contribute to R^B_{tot}. The MF prediction, L_p(MF) ≈ 14.1, greatly overestimates L_p due to artificial intermixing of A and B, and the pair approximation (not shown) does only slightly better with L_p(pair) ≈ 9.3. The hydrodynamic treatment predicts essentially no penetration of the pore, and the perturbed hydrodynamic treatment does only slightly better with L_p(ph) ≈ 1.6. None of these analytic treatments reliably captures behavior near the pore ends which is controlled by fluctuations in adsorption-desorption processes (a feature completely neglected in the standard hydrodynamic treatment).

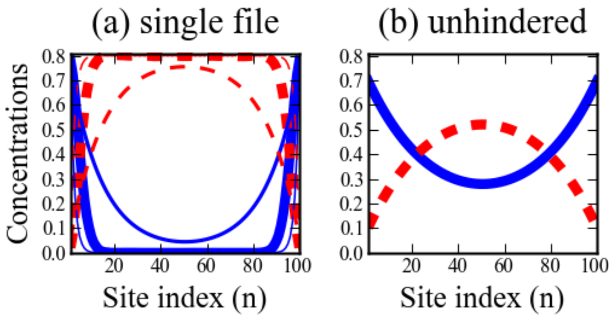

Figure 2: Steady-state concentration profiles for the A→B reaction for all sites catalytic: $W_{ads} = 0.8$, $W_{des} = 0.2$, $W_{diff} = 1$, $W_{rx}(A) = 0.001$, and L=100. (a) Single-file diffusion: KMC, MF and perturbed hydrodynamic results are shown as thick, moderate, and thin lines, respectively. (b) Unhindered passing (exact results). Solid blue lines $<A_n>$; dashed red lines $<B_n>$.

To further understand the shortcomings of analytic theories, we note that the MF, pair, and also higher-order triplet, etc. [44] approximations naturally predict a functional dependence $L_p \sim (W_{rx}/W_{diff})^{-1/2}$ for $W_{rx}/W_{diff} <<1$. The perturbed hydrodynamic treatment actually predicts the same dependence, but with a much smaller prefactor. In contrast, simulation analysis (details not shown) indicates distinct non-MF behavior, $L_p \sim (W_{rx}/W_{diff})^{-n}$ for $W_{rx}/W_{diff} <<1$, where n ≈ 1/3 [45].

Finally, we contrast single-file behavior with that for unhindered passing of A and B which can be determined analytically using the exact form of the fluxes $J_K^{n>n+1}$ described in Sec.2B. Fig.2b reveals a far greater penetration of reactant, A, into the pore in this case with L_p ≈ 31. This feature and the associated higher reactivity are expected given the more facile diffusive transport [24].

4.B. All sites catalytic (A→B→C)

In Fig.3, we show the time-evolution toward the *steady-state* for a pore of length L=25, for the single-file A→B→C sequential conversion reaction where all sites are catalytic, W_{ads} =0.2, and all species have the same hopping and desorption rates, W_{des} = 0.8, and W_{diff} = 1. We choose $W_{rx}(A) = 0.4$ and $W_{rx}(B) = 0.2$ low enough to ensure a significant population of A and B in the pore, but high enough so that center of pore is exclusively populated by C. Note that steady-state profiles for A and B are achieved quickly, but subsequent filling of the pore center (essentially just by C) occurs on a slower time scale. The steady-state has $\langle A_n \rangle + \langle B_n \rangle + \langle C_n \rangle = X_{eq} = 0.2$ for all n, but the hydrodynamic treatment would incorrectly predict that all interior sites are populated only by C with $\langle C_n \rangle = 0.2$. The perturbed hydrodynamic treatment is closer to the KMC results, but cannot correctly predict the extent of penetration of A and B into the pore. The mean-field and pair approximations capture the exact KMC behavior quite well in this case, but only because all rate parameters have similar magnitude.

Next, we consider transient behavior associated with *filling of a very long (semi-infinite) pore* for the single-file A→B→C reaction with all sites catalytic and the above parameters. Recall that the total concentration satisfies a standard discrete diffusion equation which reduces to the conventional continuum equation in the hydrodynamic regime. Thus, total concentration profiles collapse onto a single curve for increasing t after rescaling the n-axis by $(W_{diff}\, t)^{1/2}$. However, to achieve non-trivial scaling species profiles with significant populations of all species inside the pore, it is necessary to reduce the reaction rates as time is increased so that $W_{rx}(K)\cdot t$ remains constant for all K. See Ref.[22]. More precisely, we find scaling solutions for the individual species concentrations of the form

$$\langle K_n(t) \rangle \approx X_{eq}\, F^K(n/(W_{diff}\, t)^{1/2}, W_{rx}(A)t, W_{rx}(B)t), \text{ for } K = A, B, \text{ and } C, \qquad (10)$$

where $F^A(y,u,w) + F^B(y,u,w) + F^C(y,u,w) = F(y) = \text{erfc}(y/2)$. Here, erfc is the complementary error function and corresponds to the scaling solution for the classic non-reactive diffusion problem for a semi-infinite system [46]. Substitution of (12) into the hydrodynamic reaction-diffusion equations (3) consistently yields a closed coupled set of partial differential equations for the $F^K(y,u,w)$ (cf. [22]).

The observations above on fluctuation effects suggest that: (i) The MF and pair approximations should capture fluctuation-dominated behavior better for shorter t when most particles are close to the pore opening. (ii) The hydrodynamic treatment should better describe behavior for longer t where concentration profiles are smooth and broad. Indeed, this is the case as shown in Fig.4 where $W_{ads} = 0.2$, $W_{des} = 0.8$, $W_{diff} = 1$, and $W_{rx}(B) = 0.5W_{rx}(A)$ with fixed $W_{rx}(A)\cdot t=4$. The peaks in $\langle B_n\rangle$ ($\langle C_n\rangle$) of around 0.05 (0.03) in the MF and pair approximations match KMC results for smaller t (larger W_{rx}), but these values persist for longer t. In contrast, the peak in $\langle B_n\rangle$ ($\langle C_n\rangle$) in the hydrodynamic treatment increases to about 0.09 (0.07) in good agreement with KMC results for longer t (smaller W_{rx}).

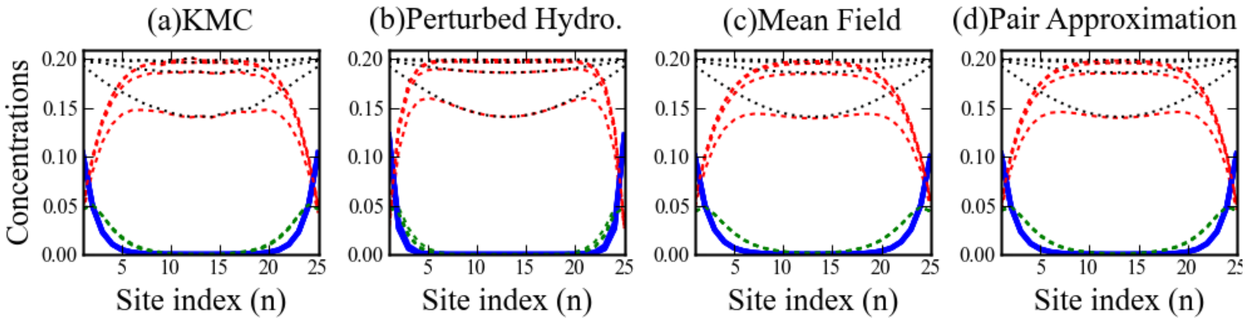

Figure 3: Concentration profiles for the A→B→C reaction for all sites catalytic: $W_{ads} = 0.2$, $W_{des} = 0.8$, $W_{diff} = 1$, $W_{rx}(A) = 0.4$, $W_{rx}(B) = 0.2$, and L=25. Solid blue lines $\langle A_n\rangle$; short-dashed green $\langle B_n\rangle$; short-dashed red $\langle C_n\rangle$; dotted black $\langle X_n\rangle = \langle A_n\rangle + \langle B_n\rangle + \langle C_n\rangle$. (a) KMC simulation; (b) perturbed hydrodynamic treatment; (c) MF and (d) pair approximations. t = 100, 200, 300, and 400 where $\langle X_n\rangle$ and $\langle C_n\rangle$ increase with t.

4.C. Peripheral sites catalytic (A→B)

We consider behavior for the A→B reaction for situations where contiguous strings of sites at each end of the pore are catalytic, but *not* those in the center. This type of distribution might result when catalytic sites are created by grafting after formation of a mesoporous material, in contrast to a co-condensation process [3]. An example of the results of KMC simulations for evolution to the steady-state is shown in Fig.5. The parameter choice is $W_{ads} = 0.8$, $W_{des} = 0.2$ (so $X_{eq} = 0.8$), $W_{diff} = 1$, and $W_{rx} = 0.001$, for a pore of length L=100 (as in Sec.4A) with just 20 catalytic sites at each end

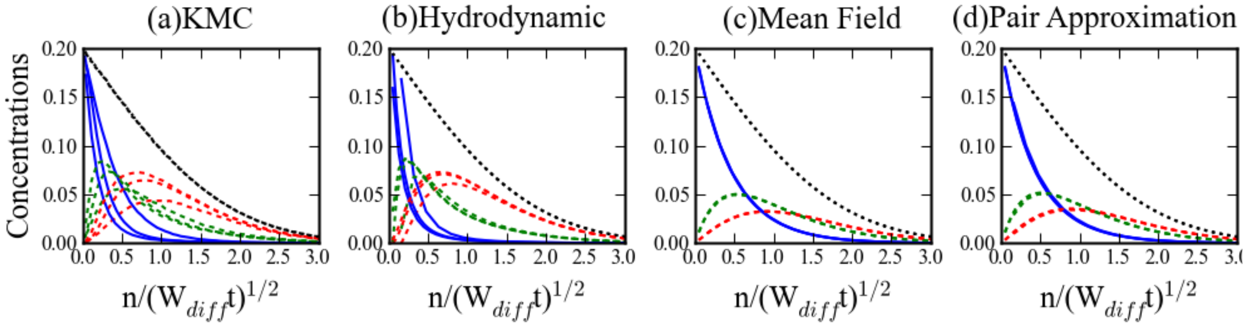

Figure 4: Scaled concentration profiles near the end of a semi-infinite pore for the A→B→C reaction with for all sites catalytic during pore filling: $W_{ads} = 0.2$, $W_{des} = 0.8$, $W_{diff} = 1$, $W_{rx}(B) = 0.5W_{rx}(A)$ with fixed $W_{rx}(A)\cdot t=4$. (a) KMC for $W_{rx}(A)= 0.01, 0.0001, 0.000001$. (b) hydrodynamic, (c) MF, and (d) pair approximations for $W_{rx}(A)= 0.1, 0.01$, and 0.001. Solid blue lines $<A_n>$; short-dashed green $<B_n>$; short-dashed red $<C_n>$; dotted black $<X_n>$ (an erfc curve). B and C profiles increase (A decreases) with t.

Characterization of behavior is naturally divided into distinct regimes. First, in the *pore-filling regime*, some A successfully “runs the gauntlet” avoiding reaction in the peripheral catalytic regions and diffuses into the central non-catalytic region (Fig.5a). Second, after pore filling where $<X_n> \sim X_{eq} \sim$ constant, a *metastable regime* persists for ~10^3-10^4 time units. In this regime, there is a peak in the quasi-static concentration of A (i.e., a “blob” of A) in the center of the pore. Third and finally, there is a *slow relaxation regime*, where the population of A in the center of the pore decreases leading to the true steady-state where the pore center is almost devoid of A by t~10^6 (Fig.5b). In fact, the final steady-state is very similar to that for a pore of length L=100 with all sites reactive in Sec.4A (cf. Fig.2)..

Fig.6 compares the KMC simulation results with predictions of analytic treatments for a finite time corresponding to the end of the pore-filling regime. The standard *hydrodynamic treatment* reasonably describes concentration profile of the central A-blob in the KMC simulations, but evolves to a steady-state close to the profile shown. This “artificial” steady-state (which corresponds to the metastable state in the actual model), and a slight difference from KMC profile shape, derive from the neglect of fluctuations. In contrast, the *MF and pair approximations* (which incorporate artificially enhanced intermixing of A and B) fail completely to predict a significant peak in the concentration of A in central region. The pair approximation prediction (incorporating a somewhat better description of diffusion) is slightly closer to exact behavior. Significantly, the *perturbed hydrodynamic treatment* describes almost perfectly the shape of the A-profile in the non-catalytic pore center. Furthermore, this treatment eliminates the artificial steady-state of the standard hydrodynamic treatment and effectively describes evolution of concentration profiles in all three regimes (Fig.5c-d). The only shortcoming is in the description of concentration profiles near the pore ends (analogous to that noted in Sec.4A).

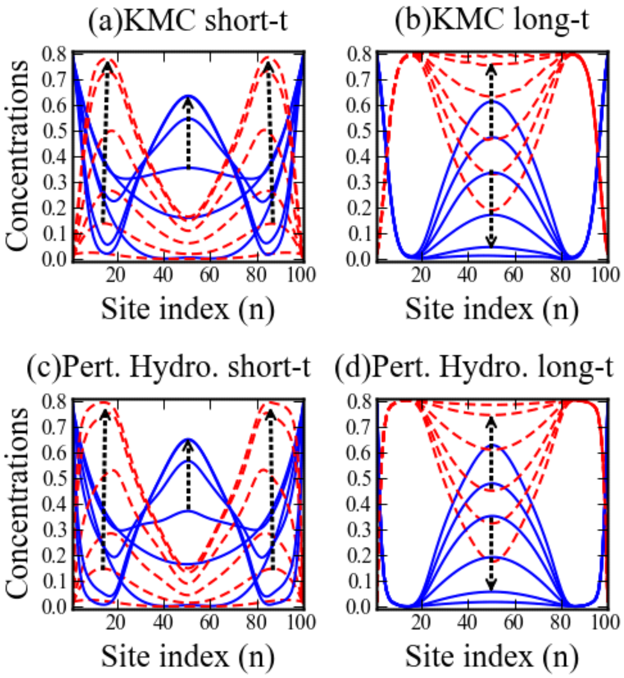

Figure 5: Complete evolution of species concentrations for the A→B reaction: W_{ads} = 0.8, W_{des} =0.2, W_{diff} =1, and W_{rx} =0.001, and L=100 with 20 catalytic sites at each end. Solid blue lines $\langle A_n \rangle$; dashed red $\langle B_n \rangle$. Top row: (a,b) KMC results. Bottom row: (c,d) perturbed hydrodynamic treatment. Left column: (a,c) pore-filling regime for t=1,5,10,20,40,60 (x10^2) where $\langle A_{50} \rangle$ grows. Right column: (b,d) late-stage evolution for t = 1,5,10,20,40,60 (x10^4) where $\langle A_{50} \rangle$ decreases. Black dotted arrows are in the direction of increasing t.

Finally, we describe in more detail the nature of fluctuation-dominated evolution in the last *slow relaxation regime*. The “blob” of A formed in the central non-catalytic region during pore filling is not frozen, but undergoes anomalous diffusion due to fluctuations allowing it to reach the peripheral catalytic regions. Eventually, essentially all of the A in this blob will be converted to B after a number of “collisions” with the catalytic regions. See Fig.7 for snapshots of this behavior from KMC simulations.

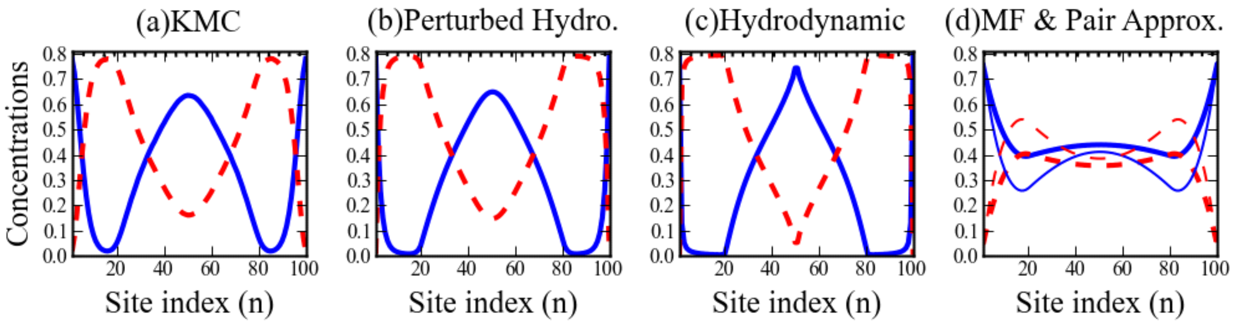

Figure 6: Behavior at the end of the pore-filling regime t ≈ 6000 for the A→B reaction: W_{ads} *= 0.8,* W_{des} *=0.2,* W_{diff} *=1,* W_{rx} *=0.001, and L=100 with 20 peripheral catalytic sites. Solid blue lines <*A_n*>; dashed red lines <*B_n*>. A in the pore center “ran the gauntlet” past catalytic regions. (a) KMC; (b) perturbed hydrodynamic; (c) hydrodynamic treatments; (d) MF (thicker lines), pair (thinner lines) approximations.*

5 Summary and Conclusions

There have been several previous experimental and theoretical studies of *catalytic conversion reactions in single-file systems* primarily motivated by catalysis in zeolites. A picture has emerged for these systems of low reactivity localized near the pore openings, but a comprehensive and reliable theoretical framework is still lacking. Similarly, for conversion reactions in functionalized MSN with narrow pores where passing of reactants and products can be severely constrained, there is also a need to provide a sound theoretical and modeling framework to enable appropriate interpretation and detailed analysis of experiments. This need motivated the current contribution from which we can draw the several key observations regarding behavior in these systems:

(i) *Dependence of reactivity on key rates*, specifically rates for reaction (W_{rx}) and diffusion (W_{diff}). The penetration depth, L_p, of reactant into the pore scales like $L_p \sim (W_{rx}/W_{diff})^{-n}$ for $W_{rx} << W_{diff}$, where n ≈ 1/3. This is distinct from the prediction n=1/2 of commonly accepted mean-field-type treatments. The scaling of L_p determines that of the overall reactivity since $R_{tot} \sim W_{rx} L_p$. As a consequence an Arrhenius analysis of reactivity, $R_{tot} \sim \exp[-E/(k_BT)]$, for temperature T yields the Arrhenius energy $E = (1-n)E_{rx} + nE_{diff}$, where E_{rx} (E_{diff}) is the activation barrier for reaction (diffusion).

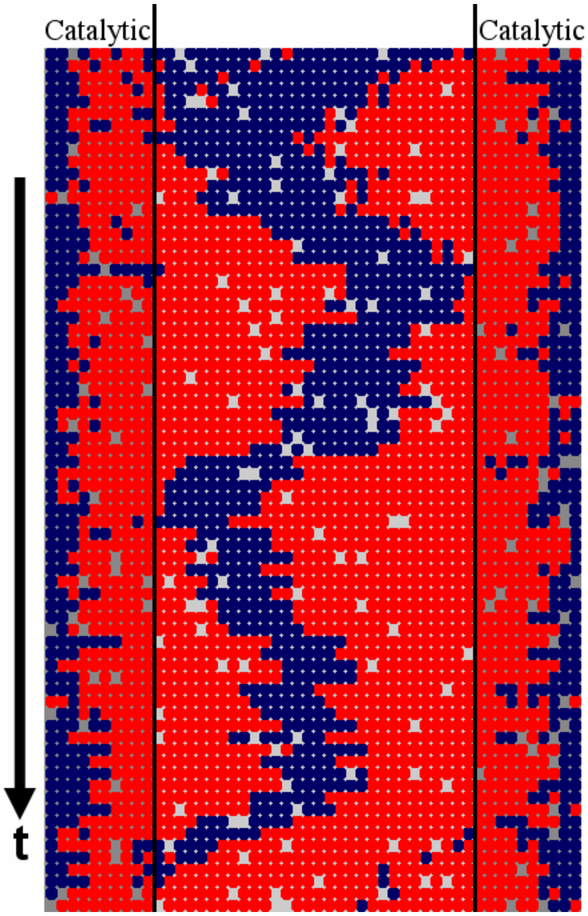

Figure 7: Sequence of KMC configurations (Δt=3000) for late-stage evolution in a pore of length L=50 with 10 catalytic sites (gray) on each end. Dark blue circles are A. Lighter red circles are B. Parameters: W_{ads}=0.9, W_{des}=0.1, W_{diff}=1, and W_{rx}=0.0005. Higher X_{eq}=0.9 makes the A-blob more visible.

(ii) *Fluctuation-dominated reactivity*. The above scaling behavior of L_p reflects the feature that reactivity in single-file systems is controlled by fluctuations in adsorption-desorption processes near the pore openings. This underlies the failure of both traditional mean-field (or related higher-order pair, etc.) approximations, as well as the standard or perturbed hydrodynamic treatments introduced here.

(iii) *Pore diameter dependence on reactivity*. The overall reactivity increases dramatically upon relaxing the single-file constraint to allow some degree of passing of reactants and products (see Fig.2). This feature translates into a strong increase of reactivity with increasing pore diameter. We are currently analyzing such behavior for the conversion of PNB to an aldol compound in the presence of acetone in MSN functionalized by catalytic amine groups. Experimental data is available for effective pore diameters ranging from 1.3 nm (very limited passing) to about 2.5 nm (facile passing) where these values account for both a reduction in diameter after functionalization by catalytic sites, and a further reduction during reaction by formation of a MSN-PNB adduct. A dramatic change from low to high yield is observed increasing pore diameter over this range [31].

(iv) *Dependence on distribution of catalytic sites*. Functionalizing pores with catalytic sites just in the peripheral regions near the openings can result in concentration profiles quite distinct from the case with the entire pore being catalytic: some reactant can “run the gauntlet” past catalytic end regions to form a robust long-lived “blob” in the unreactive interior region (which eventually dissipates). However, in terms of reactivity, there is little difference from the case where all sites are catalytic, so functionalizing just near pore openings suffices to obtain optimal reactivity.

(v) *Predictive analytic formulations for spatiotemporal behavior*. Appropriate description of chemical diffusion is key in these systems. Yet, there has been lack of recognition of the existence of an hydrodynamic form (5) for diffusion fluxes which captures aspects of single-file diffusion, and a lack of utilization of this form. Use of (5) incorporating simple form for tracer diffusion, D_{tr}, in finite systems captures almost perfectly the complex behavior described in (iv). For the fluctuation-dominated steady-state reactivity, preliminary analysis indicates the success of a treatment based on (5), with a heuristic form for D_{tr} varying from higher fluctuation-dominated values near the pore ends to a lower single-file-controlled values in the pore interior.

We have considered here only the case of species-independent hop rates and desorption rates, in the absence of interactions between various species. Exploiting Onsager’s transport theory and more general results for diffusion fluxes of the form (5), one can show that basic features of chemical diffusion carry over to more general cases where species have unequal hop rates and interactions. Again, fluctuations control aspects of evolution and steady-state reactivity near pore openings, although some features of steady-state behavior differ from the case of species-independent rates.

In summary, utilization of the theoretical and modeling framework presented above for catalytic conversion reactions in single-file systems allows us to address and elucidate numerous key issues listed above. When applied to specific catalytic reactions in nanoporous systems, this will enable more sophisticated analysis and interpretation of experimental data.

Acknowledgments

This work was supported by the Division of Chemical Sciences (Basic Energy Sciences), U.S. Department of Energy (USDOE) through the Ames Laboratory PCTC, Chemical Physics, and Catalysis projects. Ames Laboratory is operated for the USDOE by Iowa State University under Contract No. DE-AC02-07CH11358.

References

1) *Catalysis and adsorption by zeolites*; Ohlmann, G., Pfeifer, H., Fricke, G., Eds.; Elsevier, Amsterdam, 1991.

2) J.S. Beck, Vartulli, J.C; Roth, W.J.; Leonowicz, M.E.; Kresge, C.T.; Schmitt, K.D.; Chu, C.T.W.; Olson, D.H.; Sheppard, E.W. J. Am. Chem. Soc. **1992**, 114, 10834-10843.

3) Huh, S.; Wiench J.W.; Woo, J.-C.; Pruski, M.; Lin, V.S.-Y. Chem. Mater. **2003**, 15, 4247-4250.

4) Tajima, K.; Aida, T. *Nanostructured Catalysts*, Plenum, New York, 2003.

5) Reikert L. In *Advances in catalysis*; Eley, D.D., Pines, H., Weisz P.B., Eds.; Academic Press, New York, 1970, Vol.21, p.281

6) Kärger, J., Freude, D. Chem. Eng. Technol. **2002**, 25, 769-778.

7) Harris, T.E. J. Appl. Prob. **1965**, 2, 323-338.

8) Fedders, P.A. Phys. Rev. B **1978**, 17, 40-46.

9) Nicolis, G., Prigogine, I. *Self-organization in Non-equilibrium Systems*, Wiley, New York, 1977.

10) *Oscillations and Travelling Waves in Chemical Systems*, Field R.J., Berger M., Ed.s,

Wiley, New York, 1985.

11) Ala-Nissila, T.; Ferrando, R.; Ying, S.C. Adv. Physics **2002**, 51, 949-1078.

12) Imbihl, R.; Ertl, G. Chem. Rev. **1995**, 95, 697-733.

13) Engel, T.; Ertl, G. Adv. Catal. **1979**, 28, 1-78.

14) Evans, J.W.; D.-J. Liu, D.-J.; Tammaro, M. Chaos **2002**, 12, 131-143.

15) Reuter, K.; Scheffler, M. Phys. Rev. Lett. **2003**, 90, 046103

16) Liu, D.-J.; Evans, J.W. Surf. Sci. **2009**, 603, 1706-1716.

17) Krishna, R.; Vlugt, T.J.H.; Smit, B. Chem. Eng. Sci. **1999**, 54, 1751-1757.

18) Paschek, D.; Krishna, R. Phys. Chem. Chem. Phys. **2001**, 3, 3185-3191.

19) Tsikoyiannis, J.G.; Wei, J.E. Chem. Eng. Sci, **1991**, 46, 233-253.

20) Nedea, S.V.; Jansen, A.P.J.; Lukkien, J.J.; Hilbers, P.A.J.; Phys. Rev. E **2002**, 65, 066701;

21) Nedea, S.V.; Jansen, A.P.J.; Lukkien, J.J.; Hilbers, P.A.J.; Phys. Rev. E **2002**, 66, 066705.

22) Ackerman, D.M.; Wang, J.; Wendel, J.H.; Liu, D.-J.; Pruski, M.; Evans, J.W. J. Chem. Phys. **2011**, 134, 114107.

23) Okino, M.S.; Snurr, R.Q.; Kung, H.H.; Ochs, J.E.; Mavrovouniotis, M.L. J. Chem. Phys. **1999**, 111, 2210-2221.

24) Kärger, J.; Petzold, M.; Pfieffer, H.; S. Ernst, S.; Weitkamp, J. J. Catal. **1992**, 136, 283-299.

25) Rodenbeck, C.; Kärger, J.; Hahn, K. J. Catal. **1995**, 157, 656-664.

26) Rodenbeck, C.; Kärger, J.; Hahn, K. Phys. Rev. E **1997**, 55, 5697-5712.

27) Wang, X.; Chen, C.-C. Chen, S.-Y.; Mou, Y.; Cheng, S. Appl. Catal. A. **2005**, 281, 47-54**.**

28) Shouro D.; Moriya, Y.; Nakajima, T.; Mishima, S. Appl. Catal. A. **2000**, 198, 275-282**.**

29) Chen, H.-T.; Huh, S.; Wiench, J.W.; Pruski, M.; Lin, V.-S.-Y. J. Am. Chem. Soc., **2005**, 127, 13305–13311.

30) Chen, H.-T; Trewyn, B.G.; Wiench, J.W.; Pruski, M.; Lin, V.S.-Y. Top. Catal. **2010**, 53, 187-191.

31) Slowing, I.I.; Ackerman, D.M.; Althaus; S.M.; et al., **2011**, in preparation.

32) Van Kampen, N.G. *Stochastic Processes in Physics and Chemistry*, North Holland, Amsterdam, 1981.

33) Kutner, R. Phys. Lett. **1981**, 81A, 239-240.

34) Evans, J.W. Phys. Rev. B **1990**, 41, 2158-2162.

35) Spohn, H. *Large Scale Dynamics in Interacting Particle Systems*, Springer, Berlin, 1991.

36) Quastel, J. Commun. Pure Appl. Math. **1992**, 45, 623-679.

37) Tammaro, M.; Evans, J.W. J. Chem. Phys. **1998**, 108, 7795-7806.

38) Tammaro, M.; Evans, J.W. Phys. Rev. E **1998**, 57, 5087-5094.

39) Extension to the analogous multi-component case is straightforward provide all species exchange with a common rate W_{ex}: the diffusion flux for A in the N-component case follows from the 2-component result lumping all the other N-1 species into a single quasi-species.

40) Zhdanov, V.P. Surf. Sci. **1988**, 195, L217-221.

41) Evans, J.W. J. Chem. Phys. **1992**, 97, 572-577.

42) van Beijeren, H.; Kehr, K.W.; Kutner, R. Phys. Rev. B **1983**, 28, 5711-5723.

43) Hodgkin, A.L.; Keynes, R.D. J. Physiol. (London) **1955**, 128, 61-88.

44) Evans, J.W. Rev. Mod. Phys. **1993**, 65, 1281-1329.

45) This estimate of $n \approx 1/3$ revises that in Ref.[22], and can be obtained from a modified hydrodynamic treatment incorporating a non-zero effective D_{tr} suitably decreasing away from the pore openings.

46) Crank, J. *Mathematics of Diffusion*, Oxford University Press, Oxford, 1956.

CHAPTER 4. CONVERSION REACTIONS IN SURFACE-FUNCTIONALIZED MESOPOROUS MATERIALS: EFFECT OF RESTRICTED TRANSPORT AND CATALYTIC SITE DISTRIBUTION

Jing Wang[1,2], David M. Ackerman[1,3], Kapil Kandel[1,3], Igor I. Slowing[1], Marek Pruski[1,3] and James W. Evans[1,2,4]

A paper published in *Material Research Society Proceedings*

[1]Ames Laboratory – USDOE, and Departments of [2]Mathematics, [3]Chemistry,
and [4]Physics & Astronomy, Iowa State University, Ames, IA 50011, U.S.A.

Abstract

We analyze the interplay between anomalous transport and conversion reaction kinetics in mesoporous materials functionalized with catalytic groups. Of primary interest is functionalized mesoporous silica containing an array of linear pores with diameters tunable from 2-10 nm, although functionalization can produce smaller effective diameters, d. For $d < 2$ nm, transport and specifically passing of reactant and product species within the pores can be strongly inhibited (single-file diffusion). The distribution of catalytic groups can also vary depending on the synthesis approach. We apply statistical mechanical modeling (utilizing spatially discrete stochastic lattice-gas models) to explore the dependence of reactivity on the extent of inhibition of passing of species within the pore, as well as on the distribution of catalytic sites.

1 Introduction

Functionalized mesoporous materials integrate the selectivity of homogeneous catalysts with the stability and separability of heterogeneous catalysts [1,2]. In the case of mesoporous silica, nanospheres with diameters of the order of 100 nm are synthesized via a soft-templating technique wherein a silica precursor (TEOS) aggregates around a self-assembled array of cylindrical CTAB micelles. Removal of CTAB produces mesoporous silica nanospheres (MSN) with a hexagonal arrangement of parallel linear nanopores with nominal pore diameters of around 2 nm or larger [3]. Control of surface properties is achieved by functionalization with suitable anchored groups serving as catalysts, and sometimes by additional groups modifying selectivity by acting as "gatekeepers" near the pore openings [4], or tuning activity (e.g., by strongly interacting with one of the products to alter the reaction equilibrium [5]).

Functionalization by grafting of these groups after formation of the MSN should produce a higher loading of catalytic groups near the pore openings and likely also populate the exterior surface. In contrast, co-condensation during nanosphere formation produces a more uniform distribution within the pores. For MSN, it is significant to note that functionalization can reduce the effective diameter, d, *below* 2 nm. Then, transport can be strongly inhibited. The extreme case of "no passing" of reactants and products corresponds to so-called single-file diffusion [6].

There have been extensive studies of single-file diffusion systems often motivated by studies of transport and catalytic reaction in zeolites [7]. Typically, these studies emphasize the anomalous nature of tracer- or self-diffusion, this anomaly being reflected in a sub-linear increase (vs. a conventional linear increase) with time in mean-square displacement of a specific "tagged" particle [6]. Our interest is in the interplay between this type of anomalous transport and the catalytic reaction kinetics. Such behavior is traditionally described by reaction-diffusion equations (RDE). However, characterization of chemical diffusion (rather than tracer diffusion), which provides key input to these equations, has received relatively little attention for quasi-single-file systems. Its correct description is a non-trivial statistical mechanical challenge.

Our focus in this contribution is on simple first-order catalytic conversion reactions ($A \rightarrow B$) in systems with linear nanopores. A key factor impacting reactivity is the extent to which reactants and products A and B can pass each other. Passing of A with other A (or B with B) is not significant. Several previous analyses exist for the case of single-file diffusion [8-15] revealing that reactivity is strongly localized near the pore openings in this case of no-passing [9]. A perception exists that a simple mean-field (MF) type treatment of chemical diffusion (see below) is adequate [11]. Unfortunately, this is not true in regimes with large variations in the magnitude of rates for various processes (e.g., low reaction versus diffusion rates). This feature motivated our development of an alternative "hydrodynamic" description of chemical diffusion which effectively captures the single-file constraint [13]. However, this formulation did not incorporate finite-size or fluctuation effects, so additional refinement was necessary to achieve quantitative predictive capability [14,15]. We also note that an effective alternative for precise characterization of model behavior is Kinetic Monte Carlo (KMC) simulation.

In this paper, we apply statistical mechanical modeling (adopting spatially discrete stochastic lattice-gas models) to analyze A→B conversion reactions in linear nanopores with inhibited transport. Specifically, we explore the dependence of reactivity on the extent of inhibition of passing of species within the pore, as well as on the distribution of catalytic sites. We focus on precise characterization of model behavior (as is readily achieved, e.g., by KMC simulation) rather than on the above-mentioned development of theoretical methodology.

2 Catalytic Conversion Reaction in a Linear Nanopore: LG Model

2.A. Stochastic lattice-gas (LG) reaction-diffusion model prescription

In our model for A→B conversion (see Fig.1), species within a pore are localized to sites (or cells) of a 1D linear lattice traversing that pore. The cell width “a” is selected as comparable to the species size (~1 nm). To describe the surrounding fluid, we extend the 1D lattice inside the pores to a 3D lattice outside. We specify “external” reactant and product concentrations in the surrounding fluid as $<A_{out}>$ and $<B_{out}>$. These give the probabilities that sites or cells on the 3D lattice are occupied, where fluid cell occupation is assumed random due to efficient stirring.

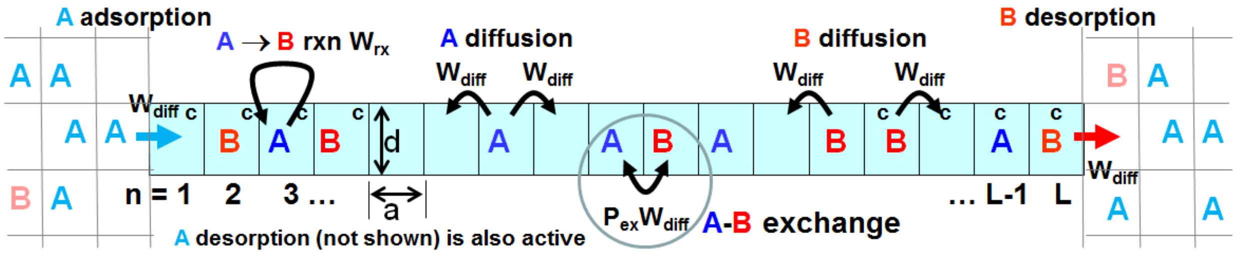

Figure 1: Schematic of the LG conversion reaction model illustrating processes within a single pore (shaded light blue), as well as coupling to the surrounding fluid. ‘c’ denotes catalytic sites.

The simplest prescription for diffusion within the pores is that A and B hop to adjacent empty (E) sites at rate W_{diff}. This would correspond to single-file diffusion with a strict no-passing constraint. We also allow positional exchange of adjacent A and B at rate $W_{ex} = W_{diff} P_{ex}$ to relax the strict single-file constraint, noting that exchange of adjacent particles of the same type has no effect. The passing propensity, $P_{ex} = P_{ex}(d)$, will increase with the effective pore diameter, d (from $P_{ex} = 0$ for d below a threshold where passing is strictly excluded due to steric effects, to $P_{ex} = 1$ for large d and unhindered passing). The other mechanistic steps in the model are: **(i)** Adsorption of external species at terminal sites of the pore at rate $W^{A}_{ads} = W_{diff} \langle A_{out} \rangle$ ($W^{B}_{ads} = W_{diff} \langle B_{out} \rangle$) for the reactant (product), provided that these end sites are unoccupied or empty (E); **(ii)** Desorption of both the reactant, A, and product, B, from terminal sites of the pore at rate W_{diff} provided that the fluid site just outside the pore is unoccupied (E_{out}). Since fluid sites are occupied with probability $\langle X_{out} \rangle = \langle A_{out} \rangle + \langle B_{out} \rangle = 1 - \langle E_{out} \rangle$, desorption of A and B occurs with effective rate $W_{des} = W_{diff} \langle E_{out} \rangle$; **(iii)** Conversion $A \rightarrow B$ at catalytic (c) sites within the pore at rate W_{rx}; c-sites may occupy all or just some sites within the pore. See Fig.1.

For our rates, the dynamics for particles X=A+B is a non-reactive diffusion process. In the steady state, sites are randomly occupied by particles, X, with probability $X_{eq} = \langle X_{out} \rangle$ [12].

2.B. Master equations and reaction-diffusion equations (RDE)

Sites within the pore(s) are labeled by n=1, 2,…, L (for pore length L), so terminal sites are n=1 and n=L. An exact description of our discrete reaction-diffusion model is provided by the master equations for the evolution of probabilities of various configurations within the pore. Often these are written in hierarchical form [8,11,12-14]. Here, we use $\langle C_n \rangle$ to denote the probability or ensemble averaged concentration for species C = A or B at site n, $\langle C_n E_{n+1} \rangle$ for the probability that C is at site n and for site n+1 to be empty (E), etc. Then, the lowest-order equations in the hierarchy describe the evolution of single-site occupancies.

For $A \rightarrow B$ conversion in the case where *all sites are catalytic*, one has that [12-14]

$$\frac{d}{dt} \langle A_n \rangle = -W_{rx} \langle A_n \rangle - \nabla J_A^{n>n+1}, \quad \frac{d}{dt} \langle B_n \rangle = +W_{rx} \langle A_n \rangle - \nabla J_B^{n>n+1}, \quad \text{for } 1<n<L. \tag{1}$$

with separate equations for terminal sites reflecting adsorption-desorption boundary conditions (BC's), e.g., $d/dt \langle A_1 \rangle = W^{A}_{ads} \langle E_1 \rangle - W_{des} \langle A_1 \rangle - W_{rx} \langle A_1 \rangle - J_A^{1>2}$. In (1), we have defined the discrete derivative, $\nabla K_n = K_n - K_{n-1}$. The *net* flux, $J_A^{n>n+1}$, of A from site n to n+1 is given by

$$J_A^{n>n+1} = W_{diff} [\langle A_n E_{n+1} \rangle - \langle E_n A_{n+1} \rangle] + W_{ex} [\langle A_n B_{n+1} \rangle - \langle B_n A_{n+1} \rangle]. \tag{2}$$

The expression for the net flux, $J_B^{n>n+1}$, of B is analogous. In the special case $P_{ex} = 1$ where $W_{ex} = W_{diff}$, transport of A including passing of B is completely unhindered (the opposite of single-file diffusion). Then, (2) reduces exactly to $J_A^{n>n+1} = W_{diff} [\langle A_n \rangle - \langle A_{n+1} \rangle] = -W_{diff} \nabla \langle A_n \rangle$ (cf. Ref. [16]). If some sites are not catalytic, then the reaction terms are absent for such sites. The total rate of production of B is given by $R^B_{tot} = W_{rx} \Sigma_{n=c} \langle A_n \rangle$, summing over all catalytic sites.

Equations (1) couple to various pair probabilities in (2). Pair probability evolution is coupled to triples, etc., producing a hierarchy. Pair, etc., probabilities are not simply related to single-site probabilities due to spatial correlations. A simple MF factorization approximation, $\langle C_n E_{n+1} \rangle \approx \langle C_n \rangle \langle E_{n+1} \rangle$, etc., produces a closed set of discrete reaction-diffusion equations (dRDE) for single-site concentrations. A higher-level pair approximation retains pair quantities, but factorizes triplets, e.g., $\langle C_n M_{n+1} N_{n+2} \rangle \approx \langle C_n M_{n+1} \rangle \langle M_{n+1} N_{n+2} \rangle / \langle M_{n+1} \rangle$, with C, M, N = A, B, or E. This generates a closed set of equations for single-site and pair quantities [8,11,12-14].

For smoothly varying concentrations within the pore, it is natural to consider a coarse-grained description where species concentrations per unit length are $K(x{=}na) \approx a^{-1} \langle K_n \rangle$, leaving the t-dependence implicit. Below, we set a=1. The continuum or hydrodynamic RDE (hRDE) for our A → B conversion reaction model with all sites catalytic then have the form [12-14]

$$\partial/\partial t\, A(x) = -W_{rx}(A)\, A(x) - \partial/\partial x\, J_A, \quad \partial/\partial t\, B(x) = +W_{rx}(A)\, A(x) - \partial/\partial x\, J_B. \qquad (3)$$

If only portions of the pore are catalytic, reaction terms appear just for those locations. BC’s for (3) at the pore ends reflect the adsorption-desorption dynamics [13]. Description of the diffusion fluxes, J_C, for C = A and B is non-trivial. In the steady-state with uniform total concentration, X_{eq}, we write $J_C = -D_{tr}(X_{eq})\, \partial/\partial x\, C(x)$ where D_{tr} is a tracer diffusion coefficient [13-15]. The MF treatment sets $D_{tr} = (1 - X_{eq})W_{diff}$ [12,13] overestimating fluxes. In a classic hydrodynamic treatment, one has $D_{tr} \sim W_{diff}/L \to 0$, as $L \to \infty$ [14], underestimating fluxes. Precise fluxes follow from a generalized hydrodynamic treatment where D_{tr} is enhanced near pore openings [15].

3 Catalytic Reaction Kinetics: LG Model Predictions

3.A. Pore completely functionalized with catalytic sites

For the case where all sites within the pore are catalytic, Fig.2a compares steady-state concentration profiles for <A_n> and <B_n> versus n for single-file diffusion (P_{ex} = 0), hindered passing of A and B with P_{ex} = ¼, and completely unhindered passing (standard diffusion) where P_{ex} = 1. Other model parameters are specified in the caption (reflecting the initial stages of reaction with no significant buildup <B_{out}>). The most dramatic feature is the strongly enhanced penetration of reactant into the pore with increasing propensity, P_{ex}, of passing of A and B. Correspondingly, the reaction rate, R^B_{tot} , increases strongly increasing P_{ex} as shown in Fig.2c.

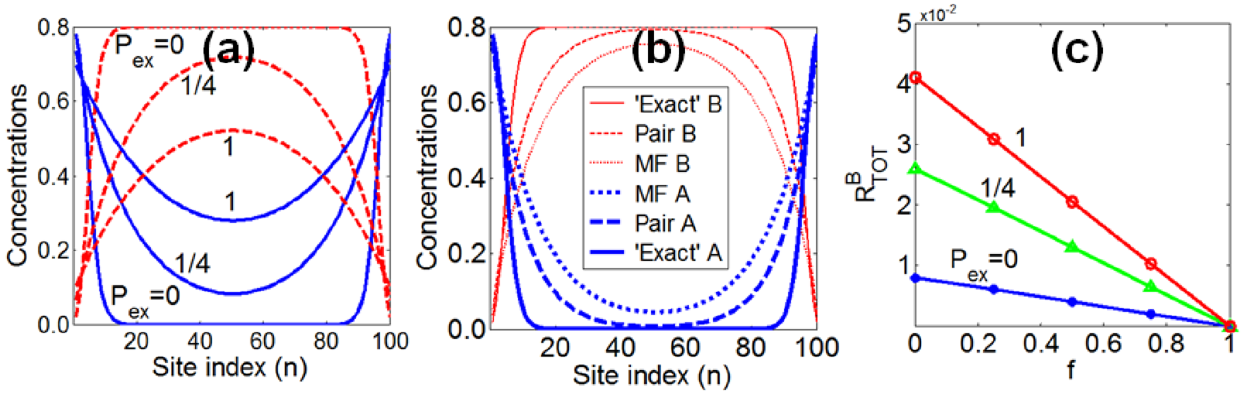

Figure 2: Steady-state concentration profiles for model parameters L=100, W_{rx} = 0.001, W_{diff} = 1, <A_{out}> = 0.8, and <B_{out}> = 0: ***(a)*** *dependence on the propensity for passing of reactants and products (P_{ex} = 0, ¼, 1); A (B) is blue, solid (red, dashed);* ***(b)*** *comparison of exact profiles for P_{ex} = 0 (single-file diffusion) with those predicted by MF and pair approximations; A (blue) is minimum and B (red) is maximum at the pore center.* ***(c)*** *Reaction rate, $R^B_{tot}(f)$, versus fraction of conversion of reactant to product, f = (X_{eq} - <A_{out}>)/X_{eq} = <B_{out}>/X_{eq}, for P_{ex} = 0, ¼, and 1.*

Given our remarks on the short-comings of MF-type treatments of chemical diffusion, it is appropriate to show the extent of this failure for the above example for single-file diffusion. (The MF treatment becomes more accurate with increasing P_{ex}, and is actually exact for P_{ex} =1.) Fig.2b compares exact behavior with that obtained from the standard MF approximation and also the pair approximation. The MF approximation greatly overestimates diffusion fluxes in the steady-state, and thus also the extent of penetration of reactant into the pore and the reactivity. The pair approximation, which at least approximately accounts for the effect of spatial correlations, shows significant improvement over MF predictions, but is still far from precise.

Next, we characterize behavior during the “extended reaction” for the above parameter choice as a significant fraction, f, of reactant outside the pore becomes converted to product. During the extended reaction, $\langle A_{out} \rangle$ decreases and $\langle B_{out} \rangle$ increases while $\langle X_{out} \rangle = \langle A_{out} \rangle + \langle B_{out} \rangle = 0.8 = X_{eq}$ remains constant. Thus, one has $f = (X_{eq} - \langle A_{out} \rangle)/X_{eq} = \langle B_{out} \rangle / X_{eq}$. Since the volume and thus the amount of reactant and product outside the pores far exceeds that inside, this induces a separation of time scales in the system. The characteristic time for change of $\langle A_{out} \rangle$ far exceeds that for relaxation to steady-state of the concentration distribution inside the pores. Thus, one can perform a sequence of simulations for different values of conversion, f, to determine the associated reaction rate, R^B_{tot} , then interpolate these results to obtain the variation of R^B_{tot} during the extended reaction. This yields the complete kinetics for conversion of A to B.

The results of this analysis shown in Fig.2c reveal that the reaction rate decreases linearly as a function of f. This reflects the linearity of the governing master equations or RDE’s, together with linearity of the BC’s controlling input of reactants and products to the pore. This result means that it suffices to determine $R^B_{tot}(f=0)$ for negligible conversion, since then $R^B_{tot}(f) = (1-f)\, R^B_{tot}(0)$. Then the reaction kinetics follow from $d/dt \langle A_{out} \rangle = -c\, R^B_{tot}(0) \langle A_{out} \rangle$ producing *exponential decay* of $\langle A_{out} \rangle$. The constant c equals the number of pores in the system divided by the total number of 3D lattice sites associated with the fluid and by X_{eq}.

3.B. Functionalization only of pore ends with catalytic sites

Next, we consider the case where only the 20 sites at each end of a pore of length L=100 are catalytic. Other parameters are selected as above. For $P_{ex}=0$, behavior is shown in Fig.3a. We find that a significant amount of A entering the pore “runs the gauntlet” to reach the non-reactive central region without conversion to B [13,14]. Thus, at the end of the first stage of pore filling, a significant blob of A remains in the pore center. Then, in a second much slower stage, this blob of A is converted to B via fluctuation-dominated diffusion from the center to the end reactive regions [14]. The pore center is devoid of A in the final steady-state. The profile is essentially the same as that when all sites reactive given that the penetration of reactant is well below 20 sites.

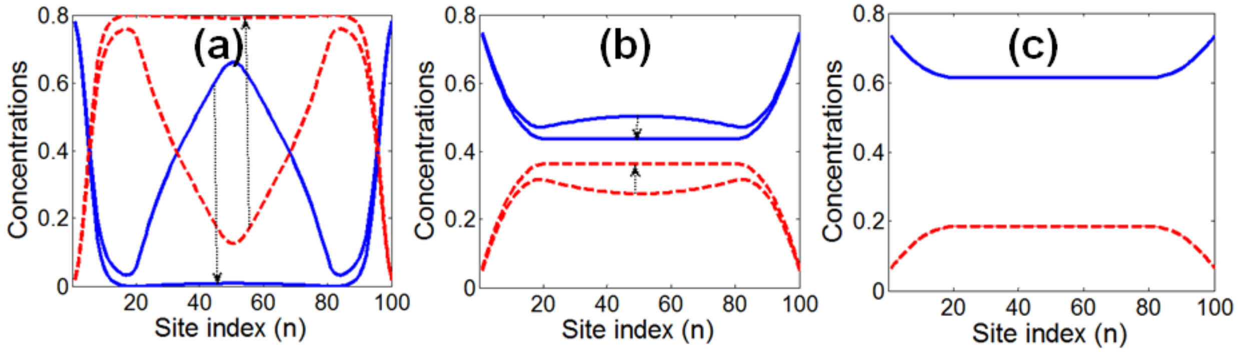

Figure 3: Steady-state concentration profiles for pores of length L=100 with just 20 catalytic sites on each end: ***(a)*** *P_{ex} = 0 (single-file diffusion);* ***(b)*** *P_{ex} = ¼; and* ***(c)*** *P_{ex} = 1 (unhindered diffusion). Profiles are shown for a time corresponding to the peak A-concentration in the pore center, as well as for long time t = 60,000 [where the system reached the steady-state, or nearly so for (a)]. Arrows indicate time evolution (e.g., reducing the A concentration in the pore center). Other model parameters are: W_{rx} = 0.001, W_{diff} = 1, $\langle A_{out} \rangle$ = 0.8, and $\langle B_{out} \rangle$ = 0.*

For P_{ex} = ¼ (Fig.3b), there is also a slight initial buildup of A in the pore center which diminishes for longer times. The final steady-state profile retains a significant uniform concentration of A in the center. This reflects the larger penetration of reactant (beyond 20 sites) for all sites reactive when P_{ex} = ¼. The uniformity of the steady-state concentration in unreactive regions follows from the governing equations. For P_{ex} = 1 (Fig.3c), the above trend is amplified, and now there is no transient maximum of concentration of reactant in the pore center.

4 Conclusions

The catalytic activity of mesoporous materials containing functionalized linear nanopores is shown to be strongly dependent of the propensity for passing of reactants and products within the pores. Limited passing means that most of completely functionalized pores are actually catalytically unproductive, being filled with “trapped” product. For this reason, pores with only the ends functionalized will have the same reactivity (unless passing of reactants and products is sufficiently facile that the reactant can penetrate to the central region of the pore).

Acknowledgments

This work was supported by the Division of Chemical Sciences, Office of Basic Energy Sciences, U.S. Department of Energy (USDOE). It was performed at Ames Laboratory which is operated for the USDOE by Iowa State University under Contract No. DE-AC02-07CH11358.

References

1) *Catalysis and Adsorption by Zeolites*; G. Ohlmann, H. Pfeifer, G. Fricke, Eds.; Elsevier, Amsterdam, 1991.

2) K. Tajima and T. Aida, *Nanostructured Catalysts*, Plenum, New York, 2003.

3) J.S. Beck, J.C. Vartulli, W.J. Roth, M.E. Leonowicz, C.T. Kresge, K.D. Schmitt, C.T.W. Chu, D.H. Olson, and E.W. Sheppard, J. Am. Chem. Soc. **114**, 10834-10843 (1992).

4) S. Huh, J.W. Wiench, J.-C. Woo, M. Pruski, and V.S.-Y. Lin, Chem. Mater. **15**, 4247 (2003).

5) C.-H. Tsai, H.-T. Chen, S.M. Althaus, K. Mao, T. Kobayashi, M. Pruski, and V.S.-Y. Lin, ACS Cat. **1**, 729 (2011).

6) T.E. Harris, J. Appl. Prob. **2**, 323 (1965).

7) J. Kärger and D. Freude, Chem. Eng. Technol. **25**, 769 (2002).

8) J.G. Tsikoyiannis and J.E. Wei, Chem. Eng. Sci, **46**, 233 (1991).

9) J. Kärger, M. Petzold, H.S. Pfieffer, S. Ernst, and J. Weitkamp, J. Catal. **136**, 283 (1992).

10) C. Rodenbeck, J. Kärger, and K. Hahn, Phys. Rev. E **55**, 5697 (1997).

11) M.S. Okino, R.Q. Snurr, H.H. Kung, J.E. Ochs, and M.L. Mavrovouniotis, J. Chem. Phys. **111**, 2210 (1999).

12) S.V. Nedea, A.P.J. Jansen, J.J Lukkien, and P.A.J. Hilbers, Phys. Rev. E **65**, 066701 (2002).

13) D.M. Ackerman, J. Wang, J.H. Wendel, D.-J. Liu, M. Pruski, and J.W. Evans, J. Chem. Phys. **134**, 114107 (2011).

14) D.-J. Liu, J. Wang, D.M. Ackerman, I.I. Slowing, M. Pruski, H.-T. Chen, V.S.-Y. Lin, and J.W. Evans, ACS Catalysis **1**, 751 (2011).

15) D.M. Ackerman, J. Wang, and J.W. Evans, Phys. Rev. Lett., submitted (2012).

16) R. Kutner, Phys. Lett. **81A**, 239 (1981).

CHAPTER 5. GENERALIZED HYDRODYNAMIC TREATMENT OF THE INTERPLAY BETWEEN RESTRICTED TRANSPORT AND CATALYTIC REACTION IN NANOPOROUS MATERIALS

David M. Ackerman,[1,2] Jing Wang,[1,3] and James W. Evans[1,3,4]

A paper published in *Physical Review Letters*

[1]Ames Laboratory – USDOE, and Departments of [2]Chemistry, [3]Mathematics,
and [4]Physics & Astronomy, Iowa State University, Ames, Iowa 50011

Abstract

Behavior of catalytic reactions in narrow pores is controlled by a delicate interplay between fluctuations in adsorption-desorption at pore openings, restricted diffusion, and reaction. This behavior is captured by a generalized hydrodynamic formulation of appropriate reaction-diffusion equations (RDE). These RDE incorporate an unconventional description of chemical diffusion in mixed-component quasi-single-file systems based on a refined picture of tracer diffusion for finite-length pores. The RDE elucidate the non-exponential decay of the steady-state reactant concentration into the pore and the non-mean-field scaling of the reactant penetration depth.

1 Introduction

Anomalous tracer diffusion of a “tagged” particle in a single-file system, where particles within narrow pores cannot pass each other, was proven in the 1960’s for hard-core interactions [1] and later for general interactions [2]. Often motivated by early investigations of biological transport across membranes [3,4], numerous studies have considered single-file tracer diffusion in finite open [5], periodic [6,7], or closed [8] “pores”, and in other systems [9]. This type of inhibited transport has also been recognized to impact reactivity for catalysis in zeolites and other functionalized nanoporous materials [10-15]. For the latter reaction-diffusion phenomena which are of interest here, it is actually chemical diffusion [16] which controls behavior [15], and for which the connection to tracer diffusion is not well recognized. Another key aspect of these open reaction-diffusion systems is that steady-state behavior is not described by a classic Gibbs thermodynamic ensemble. In fact, a fundamental understanding of these steady-states, which depend on both the reaction kinetics and transport, remains a significant challenge [17-19].

Our specific focus is on first-order conversion reactions, A → B, occurring inside a parallel array of linear nanopores of a catalytically functionalized material such as mesoporous silica. Reactants, A, enter the pore openings, diffuse to catalytic sites, convert to a product, B, with microscopic rate k, and both reactants and products can diffuse out of the pore [11-15]. Furthermore, we assume that these pores are sufficiently narrow that passing of reactant and product species is inhibited or even excluded. It was recognized that reactivity can be strongly inhibited for single-file diffusion (SFD) relative to unhindered passing [12]. The reason is that except near their ends, the pores tend to be exclusively populated by product which is not readily extruded. Thus, the pore center does not participate in the conversion A → B.

Some studies have suggested that this type of behavior, even for inhibited transport, can be captured by mean-field-type treatments of reaction-diffusion [13] which predict an exponential decay of reactant concentration into the pore with penetration depth scaling like $L_p \sim k^{\xi}$ with $\zeta = -½$ [14,15]. However, we will find fundamental short-comings in these mean-field treatments, noting that exact behavior for SFD even exhibits different scaling of L_p with $\zeta \neq -½$. A deterministic hydrodynamic treatment [20] accounting for SFD [15] can describe reaction-diffusion behavior in the regime of slowly varying concentration profiles (for long pores) even for SFD, but this treatment completely fails to describe steady-state reactivity [15]. The reason for this failure is that steady-state behavior is controlled by the stochastic nature of adsorption and desorption of species at the pore openings. Thus, to correctly capture behavior, in this Letter, we pursue a generalized hydrodynamic formalism. This formalism requires an appropriate description of chemical diffusion in mixed-component systems, including the case of SFD, based on a relationship between chemical and tracer diffusion deriving from interacting particle systems theory. However, it also requires a refined picture of tracer diffusion for finite-length pores.

2 Model Description

In our model for A → B conversion (Fig.1), we consider a catalytic material composed of an array of similar parallel linear nanopores. Species within any pore are localized at a linear array of cells (or sites) labeled n=1 - L traversing the pore. The cell width “a” is chosen as a~1 nm comparable to species size. To describe the surrounding fluid, we can extend the 1D lattice inside the pores to a 3D lattice outside. But the fluid is assumed well-stirred, so that cells of the 3D lattice are randomly occupied with specified probabilities, $<A_{out}>$ and $<B_{out}>$, corresponding to the suitably normalized external reactant and product concentrations, respectively. The total concentration, $<X_{out}> = <A_{out}> + <B_{out}> = \chi$, say, is fixed, whereas $<B_{out}>$ slowly increases from an initial value of zero during extended reaction. This slow time-scale is controlled by the fluid volume and far exceeds that for relaxation of the concentration profile within the pore.

In the simplest prescription corresponding to SFD within the pores, A and B hop to adjacent empty (E) cells at rate h per direction. We can also allow positional exchange of adjacent A and B at rate $h_{ex} = h\,P_{ex}$ to relax the strict SFD constraint, noting that exchange of adjacent particles of the same type has no effect. The passing propensity, P_{ex}, will increase with pore diameter d from $P_{ex} = 0$ below a SFD-threshold to $P_{ex} \sim 1$ for unhindered passing. Other mechanistic steps in the model are: **(i)** Impingement of external species at terminal cells $n=1$ and $n=L$ of the pore at rate $i_A = h<A_{out}>$ ($i_B = h<B_{out}>$) for the reactant A (product B), successful adsorption occurring if these end cells are unoccupied or empty (E); **(ii)** Attempted desorption of both A and B from terminal cells of the pore at rate h, success occurring with probability $<E_{out}> = 1 - <X_{out}>$ for the neighboring fluid site to be unoccupied (E_{out}); **(iii)** Conversion $A\rightarrow B$ at rate k at catalytic cells.

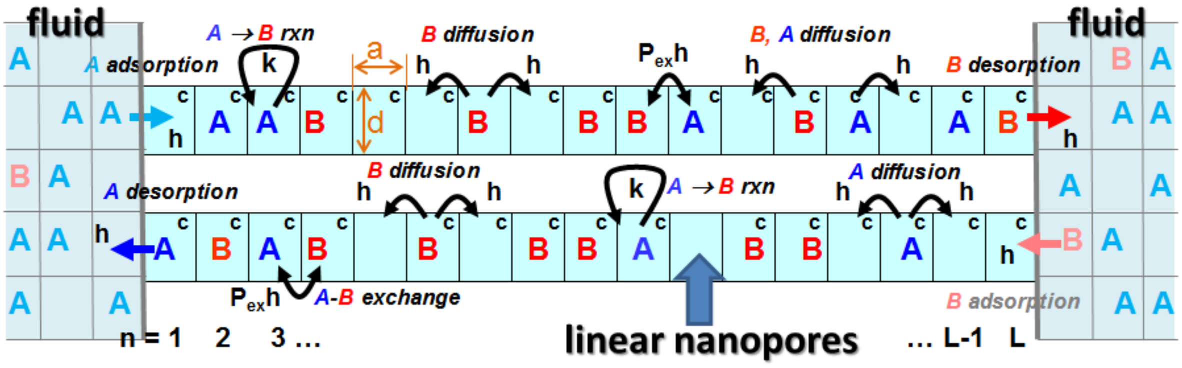

Figure 1: Schematic of the key steps in our $A\rightarrow B$ catalytic conversion reaction model. “c” denote catalytic cells where reaction occurs at rate k. Behavior is shown in two adjacent pores which should be regarded as part of a larger array of pores.

For the above rate choice, which follows previous studies [11-15], the “species blind” dynamics for particles X = A or B corresponds to a non-reactive diffusion process. In the steady-state, cells within the pore are randomly occupied by particles, X, with probability $\langle X_{out} \rangle = \chi$ [14]. We will assess typical concentration profiles within a pore, corresponding to averaging over many pores. Both time evolution and steady-state behavior (see Fig.2 for examples for the initial stages of reaction with $\langle B_{out} \rangle \approx 0$) can be assessed precisely by Kinetic Monte Carlo (KMC) simulation.

An exact description of our discrete reaction-diffusion model is provided by hierarchical master equations for the evolution of probabilities of various configurations of subsets of cells within the pore [11,13-15]. Let $\langle C_n \rangle$ denote the probability that species C = A or B is at cell n, $\langle C_n E_{n+1} \rangle$ that C is at cell n and that cell n+1 is empty (E), etc. Then, the total conversion rate is $R_{tot} = k\, \Sigma_{n=c} \langle A_n \rangle$ with the sum extending over all catalytic cells. Below we consider only the case of all cells catalytic (c). Then, the lowest-order equations in the hierarchy are [14,15]

$$d/dt \langle A_n \rangle = -k \langle A_n \rangle - \nabla J_A^{n>n+1},\quad d/dt \langle B_n \rangle = +k \langle A_n \rangle - \nabla J_B^{n>n+1},\quad \text{for } 1<n<L. \tag{1}$$

Separate equations for terminal cells reflect adsorption-desorption boundary conditions (BC's), e.g., $d/dt \langle A_1 \rangle = h(\langle A_{out} \rangle \langle E_1 \rangle - \langle E_{out} \rangle \langle A_1 \rangle) - k \langle A_1 \rangle - J_A^{1>2}$. In (1), we have defined the discrete derivative, $\nabla K_n = K_n - K_{n-1}$. The *net flux*, $J_A^{n>n+1}$, of A from site n to n+1 is given by

$$J_A^{n>n+1} = h\,[\langle A_n E_{n+1} \rangle - \langle E_n A_{n+1} \rangle] + h_{ex}\,[\langle A_n B_{n+1} \rangle - \langle B_n A_{n+1} \rangle]. \tag{2}$$

The first term gives the contribution from hopping to adjacent empty cells, and the second from exchange. The expression for the net flux, $J_B^{n>n+1}$, of B is analogous. In the special case of unhindered transport where $P_{ex} = 1$ so $h_{ex} = h$, (2) reduces exactly to $J_A^{n>n+1} = -h\, \nabla \langle A_n \rangle$ [15,21].

Equations (1) couple to pair probabilities in (2). Pair probability evolution couples to that of triples, etc., producing a hierarchy. Multi-site probabilities are not simply related to single-cell probabilities due to spatial correlations. The lowest-order site-approximation, $\langle C_n E_{n+1} \rangle \approx \langle C_n \rangle \langle E_{n+1} \rangle$, etc., produces a closed set of discrete reaction-diffusion equations (RDE) for single-cell concentrations. A pair approximation factorizes triples in terms of pair and single-cell quantities generating a closed set of equations for these [13-15]. The triplet approximation factorizes quartets in terms of triplets, etc. [22]. However, these and all higher-order mean-field (MF) like truncation approximations suffer fundamental shortcomings. While accuracy increases with the order of the approximation, convergence to exact behavior can be slow. See Fig.2a.

An alternative coarse-grained description considers concentrations per unit length, $C(x=na, t) \approx a^{-1} \langle C_n \rangle$, for C = A or B, smoothly varying with position x, which satisfy the continuum RDE

$$\partial/\partial t\, A(x, t) = -k\, A(x, t) - \partial/\partial x\, J_A,\ \partial/\partial t\, B(x, t) = +k\, A(x, t) - \partial/\partial x\, J_B. \qquad (3)$$

BC's for (3) at the pore ends reflect the adsorption-desorption dynamics [15]. Description of the diffusion fluxes, J_A and J_B, is critical. Setting $X(x,t)=A(x,t)+B(x,t)$, we exploit a little-used result from interacting particle systems theory for mixtures of particles with identical dynamics [23]

$$J_A = -D(A/X)\partial X/\partial x - D_{tr}[(B/X)\partial A/\partial x - (A/X)\partial B/\partial x] \rightarrow -D_{tr}\, \partial A/\partial x \quad \text{for uniform } X=a^{-1}\chi, \qquad (4)$$

The form of J_B is analogous. Here $D = a^2h$ is the chemical diffusion coefficient for particles X, and $D_{tr} = D\, F_{tr}$ is a tracer diffusion coefficient. The site-approximation described above implies the mean-field form $F_{tr} = 1 - \chi$ [14,15] as is evident after coarse-graining of the discrete RDE. This choice overestimates fluxes for SFD. A classic analysis of SFD for infinite systems [1] finds that $F_{tr} = 0$. The associated "hydrodynamic" RDE can describe the evolution of slowly varying profiles during filling of long pores [15]. However, this formulation which sets the diffusion fluxes to zero and neglects fluctuations near pore openings completely fails to describe steady-state profiles [15] as shown in Fig.2a. A refined treatment setting $F_{tr} \sim 1/L$, motivated by studies of finite-sized SFD systems [3,4,6,7], does not resolve this basic shortcoming.

3 Implementation and Results

Our strategy is to develop a "generalized hydrodynamic" form for F_{tr} which captures the mesoscale fluctuations near pore openings being enhanced in these regions. A discrete form of (4) incorporating this F_{tr} then provides fluxes in (1) which are integrated to determine steady-state behavior. One strategy to determine this $F_{tr}(n)$ at cell n [24] for a pore with uniform $\langle X_n \rangle = \chi$ is based analysis of the "exit time", $t_n(\chi)$, for a tagged particle starting at this cell to reach a pore opening in the sense that its root-mean-square (rms) displacement grows to match the distance from the nearest pore opening. Specifically, we set $F_{tr}(n) = t_n(0+)/t_n(\chi)$ since diffusivity is inversely proportional to the time for the rms displacement to reach some specified value. This recovers the correct limiting value $F_{tr}(n) \rightarrow 1$ as $\chi \rightarrow 0+$. Results for $F_{tr}(n)$ in Fig.3a for SFD in finite pores reveal a central plateau of magnitude ~$1/L$ (consistent with [3,4,6,7]), but with significantly larger values near pore openings. Use of this variable $F_{tr}(n)$ in appropriate RDE to determine steady-state profiles yields excellent agreement with precise results from KMC simulation for SFD with L=100, in marked contrast to all other treatments. See Fig.4 for profiles with $\langle B_{out} \rangle \approx 0$ (the initial stages of the reaction), and results in Table I for the penetration depth, L_p, naturally defined as $L_p = \Sigma\Sigma_{1 \le n \le L/2} \langle A_n \rangle / \langle A_1 \rangle$.

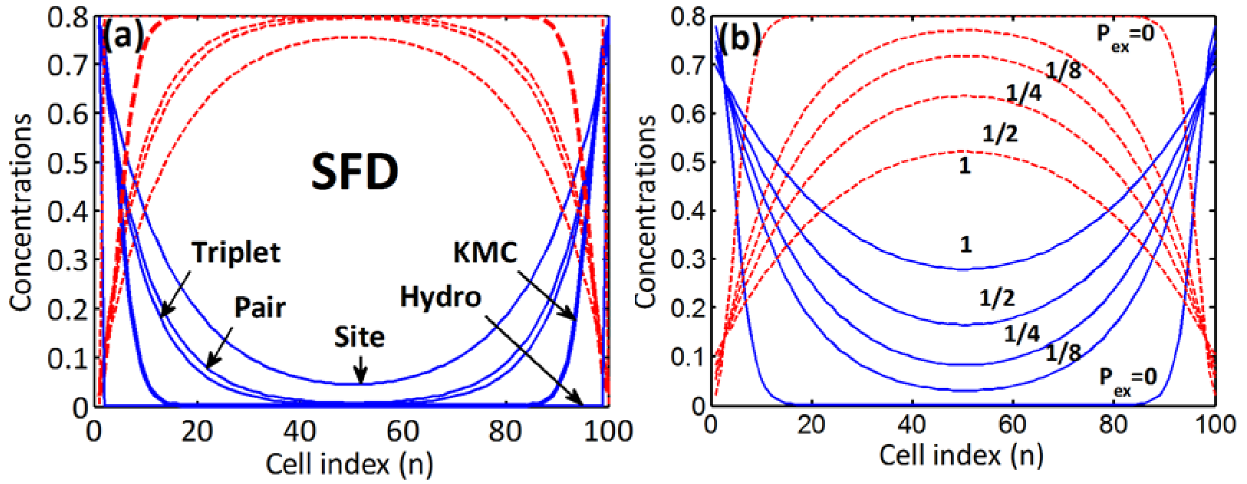

Figure 2: Steady-state concentration profiles (A=solid, blue; B=red, dashed) for pore length L=100, k= 0.001, h=1, and χ=0.8: (a) predictions of site, pair, triplet approximations and the standard hydrodynamic treatment (hydro) versus precise KMC results for SFD (P_{ex}=0); (b) KMC results for restricted passing with various P_{ex} ≥0.

Table 1: Comparison of reactant penetration depths, L_p (in units of 'a'), with h=1 and L=100, for KMC, generalized hydrodynamic (GHydro) and mean-field site-approximation (MF) analyses.

χ=0.2	*k*=1	*k*=0.1	*k*=0.01	*k*=0.001	χ=0.8	*k*=1	*k*=0.1	*k*=0.01	*k*=0.001
KMC	1.47	2.92	6.77	15.2	KMC	1.10	1.47	2.64	5.21
GHydro	1.49	3.10	7.19	15.8	GHydro	1.06	1.43	2.61	5.15
MF	1.53	3.37	9.46	27.8	MF	1.17	2.00	5.00	14.7

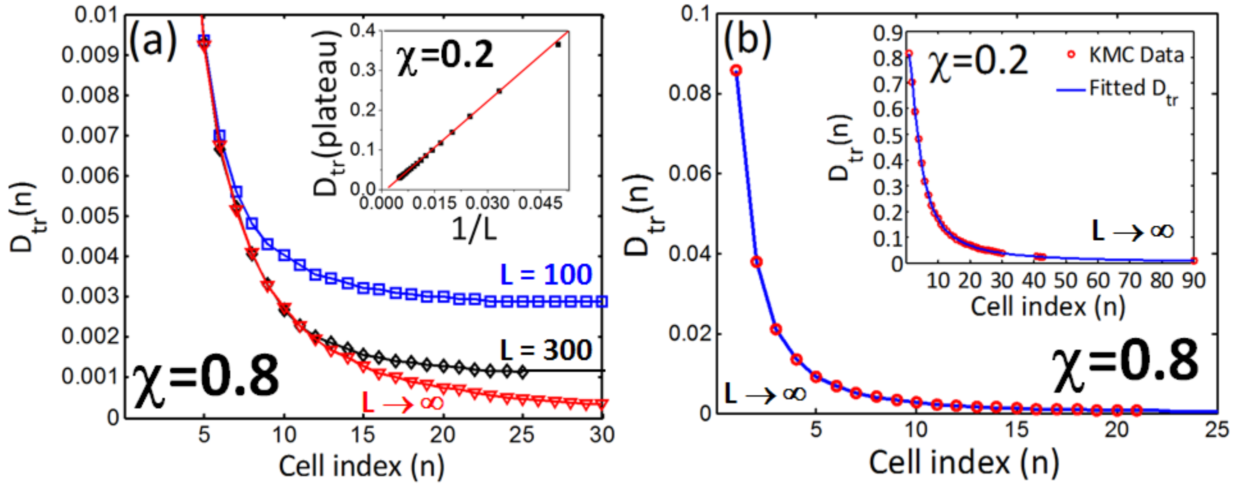

Figure 3: KMC results for $D_{tr}(n)$ [$=F_{tr}(n)$ for $a=h=1$]: (a) n-dependence for various pore lengths L for $\chi=0.8$ (inset shows L-dependence of central plateau value of D_{tr} for $\chi=0.2$); (b) fitting of the decay of $D_{tr}(n)$ with n for semi-infinite pore. Using the form in text, we choose $\alpha=0$, $\beta=1.543$, $\gamma=0.944$ for $\chi=0.8$ (inset: $\alpha=0.753$, $\beta=0.371$, $\gamma=0.0064$ for $\chi=0.2$).

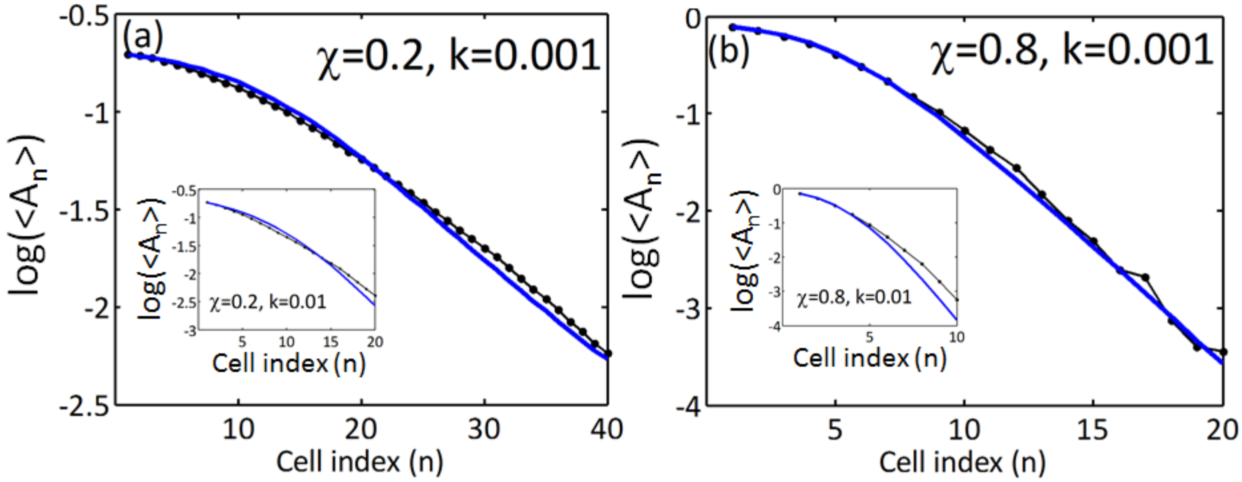

Figure 4: Comparison of results for steady-state concentration values for $L=100$, $k=0.001$ (inset: $k=0.01$), and $h=1$ from KMC (symbols + line) with generalized hydrodynamic RDE predictions (thicker blue curves): (a) $\chi=0.2$; (b) $\chi=0.8$ (log is base 10).

Next, we turn to the fundamental issue of the form of the concentration profiles and the scaling of the penetration depth, L_p, for SFD in a semi-infinite pore with $1\le n<\infty$. Clearly now $F_{tr}(n)\to 0$, as $n\to\infty$, but how? Deep inside the pore where classic SFD should apply, the rms displacement increases like $t^{1/4}$ [1], so one expects that $t_n(\chi>0) \sim n^4$. In contrast, $t_n(0+) \sim n^2$ for conventional diffusion. This suggests that $F_{tr}(n) \sim 1/n^2$, as $n\to\infty$. Simulation results indicate that this behavior is achieved quickly for high total concentration χ=0.8, but more slowly for low

$\chi=0.2$ which displays an intermediate regime better described by $F_{tr}(n) \sim 1/n$ scaling. Data in both cases is fit well for all n by the form $F_{tr}(n) = F_{tr}(1)(1-\alpha+\beta+\gamma)/(1-\alpha\cdot n^{1/2}+\beta\cdot n+\gamma\cdot n^2)$. See Fig.3b.

Insight into the consequences of this decay of $F_{tr}(n)$ comes from analysis of the steady-state solutions of the continuum RDE for a semi-infinite pore $x \geq 0$ using (4) with the form $F_{tr}(x) \sim 1/x^p$. One finds solutions which for small k and large L_p have the dominant form

$$A(x) \sim \exp[-(x/L_p)^q] \text{ where } q=(2+p)/2, \text{ and } L_p \sim (k/D)^{\zeta} \text{ with } \zeta = -1/(2+p). \tag{5}$$

Thus, the true asymptotic scaling exponent is $\zeta = -1/4$ (for $p=2$), but behavior mimicking $\zeta \approx -1/3$ (for $p=1$) might be seen for lower χ, both contrasting MF behavior $\zeta = -1/2$ (for $p=0$) [14,15]. These predictions are confirmed by numerical analysis of discrete generalized hydrodynamic RDE's exploiting the capability of this deterministic treatment to obtain much more precise ζζ-values than possible by KMC. See Fig.5. Concentration profiles also exhibit the predicted non-exponential decay, a feature which is already indicated in the non-linear form of the log-linear plots in Fig.4 (the downward bend corresponding to an effective exponent $q>1$ due to $p>0$).

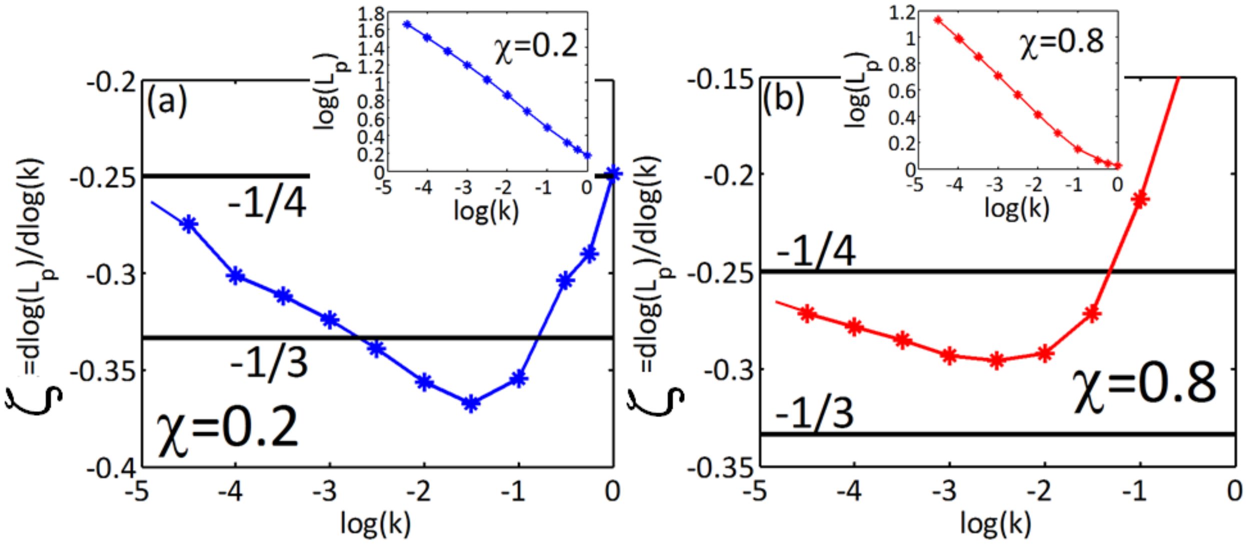

Figure 5: Predictions of generalized hydrodynamic RDE for the effective scaling exponent $\zeta = d\log(L_p)/d\log(k)$ for a semi-infinite pore: (a) $\chi=0.2$; (b) $\chi=0.8$. Upper insets: L_p versus k.

We now mention various extensions of the above analysis. All results were presented for initial stages of reaction where $\langle B_{out} \rangle \approx 0$. However, analysis is readily extended to treat arbitrary fraction of conversion $f = \langle B_{out}\rangle/\langle X_{out}\rangle$, and we find an exact linear variation with f of the total conversion rate $R_{tot}(f) = R_{tot}(0)(1-f)$ by virtue of the linearity of the RDE's and BC's. Dropping the SFD constraint, we have also analyzed $F_{tr}(n)$ which still decreases with increasing n but now retains a substantial non-zero L-independent value in the pore center corresponding to tracer diffusion with exchange in an infinite pore. The corresponding generalized hydrodynamic treatment readily recovers behavior shown in Fig.2b. The greatest challenge in developing a predictive analytic treatment is for complete or near SFD, as other cases have more MF-like behavior. One can also readily extend the analysis to treat reversible reaction A ↔ B using the same $F_{tr}(n)$ as determined above.

Finally, we consider more general diffusional dynamics with unequal diffusion coefficients, D_A and D_B, for A and B, respectively. Analysis for SFD reveals behavior entirely analogous to the case of equal hop rates with penetration of reactant into the pore, but the pore center populated only by product. Again, MF treatments overestimate diffusion fluxes and fail to describe steady-state behavior. The key is to describe chemical diffusion for the mixed system (cf. [19,25]). We apply Onsager theory to determine the hydrodynamic form (corresponding to zero tracer diffusion) of $J_A = -A(A/D_A+B/D_B)^{-1}\,\partial X/\partial x$ for SFD, and J_B is analogous. Since the total flux, $J_X = J_A + J_B$, must vanish in the steady state, this implies that X is constant, so J_A vanishes which in turn implies that A must be absent from the pore interior due to conversion to B. This failure of the hydrodynamic description to describe reactant penetration must again be overcome by accounting for fluctuation effects at the pore openings.

4 Conclusion

In summary, the location-dependence of tracer diffusion near the openings of narrow pores is shown to control non-MF scaling of reactant penetration depth and thus reactivity for conversion reactions. Generalized hydrodynamic RDE's provide a powerful tool with which to analyze this behavior. This work is supported by the Division of Chemical Sciences – BES, USDOE. Ames Laboratory is operated for the USDOE by ISU under Contract No. DE-AC02-07CH11358.

References

1) T.E. Harris, J. Appl. Prob. 2, 323 (1965).

2) M. Kollman Phys. Rev. Lett. 90, 180602 (2003).

3) A.L. Hodgkin and R.D. Keynes, J. Physiol. 128, 61 (1955).

4) E.J. Harris, “Transport and accumulation in biological systems” (AP, New York, 1960).

5) J.E. Santos and G.M. Schutz, Phys. Rev. E 64, 036107 (2001).

6) H. van Beijeren, K.W. Kehr, and R. Kutner, Phys. Rev. B 28, 5711 (1983).

7) A. Taloni and F. Marchesoni, Phys. Rev. E 74, 051119 (2006).

8) L. Lizana and T. Ambjornsson, Phys. Rev. Lett. 100, 200601 (2008).

9) E. Barkai and R. Silbey, Phys. Rev. Lett. 102, 050602 (2009).

10) “Catalysis and adsorption in zeolites”, G. Ohlman, H. Pfeifer, G. Fricke, Ed.s (Elsevier, Amsterdam, 1991).

11) J.G. Tsikoyiannis and J.E. Wei, Chem. Eng. Sci 46, 233 (1991).

12) C. Rodenbeck, J. Karger, and K. Hahn, J. Catal. 157, 656 (1995).

13) M.S. Okino, R.Q. Snurr, H.H. Kung, J.E. Ochs, and M.L. Mavrovouniotis, J. Chem. Phys. 111, 2210 (1999).

14) S.V. Nedea, A.P.J. Jansen, J.J. Lukkien, and P.A.J. Hilbers, Phys. Rev. E 65, 066701 (2002).

15) D.M. Ackerman, J. Wang, J.H. Wendel, D.-J. Liu, M. Pruski, and J.W. Evans, J. Chem. Phys. 134, 114107 (2011).

16) R. Krishna, J. Phys. Chem. C 113, 19765 (2009).

17) G. Nicolis and I. Prigogine, “Self-organization in non-equilibrium systems” (Wiley, New York, 1977).

18) J. Marro and R. Dickman, “Non-equilibrium Phase Transitions in Lattice-Gas Models” (CUP, Cambridge, 1999).

19) J.W. Evans, D.-J. Liu, and M. Tammaro, Chaos 12, 131 (2002).

20) H. Spohn, “Large scale dynamics of interacting particles” (Springer, Berlin, 1991).

21) R. Kutner, Phys. Lett. 81A, 239 (1981).

22) J.W. Evans, Rev. Mod. Phys. 75, 1281 (1993).

23) J. Quastel, Commun. Pure Appl. Math. 45, 623 (1992).

24) We obtain consistent results by creating steady-states with varying $\langle A_n \rangle$, but constant $\langle X_n \rangle = \chi$, and obtaining varying D_{tr} from simulation results for a discrete version of the ratio $-J_A/\partial A/\partial x$.

25) K.W. Kehr, K. Binder, and S.M. Reulein, Phys. Rev. B 39, 4891 (1989).

CHAPTER 6. DRIVEN DIFFUSION CALCULATION OF TRACER DIFFUSION COEFFICIENTS

1 Introduction

The generalized hydrodynamic theory previously developed [1] requires tracer diffusion values, $D_{tr}(i)$, for each site i in the pore. Previous work has generated these values using a random walk approach. An alternative method using Fick's Law and flux calculations is described below. This method has a few advantages over the random walk approach. A single simulation cycle can generate diffusion coefficients for all sites in the pore leading to faster generation of results for smaller pore. There is no ambiguity of the choice of definition of $D_{tr}(i)$ as there is in the random walk approach. The resulting D_{tr} values apply to the transition between sites (site i to site i+1) rather than at a specific site. This better matches the values needed for the generalized hydrodynamic formulation. However, it also means the results are not exactly comparable to the D_{tr} values from the random walk approach. Both an overall pore averaged diffusion value and individual site specific values are calculated using the same method. A significant downside is the inability to calculate values for very long pores.

The kinetic Monte Carlo model used is described in Sec 1, followed by the description of the multiple definitions of the diffusion coefficients as derived from Fick's Law in Sec 2. In Sec. 3, the long time correlations inherent in the system are discussed. Results are presented for the single file diffusion case as well as cases with varying degrees of passing in Sec 4. Finally, in the appendix, comparison is made with a similar method by Nelson *et al*.

2 Model and Kinetic Monte Carlo (KMC)

This study models a single, linear pore which forms part of a larger system containing many pores such as mesoporous silica or zeolites. The model, see figure 1, has a linear pore split into L discrete sites of uniform size. The sites are of width (diameter) d and length a, with 'a' on the order of 1nm, comparable to the size of a single molecule. Thus, the overall physical pore length is $L_{total} = aL$. The pore is contained within an external fluid and open at both ends which allows particles to diffuse into and out of the pore at the end sites, n=1 and n=L. Outside each end of the pore is an external site of the same size as the pore sites. This is occupied with probability X_{out}. Connecting with a physical system, X_{out} can be related to a fluid concentration using the size of the external site. Assuming the external site to be the same size as a site within the cylindrical pore, the fluid concentrations, C_{out}, is given by $X_{out}/(\pi$

$(d/2)^2a)$.

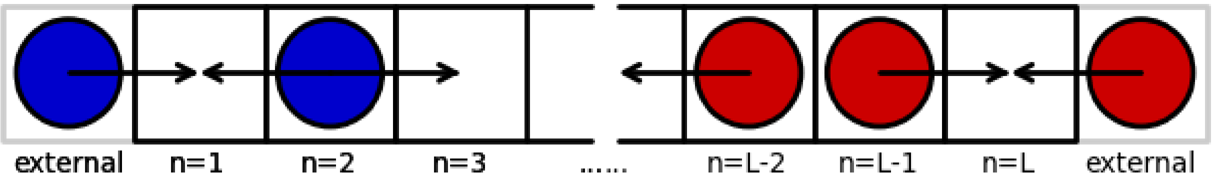

Figure 1: Schematic of pore, showing A (in blue) entering from one end of the pore, with B (in red) entering form the other. Hopping occurs to neighboring empty sites as shown at n=2. Exchange of occupied sites (e.g. n=L-2 and n=L-1) may or may not be allowed.

A kinetic Monte Carlo (KMC) simulation is used to generate a steady state configuration and calculate average site occupancies. The simulation is performed by making a series of discrete moves from one configuration to another. The possible moves are as follows: (i) particles in the pore can hop to a nearest neighbor site, undergoing a discrete random hopping process which leads to a diffusional motion within the pore. The rate of hopping to an unoccupied site is h. For an occupied site, a hopping process is an exchange of the particles at neighboring sites. The rate for this process is P_{ex} h, where P_{ex} is an exchange factor (in range [0,1]) representing the ease of particles passing each other within the pore. P_{ex} is primarily based on the diameter of the pore being large enough to allow particles to pass. $P_{ex}=0$ is a strict single file case where passing is prohibited as the pore is too narrow. In the single file case, hops can then only be made to empty sites. When $P_{ex}>0$, particles are able to hop to occupied sites at the reduced rate P_{ex} h and also hop to empty sites at the normal rate h. At the extreme, $P_{ex}=1$ would be a very wide pore where particles can pass each other unhindered, essentially becoming a single particle diffusion problem. The intermediate case of $0<P_{ex}<1$ represents a partial relaxation of the single restriction and is called hindered passing. All three cases are treated below. (ii) Particles can hop into the pore at either end site. The external fluid is assumed to be well-stirred and to move at a faster rate than the fluid inside. Since the fluid particles just outside the pore move rapidly the occupancy of the external fluid site is not tracked. Instead it is represented by the average occupancy X_{out}. The rate to hop in is $w_{ads} = h\ X_{out}$, reflecting the standard hopping rate scaled by the probability of the site just outside of the pore to be occupied. In this model, the relaxation of the single file constraint (i.e. cases where $P_{ex}>0$) does not change the adsorption rules. (iii) A particle at an end site can hop out of the pore. The rate for this desorption is $w_{des} = h\,(1-X_{out})$, with the $1-X_{out}$ factor representing the probability of the external site being empty. As with adsorption, the desorption process is unchanged when passing is added to the system. This adsorption/desorption scheme results in the steady state concentration inside the pore being equal to the concentration of the external fluid.

In this model, there are two types of particles labeled A and B. At the start of the pore, n=1, only atoms of type A enter the pore. At the end of the pore, n=L, only atoms of type B can enter. Once in the pore, they move as described above, and both types can exit from either end. There is no conversion between types. The properties of each type are identical, leaving the label only as a convenient method of bookkeeping. Atoms of type A that exit at site n=L have managed to diffuse through the entire pore to reach the other end. Similarly atoms of type B that exit from n=1 have made it through the pore. This allows determination of the flux through the pore, despite the fact that steady state requires the net flux out each end to be zero.

The initial occupancy of each site is determined by filling it with a probability given by the desired loading, X_{out}. The species of each atom is determined by a probability which varies linearly from 100% A at one end to 100% B at the other. This approximates the final averaged concentration. See section 4 for further details.

The simulation is tracked over time. After an initial equilibration period, the occupancy of every site is recorded and the number of atoms exiting the pore is counted. Atoms exiting the end they entered from are ignored, but ones exiting the opposite end (at site L for type A and site 1 for type B) are counted for as part of the flux analysis.

3 Theory and Simulations

We consider only the case where the total concentration X=A+B s constant. In this case, dA/dx=-dB/dx. In this “counter diffusion” mode, one has a refined version of Fick's [2] first law that gives[3]:

$$J=-D_{tr}\frac{\delta c}{\delta x} \tag{1}$$

with J as the flux of either A or B atoms, and δc/δx the concentration gradient of A or B. The gradient and flux are defined such that D is positive. All further equations are written assuming species A which enters the pore at site 1 and exits at site L.

3.A. Pore averaged tracer diffusion coefficient (D_{tr})

Equation (2) can be used in two manners. The first is as an overall value for diffusion across the length of the pore. This is an averaged D value for an atom moving from one end to another. In this case, the flux is then the atoms that pass out the end opposite of where they entered, and the gradient of interest is the concentration change from one end to the other. These values are:

$$J = w_{des} c_1 \tag{2}$$

$$\frac{\delta c}{\delta x} = \frac{2c_1 - X_{eq}}{(L-1)} \tag{3}$$

where w_{des} is the rate of hopping out of the pore, and c_1 is the concentration at site 1. By symmetry, the concentration at the other end must be $X_{out} - c_1$. A factor of a, representing a characteristic length, is omitted from equation (3) and all future equations for the gradient and diffusion coefficients. The diffusion coefficients presented are reduced values: D = D'/a

Plugging these into the Fick's law and rearranging yields the expression for D:

$$D(L) = \frac{w_{des} c_1 (L-1)}{(X_{out} - 2c_1)} \tag{4}$$

An exact solution is possible only with a knowledge of c_1, but an analytic expression for c_1 has proven elusive. A simplifying approximation for large L comes when $X_{out} >> 2c_1$:

$$D(L) = \frac{w_{des} L}{X_{out}} * c_1(L) \tag{5}$$

c_1 decreases with increasing L. As D(L) also decreases with increasing L, $c_1(L)$ must decrease faster than 1/L.

3.B. Site specific D_{tr}

The second method uses equation (2) to calculate the diffusion coefficient between two sites. In this case, the gradient is defined as being between two adjacent sites:

$$\frac{\delta c}{\delta x} = c_i - c_{i+1} \tag{6}$$

With this definition, the D value is actually the value between sites rather than at specific sites as found by the random walk method. The flux is the same as before as it must be uniform throughout the pore. This yields the equation for D(i+0.5), which is defined as the site specific tracer diffusion coefficient, $D_{tr}(i)$:

$$D_{tr}(i) \equiv D(i+0.5) = \frac{w_{des} c_1}{c_{i+1} - c_i} \tag{7}$$

The per site diffusion coefficient is roughly constant in the center of the pore as the concentration profile there is linear. Near the end of the pore, the non-linear concentration curve results in an increase of D_{tr}. Correspondingly, the D_{tr} values in the center region must be smaller than the pore averaged D value (this can also be seen by noting that the concentration slope in the center region is greater than the pore averaged slope - see figure 3). This effect is greatest for short pores where the non-linear region is a significant fraction of the overall length. For a long pore, if this non-linear region is taken to be small compared to the total length, the value of $D_{tr}(L/2)$ will approach the value of D for the pore. This is easily seen by noting that for the limit of large L, $c_{L/2+1} - c_{L/2} = X_{out}/L$, recovering equation (5) from equation (7).

3.C. Minimum D_{tr}

The value for the minimum value of D_{tr} is given as:

$$D_{tr}(min) = \frac{1 - X_{eq}}{1 + X_{out}(L-1)} \tag{8}$$

Equating this to the large L equation from Fick's law, eq. (5), (but retaining the L-1) gives:

$$\frac{w_{des} c_1 (L-1)}{X_{out}} = \frac{1 - X_{out}}{1 + X_{out}(L-1)} \qquad (9)$$

Noting that $w_{des} = h(1 - X_{out})$, under the condition h = 1, c_1 is given by:

$$c_1 = \frac{1}{\frac{(L-1)}{X_{out}} + (L-1)^2} \qquad (10)$$

3.D. Simulation flux and concentration profiles

Calculating the D_{tr} values requires the flux of each type of particle as well as the concentration profile to calculate the concentration gradient. The flux is easily found by recording the number of particles that exit from the opposite end as they entered. Labeling the particles by which end they enter makes this process trivial and is the only purpose for the A/B labels of otherwise identical particles.

The concentration profile is a time weighted average of the occupancy at each site:

$$\langle K_i \rangle = \frac{\sum_{m=1}^{N} \Delta t_m O_i(K)}{\sum_{m=1}^{N} \Delta t_m} \qquad (11)$$

$$O_i(K) = \begin{cases} 1, \text{if site i is occupied by particle of type K} \\ 0, \text{otherwise} \end{cases} \qquad (12)$$

where K is the particle type, either A or B, and $O_i(K)$ denotes whether site i is occupied by a particle of type K. Calculating this requires knowing how long each type of atom remained at each site. As the time steps in the kinetic Monte Carlo algorithm are different, eq (11) is used to generate a time weighted average of how long each site is occupied by each particle type. Implementing this requires some care to do correctly and efficiently. The simplest method is to update the sums at each time step - either during the simulation or by recording the configuration at each time step for later analysis. An easy way to gather this data is to store the occupancy at each site at each configuration change (i.e. after each change, update the statistics to note that the particle type at each site has been there for Δt_n, the length of time for this move). While this is simple, it is very inefficient. A single configuration change affects, at most, two sites. The others are unchanged. Updating sites only when they change dramatically reduces the number of calculations performed.

To only update the sites that change, we need to track the time at which each site's occupancy was last changed (particle is added/removed/swapped from the site). The algorithm used is as follows: We create a listing of the last modified time for each site. At the end of the equilibration phase we set the values for all sites to the current time, which is the start of the production part of the simulation. These times are updated every time a site's occupancy changes. At any time, the time a particle has been in the site is the current time less our stored time of when the site's status last changed. At each time step, this value is calculated only for the sites where a change occurs. Those values are added to the accumulated stats. No calculation is made for any other sites. In this way, particles that don't move are ignored. At the end of the simulation, the occupancy time is calculated for all sites and added to the total. Failure to do so would omit the current configuration from the averaging.

This method ensures that the time spent on calculating statistics for each time step is independent of the size of the system, compared to the simple method which requires more time for larger systems. The cost of this faster method is the additional bookkeeping of the last time each particle was moved. For all but the smallest system sizes, this overhead should be significantly less than the time saved by not updating occupancy times for particles that have not moved.

4 Correlations

As noted above, the initial configuration is generated as a linear gradient with $A=X_{out}$, $B=0$ at one end and $A=0$, $B=X_{out}$ at the other. This artificial initial configuration, Figure 2a, will evolve into the actual steady state profile which displays non-linear behavior near the pore ends as seen in Figure 2b. The non-linear effects should increase with decreasing pore loading.

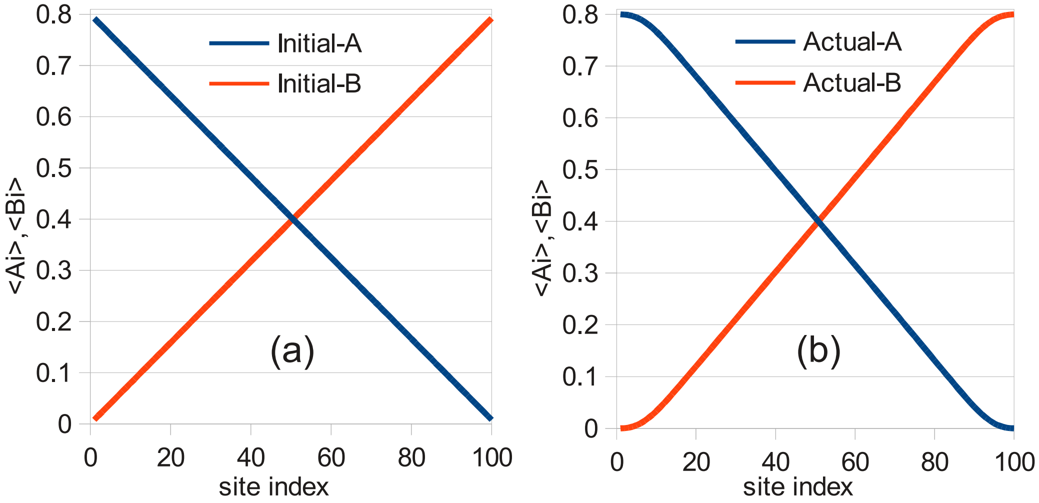

Figure 2: Example of - (a) initial concentration profile and (b) steady state concentration profile, showing non-linear end effect and greater slope in the center region. Both plots correspond to X_{out}=0.8 and L=100.

4.A. Pore loading correlation

During the change from the initial concentration profile to the steady state profile, the single file motion creates correlations within the system. This occurs as the initial loading of each site - which is completely independent of the loading of surrounding sites - relaxes to the steady state profile. A challenge in this type of simulation is to determine when the system has reached this steady state. One method of quantitatively tracking the evolution is to follow these correlations and related quantities over time. They will evolve from their artificial initial values and reach the steady state values. There are several quantities of interest. The total number of particles is N, and the number of A and B particles is N_A and N_B, respectively. Variations in these values are described by the variance(Var) and covariance(Cov) [4] as defined below:

$$Var(N)=\langle(N-\langle N\rangle)^2\rangle=\langle N^2\rangle-\langle N\rangle^2 \quad (13)$$

$$Var(N_A)=\langle(N_A-\langle N_A\rangle)^2\rangle=\langle N_A^2\rangle-\langle N_A\rangle^2 \quad (14)$$

$$Var(N_B)=\langle(N_B-\langle N_B\rangle)^2\rangle=\langle N_B^2\rangle-\langle N_B\rangle^2 \quad (15)$$

$$Cov(N_A,N_B)=Cov(N_B,N_A)=\langle(N_A-\langle N_A\rangle)*(N_B-\langle N_B\rangle)\rangle=\langle N_A N_B\rangle-\langle N_A\rangle\langle N_B\rangle \quad (16)$$

The average values <N_A>, <N_B>, and <N> are calculated as an ensemble average of the number of A, B, and N atoms present at a given time point. The expected value for Var(N) can be calculated by treating all site loadings as uncorrelated:

$$Var(N)=\frac{L*w_{des}*w_{ads}}{(w_{ads}+w_{des})^2}=L\,X_{out}(1-X_{out}) \tag{17}$$

The quantities in eq. (13) - (16) are related [4]:

$$Var(N)=Var(N_A)+Var(N_B)+2*Cov(N_A,N_B) \tag{18}$$

As A and B are indistinguishable, the variance of both must have the same convergence time. By construction, Var(N) of the initial configuration is at its expected value and remains constant. Thus, Cov(N_A, N_B) must have the same convergence time as Var(N_A) and Var(N_B), making any of the 3 quantities equally valid for tracking convergence.

Equation (18) above can also be written as:

$$Var(N)=\langle N_A^2\rangle-\langle N_A\rangle^2+\langle N_B^2\rangle-\langle N_B\rangle^2+2*(\langle N_A N_B\rangle-\langle N_A\rangle\langle N_B\rangle) \tag{19}$$

Again noting that A and B are indistinguishable, it follows that <N_A> = <N_B> and <N_A^2> = <N_B^2>, yielding:

$$Var(N)=2*\langle N_A^2\rangle-4*\langle N_A\rangle^2+2*\langle N_A N_B\rangle \tag{20}$$

Figure 3a shows the convergence of the values given above (the A and B curves nearly overlap and aren't distinguishable on the plot). The total variance in the number of particles is essentially constant. The variances of A and B and the covariance take a significant time to converge, but all do so on the same time scale, as expected. Figure 3b shows the evolution of the variance in A as it approaches the steady state value.

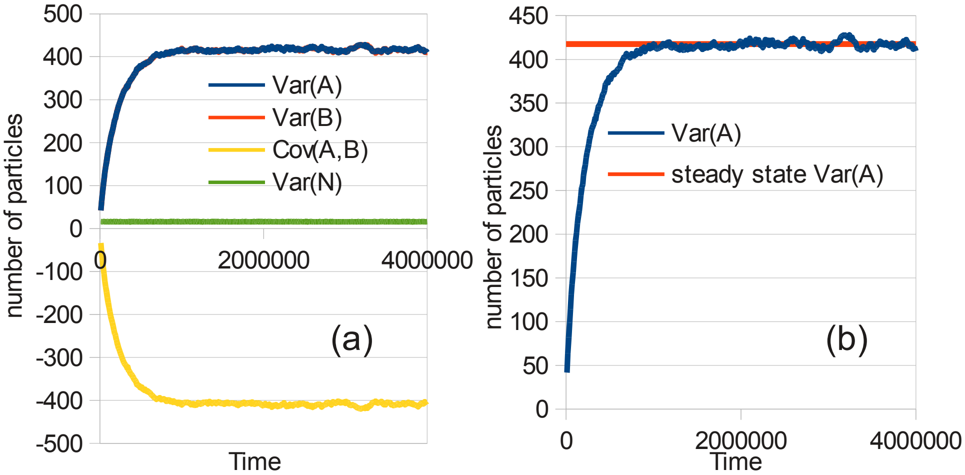

Figure 3: Relaxation of particle numbers over time for X_{out}*=0.8, L=100. (a) shows all values, while (b) shows details of* N_A *reaching the steady state value.*

4.B. Pair correlations

In addition to the total site occupancies, the variance in the values of site concentrations can be calculated. Individual site concentrations should all have the same variance. However, the correlation of neighboring sites can be calculated and will vary at different sites in the pore. In principle, correlations could be calculated for any two sites. In practice, it was only done for adjacent sites.

The covariance of any two site occupancies is defined as:

$$Cov(A_i, A_j) = \langle (A_i - \langle A_i \rangle) * (A_j - \langle A_j \rangle) \rangle = \langle A_i A_j \rangle - \langle A_i \rangle \langle A_j \rangle \qquad (21)$$

The case of adjacent sites gives:

$$Cov(A_i, A_{i+1}) = \langle A_i A_{i+1} \rangle - \langle A_i \rangle \langle A_{i+1} \rangle \qquad (22)$$

The correlations increase for sites further in the pore. Pairs of sites near the pore end appear to show faster convergence to a steady state value than those further in the pore. Figure 4 shows the curves for several i values. Note the different Y-axis scale on the two plots.

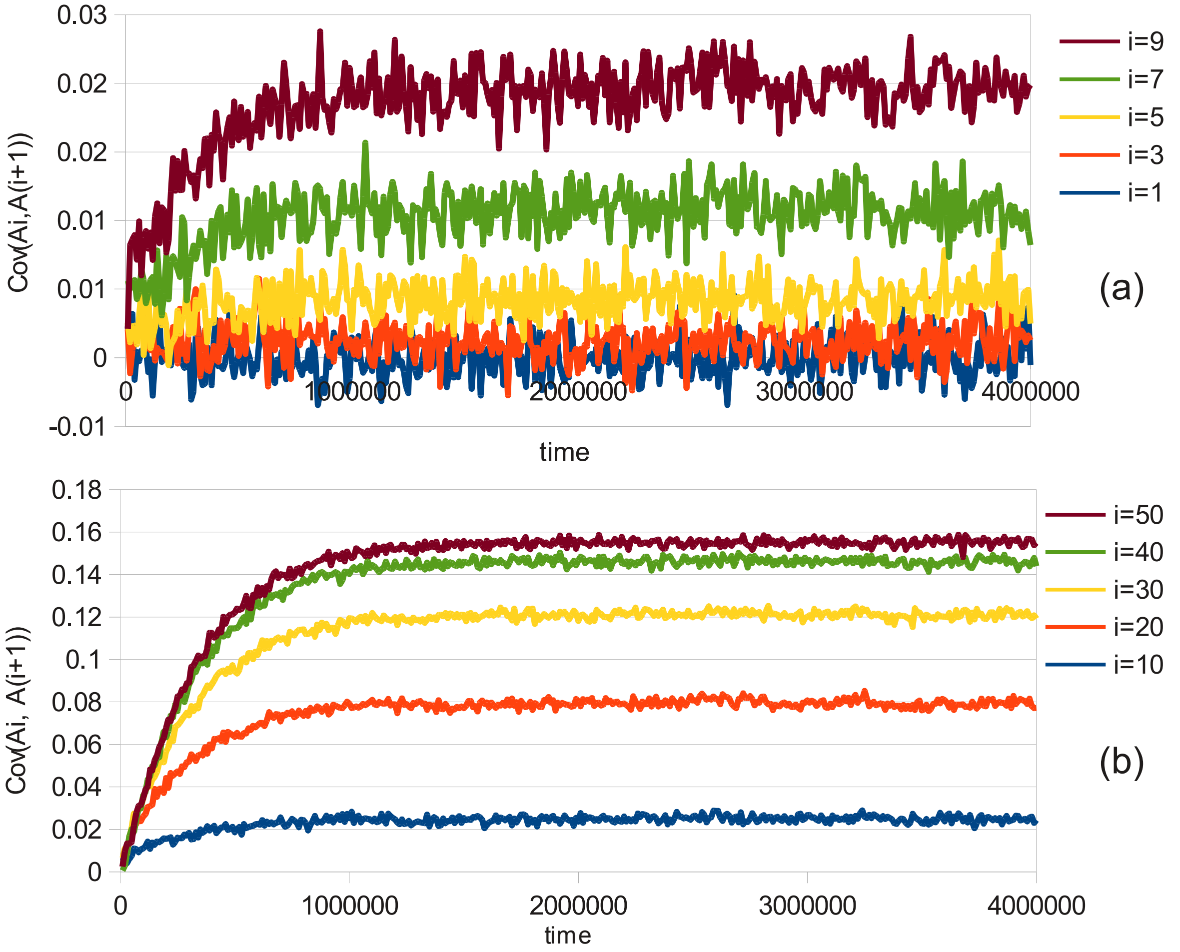

Figure 4: Pair correlation curves for Xout=0.8 and L=100. (a) shows curves for sites i=1,3,5,7,9 (from bottom to top). (b) curves for for sites i=10,20,30,40,50. Note the different scales on the y axis in (a) and (b).

5 Simulation Results

Simulations were run for the strict single file case (P_{ex}=0), the complete passing case (P_{ex}=1), and the intermediate obstructed passing case (0<P_{ex}<1). Results are shown for multiple pore lengths. Three diffusion coefficients were derived as described previously. These values are: D_{tr}(i), the tracer diffusion coefficient based on the flux between site i and i + 1 (equation (7)); D_{tr}(min), a minimum value calculated from the pore length and X_{out} values as given by equation (8); and D(pore averaged), the diffusion coefficient calculated using the flux across the entire pore (equation (4)). D(pore averaged) will be larger than D_{tr}(min) but should approach that value as the pore length increases. D_{tr}(min) is calculated from the system parameters without any simulations. A corresponding value can be calculated from the KMC data by taking an average of $D_{tr}(i)$ values in the pore center.

5.A. Single-file diffusion

Two cases were considered for the diffusion studies, a high loading case with $X_{out}=0.8$ and a low loading case with $X_{out}=0.2$. The former would exhibit stronger single file effects as the individual particles are more confined by neighboring particles. For the high loading case, parameters are $P_{ex}=0$, $w_{ads}=0.8$, $w_{des}=0.2$, and $h=1$. Pore length ranged between 10 and 500. Results for the flux and pore averaged values of D_{tr} are in table 1 below. Figures 5 and 6 show the first few D_{tr} values. A line is shown on each plot indicating the expected minimum value of D_{tr}.

Next to each plot of D_{tr} values in figures 5 and 6 is a graph of the convergence of the variances of A and site pair data in the pore center. This was used to determine where to start averaging the data for the flux calculations. The start time used is shown on the plots. The end time is not shown.

The pair correlation curve was scaled vertically to fit on the plot to show comparison of the time required to reach a steady state value.

For the low loading case of $X_{out}=0.2$, parameters are $P_{ex}=0$, $w_{ads}=0.2$, $w_{des}=0.8$, and $h=1$. Results are given in table 2 and plots are shown in figures 7 and 8. Format of the tabulated and plotted results is the same as for the high loading case.

Table 1: Calculated and expected values for flux, c_1*, and tracer diffusion coefficients for* X_{out}*=0.8. * Expected* c_1 *value is calculated using eq. (10), ** Expected flux is calculated from with eq. (2) ,using actual* c_1 *values. *** "Minimum" value for the actual case is an average of values from the center 20% of the pore. ****Calculated from eq. (4), using the actual* c_1 *value.*

Pore length	c_1 **actual (expected*)**	**flux actual (expected**)**	D_{tr}**(min) actual*** (expected)**	D_{tr}^{****} **pore average**
10	0.01230 (0.01084)	2.461x10^{-3} (2.460x10^{-3})	0.02301 (0.02439)	0.02856
30	1.34x10^{-3} (1.14x10^{-3})	2.684x10^{-4} (2.684x10^{-4})	7.998x10^{-3} (8.264x10^{-3})	9.761x10^{-3}
50	4.699x10^{-4} (4.0613x10^{-4})	9.397x10^{-5} (9.397x10^{-5})	4.873x10^{-3} (4.975x10^{-3})	5.763x10^{-3}
100	1.1278x10^{-4} (1.0076x10^{-4})	2.2556x10^{-5} (2.2556x10^{-5})	2.458x10^{-3} (2.494x10^{-3})	2.792x10^{-3}
300	1.20x10^{-5} (1.111x10^{-5})	2.402x10^{-6} (2.402x10^{-6})	8.31x10^{-4} (8.33x10^{-4})	8.98x10^{-4}
500	4.21x10^{-6} (4.006x10^{-6})	8.4118x10^{-7} (8.4113x10^{-7})	4.934x10^{-4} (4.998x10^{-4})	5.247x10^{-4}

Table 2: Calculated and expected values for flux, c_1*, and tracer diffusion coefficients for* X_{out}*=0.2. * Expected* c_1 *value is calculated using eq. (10) ** Expected flux is calculated with eq. (2) ,using the actual* c_1 *value. *** "Minimum" value for the actual case is an average of values from the center 20% of the pore. ****Calculated from eq. (4), using the actual* c_1 *value.*

Pore length	c_1 **actual (expected*)**	**flux actual (expected**)**	D_{tr}**(min) actual*** (expected)**	D_{tr}^{****} **pore average**
10	0.01038 (7.937x10^{-3})	8.305x10^{-3} (8.304x10^{-3})	0.3595 (0.2857)	0.4170
30	1.623x10^{-3} (1.014x10^{-3})	1.298x10^{-3} (1.298x10^{-3})	0.1333 (0.1176)	0.1913
50	5.949x10^{-4} (3.779x10^{-4})	4.760x10^{-4} (4.760x10^{-4})	0.07864 (0.07407)	0.1173
100	1.1428x10^{-4} (9.7125x10^{-5})	1.1433x10^{-4} (1.1426x10^{-4})	0.03880 (0.03846)	0.05664
300	1.4217x10^{-5} (1.1002x10^{-5})	1.1376x10^{-5} (1.1373x10^{-5})	0.01308 (0.01316)	0.01701
500	4.90x10^{-6} (3.9762x10^{-6})	3.9212x10^{-6} (3.9222x10^{-6})	0.007940 (0.007937)	0.009786

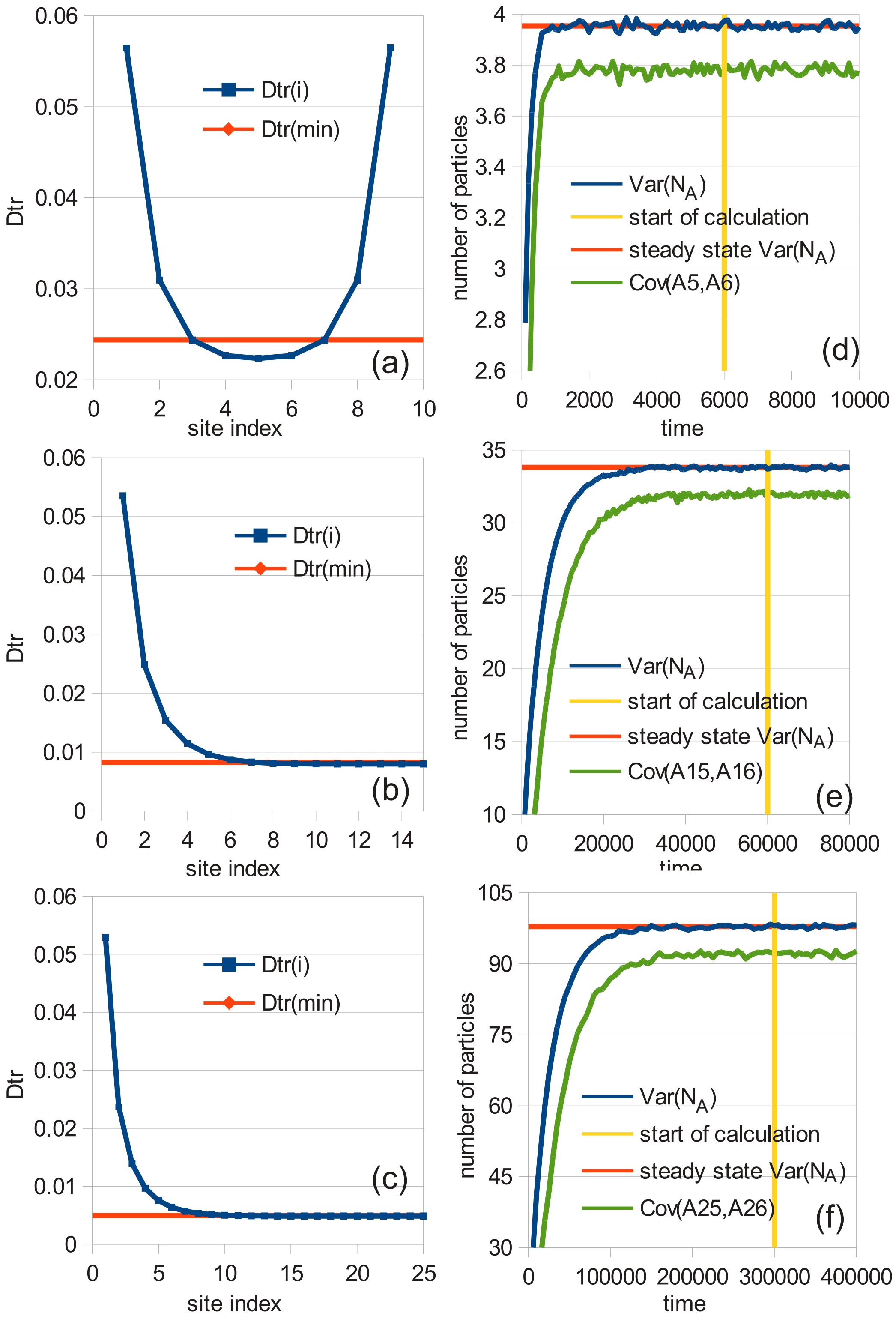

Figure 5: Tracer diffusion values and correlation curves. For all plots, X_{out}=0.8, P_{ex}=0, h=1. L=10 for (a) & (d). L=30 for (b) & (e). L=50 for (c) & (f).

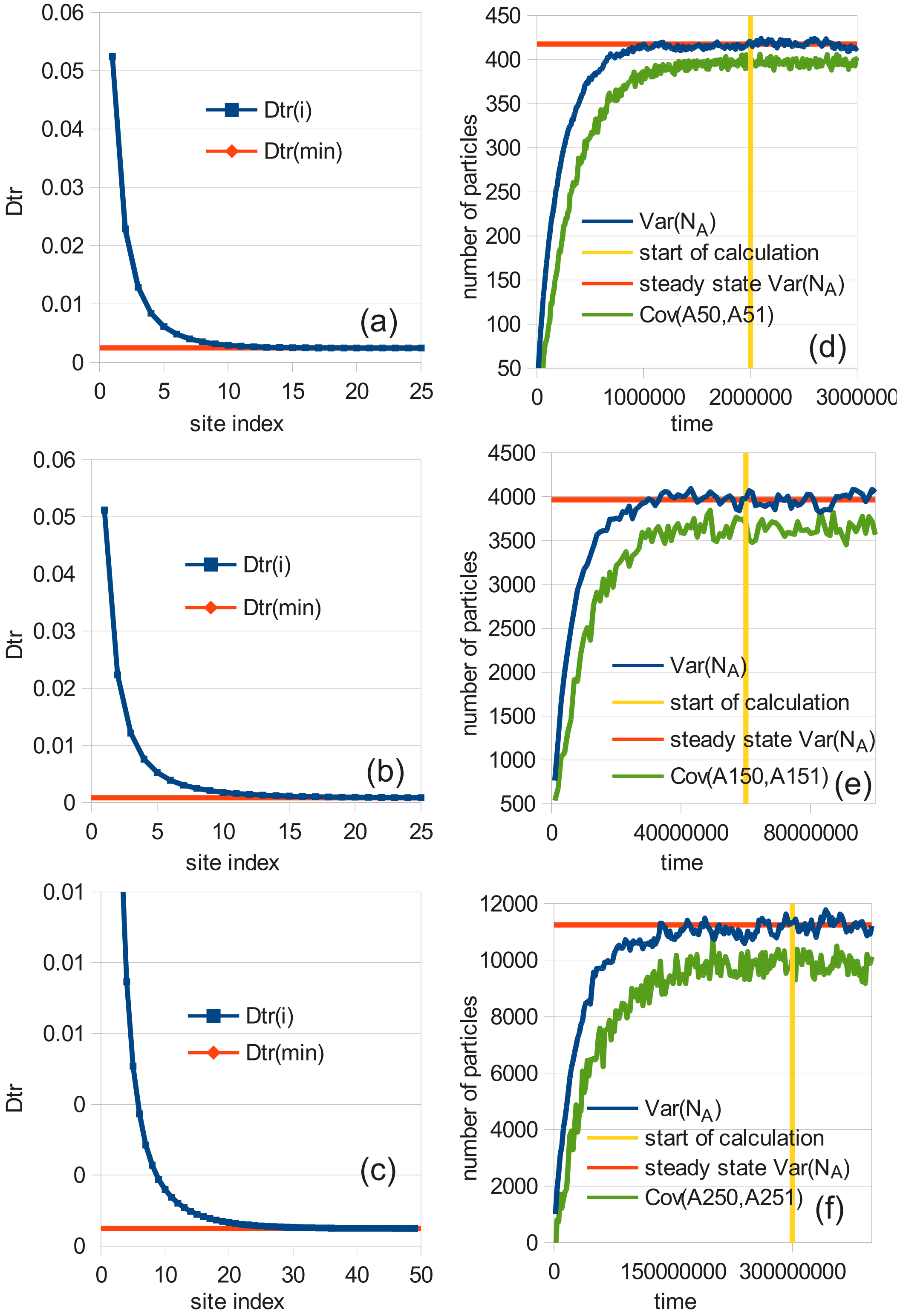

Figure 6: Tracer diffusion values and correlation curves. For all plots, X_{out}=0.8, P_{ex}=0, h=1. L=100 for (a) & (d). for L=300 for (b) & (e). L=500 for (c) & (f).

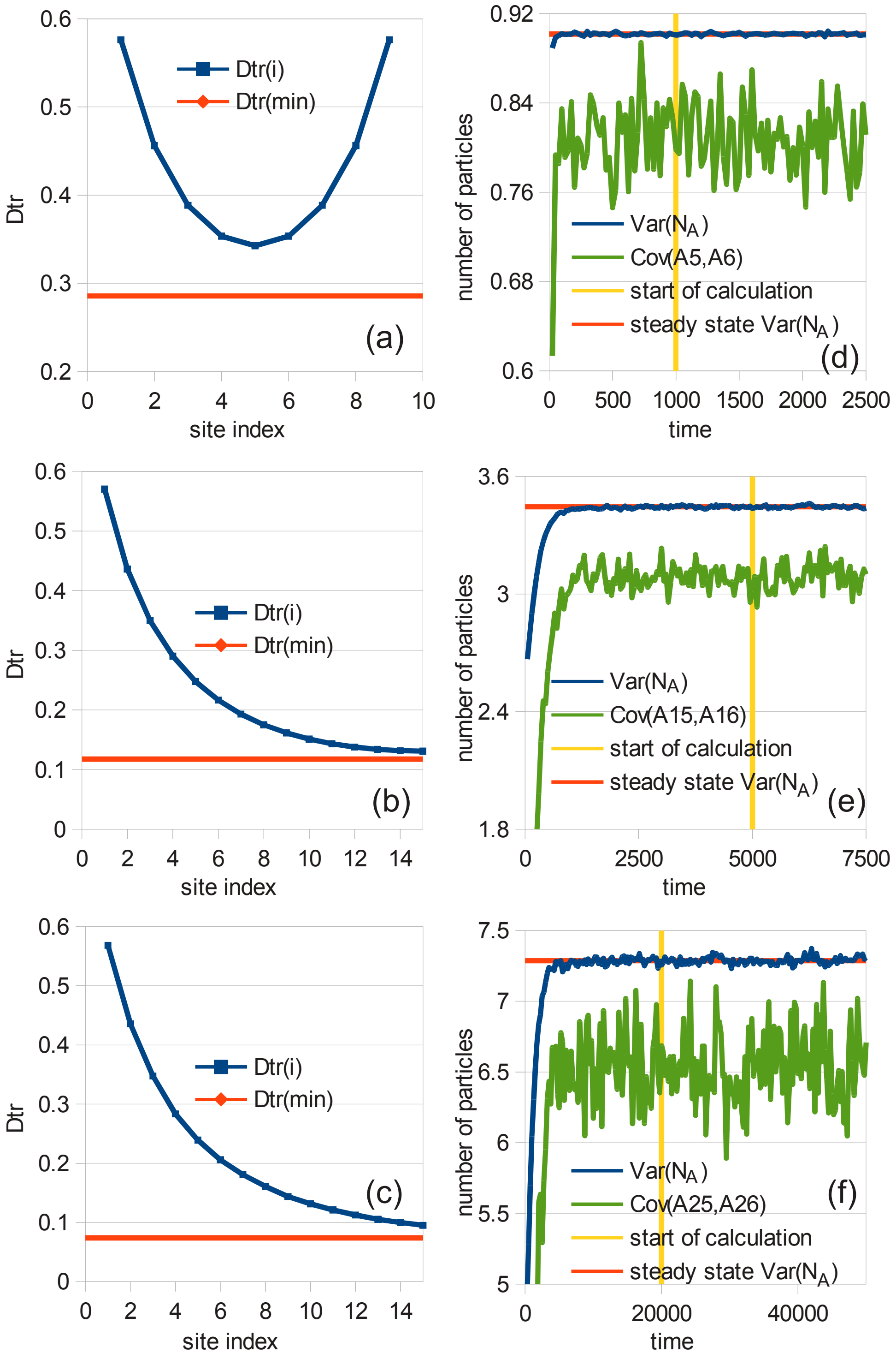

Figure 7: Plots of tracer diffusion values and correlation curves used to determine onset of steady state. For all plots, X_{out}*=0.2,* P_{ex}*=0, h=1 (a) and (d) for L=10, (b) and (e) are L=30, (c) and (f) are L=50.*

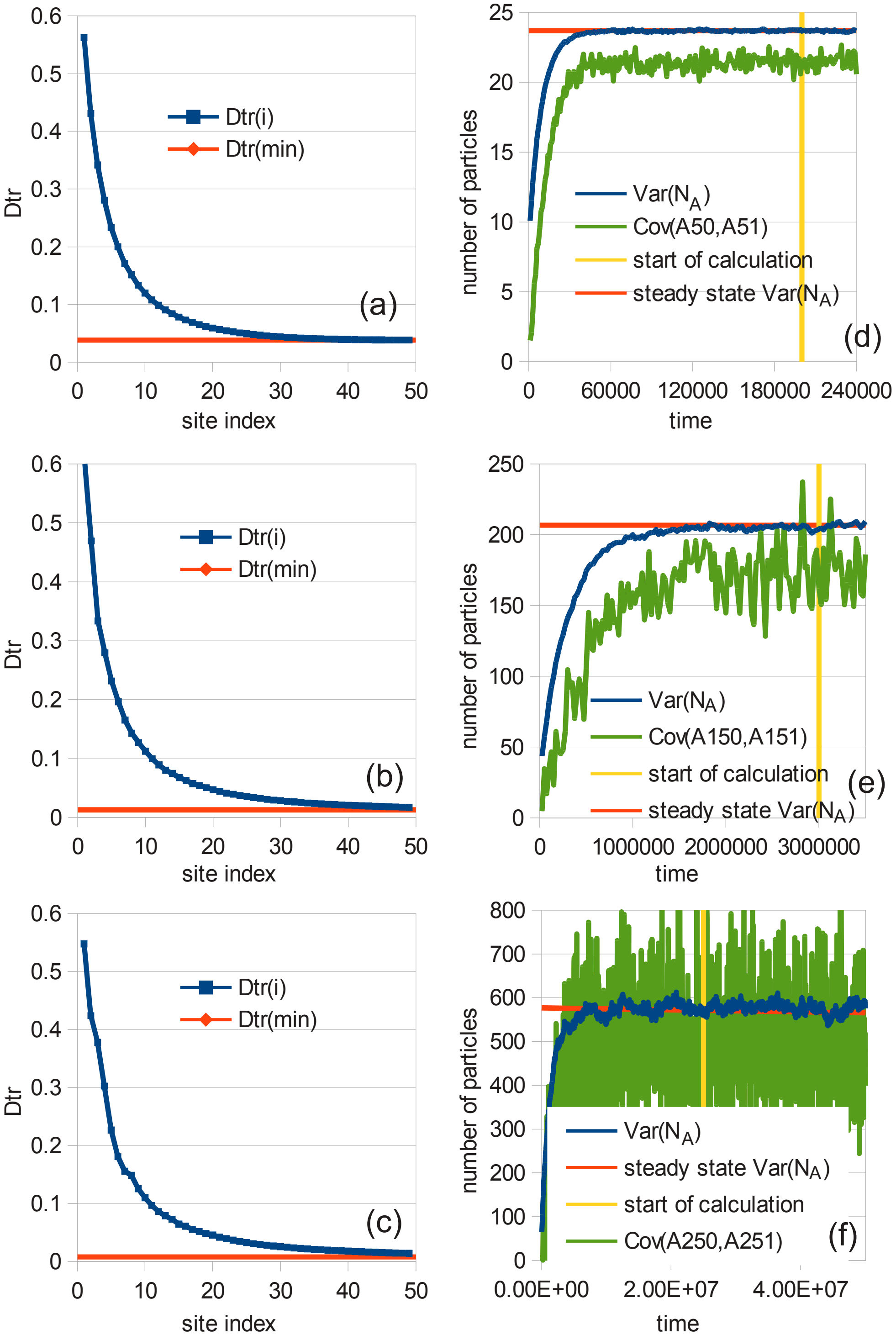

Figure 8: Plots of tracer diffusion values and correlation curves used to determine onset of steady state. For all plots, X_{out}=0.2, P_{ex}=0, h=1 (a) and (d) for L=100, (b) and (e) are L=300, (c) and (f) are L=500.

5.B. With passing

A pore diameter larger than twice of the size of the hopping particles can allow room for particles to pass each other. This behavior is modeled using a non-zero P_{ex} value. For a very wide pore, $P_{ex}=1$ and the particles can move unhindered by their neighbors. This is also equivalent to the case of single particle diffusion and is exactly solvable. The tracer diffusion values are trivially determined as D=h for all sites. The results are more interesting for the case with passing and $P_{ex}<1$. Simulations were run for pores of length 100 with both high ($X_{out}=0.8$) and low ($X_{out}=0.2$) loading and several values of P_{ex}. The correlation data is shown is figure 9. Comparison with results for figures 6e and 8e shows there is very little correlation apparent in the systems. The introduction of passing allows any correlations that might form to relax rapidly. The variation in the number of particles of each type quickly reaches the steady state value. Meanwhile, the pair correlation in the center of the pore is essentially zero.

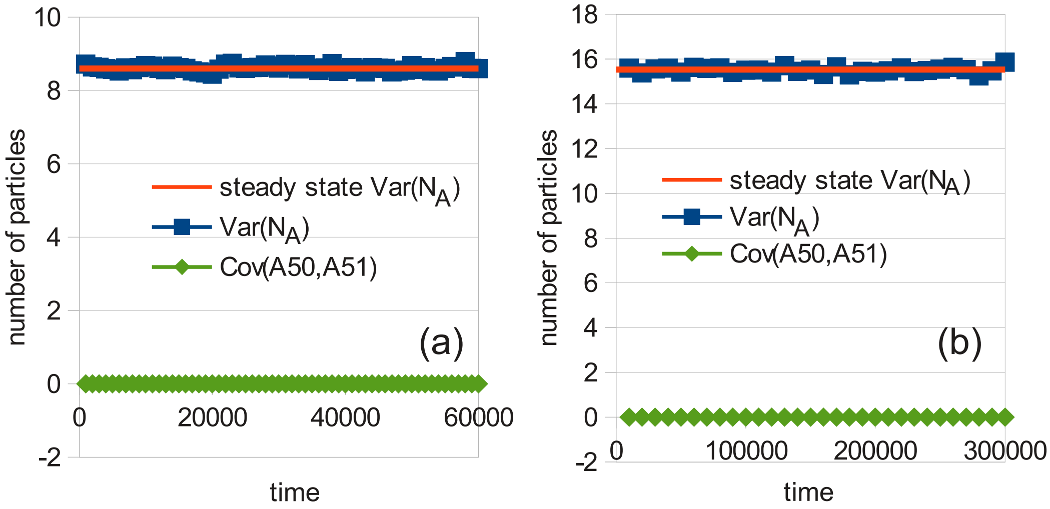

Figure 9: Particle number variation and pair correlation in the pore center for L=100, h=1, $P_{ex}=0.25$. (a) shows the low loading, $X_{out}=0.2$ (b) shows the high loading $X_{out}=0.8$. Note: Unlike previous plots, the pair correlations have not been scaled as they are mostly noise around zero.

Figure 10 shows plots of the tracer diffusion coefficients for several P_{ex} values. The results match the expected values and previous results.

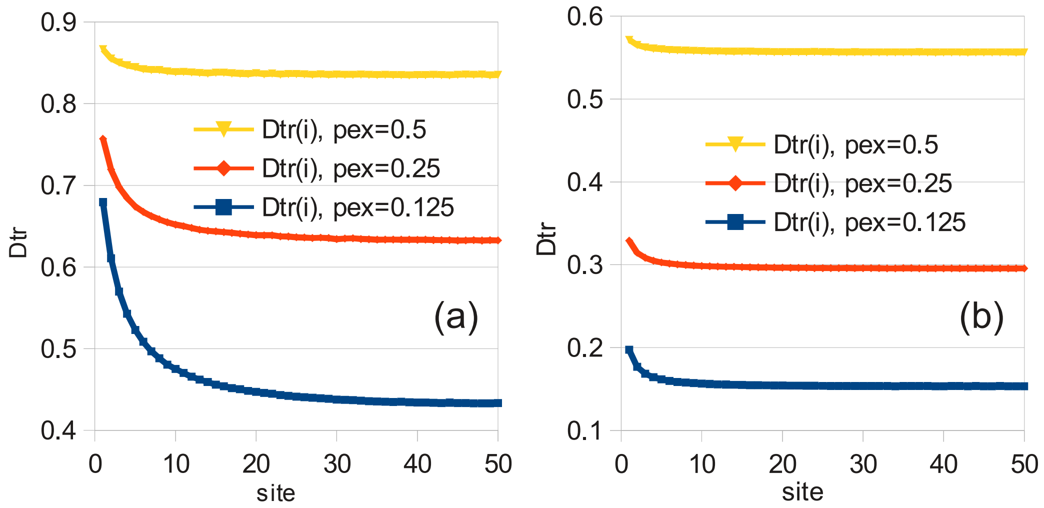

Figure 10: Tracer diffusion values as calculated with passing. (a) shows high loading, X_{out}=0.8 (b) shows high loading X_{out} =0.2.

6 Conclusions

The method of calculating D_{tr} values presented here shows qualitative agreement with previous results. The values do not exactly match the random walk method used in previous studies and exact agreement is not expected as the quantities being calculated are different. The primary advantage of this approach is the ability to simultaneously calculate $D_{tr}(i)$ for all sites with a method free from the ambiguity inherent in the random walk case.

An extensive study of correlations leading to steady state behavior was made. It shows a significant time required from the initial condition to reach the steady state in a single file system. When the single file condition is relaxed, the correlations are weaker. This agrees with the intuition that a system that can allow easy mixing will not form the same degree of correlations as one where the motion is more confined and particles can't change neighbors without reaching a pore end.

The method presented is a complete working description of D_{tr} calculations. The values can be used interchangeably with previous results from the random walk approach. Future studies of this method could entail adding a swapping behavior at the end of the pore where a particle in an end site will make a single step exchange with the particle at the external site. This behavior was omitted from the model and has shown to affect the results in the vicinity of the pore openings.

Appendix A: Mixed Type Adsorption

A more general case of this model has the adsorption at each end being a mixture of types, with some fraction being A and the rest being B. The opposite end would then have the same ratio of adsorption with the types reversed. The resulting D_{tr} values should be the same as before since the hopping process is independent of the type of particle adsorbed. This treatment is included to validate the method. Fick's law, equation (2), applies as before; however, in this case the flux is the net flux at the end:

$$\begin{aligned} J &= J_{out} - J_{in} \\ &= c_1^* w_{des} \\ &= c_1^* w_{des} - (1 - X_{out}) w_{ads}^B \\ &= c_1^{XS} w_{des} \end{aligned} \tag{23}$$

$$\begin{aligned} c_1^{XS} &\equiv c_1^* - X_{out}^B \\ X_{out}^B &\equiv \frac{w_{ads}^B}{(w_{ads} + w_{des})} \end{aligned} \tag{24}$$

where w^B_{ads} is the adsorption rate of B at site n=1 (which was zero in the previous case). c_1^{XS} is the excess B at site n=1 that is present due to diffusion through the pore. The * in c_1* is included to distinguish from the previous case where only one type enters at each end (hereafter referred to as the pure adsorption case). The gradient is given as:

$$\frac{\delta c}{\delta x} = \frac{2c_1^* - X_{eq}}{(L-1)} = \frac{2c_1^{XS} + 2X_{out}^B - X_{out}}{(L-1)} \tag{25}$$

The equation for D is found from Fick's law:

$$D = \frac{w_{des} c_1^{XS} (L-1)}{(X_{eq} - 2c_1^{XS} - 2X_{out}^B)} \tag{26}$$

With $w^B_{ads} = 0$, this matches the previous result in equation (4). Comparison of the two equations shows that they are equivalent if:

$$\begin{aligned} \frac{c_1^{XS}}{c_1} &= (1-2S) \\ S &\equiv w_{ads}^B / w_{ads} \end{aligned} \tag{27}$$

where S is the splitting factor and is just the fraction of the adsorbed particles that are type B. The range is 0 (pure adsorption case) to 0.5 (equal split of A and B).

The site-specific diffusion coefficients generated using this method will be equal to the pure adsorption case if the differences of site concentrations follows equation (28).

$$\frac{c_{i+1}^{XS} - c_i^{XS}}{c_{i+1} - c_i} = \frac{\Delta c_i^{XS}}{\Delta c_i} = (1-2S) \tag{28}$$

The two cases investigated were S=0.2 and S=0.4 (the S=0 case is the pure adsorption for comparison). These were done for both low loading (X_{out}=0.2) and high loading (X_{out}=0.8) and for both single file (P_{ex}=0) and a case with hindered passing, P_{ex}=0.5. Plots are labeled with the parameters used. Figure 11 shows that the diffusion coefficients are comparable for the three splitting factors investigated.

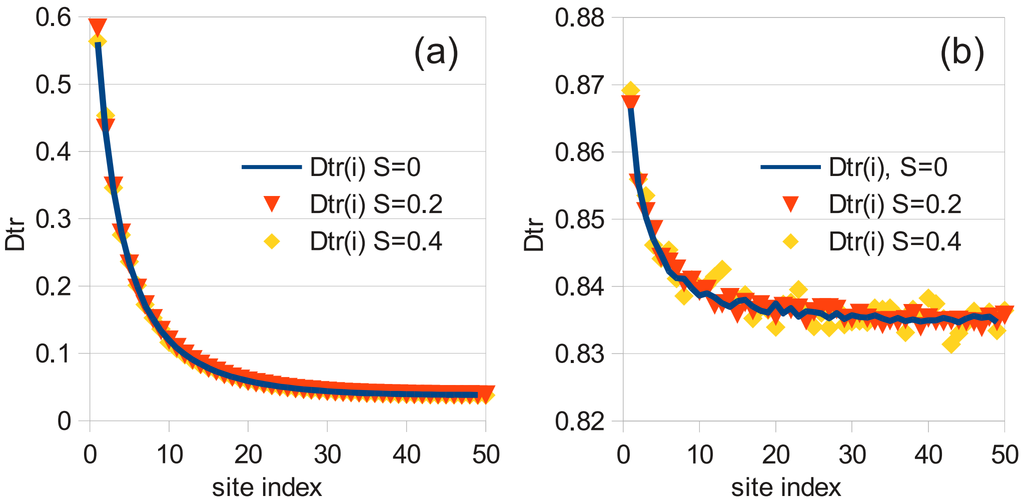

Figure 11: Comparison of diffusion coefficients calculated with and without mixed adsorption for X_{out}=0.2. (a) shows P_{ex}=0 (b) shows P_{ex}=0.5.

The ratio of the difference of excess concentrations at each pair of sites to the difference of concentrations for the same sites in the pure adsorption case should be a constant as given by equation (28). Figure 12 shows the strong agreement with this equation for the case with hindered passing, $P_{ex}=0.5$. The actual c_i^{XS} values depend on the passing rate, but the difference between two neighboring sites does not. This means the plots for different degrees of passing will look the same.

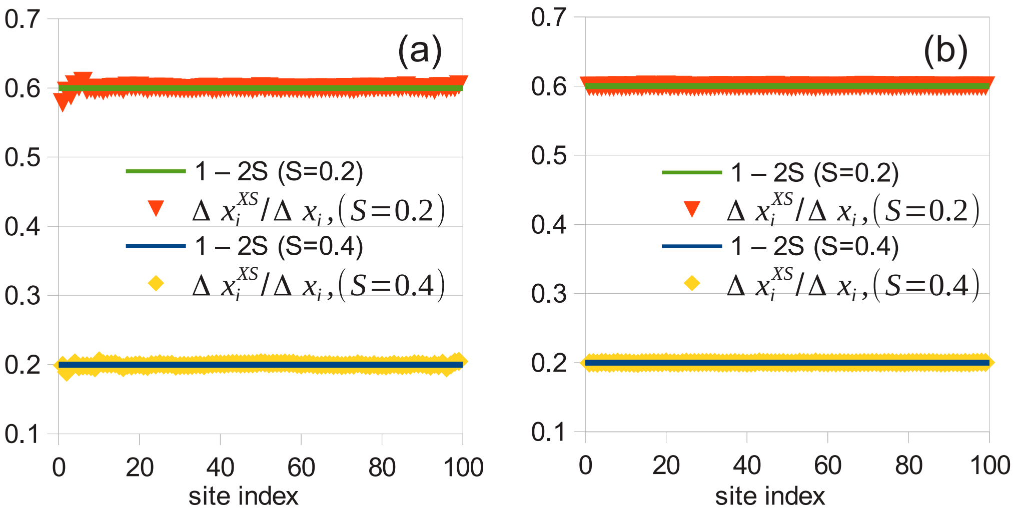

Figure 12: Agreement of simulation results with expected values as derived in equation (28) (a) shows $P_{ex}=0$ (b) shows $P_{ex}=0.5$.

Figure 13 shows the same behavior as above in the strict single file case for $X_{out}=0.8$.

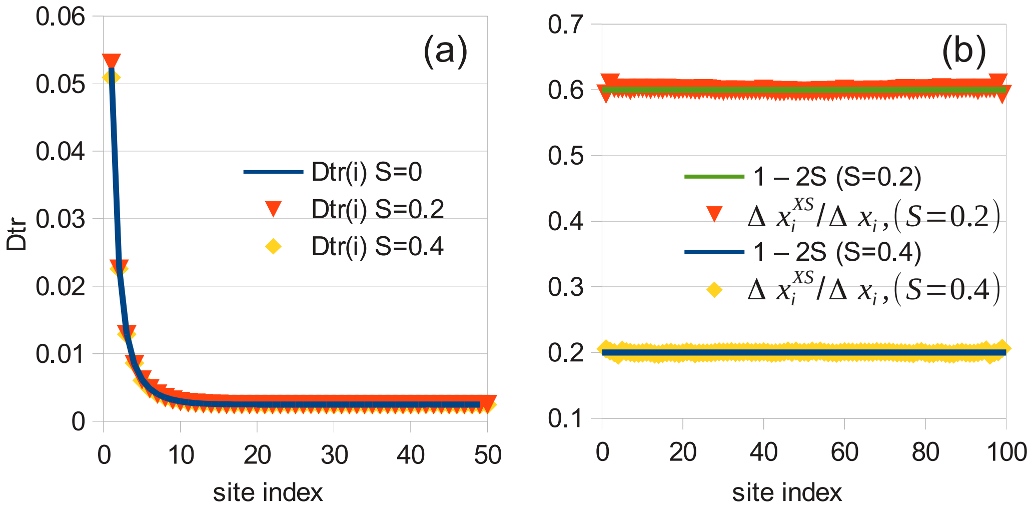

Figure 13: High loading, $X_{out}=0.8$ results using mixed diffusion with $P_{ex}=0$. (a) shows the tracer diffusion values (b) shows agreement with equation (28).

Appendix B: Counter Diffusion

Nelson *et al* have performed work [5,6,7,8] in a similar vein to this method. They name their method Tracer Counter Diffusion (TCP). Rather than structures with linear pores, the systems modeled in their approach are zeolites with interconnected pores. The lattice sites in the model represent the intersection of the channels in the crystal. (The choice of a 2D lattice was made for simplicity; the actual system is three-dimensional). Similar to this work, they start with the constraint of A particles entering one side and identical (except for labeling) B particles entering the other. Once in the system, they diffuse and can eventually exit from the opposite side. In the TCP approach, a 2D matrix of sites is used instead of a 1D array of sites. The hopping within the matrix is to the four nearest neighbors. Hop rates in the x and y direction may be different. Motion through the channels is governed by the rate constants.

This work treats passing as a probability of A and B exchanging places which represents the motion of molecules sliding past each. In the TCP model, passing occurs by hopping around a site using the 2D lattice which represents molecules taking alternate paths in the crystal to move around a site. Particles pass by hopping to sites around each other.

The TCP system has an anisotropy parameter, $\eta = k_y/k_x$, where k_x and k_y are the rate constants for hopping in the x and y directions, respectively. A value of zero in one direction corresponds to single file diffusion. There isn't an exact correlation between the anisotropy parameter and the P_{ex} parameter as they are fundamentally different diffusion processes. It is not possible to directly compare results. The significance of this difference is clear at higher loadings. The 2D lattice model requires vacancy motion for all motion including passing while the passing method presented here does not. In the limit of a completely filled system, there is no motion within the TCP system regardless of the anisotropy. With the approach presented here, a completely filled pore with passing will still have motion as atoms swap places based on the passing rate.

Nelson has the diffusion coefficient defined as: $D_s(\theta_T) = D_0*(1-\theta_T)*f(\theta_T)$. D_0 is the transport diffusivity and equal to the self diffusion coefficient at infinite dilution, θ_T is the total loading, and f is the correlation factor resulting from an increased probability to return to the site just vacated by the particle. This f value is the result reported. It ranges from 0 to 1. Based on the description in Nelson's work, this should be a function of the occupancy of a site and the time it takes for a site to fill after being vacated, although this isn't discussed.

The individual diffusion coefficient values to pass between sites are determined from Fick's law, J=D $\Delta\theta_i$, where $\Delta\theta_i$ is the concentration difference between sites i and i+1.

The primary focus is the bulk diffusion values far from the edges. This is equivalent to the center minimum value in diffusion coefficients shown in figures 5, 6, 7, and 8. The system sizes studied are L=10 to L=100. Fitting is done to extract limiting results for larger L. For the case where $\eta \neq 0$, there is a finite limit on the bulk value. This limit is independent of the pore length beyond some critical L value. For $\eta > 0.01$, this L value is less than 10. For $\eta = 0.001$, it is around 70. For $\eta = 0$, there is no limit, and the value always depends on the pore length. Nelson finds the limiting value approaching zero as 1/L.

The results in Nelson's papers are for high loading, $\theta_T = 0.9$, where the correlation effects are strongest. The system is initially empty - though the paper mentions that this is not the most desirable way to start the simulation. There is no mention of correlations in site occupancies in the equilibration process. While in the current work, correlations with passing are very limited when passing is introduced, it is not clear if this will also be the case in the two-dimensional method of passing as the motion is still limited by site exclusion criteria preventing particles from moving until they find an empty site. This limit is the origin of the correlations in the single file case discussed here.

The only concentration profile across an entire pore is shown in figure 4 of ref 6 for L=20 and $\eta = 1$. It is mostly linear with barely perceptible deviations at the end sites. The f values at the ends show noticeable deviations from the value expected for a linear profile. Based on the plots of f for different configurations, the profiles are likely linear for all but the smallest η values. The profile is presented with multiple sizes scaled to a single plot. This misses an important feature of the diffusion coefficients that is evident when data from multiple pore lengths is plotted on a single graph (figure 14). Diffusion coefficients from all pore lengths follow the same master curve which breaks off when the diffusion coefficient reaches the limiting value for that pore length. This behavior matches with previous theory of diffusion coefficient values in pores.

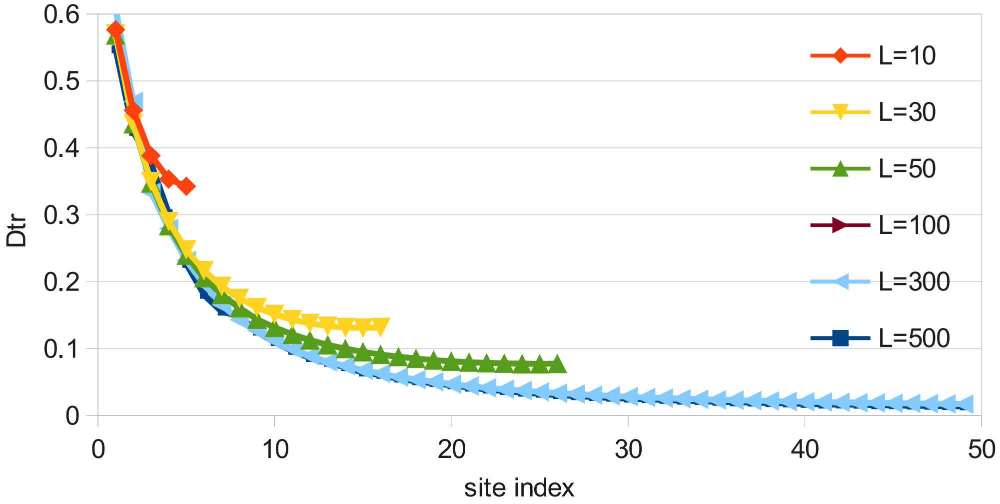

Figure 14: Tracer diffusion values for all pore lengths studied at Xout=0.2. The values beyond the center of the pore were truncated. The curves for L=100 and L=500 are directly below the L=300 curve.

While the TCP method bears a strong resemblance to the work discussed in this chapter, there are important distinctions that become clear when looking at the underlying model. The nature of the passing is fundamentally different. The TCP method is best applied to a system of interconnected channels such as a zeolite structure. It would be inappropriate to apply the TCP method to a linear system with passing hindered by steric constraints.

References

1) Ackerman, D. M.; Wang J.; Evans, J. W. Physical Review Letters **2012**, 108, 228301.

2) Fick, A. Phil. Mag. **1855**, 10, 30.

3) Quastel, J. Commun. Pure Appl. Math. **1992**, 45, 623.

4) Covariance. Encyclopedia of Mathematics. URL: http://www.encyclopediaofmath.org/index.php?title=covariance

5) Nelson, P. H.; Kaiser, A. B.; Bibby D. M. Journal of Catalysis **1991**, 127, 101.

6) Nelson, P. H.; Auerbach, S. M. Chemical Engineering Journal **1999**, 74, 43.

7) Nelson, P. H.; Auerbach, S. M. Journal of Chemical Physics **1999**, 110, 9235.

8) Nelson, P. H.; Bibby D. M.; Kaiser, A. B. Zeolites **1991**, 11, 337.

CHAPTER 7. CONTROLLING REACTIVITY OF NANOPOROUS CATALYST MATERIALS BY TUNING REACTION PRODUCT-PORE INTERIOR INTERACTIONS: STATISTICAL MECHANICAL MODELING

Jing Wang[1,2], David M. Ackerman[1,3],Victor S.-Y. Lin[1,3], Marek Pruski[1,3],
and James W. Evans[1,2,4]

A paper published in *The Journal of Chemical Physics*

Ames Laboratory[1] – USDOE, and Departments of Mathematics[2], Chemistry[3],
and Physics & Astronomy[4], Iowa State University, Ames, IA 50011, U.S.A.

Abstract

Statistical mechanical modeling is performed of a catalytic conversion reaction within a functionalized nanoporous material to assess the effect of varying the reaction product – pore interior interaction from attractive to repulsive. A strong enhancement in reactivity is observed not just due to the shift in reaction equilibrium towards completion, but also due to enhanced transport within the pore resulting from reduced loading. The latter effect is strongest for highly restricted transport (single-file diffusion), and applies even for irreversible reactions. The analysis is performed utilizing a generalized hydrodynamic formulation of the reaction-diffusion equations which can reliably capture the complex interplay between reaction and restricted transport.

1 Introduction

Advances in synthesis of nanomaterials have led to broad capabilities for multifunctionalization of mesoporous or nanoporous catalysts. Such capabilities allow for not only effective functionalization with catalytic groups, but also the possibility to tune the interaction between reaction products and the interior pore environment [1-3]. This can in turn significantly impact and potentially enhance catalytic reactivity. For example, creation of an unfavorable environment for product species within pores can lead to enhanced product extrusion or inhibited product re-entry. This feature would shift the equilibrium of reversible reactions towards completion. Other possible scenarios are discussed below.

One class of examples of the above type is provided by dehydration reactions such as esterification (acid + alcohol ↔ ester + water) in mesoporous silica nanoparticles (MSN). Multifunctionalization of MSN to include hydrophobic groups, as well as catalytic groups, has been observed to significantly enhance reactivity in several such systems [4-6]. This effect has been explained as a result of functionalization converting an intrinsically hydrophilic interior pore surface of MSN into a hydrophobic environment thereby "expelling" the product water and shifting the equilibrium of the reversible esterification reaction. The greatest enhancement to date has been achieved through solvent-mediated control of the configuration of hydrophobic 3-(pentafluorophenyl) propyl groups to lie prone on silica surface thereby minimizing the interaction of the product water with the hydrophilic MSN surface groups [6,7].

In fact, there are several possible scenarios wherein functionalization to tune product-pore interactions can influence both the thermodynamics and the kinetics of transport and reaction, and thereby impact reactivity in meso- or nanoporous reaction systems. *First*, we discuss thermodynamic factors. Accounting for detailed-balance requirements, it follows that creating an unfavorable environment for a reaction product within the pore increases the *ratio* of the rate of product desorption from the pore opening to that for product (re-)adsorption. One should note that product re-adsorption can become significant for substantial conversion of reactant to product in the surrounding fluid. However, even constraining rates to satisfy detailed-balance, there are still many distinct possibilities for rate behavior: (i) the product desorption rate could be tied to the rate of diffusion within the pore, and thus the rate of re-adsorption would be inhibited for stronger interior pore-product repulsion; (ii) the product re-adsorption rate could be tied to the rate of external diffusion, and thus the rate of desorption would be enhanced for stronger interior pore-product repulsion; (iii) more general cases where both rates change. Any of these cases will result in a shift of equilibrium for reversible reactions.

Second, we discuss other kinetic factors that can impact reactivity, but which are unrelated to shift of equilibrium for reversible reactions. Although not dictated by thermodynamic considerations, diffusive transport within the pore can also be modified by multifunctionalization. An unfavorable environment could enhance diffusion removing localized regions of strong binding and thereby “smoothing” interaction with the pore walls. Another possible scenario is that modifying the interior pore environment can change loading of product in the pore even for irreversible reactions. The loading can have a dramatic effect on effective transport for narrow pores, especially in the single-file diffusion (SFD) regime where species cannot pass each other in the pore, and this in turn greatly impacts reactivity. To test this latter effect, we will naturally consider the special case of irreversible reactions.

Our focus in this contribution is on exploring the effects of multifunctionalization for simple first-order catalytic conversion reactions (A to B) in mesoporous or nanoporous materials such as MSN consisting of parallel arrays of effectively identical linear nanopores. A key factor impacting reactivity is the extent to which reactants and products A and B can pass each other. Previous analyses for SFD or restricted passing [8-15] reveal that reaction is strongly localized near the pore openings [9]. While simple mean-field type reaction-diffusion equations [8,11-13] are not adequate, recent studies have shown that behavior in this regime is captured by a “generalized hydrodynamic” formulation which accounts for both the effect of restricted passing on chemical diffusion as well as fluctuation effects in adsorption-desorption at pore openings [14]. Here, we adopt the latter rather than computationally more expensive Kinetic Monte Carlo simulation which could also provide a precise characterization of model behavior.

In Sec. 2, we describe our model for conversion reaction in linear nanopores, the associated exact master equations, and associated generalized hydrodynamic reaction-diffusion equations (RDE). In Sec.3, we present results for both irreversible and reversible conversion reactions focusing on reactivity (i.e., turn-over frequency) per pore as a function of the fraction of reactant converted to product, and contrasting behavior for pores where product entry in enhanced versus inhibited. Our conclusions are presented in Sec.4.

2 Spatially-Discrete Model for Catalytic Conversion Inside Linear Nanopores

2.A. Spatially-discrete stochastic reaction-diffusion model prescription

Our model for catalytic conversion describes nanoporous materials which consist of a parallel array of linear pores by partitioning the continuous-space pores into adjacent sites labeled n = 1 to L [8-14]. The site width “a” is selected to be comparable to the species size ~1 nm. Species within pores are regarded as localized to specific sites, and diffusive transport is treated as hopping or exchange between adjacent sites. To describe the surrounding fluid, we extend the 1D lattice of sites inside the pores to a 3D lattice outside. See Fig. 1. We specify “external” reactant and product concentrations in the surrounding fluid at each stage of the reaction as $\langle A_{out} \rangle$ and $\langle B_{out} \rangle$, for a fixed total concentration $\langle X_{out} \rangle = \langle A_{out} \rangle + \langle B_{out} \rangle$. These correspond to the probabilities that sites or sites on the 3D lattice are occupied by various species, where fluid site occupation is assumed random due to efficient stirring. Then, $\langle A_{out} \rangle$ will decrease from an initial value of $\langle X_{out} \rangle$, and $\langle B_{out} \rangle$ will increase from zero with increasing fraction, $F = \langle B_{out} \rangle / \langle X_{out} \rangle$ ($= 1 - \langle A_{out} \rangle / \langle X_{out} \rangle$), of the initial reactant converted to product [14,15].

Following most previous stochastic modeling of reaction-diffusion processes in linear nanopores [8-15], the simplest prescription for diffusion dynamics within the pores is that A and B hop to adjacent empty (E) sites at rate h, corresponding to a diffusion rate of $D_0 = a^2h$ for isolated particles. This simple prescription would correspond to single-file diffusion with a strict no-passing constraint. For a more general treatment of diffusional dynamics, we also allow positional exchange of adjacent A and B at rate P_{ex} h, thereby relaxing the strict single-file constraint. (Note that exchange of adjacent particles of the same type has no effect.) The passing propensity, P_{ex}, will increase with the effective pore diameter, d, from $P_{ex} = 0$ for d below a threshold for SFD, to $P_{ex} = 1$ for large d and unhindered passing.

In addition to hopping or exchange within the pore, the other mechanistic steps in the model (see Fig. 1) are as follows: (i) Adsorption of external reactant A (product B) to terminal pore sites n=1 and n=L at rate h (αh), provided that these end sites are unoccupied or empty (E). We emphasize that the factor α will account for the effects of multifunctionalization modifying the interior pore – reaction product interaction. (ii) Desorption of both the reactant, A, and product, B, from terminal sites of the pore at rate h provided that the fluid site just outside the pore is unoccupied (E_{out}). The probability for this fluid site to be unoccupied is given by $\langle E_{out}\rangle = 1 - \langle X_{out}\rangle$. (iii) Conversion A → B at catalytic (c) sites within the pore at rate k, as well as the reverse reaction B → A at rate k´. Our model can treat general distributions of catalytic sites, but here we shall assume that all sites are catalytic. (iv) One could also consider exchange in and out of the pore. One choice is to ignore such processes. Another plausibly more realistic choice is to specify that A (B) just outside exchanges with B (A) inside at n = 1 or L at rate $P_{ex}h$ ($\alpha P_{ex}h$). Both choices (and others) are consistent with detailed-balance. We expect that the choice will not greatly effect of reactivity (except in the special regime of both high P_{ex} and high loading).

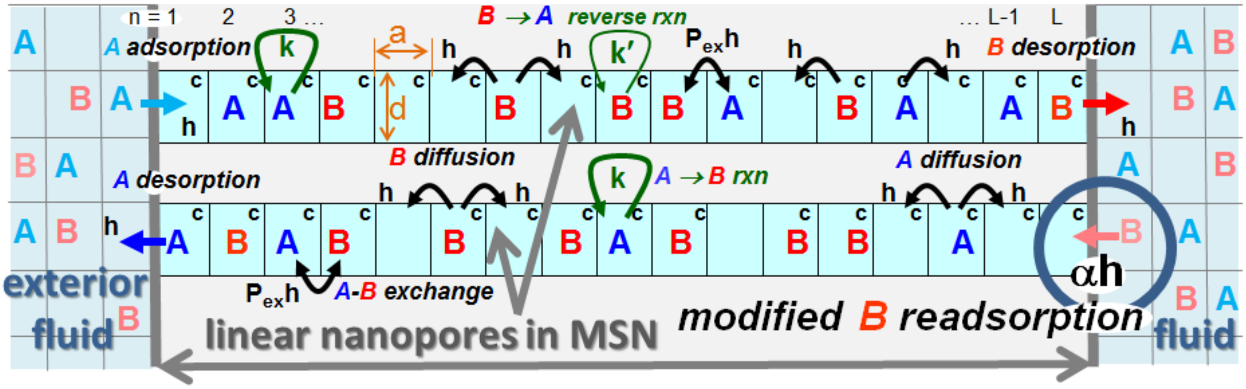

Figure 1: Schematic of the A to B conversion reaction model illustrating processes within pores (shaded light blue), as well as coupling to the surrounding fluid. In-out exchange processes are not shown (but are active in our modeling). 'c' denote catalytic sites.

It should be emphasized that there is a natural "separation of time scales" for "local" relaxation (in time) of concentration profiles within the pore, and for "global" equilibration of the entire system including the fluid. Relaxation of concentration profiles to a local steady state form determined by the current values of $\langle A_{out}\rangle$ and $\langle B_{out}\rangle$ should be effectively instantaneous on the time scale of global equilibration of the entire system (which in experiments is on the order of hours). Thus, the main challenge is to solve the non-trivial statistical mechanical local steady-state problem to determine reactant and product concentration profiles, and thus the reactivity, as a function of the fractional conversion, $F=\langle B_{out}\rangle/\langle X_{out}\rangle$, of reactant to product. It should also be noted that the global equilibrium values of $\langle A_{out}\rangle$ and $\langle B_{out}\rangle$, and thus of $F = F_{eq}$, are determined not just by the equilibrium constant $K_c = k/k'$ for the conversion reaction within the pores, but *also* by the parameter α. This issue is addressed immediately below.

For the above model, it is clear that the "color-blind" dynamics for particles X = A+B (i.e., A or B) is described by a non-reactive diffusion process where particles hop within the pore and desorb at rate h. At a specified fractional conversion, F, particles adsorb at an effective rate $h_{ads} = h_{ads}(F) = e_{ads}(F)\, h$ with $e_{ads} = e_{ads}(F) = (1-F) + \alpha F$, where the first (second) term is the weighted contribution from A (B) adsorption. In the local steady state for fixed F, all sites within the pore are randomly occupied by particles, X, with equal probability $<X_{in}> = <X_{in}(F)>$, say. Then, balancing the adsorption flux, J_{ads}, and desorption flux, J_{des}, for particles X where

$$J_{ads} = h_{ads}(F)<X_{out}>(1-<X_{in}>) \text{ and } J_{des} = h(1-<X_{out}>)<X_{in}> \text{ yields} \tag{1}$$

$$<X_{in}> = e_{ads}<X_{out}>/[1+(e_{ads}-1)<X_{out}>] = [1+(\alpha-1)F]<X_{out}>/[1 + (\alpha-1)F<X_{out}>]. \tag{2}$$

We recall that $<X_{out}>$ remains constant at its initial value. As expected, (2) demonstrates that $<X_{in}>$ exceeds $<X_{out}>$ for $\alpha>1$ (enhanced product reentry), and that $<X_{out}>$ exceeds $<X_{in}>$ for $\alpha<1$ (inhibited reentry).

A simple analysis of individual species concentrations in the local steady state is not possible since these concentrations exhibit non-trivial spatial profiles within the pore. However, in the final global equilibrium state, concentrations of both species within the pore, $<A_{in}>_{eq}$ and $<B_{in}>_{eq}$, are spatially uniform, and satisfy $<B_{in}>_{eq}/<A_{in}>_{eq} = K_{eq}$. Then, separately balancing the adsorption and desorption fluxes for species A and for species B yields

$$\begin{aligned}&<A_{out}>_{eq}(1-<X_{in}>_{eq}) = <A_{in}>_{eq}(1-<X_{out}>) \text{ and } \alpha<B_{out}>_{eq}(1-<X_{in}>_{eq})\\ &= <A_{in}>_{eq}(1-<X_{out}>),\end{aligned} \tag{3}$$

$$\text{so that } <B_{out}>_{eq}/<A_{out}>_{eq} = \alpha^{-1} <B_{in}>_{eq}/<A_{in}>_{eq} = K_c/\alpha, \text{ and } F_{eq} = K_c/(K_c + \alpha). \tag{4}$$

The latter result characterizes the shift in equilibrium for our model associated with tuning of the reaction product – pore interior interaction via multifunctionalization. We thus find that $<X_{in}>$ changes from its initial value of $<X_{out}>$ at the onset of the reaction (F=0) to

$$<X_{in}>_{eq} = \alpha(1+K_c)<X_{out}>/[\alpha(1+K_c<X_{out}>)+K_c(1-<X_{out}>)], \text{ when } F=F_{eq}, \tag{5}$$

at completion of the reaction. This result (5) recovers the requirement that $\langle X_{in}\rangle_{eq} = 0$ for blocked product reentry $\alpha=0$. It also shows that for enhanced reentry with, e.g., $\alpha=5$ and $\langle X_{out}\rangle=0.8$ (the case considered below), one has $\langle X_{in}\rangle_{eq}/\langle X_{out}\rangle = (1+K_c)/(1+0.84K_c) > 1$.

2.B. Exact master equations and discrete reaction-diffusion equations

An exact description of our discrete reaction-diffusion model is provided by the master equations for the evolution of probabilities of various configurations within the pore. Often these are written in hierarchical form [8,11-15]. Here, we use $\langle C_n\rangle$ to denote the probability or ensemble averaged concentration for species C = A or B at site n (or for this site to be empty when C = E), $\langle C_nE_{n+1}\rangle$ for the probability that C is at site n and for site n+1 to be empty (E), etc. Then, the lowest-order equations in the hierarchy describe the evolution of single-site occupancies.

For A to B conversion in the case where *all sites are catalytic*, one has that

$$d/dt\,\langle A_n\rangle = -k\langle A_n\rangle + k'\langle B_n\rangle - \nabla J_A^{n>n+1} \text{ and} \tag{6a}$$

$$d/dt\,\langle B_n\rangle = +k\langle A_n\rangle - k'\langle B_n\rangle - \nabla J_B^{n>n+1} \quad \text{for } 1<n<L, \tag{6b}$$

where we have defined the discrete derivative, $\nabla G_n = G_n - G_{n-1}$. The *net* diffusion flux, $J_A^{n>n+1}$, of A from site n to n+1 due to both hopping and exchange is given by

$$J_A^{n>n+1} = h\,[\langle A_nE_{n+1}\rangle - \langle E_nA_{n+1}\rangle] + P_{ex}\,h\,[\langle A_nB_{n+1}\rangle - \langle B_nA_{n+1}\rangle]. \tag{7}$$

The expression for the net flux, $J_B^{n>n+1}$, of B is analogous. Separate equations for terminal sites reflect adsorption-desorption boundary conditions (BC's). In the presence of in-out exchange with rates as specified in Sec. 2A, one has that

$$\begin{aligned} d/dt\,\langle A_1\rangle = {} & h\langle A_{out}\rangle\langle E_1\rangle - h\langle E_{out}\rangle\langle A_1\rangle + P_{ex}\,h\,\langle A_{out}\rangle\langle B_1\rangle - P_{ex}\,\alpha h\,\langle B_{out}\rangle\langle A_1\rangle \\ & - k\,\langle A_1\rangle + k'\langle B_1\rangle - J_A^{1>2}, \text{ and} \end{aligned} \tag{8a}$$

$$\begin{aligned} d/dt\,\langle B_1\rangle = {} & \alpha h\langle B_{out}\rangle\langle E_1\rangle - h\langle E_{out}\rangle\langle B_1\rangle + P_{ex}\,\alpha h\,\langle B_{out}\rangle\langle A_1\rangle - P_{ex}\,h\,\langle A_{out}\rangle\langle B_1\rangle \\ & + k\,\langle A_1\rangle - k'\langle B_1\rangle - J_B^{1>2}, \end{aligned} \tag{8b}$$

with analogous equations for concentrations at site n=L. If some sites are not catalytic, then the reaction terms are absent for such sites. Defining $\langle \Delta A_n \rangle = \langle A_n \rangle - K_c^{-1} \langle B_n \rangle$ as the “excess” reactant concentration, the net overall rate of production of B per pore is given by

$$R^{B}_{rxn} = \Sigma_{n=c} (k\langle A_n\rangle - k'\langle B_n\rangle) = k\, \Sigma_{n=c} \langle \Delta A_n \rangle \qquad (9)$$

summing over all catalytic sites, c.

Equations (6) couple to various pair probabilities in (7). Pair probability evolution is coupled to triples, etc., producing a hierarchy. Pair and multisite probabilities are not simply related to single-site probabilities due to spatial correlations. A simple mean-field (MF) factorization approximation, $\langle C_n E_{n+1} \rangle \approx \langle C_n \rangle \langle E_{n+1} \rangle$, etc., produces a closed set of discrete reaction-diffusion equations (RDE) for single-site concentrations. However, this approximation, and even higher-order pair, triplet, etc., approximations, fundamentally fail to capture model behavior, at least for low reactivity $k/h \ll 1$ when $P_{ex} \ll 1$ [13-15]. Thus, below we discuss an alternative “generalized hydrodynamic” approach which does reliably describe model behavior.

As an aside, in the special case $P_{ex} = 1$ (unhindered passing of A and B), (7) reduces exactly to $J_A^{n>n+1} = h\,[\langle A_n \rangle - \langle A_{n+1} \rangle] = -h\,\nabla \langle A_n \rangle$, and similarly for $J_B^{n>n+1}$ [14-16]. This yields an exact set of discrete RDE matching the MF approximation.

2.C. Generalized hydrodynamic reaction-diffusion equations

For smoothly varying concentrations within the pore, it is natural to consider a coarse-grained description of the spatially-discrete reaction-diffusion model which regards the species concentrations per unit length, $C(x=na) \approx a^{-1} \langle C_n \rangle$, as functions of a continuous spatial variable x (leaving the t-dependence implicit), and denote the total concentration by $X(x) = A(x) + B(x)$. The continuum RDE for our A to B conversion reaction model with all sites catalytic then have the form

$$\begin{aligned} \partial/\partial t\, A(x) &= -k\, A(x) + k'\, B(x) - \partial/\partial x\, J_A, \text{ and } \partial/\partial t\, B(x) \\ &= +k\, A(x) - k'\, B(x) - \partial/\partial x\, J_B. \end{aligned} \qquad (10)$$

If only portions of the pore are catalytic, then reaction terms appear just for those locations. BC’s for (10) at the pore ends reflect the adsorption-desorption dynamics, i.e., one balances the diffusion fluxes at the end of the pore with the net adsorption-desorption rate for each species. Description of the diffusion fluxes, J_A and J_B, is non-trivial.

Analysis from the theory of interacting particle systems [17,18] for the hydrodynamic regime of slowly varying concentrations suggests the general form [13,14,17,18]

$$J_A = -D_0[1- X^{-1}(1-F_{tr})B]\, \partial A/\partial x - D_0 X^{-1}(1-F_{tr})A\, \partial B/\partial x. \tag{11}$$

In this expression, one has $D_0 = a^2h$ and F_{tr} is related to a tracer diffusion coefficient for particles within the pore by $D_{tr} = D_0F_{tr}$. In applying the form (11), we utilize the feature that the diffusive dynamics for both A and B within the pore is identical. An analogous expression applies for J_B. Here, it suffices to consider the local steady-state regime with uniform total concentration, $X = <X_{in}> = <X_{in}(F)>$, corresponding to a counter-diffusion mode [19] where $\partial A/\partial x = -\partial B/\partial x$. Then, (11) and the analogous expression for J_B simply reduce to [13,19]

$$J_A = -D_{tr}\, \partial A/\partial x \text{ and } J_B = -D_{tr}\, \partial B/\partial x. \tag{12}$$

In the MF treatment, $X^{-1}(1-F_{tr})$ in (11) is replaced by $1-P_{ex}$ which corresponds to the assignment $F_{tr} = F_{tr}(MF) = 1- (1-P_{ex})X$. However, this MF choice *overestimates* diffusion fluxes within the pore, and thus *overestimates* overall reactivity, especially for the quasi-SFD regime, $P_{ex}<<1$ and $F_{tr}(MF) \approx 1 - X$ [12,13]. A contrasting deterministic hydrodynamic (DH) formulation of F_{tr}, applicable for large systems (very long pores) with slowly varying concentrations and negligible fluctuation effects, follows from a precise analysis of tracer diffusion for effectively infinite systems. One finds that the corresponding $F_{tr} = F_{tr}(DH) = F_{tr}(X, P_{ex})$ has the form shown in Fig.2. Simple limiting behavior includes:

$$\begin{gathered} F_{tr}(DH) \to 1, \text{ as } P_{ex} \to 1;\ F_{tr}(DH) \to P_{ex}, \text{ as } X \to 1; \text{ and} \\ F_{tr}(DH) \to 0, \text{ as } P_{ex} \to 0 \text{ (for } X>0). \end{gathered} \tag{13}$$

The latter behavior for $P_{ex} =0$ is in marked contrast to the MF form, and reflects the anomalous nature of SFD wherein the mean-square displacement of a tagged particle increases sub-linearly [20]. To account for the finite length of pores, we have considered a refinement of the DH choice where $F_{tr} \sim 1/L$ for SFD when $P_{ex} =0$ [21]. This modified choice was motivated by analyses of transport through channels across membranes of finite width [22]. However, choosing either $F_{tr} = 0$ or $F_{tr} \sim 1/L$ for SFD *underestimates* diffusion fluxes at least near pore openings, and thus underestimates *underestimates* the overall reactivity [21].

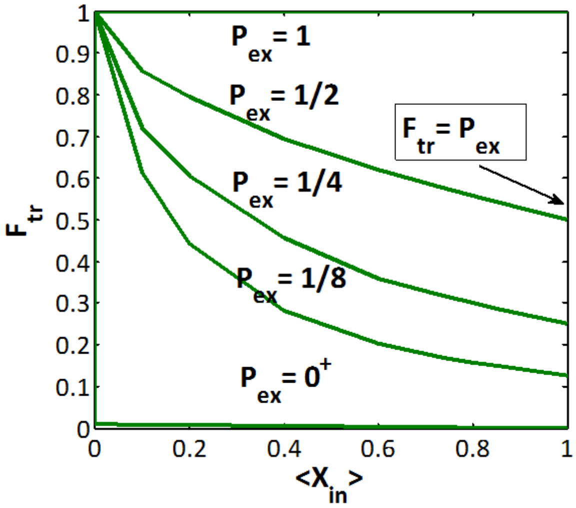

Figure 2: Behavior of the conventional (DH) tracer diffusion coefficient, F_{tr}(DH), for infinite systems as a function of pore loading $<X_{in}>$ for various passing probabilities, P_{ex} (shown).

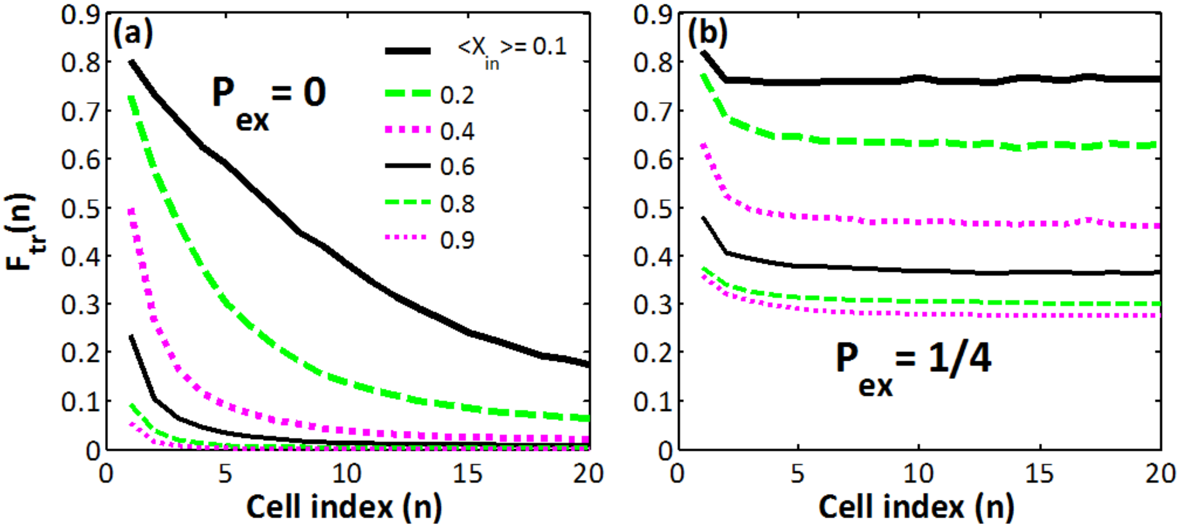

Figure 3: Variation of the generalized hydrodynamic tracer diffusion coefficient, $F_{tr}(n) = D_{tr}(n)/D_0$, with distance x=na into the left end of the pore for a pore on length L=100 a. The plateau value near the pore center corresponds to F_{tr}(DH). Results are shown for fixed $<X_{out}> = 0.8$ and varying $<X_{in}>$ for: (a) single-file diffusion, $P_{ex} = 0$; and (b) exchange with $P_{ex}=0.25$.

To address the shortcomings of the MF and DH approaches described above, we will utilize a generalized hydrodynamic (GH) treatment [23] which incorporates a position-dependent $F_{tr}(x=na) = F_{tr}(GH)$. This $F_{tr}(x=na)$ is enhanced near pore openings *above* the deterministic hydrodynamic value of $F_{tr}(DH)$ [14]. This enhancement of $F_{tr}(DH)$ reflects the influence of stochastic adsorption-desorption processes which facilitate transport in and out of the pore near these pore openings [14]. Results are shown in Fig.3 where $F_{tr}(x)$ approaches $F_{tr}(DH)$ for x or n corresponding to the central region of the pore. The algorithm which we use to determine this location-dependent $F_{tr}(GH)$ is described in Ref. [14] and also in the Appendix. Roughly speaking, we set $F_{tr}(x=na) = t_0(x=na)/\ t_X(x=na)$ where t_X is time for a tagged particle starting at a specific location, x=na, in a pore with concentration X of other particles to reach the closest pore opening. This choice is based on the classic result that diffusivity scales like the mean-square displacement divided by time. See Ref. [19] for an alternative formulation. Thus, it is immediately clear that $F_{tr}(x) \rightarrow 1$, as $X \rightarrow 0$ (as required). Introducing these variable $F_{tr}(x=na) = F_{tr}(n)$ into a discrete form of (10) and (11) [24] recovers almost exactly the results of precise KMC simulations of model behavior, but much more efficiently [14]. This formalism will be used to generate results in the following sections.

3 Catalytic Reaction Kinetics: Reactivity Versus Conversion

In this section, we present simulation results for the reactivity (i.e., the turn-over frequency) per pore as a function of fractional conversion of reactant to product. We also provide more detailed information on concentration profiles within the pores. In all cases below, we consider a pore of length L=100 a in which all sites are catalytic. The hop rate is set to unity h=1, which determines the time scale. The rate of the forward reaction $A \rightarrow B$ chosen as k=0.001. The initial reactant concentration, and thus the total concentration in the exterior fluid, is set to $\langle X_{out} \rangle = 0.8$. This high $\langle X_{out} \rangle$ results in a high loadings inside the pore, and thus strong SFD effects in the absence of exchange diffusion when $P_{ex} = 0$. We will consider and compare behavior for three cases: (i) significantly enhanced product reentry with $\alpha=5$ (mimicking hydrophilic pores for dehydration reactions); (ii) neutral product reentry with $\alpha=1$; (iii) blocked product reentry with $\alpha=0$ (mimicking strongly hydrophobic pores for dehydration reactions).

3.A. Irreversible reaction

For irreversible reaction, A→B, where k´=0, Fig.4a shows the local steady state concentration profiles for $<A_n>$ and $<B_n>$ versus n at the onset of the reaction (F=0) for various passing probabilities ranging from SFD ($P_{ex} = 0$) to completely unhindered passing ($P_{ex} = 1$). Behavior for F = 0 is independent of α due to the lack of product in the exterior fluid. Note the strongly enhanced penetration of reactant into the pore with increasing passing propensity, P_{ex}. This results in a strong increase in reactivity, R^{B}_{net}, as discussed further below. Fig.4b-4d show the concentration profiles for A→B when F = 0.625 for α = 5, 1, and 0, respectively. Here the α-dependence on behavior is seen clearly not just in the increased values of $<X_{in}>$ for larger α, but also in the increased dominance of product over reactant within the pore.

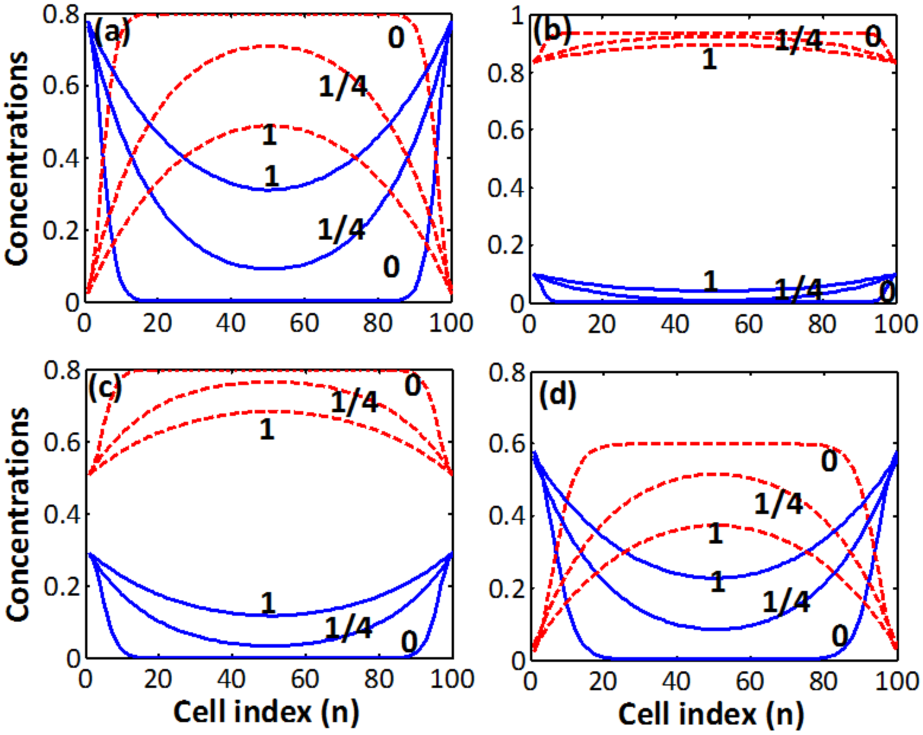

Figure 4: Local steady-state concentration profiles for irreversible reaction A→B with L=100 a, k = 0.001, h = 1, and $<X_{out}>$ = 0.8. A (B) is blue, solid (red, dashed). Behavior for: the onset of the reaction F=0 (a) for all α; and for F = 0.625 with (b) α=5; (c) α=1; (d) α=0.

Our main focus here is on a comprehensive characterization of the variation of reactivity during the “extended reaction”. Of particular significance is our demonstration of a dramatic difference between behavior for enhanced versus blocked product reentry to the pore. In Fig.5, we show the reactivity, R^B_{rxn}, as a function of the fraction, F, of reactant outside the pore converted to product for the irreversible reaction A→B. The key observation is the contrasting strong decrease of R^B_{rxn} with increasing F for enhanced product reentry (α=5) *versus* the slow decrease of R^B_{tot} (or even an initial slight increase with P_{ex}=0) for blocked product reentry (α=0). Thus, blocking reentry greatly enhances the effective reactivity of the system. The neutral case where reentry is neither enhanced or inhibited (α=1) exhibits intermediate behavior with a linear decrease of $R^B_{rxn}(F) = (1-F)\ R^B_{rxn}(0)$ versus F, as explained below.

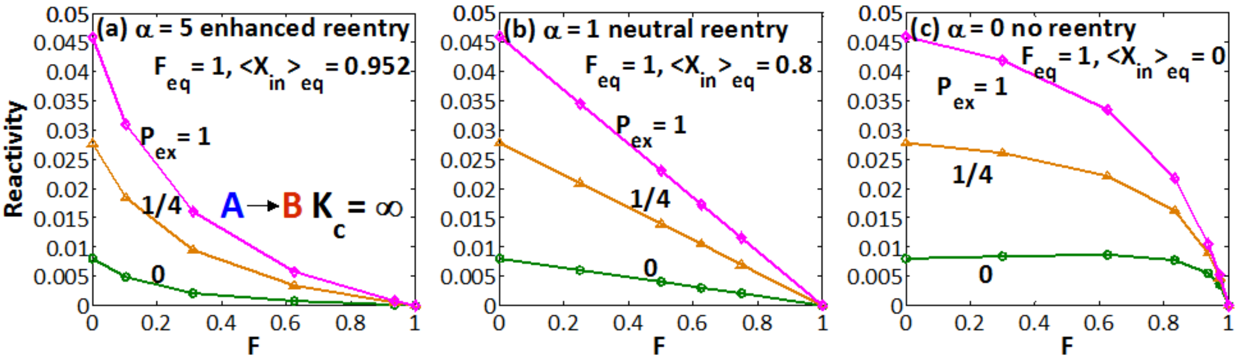

Figure 5: Net reactivity per pore, R^B_{net}, as a function of the fraction F of reactant converted to product for irreversible reaction A→B with L=100 a, k = 0.001, h = 1, and $\langle X_{out}\rangle$ = 0.8. (a) enhanced product reentry α=5; (b) neutral reentry α=1; (c) blocked reentry α=0.

The enhanced reactivity upon converting from enhanced reentry (α>1) to blocked reentry (α=0) reflects the reduction in pore loading $\langle X_{in}\rangle$. For example, when $\langle X_{out}\rangle$ = 0.8 and F=1/2, one has $\langle X_{in}\rangle$ = 0.92 for α=0 versus $\langle X_{in}\rangle$ = 0.67 for α=5. Lower $\langle X_{in}\rangle$ (or higher $\langle E_{in}\rangle$) impacts the rate of adsorption of reactant A via hopping into the pores,

$$R_A^{ads}(hop) = h\langle A_{out}\rangle\langle E_{in}\rangle = h\langle X_{out}\rangle\langle E_{out}\rangle(1-F)/[1+(\alpha-1)F\langle X_{out}\rangle]\ . \qquad (14)$$

Thus, $R_A^{ads}(hop)$ increases with decreasing α, for F>0, which naturally boosts reactivity. Note, however, that the rate of exchange adsorption of reactant for P_{ex}>0 may decrease for lower $\langle X_{in}\rangle$. More significantly, lower $\langle X_{in}\rangle$ greatly increases the tracer diffusion coefficient $F_{tr}(GH)$ which strongly increases penetration of reactant into the pore, and thus also boosts reactivity. This strong increase in reactivity in changing from enhanced to blocked product re-adsorption is purely kinetic in origin rather than thermodynamic (noting that the reaction is irreversible).

Finally, we provide some further comments on reaction kinetics. *First*, for the neutral case

α=1, we describe the origin of the linear decrease of $R^{B}_{net}(F) \propto (1-F)$ with F. This behavior is a consequence of two features. One is the homogeneous F-independent linear form of the steady-state master equations, $0 = -k\langle A_n\rangle - \nabla J_A{}^{n>n+1}$, noting that $F_{tr}(GH) = F_{tr}(n)$ is independent of F when α=1. The other relates to the feature that the BC terms for $\langle A_n\rangle$ when n=1 or n=L adopt an inhomogeneous linear form with driving term proportional to 1-F [25]. This implies that all $\langle A_n\rangle \propto (1-F)$ and thus one has $R^{B}_{rxn}(F) = (1-F)\, R^{B}_{rxn}(0)$. A detailed derivation of the analogous result for the more general reversible case is provided in Sec.3B.

Second, we note that if $\alpha \neq 1$, $R_A{}^{ads}(hop)$ in (14) exhibits a non-linear decrease with F, and also the position-dependent tracer diffusion coefficient adopts a non-trivial non-linear dependence of F. As a result, it is not possible to provide a simple analytic expression for the non-linear dependence of $R^{B}_{rxn}(F)$ on F when $\alpha \neq 1$.

Third, we emphasize that our results for the F-dependence of $R^{B}_{rxn}(F)$ encode complete information about the reaction kinetics through the equation

$$d/dt \langle A_{out}\rangle = \varepsilon R^{B}_{rxn}(F), \text{ where } F = 1- \langle A_{out}\rangle/\langle X_{out}\rangle). \tag{15}$$

Here, the constant ε equals the number of pores in the system divided by the total number of 3D lattice sites associated with the fluid. Thus, for no product reentry α=0 where $R^{B}_{rxn}(F) \approx R^{B}_{rxn}(0)$ is roughly independent of F (up to F ≈ ¾), one has a sustained fast linear decrease in time t of $\langle A_{out}\rangle \approx \langle X_{out}\rangle[1- \varepsilon R^{B}_{rxn}(0)\langle X_{out}\rangle^{-1} t)]$. For α=1 where $R^{B}_{rxn}(F) \propto (1-F)$, one has exponential decay $\langle A_{out}\rangle \approx \langle X_{out}\rangle \exp[- \varepsilon R^{B}_{rxn}(0)\langle X_{out}\rangle^{-1} t]$. For α>1, one has slower decay. All cases exhibit the same α-independent initial decay rate.

3.B. Reversible reaction

Next, consider the reversible reaction, $A \leftrightarrow B$, with k=0.001 as above, but now k´=0.0005 is non-zero corresponding to a finite equilibrium constant $K_c = 2$. Fig.6a shows the local steady state concentration profiles for $\langle A_n\rangle$ and $\langle B_n\rangle$ versus n at the onset of the reaction (F=0) for various passing probabilities P_{ex}. Behavior for F = 0 is independent of α as for irreversible reaction, and penetration of “excess” reactant, $\langle \Delta A_n\rangle = \langle A_n\rangle - K_c^{-1}\langle B_n\rangle$, into the pore is strongly enhanced with increasing passing propensity, P_{ex}. Fig.6b-6d show the concentration profiles for A → B when $F/F_{eq} = 0.625$ for $\alpha = 5$, 1, and 0, respectively. Here, the reduction in excess reactant with increasing α is evident.

In Fig.7, we show the reactivity, R^B_{rxn}, versus F for the reversible reaction. The contrast between the strong decrease of R^B_{rxn} with increasing F for enhanced product reentry (α=5) *versus* the slow decrease or even slight increase of R^B_{tot} for blocked product reentry (α=0) is even greater than for irreversible reaction. This is due to opposite shifts in the global equilibrium for enhanced versus blocked reentry. The neutral case (α=1) exhibits intermediate behavior with a linear decrease of $R^B_{rxn}(F) = (1-F/F_{eq})\, R^B_{rxn}(0)$ versus F, as explained below.

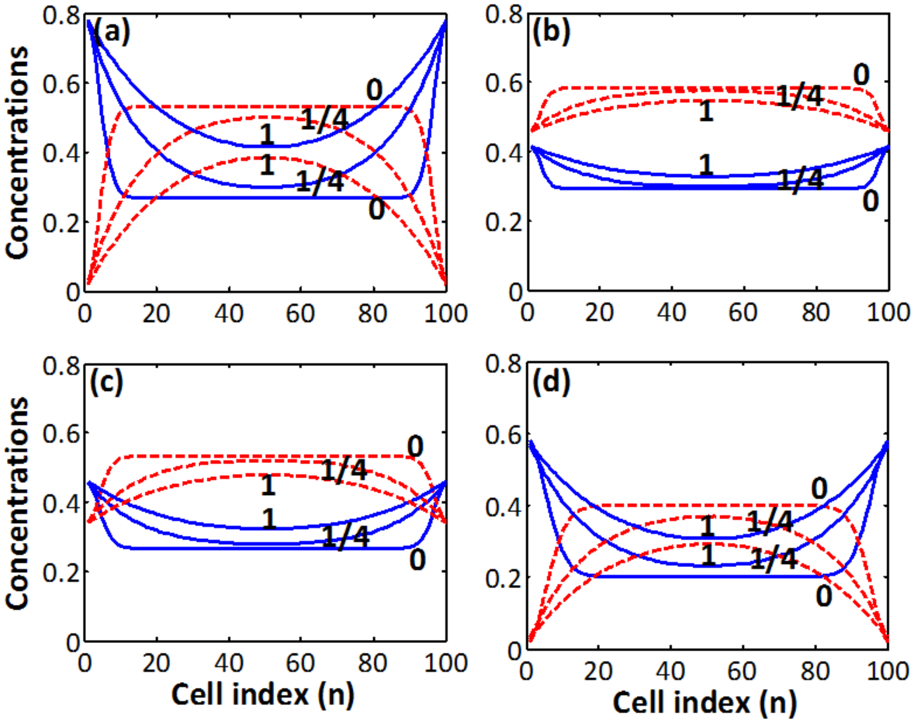

Figure 6: Local steady state concentration profiles for reversible reaction A ↔ B with L=100 a, k = 0.001, k´=0.0005, h = 1, and $\langle X_{out}\rangle$ = 0.8. A (B) is blue, solid (red, dashed). Behavior for: the onset of the reaction F=0 (a) for all α; and for F/F_{eq} = 0.625 with (b) α=5; (c) α=1; (d) α=0.

The enhanced reactivity upon converting from enhanced reentry (α>1) to blocked reentry (α=0) partly reflects kinetic effects due to the reduction in pore loading $\langle X_{in}\rangle$. R_A^{ads}(hop) is still given by (14) and increases with decreasing α, thus boosting reactivity. More significant is that lower $\langle X_{in}\rangle$ greatly increases the tracer diffusion coefficient F_{tr}(GH) which boosts reactant penetration of excess reactant and thus reactivity. However, a synergistic factor is the strong shift in equilibrium with varying α, noting that blocked reentry allows completion of the reversible reaction to F=1!

Finally, we provide some further comments on reaction kinetics. *First*, for the neutral case α=1, we describe the origin of the linear decrease $R^{B}_{net}(F) \propto (1-F/F_{eq})$ where $F_{eq} = K_c/(K_c+1)$. To this end, it is instructive to consider steady-state equations for $\langle \Delta A_n \rangle = \langle A_n \rangle - K_c^{-1}\langle B_n \rangle$. Subtracting K_c^{-1} times (6b) from (6a) yields the homogeneous F-independent equations

$$0 = -k(1+K_c^{-1})\,\langle \Delta A_n \rangle - \nabla J_{\Delta A}^{n>n+1} \text{ where } J_{\Delta A}^{n>n+1} = -h\,F_{tr}\,\nabla(\langle \Delta A_n \rangle). \qquad (16)$$

For the BC at n=1, subtracting K_c^{-1} times (8b) from (8a) yields

$$\begin{aligned} 0 = {} & h\langle E_{out}\rangle\langle \Delta A_{out}\rangle - [h\langle E_{out}\rangle + k(1+K_c^{-1})]\,\langle \Delta A_1 \rangle + \\ & (1+K_c^{-1})\,R_A^{ads\text{-}des}(ex) - J_{\Delta A}^{1>2}. \end{aligned} \qquad (17)$$

where $\langle \Delta A_{out} \rangle = \langle X_{out} \rangle(1- F/F_{eq})$ and $R_A^{ads\text{-}des}(ex)$ denotes the net rate of exchange of reactant A into the pore at n=1. Using that $\langle A_1 \rangle + \langle B_1 \rangle = \langle X_{out} \rangle$ for α=1, one can also write

$$(1+K_c^{-1})\,R_A^{ads\text{-}des}(ex) = P_{ex}\,h\langle X_{out}\rangle^2(1- F/F_{eq}) - P_{ex}\,h\langle X_{out}\rangle\langle \Delta A_1 \rangle. \qquad (18)$$

Thus, the BC adopt an inhomogeneous linear form with driving term proportional to $1-F/F_{eq}$. This implies that all $\langle \Delta A_n \rangle \propto (1-F/F_{eq})$, and thus one has $R^{B}_{rxn}(F) = (1-F/F_{eq})\,R^{B}_{rxn}(0)$.

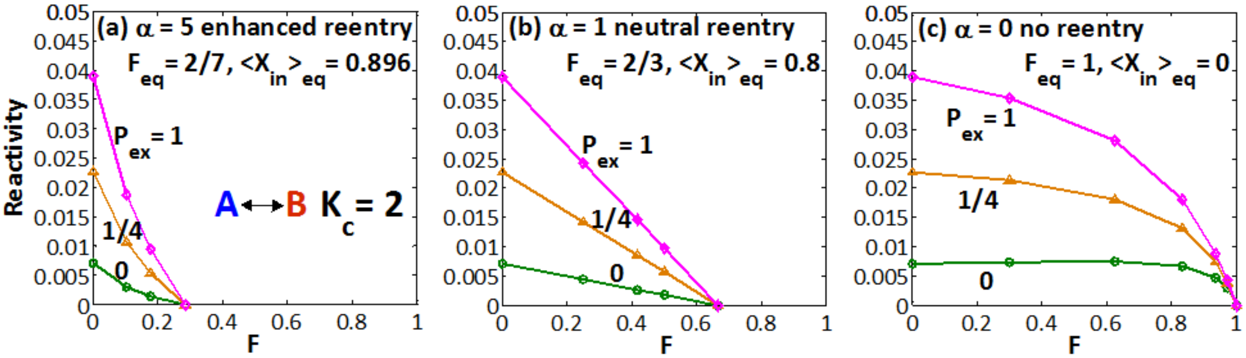

Figure 7: Net reactivity per pore, R^{B}_{rxn}, as a function of the fraction F of reactant converted to product for reversible reaction A↔B with L=100 a, k = 0.001, k´=0.0005, h = 1, and $\langle X_{out} \rangle$ = 0.8. (a) enhanced product reentry α=5; (b) neutral reentry α=1; (c) blocked reentry α=0.

Second, the above analysis is useful for understanding the change in initial reactivity (for F=0 where behavior is independent of α) going from irreversible reaction (where $1+K_c^{-1}=1$) to reversible reaction (where $1+K_c^{-1}>1$). Equation (17) indicates that one should have quite similar values of $<\Delta A_1>$ since k<<h (with $<\Delta A_1>$ marginally lower in the reversible case), and (16) indicates that $<\Delta A_n>$ should decay somewhat faster into the pore for the reversible case. Mainly the latter effect produces a slightly lower initial reactivity for the reversible case. In Fig.8, we compare $<\Delta A_n>$ profiles for F=0 and α=1 to confirm this picture.

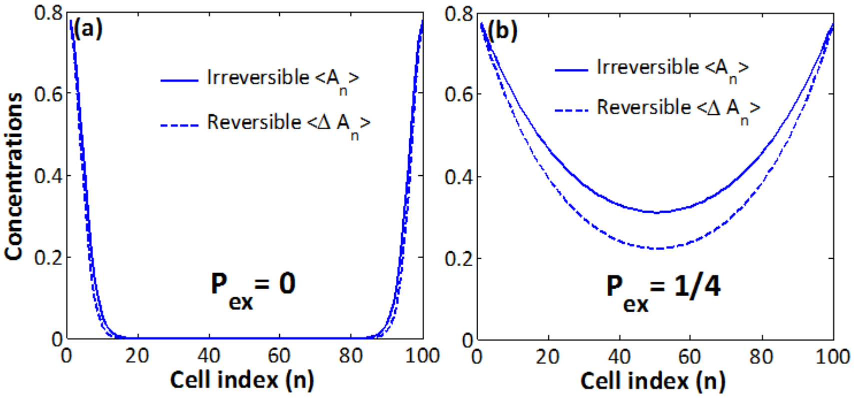

Figure 8: Fig.8. Comparison of excess reactant concentration, $<\Delta A_n>$, for irreversible reaction (where $<A_n> = <\Delta A_n>$) and reversible reaction at the onset of reaction (F=0) with L=100 a, k = 0.001, k´=0.0005, h = 1, α=1, and $<X_{out}> = 0.8$. The net reactivity R^B_{rxn} corresponds to the area under these curves.

Third, non-linear variation of $R^B_{rxn}(F)$ on F when α≠1 has similar origins to those for the irreversible case. *Fourth*, our results for the F-dependence of $R^B_{rxn}(F)$ encode complete information about the reaction kinetics as discussed for the irreversible case.

4 Conclusions

The catalytic activity of nanoporous materials containing multifunctionalized linear nanopores is shown to be strongly dependent on the tunable interaction between reaction products and the interior pore environment. Making the pore interior unfavorable to products not only modifies the reaction equilibrium towards completion, but also reduces pore loading which can significantly enhance diffusivity and thus reactivity especially in the SFD regime. As noted in previous studies, catalytic activity is also strongly dependent on the propensity for passing of reactants and products within the pores [9,14,15,21]. Our generalized hydrodynamic formulation of reaction-diffusion phenomena provides an efficient tool to explore behavior over a broad phase-space of model parameters. This approach can reliably capture the complex interplay between reaction and restricted transport which results in subtle spatial correlations and fluctuations of reactants and products within the pore. These effects are not described by traditional mean-field approaches.

There are numerous possible modifications and extensions of our modeling which could be performed either utilizing refined generalized hydrodynamic RDE or with KMC simulation.

In this contribution, we have considered the benchmark case of equal mobility of reactants and products within the pore, following previous studies of conversion reactions in nanoporous systems [8-14]. However, the basic features of the reaction-diffusion process and the variation for enhanced versus blocked product reentry to the pore will be preserved for unequal mobilities. Some comments pertaining to the required refinement of refined GH formulation are found in Ref. [14]. Another natural extension of our modeling is to consider different reaction mechanisms, e.g., $A+B \leftrightarrow C+D$ better matching esterification reactions, and to consider the scenario where pore reentry of just one of the two products is enhanced versus blocked. The approximate MF and precise GH formalism described above are readily extended to treat this more complex situation, and preliminary studies reveal analogous behavior to that discussed above for the simpler $A \leftrightarrow B$ conversion reaction mechanism.

Acknowledgments

This work was supported by the U.S. Department of Energy (USDOE), Office of Basic Energy Sciences, Division of Chemical Sciences, Geosciences, and Biosciences through the Ames Laboratory. It was performed at Ames Laboratory which is operated for the USDOE by Iowa State University under Contract No. DE-AC02-07CH11358.

Appendix: Random Walk Analysis of GH Tracer Diffusivity $F_{tr}(n)$.

The position-dependent tracer diffusion coefficient, $F_{tr}(x=na) = F_{tr}(n)$, for a tagged particle starting at site n in a pore with a concentration *X* of other particles is central to our generalized hydrodynamic formulation. This quantity is determined by simulations involving a finite concentration of a single type of particle in the pore with dynamics of all particles identical to the tagged particle. This dynamics is naturally selected to match the (equivalent) dynamics A or B particles within the pore: hopping to neighboring empty sites at rate h; exchange with adjacent particles within the pore at rate P_{ex} h; desorption from end sites n=1 and n=L by hopping to empty sites just outside the pore. If the reaction model excludes (includes) exchange in and out of the pore, then this process is excluded (included) in the simulations to determine F_{tr}. If included with rates described in Sec. 2A, then the corresponding single-particle dynamics includes exchange in and out of the pore at rate $e_{ads}P_{ex}h$. This choice recovers the appropriate values for α=1 (where e_{ads} =1) and for F=1 with only B in the fluid (where e_{ads} =α).

Our explicit algorithm to determine $F_{tr}(n)$ is based on a suitably defined "exit time" $t_X(x=na)$ for the tagged particle to exit the pore (where exiting the pore corresponds to reaching a site just outside the pore opening). Given anomalous features of random walks in one-dimension, such as long time-tails in return-time distributions [26], a judicious choice of definition for t_X is appropriate. Rather than simply average exit times over many simulation trials, we define $t_X(x=na)$ as the time when the root-mean-square displacement of the tagged particle reaches the distance to the closest pore opening (i.e., a distance n for n<L/2). Then, we assign $F_{tr}(n) = t_0(n)/t_X(n)$, motivated by the classic result that diffusivity scales like the mean-square displacement divided by time. Here, $t_0(n)$ corresponds to the exit time for an isolated particle in the pore, which can be determined analytically. Thus, one has that $t_X(n) \sim t_0(n)$ and $F_{tr}(n) \to 1$ for all n, as $X \to 0$.

For a *semi-infinite pore* $L \to \infty$, it is clear that $F_{tr}(n) \to F_{tr}(DH) = F_{tr}(X, P_{ex})$, as $n \to \infty$, recalling that $F_{tr}(DH)$ is the standard tracer diffusion coefficient for an infinite system. Thus, one has that $F_{tr}(n) \to 0$, as $n \to \infty$ for SFD ($P_{ex}=0$) when $X > 0$. The anomalous diffusion observed for SFD in infinite systems [20] suggests that $t_X(n) \sim n^4$ [14] versus $t_0(n) \sim n^2$ for classic diffusion. Together, these imply that $F_{tr}(n) \sim 1/n^2$, as $n \to \infty$, for SFD. Numerical studies show that behavior for SFD is fit well by a more general form $F_{tr}(n) \propto 1/(n^2 + a\, n + bn^{1/2} + c)$ over a broad range of n [14]. For *finite pores* L<∞, usually $F_{tr}(n) \to F_{tr}(DH)$ quickly upon entering the pore interior if $P_{ex} > 0$. See Fig. 3b. For SFD ($P_{ex}=0$), numerical studies reveal that $F_{tr}(na \approx L/2) \sim 1/L$ at the pore center.

To generate optimal numerical data for $F_{tr}(n)$, we sometimes smooth simulation results using a fit $\delta F_{tr}(n) = F_{tr}(n) - F_{tr}(DH) \propto 1/(n^2 + an + c)$, for larger n. Simulations are typically used to generate $F_{tr}(n)$ data for a selected set of values of $X = \langle X_{in} \rangle$. Data for other intermediate X-values can be readily and reliably obtained by interpolation.

References

1) J.A. Melero, R. Van Grieken, and G. Morales, Chem. Rev. 106, 3790 (2006)

2) E.L. Margelefsky, R.K. Zeiden, and M.E. Davis, Chem. Soc. Rev. 37, 1118 (2008).

3) J.M. Thomas and R. Raja, Acc. Chem. Res. 41, 708 (2008).

4) I.K. Mbaraka and B.H. Shanks, J. Catal. 229, 365 (2005).

5) J.-P. Dacquin, H.E. Cross, D.B. Brown, T. Duren, J.J. Williams, A.F. Lee, and K. Wilson, Green Chem. 12, 1383 (2010).

6) C.-H. Tsai, H.-T. Chen, S.M. Althaus, K. Mao, T. Kobayashi, M. Pruski, and V.S.-Y. Lin, ACS Cat. 1, 729 (2011).

7) K. Mao, T. Kobayashi, J.W. Wiench, H.-T. Chen, C.-H. Tsai, V.S.-Y. Lin, and M. Pruski, J. Am. Chem. Soc. 132, 12452 (2010).

8) J.G. Tsikoyiannis and J.E. Wei, Chem. Eng. Sci. 46, 233 (1991).

9) J. Kärger, M. Petzold, H.S. Pfieffer, S. Ernst, and J. Weitkamp, J. Catal. 136, 283 (1992).

10) C. Rodenbeck, J. Kärger, and K. Hahn, J. Catal. 157, 656 (1995).

11) M.S. Okino, R.Q. Snurr, H.H. Kung, J.E. Ochs, and M.L. Mavrovouniotis, J. Chem. Phys. 111, 2210 (1999).

12) S.V. Nedea, A.P.J. Jansen, J.J Lukkien, and P.A.J. Hilbers, Phys. Rev. E 65, 066701 (2002); 66, 066705 (2002); 67, 046707 (2003).

13) D.M. Ackerman, J. Wang, J.H. Wendel, D.-J. Liu, M. Pruski, and J.W. Evans, J. Chem. Phys. 134, 114107 (2011). *(2011 Editors' Choice)*

14) D.M. Ackerman, J. Wang, and J.W. Evans, Phys. Rev. Lett., 108, 228301 (2012).

15) J. Wang, D.M. Ackerman, K. Kandel, I.I. Slowing, M. Pruski, and J.W. Evans, MRS

Symp. Proc. Vol. 1423 (MRS, Pittsburgh, 2012) DOI: 10.1557/opl.2012.229

16) R. Kutner, Phys. Lett. 81A, 239 (1981).

17) J. Quastel, Commun. Pure Appl. Math. 45, 623 (1992).

18) H. Spohn, *Large Scale Dynamics of Interacting Particles* (Springer, Berlin, 1991).

19) P.H. Nelson and S.M. Auerbach, Chem. Eng. J. 74, 43 (1999).

20) T.E. Harris, J. Appl. Probab. 2, 323 (1965).

21) D.-J. Liu, J. Wang, D.M. Ackerman, K. Kandel, I.I. Slowing, M. Pruski, H.-T. Chen, V.S.-Y. Lin, and J.W. Evans, ACS Cat. 1, 751 (2011).

22) D.G. Levitt and G. Subramanian, Biochimica et Biophysica Acta 373,132 (1974).

23) B.J. Alder and W.E. Alley, in Physics Today (January 1984), p.56.

24) We use the discretization $\nabla J_A \rightarrow \nabla J_A^{n>n+1} = \frac{1}{2}[F_{tr}(n)+F_{tr}(n+1)]\nabla\langle A_n\rangle$.

25) For irreversible reaction with $\alpha=1$, one can show that net rate of reactant adsorption via hopping at n=1 satisfies $R_A^{ads\text{-}des}(hop) = h\langle X_{out}\rangle\langle E_{out}\rangle(1-F) - h\langle E_{out}\rangle\langle A_1\rangle$, and via exchange at n=1 satisfies $R_A^{ads\text{-}des}(ex) = P_{ex}h(\langle X_{out}\rangle)^2(1-F) - P_{ex}h\langle X_{out}\rangle\langle A_1\rangle$. The inhomogeneous BC for species A at cell n=1 come from $R_A^{ads}(hop) - R_A^{des}(hop) + R_A^{ads\text{-}des}(exch) - J_A^{1>2} = 0$. One can also show that $\langle A_1\rangle < (1-F)\langle X_{out}\rangle$.

26) S. Redner, *A Guide to First-Passage Processes* (Cambridge University Press, Cambridge, 2001).

CHAPTER 8. LANGEVIN PASSING DYNAMICS OF CIRCLES AND SPHERES

1 Introduction

The previously-described hydrodynamic and kinetic Monte Carlo (KMC) methods [1,2,3] for tracking diffusion and reaction in a pore can allow limited passing of particles. Physically, this is representative of the size of the pore being large enough to allow some degree of passing between particles. This passing was modeled with a passing parameter, P_{ex}, which ranged from 0 in the strict single file case to 1 in the complete passing case. The value is a scaling factor for the exchange motion of the particles. As such, its behavior is clear, but there was no direct physical connection between pore size and particle size that gives a specific P_{ex} value. The goal of this work is to determine the probability of passing for two molecules in a narrow pore and investigate the degree of passing as a function of the diameter of the pore and the size and shape of the molecules. The general case of a molecule of arbitrary shape is complicated by the rotational freedoms of an arbitrary three dimensional shape. To better understand the behavior of molecules in the pore and isolate the size dependence, the simpler case with no rotational motion was investigated. Both two dimensional (circles) and three dimensional (spheres) particles were studied.

2 System Description

Two particles are contained within a linear pore that constrains their motion perpendicular to the pore axis which hinders the passing behavior. The desired information is the probability that the two neighboring particles will move in such a way to pass each other. The particles are started with a defined separation, and the positions are allowed to evolve over time. The particles are free to move in any direction provided that they do not overlap each other or cross the pore wall. The pore is treated as infinite, so there is no possibility of particles leaving through the end of the pore. The ending configuration is either the particles passing each other or moving a given distance apart as shown in figure 1. The lines between particles in the figure denote a characteristic length of the system. It is intended to correspond to the the distance between sites in single file hopping systems [1-5] which is on the order of the size of a single molecule.

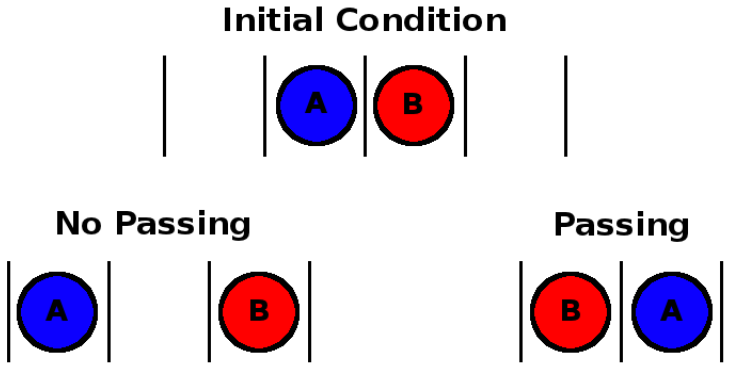

Figure 1: Initial configuration and the two options for final configuration: passing and no passing.

In the 3D case, particles are spheres contained within an infinitely long cylindrical pore aligned with, and centered on, the z-axis. The surface of the pore is smooth and defined by $x^2+y^2 = R_p^2$ for all z. The 2D case consists of circles contained within an infinitely wide rectangular pore in the x-z plane. The pore is aligned along the z-axis with the boundary defined as abs(x) = R_p, with R_p as half the width of the rectangle (effectively the “radius” of the rectangle).

The system's evolution is described by Langevin [6,7] equations of motion governing the degrees of freedom. The pore is stationary while the particles are confined to move inside. In the most general case, each particle has six degrees of freedom – three rotational angles (θ_1, θ_2, θ_3) and three translational positions r_i for i={x, y, z}. The symmetry of the circle and sphere case reduces the degrees of freedom by removing rotational motion. This leaves only the translational degrees of freedoms: 2 for each circle and 3 for each sphere. In principle, a further degree of freedom can be eliminated by noting that the absolute values of z for each particle are not needed. Only the separation distance between particles is relevant. This reduction was not used in this work as it poses issues generalizing to the case of an arbitrary shaped particle. Examples of the particle evolution are shown in figures 2 (circles) and 3 (spheres).

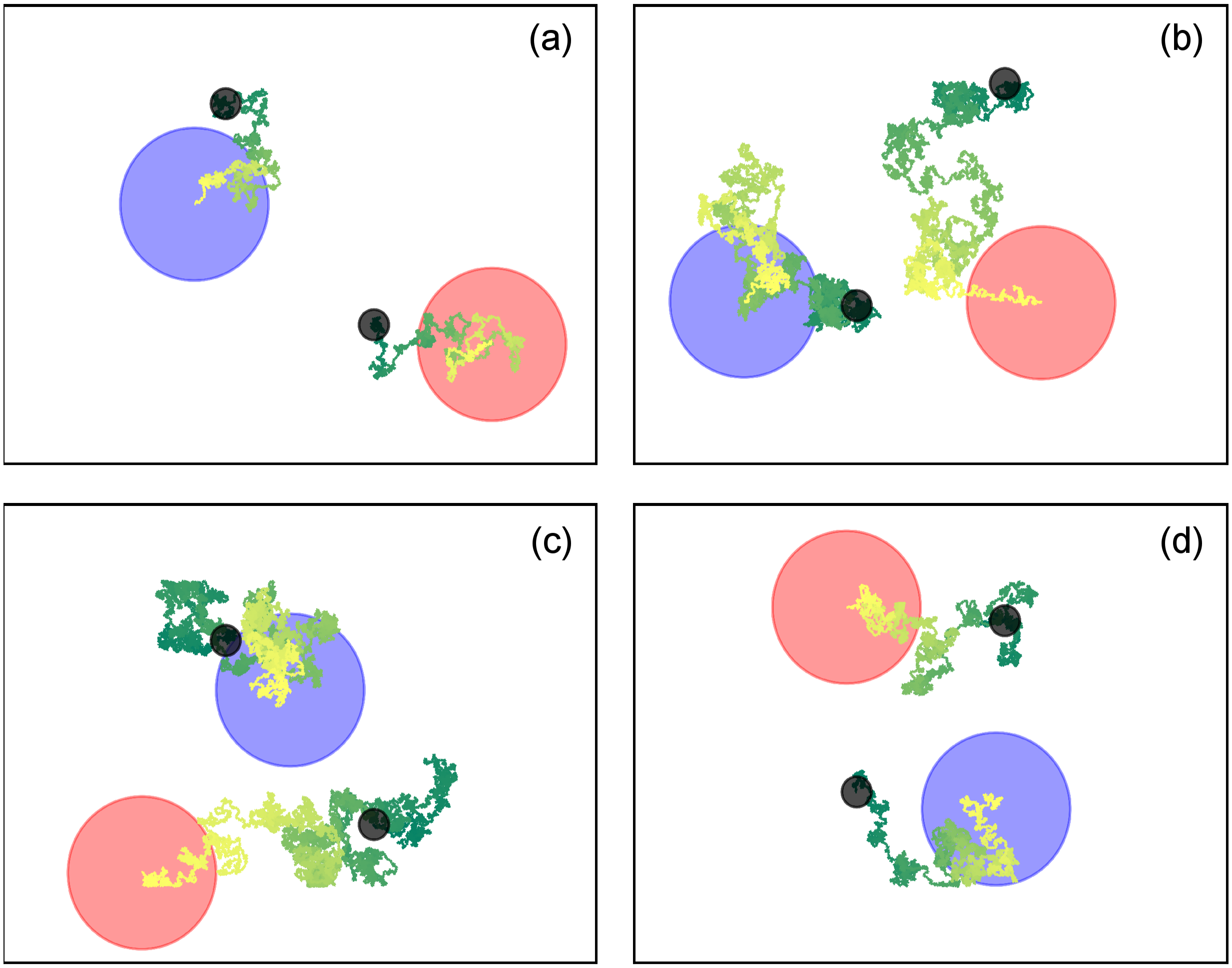

Figure 2: Motion of particles that separate (a), (b) and pass (c), (d). Starting position of each particle is given by the black dots. The center of mass paths are shown, going from dark green at the start of the simulation to light yellow at the end. Matching colors on both paths can be used to determine the relative location the particles over the course of the simulation. Parameters, details described later, are gap=2R (gap defined as rectangle width – 4R, with R=circle radius), time step=0.0001, D=1. Upper and lower edges of boxes correspond to pore boundaries. Side edges are not meaningful and do not constrain motion in that direction.

The translational positions obey the Langevin equations:

$$m\ddot{r}_i(t)+m\zeta_i\dot{r}_i(t)+\frac{\partial}{\partial r_i}V(r_i,t)=F_i(t) \qquad (1)$$

where m is the particle's mass, ζ is the frictional damping coefficient from the surrounding fluid, V is an external potential, and $F_i(t)$ is a Gaussian random force with the properties:

$$\langle F_i(t)\rangle = 0$$
$$\langle F_i(t)\, F_i(t')\rangle = 2kTm\zeta_i\delta(t-t') \tag{2}$$

With no external potential and assuming an over-damped system ($\ddot{r}_i = 0$), equation (4) becomes:

$$m\zeta_i \dot{r}_i(t) = F_i(t) \tag{3}$$

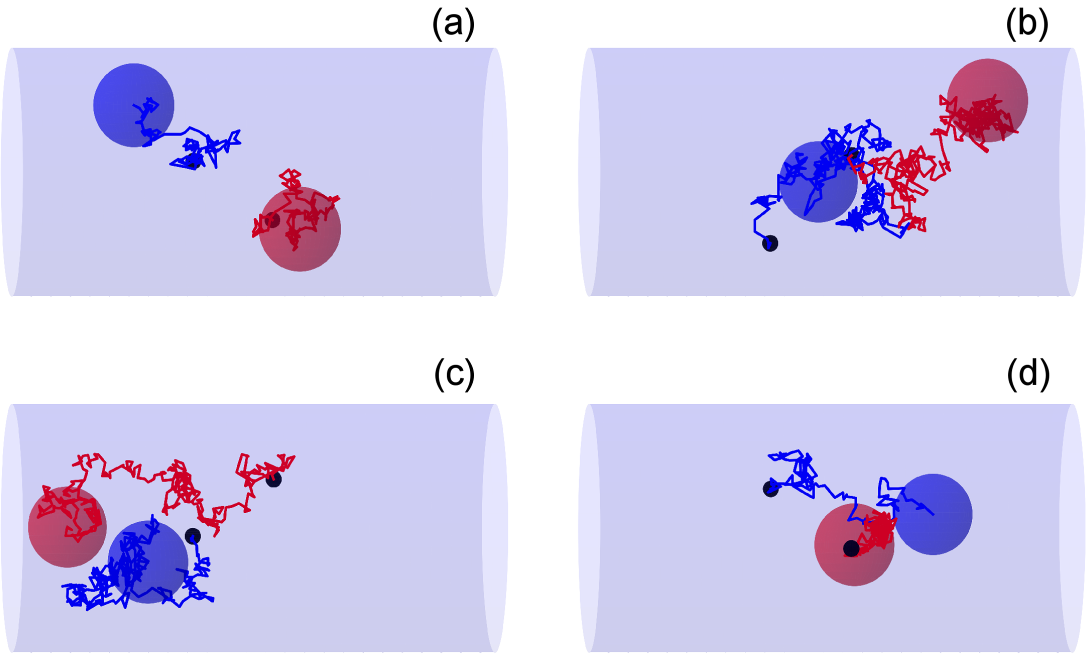

Figure 3: Motion of particles that separate (a), (b) and pass (c), (d). Starting position of each particle is given by the black dots, with the path to the final position, indicated by the large spheres, shown. Parameters are gap=2R (gap defined as pore diameter – 4R, with R=sphere radius), time step=0.01, D=1. The cylindrical boundary is shown.

3 Simulation

The simulation is performed by moving the pair of particles through a number of discrete configuration changes governed by the Langevin equations as given in equations (5) and (6). Configuration changes are attempted until one of the two ending conditions is reached. Each trial change is accepted if it results in a configuration where both particles are entirely within the pore and the particles do not intersect. If any of the above conditions are violated, the trial move is rejected and the system is restored to the previous condition. This acceptance criteria is written as:

$$Acc = Acc_{\text{int}} \wedge Acc_{\text{pore}}^{A} \wedge Acc_{\text{pore}}^{B} \tag{4}$$

where Acc is the acceptance function (True/False) and Acc_{int}, Acc_{pore} are the acceptance functions determined from whether particles intersect or are contained within the pore, respectively. The Λ term is the logical conjunction (A Λ B is true iff both A and B are true).

The intersection component is greatly simplified from the general case as the particles are symmetric. For both the sphere and circle case, the function is given by:

$$Acc_{\text{int}} = \begin{cases} True\text{, if } \|\boldsymbol{r}_A - \boldsymbol{r}_B\| \geq (R_A + R_B) \\ False\text{, otherwise} \end{cases} \tag{5}$$

where $\mathbf{r}_i$, and R_i are the position and radius, respectively, of particle i.

The criteria for particle i being within the pore for the two dimensional case is given by:

$$Acc_{\text{pore}}^{i} = \begin{cases} True\text{, if } |x_i| + R_i \leq R_p \\ False\text{, otherwise} \end{cases} \tag{6}$$

The three dimensional case is given by:

$$Acc_{\text{pore}}^{i} = \begin{cases} True\text{, if } \sqrt{x_i^2 + y_i^2} + R_i \leq R_p \\ False\text{, otherwise} \end{cases} \tag{7}$$

In this study, both particles are treated as identical with a reduced mass of 1.0 and radii of 1.0. The pore radius size is varied giving a pore gap defined as R_p-$2R_i$. While this can result in a negative gap value for some choices of R_p and R_i, passing can only occur when the gap is equal to or greater than zero. A friction value for translation must be specified as well. The particles are initially placed at a separation of $\Delta z = z_0 = R_1 - R_2$ (see Appendix B for a discussion of initial separation). They move via a series of configuration changes until they separate, moving to a separation of $\Delta z = 2z_0$, or pass each other by moving to a separation of $\Delta z = -z_0$.

3.A. Algorithm

A single simulation run proceeds until either of the end conditions are met. Multiple runs are required to determine the passing probability. Each run is performed using the following sequence:

1) *Set up the initial configuration*. The particles are placed at a separation distance of z_0. For spheres, the starting x and y positions are randomly chosen to place both particles within the pore. For circles, the y position is fixed at zero and the x position is chosen randomly to place the particle within the rectangle.

2) *Perform configuration changes.* Changes are continued until the system meets one of the ending conditions. Until then, this step is an infinite loop doing the following:

    a) *Select random distances.* The translations are selected randomly from a zero centered Gaussian, F_i, and scaled to match the appropriate distribution given by equation (5). The discrete value for F_i is determined from the continuous F(t):

    $$F_n = \frac{1}{\Delta t} \int_{t_n}^{t_{n+1}} F(t)$$
    $$\langle F_n^2 \rangle = \frac{2kT\zeta}{\Delta t} \qquad (8)$$
    $$F_n = \sqrt{\frac{2kT\zeta}{\Delta t}} w_n$$

    where w_n is a random number with a unit normal distribution. For spheres, translations are generated for the x, y, and z directions; while for circles, translations are only generated for the x and z directions.

    b) *Apply translations.* The particles are moved by the amounts determined in the previous step. Using the random force given in equation (8), the translation is given by:

    $$x_{n+1} = x_n + \frac{F_n}{m\zeta} \Delta t \qquad (9)$$

    c) *Check acceptance criteria.* The particles are checked to see if the new positions result in both particles being within the pore and not overlapping.

   i. *If accepted*, the move acceptance counter is incremented and the program continues to step (3)
   ii. *If not accepted*, the move denial counter is incremented, the system is reverted to the previous configuration, and a new trial move is selected, starting from step (2a)

3) *Check completion criteria for simulation.* The separation of the particles along the z axis is tested against the pass and no pass end conditions.
   a) *If either criteria is met*, the statistics for pass/no pass are updated. If more simulations need to be run, the loop is repeated from step (1). Otherwise, the simulation is complete.
   b) *If neither criteria is met*, the simulation continues with trial moves from step (2a).

The resulting data is the number of runs that end in a passing configuration (N_{pass}) and the number that end in a non passing configuration (N_{nopass}). The passing probability P is simply given by $N_{pass}/(N_{pass}+N_{nopass})$. The desired value is the scaling factor for passing, P_{ex}, used in the kinetic Monte Carlo simulations. With a starting separation of z_0 and ending criteria of $z_{pass} = -z_0$, $z_{nopass}=2z_0$, the passing value is given by:

$$P = \frac{p_{ex}}{(2 + p_{ex})} \tag{10}$$

where P is the fraction of simulations where the particles end in the passing configuration (which can have values between 0 and 1/3), and P_{ex} is the probability of exchange as given in the hopping system. The parameter P_{ex} is then given by (see figure 4).

$$p_{ex} = \frac{2P}{1 - P} \tag{11}$$

3.B. Time step selection

A time step must be selected for the simulation in order to implement equations (8) and (9). Proper selection of the time step is necessary for accurate and efficient results. A large time step is desirable as it leads to faster simulations. However, large time steps can lead to inaccurate results for two reasons. First, a large time step can allow particles to pass through each other in an nonphysical way leading to an erroneously high passing probability. Second, the larger steps can make it difficult for particles to fully explore the phase space due to steric limitations on possible moves. This makes passing through small gaps more difficult. It would be expected that very small gaps would require smaller time steps to get accurate results. The relative error is smaller for large gaps. In practice, the desired time step is the largest one that produces acceptable results. This can be determined by trial of a series of data sets with progressively smaller time steps to identify the time step where the results converge. If a larger time step leads to results that are within an acceptable error of the results from the smaller time step, the larger one is sufficient to use.

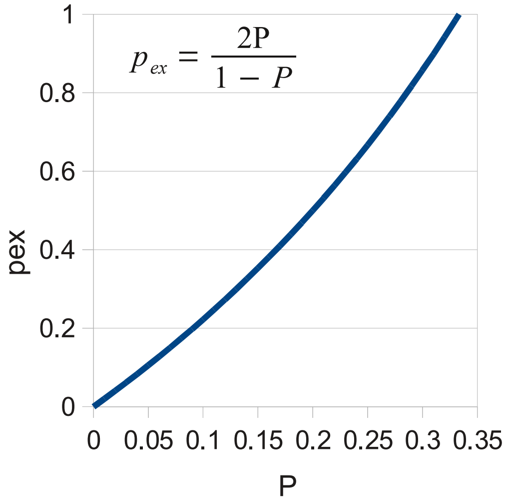

Figure 4: Connection between P and P_{ex}

4 Results

Both the circle and sphere cases were investigated. The results are given separately below. For all of the data below, circles and spheres of equal radius (R_A=R_B=R) were used. These radii were set to 1.0, and the pore radius was chosen as a multiple of that. Due to steric limitations, passing will only be possible when the gap is greater than or equal to 0.0. All friction values were set to 1.0, and kT was set to 1.0, which yields D=1.0 (see Appendix A).

4.A. Circle passing data

The passing rate, P, was measured as a function of the pore gap (R_p-2R). The initial separation, z_0, was chosen as twice the radius of the circle with the no passing end condition being $z_{nopass} = 2z_0 = 4R$, and the passing end condition being $z_{pass} = -z_0 = -2R$. Figure 5 shows data taken using six different time steps to determine the optimal time step to use for further simulations. All other parameters are the same for each curve. The probabilities are taken from 100,000 independent runs.

The smallest time step curve is taken to be most accurate as it is least impacted by the artificial jump from position to position in the discrete moves. The plot shows that, at the largest time step, there is substantially increased passing. This is explained by the circles moving so far in each step that they can artificially pass through each other. The remaining curves show reduced passing with increasing time step. This is likely due to the moves being too large to slide through the small spacing available for passing. This effect would decrease as the gap increases. That change is evident in the plot below. The curves for t=0.0001 and smaller show the converged behavior with errors between them on the order of the error in the simulation. Thus, it is reasonable to consider t=0.0001 the largest value of the time step that produces acceptable results.

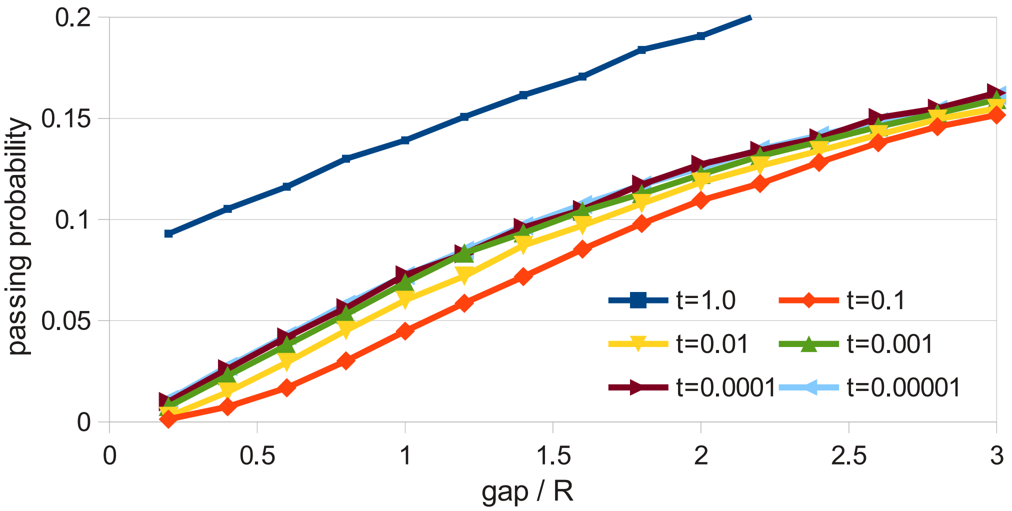

Figure 5: Circle passing probability as a function of gap for several time steps

The curves in figure 5 show data down to a gap of 0.2. Figure 6 shows how that changes when the the radius of the rectangle is only slightly larger than the sum of the radii of the two circles. The passing rate drops off at a faster rate as it approaches zero. The curve for t=0.0001 shows a larger relative deviation at smaller radius ratios. This suggests that, for very small gaps, a smaller time step is required.

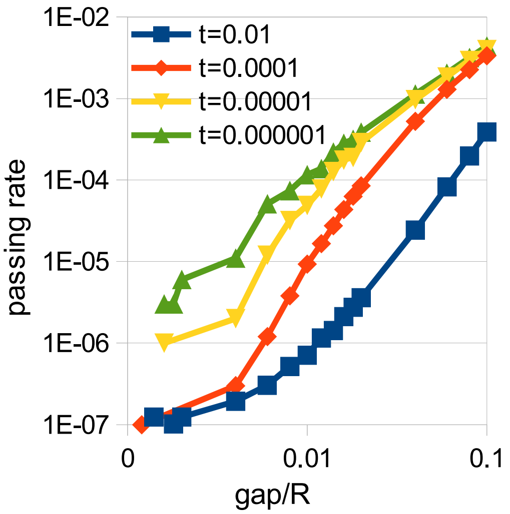

Figure 6: Passing rates for circles in pores with small gaps.

4.B. Sphere passing data

The simplest three-dimensional case has both particles as spheres with radius R_A=R_B=R. In this case, the six degrees of freedoms are: x_A, x_B, y_A, y_B, z_A, z_B . The initial separation, z_0, was twice the radius of the particle with the no passing end condition being $z_{nopass} = 2z_0$ and the passing end condition being $z_{pass} = -z_0$.

Figure 7 shows behavior similar to the circle case for seven choices of time steps. Each data point is an average over 100,000 simulations. As with the circle case, a time step of t=0.0001 is an appropriate choice. For the larger gaps, above about 2.0, a larger time step of t=0.001 appears to be sufficient. At smaller gaps, that time step is too large for an accurate result.

The passing rate for smaller gaps is shown in figure 8. The drop off in the approach to zero mimics that seen in the case of circles. The t=0.01 data below is from 5,000,000 runs; the other data is from 500,000 runs. Statistics are poor due to very rare passing.

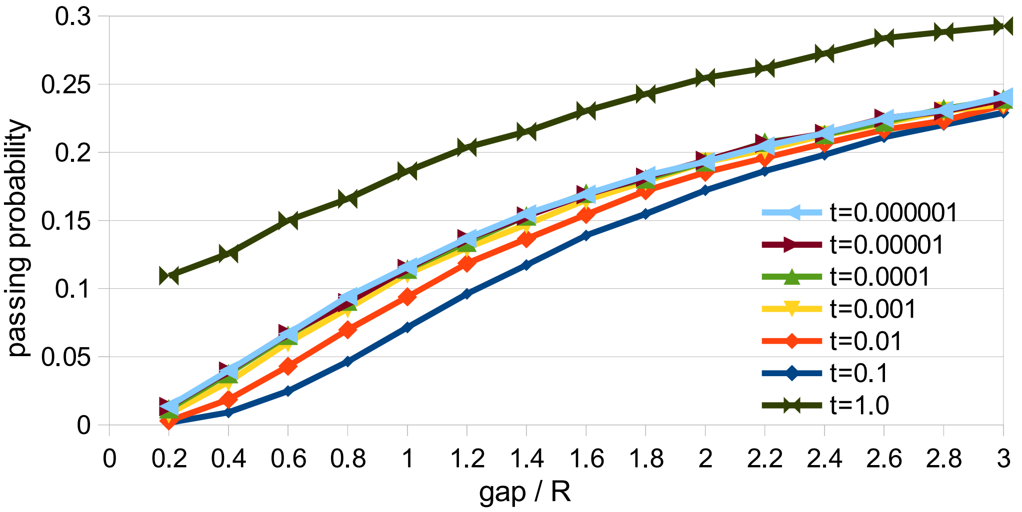

Figure 7: Sphere passing probability as a function of gap for several time steps

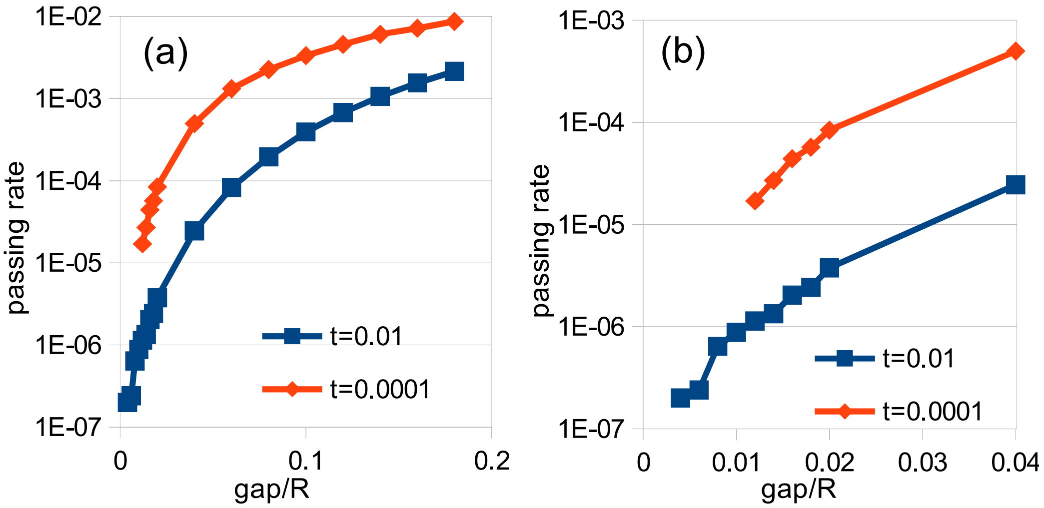

Figure 8: Passing rate for spheres at small gap sizes.

4.C. Time step

Representative values for approximate simulation run times for each data point are listed in table 1. The run time scales as ~1/time step which illustrates the value in selecting the largest time step that gives acceptable results. Figures 5 and 7 suggested a value 0.0001 was appropriate over the range plotted. From the table of times, the very small difference in accuracy gained from going to the next smaller time step would require simulations taking ten times longer.

Table 1: Simulation run time for two circles using several time steps for circles (left) and spheres (right).

Timestep	Runtime	Timestep	Runtime
1	<5 seconds	1	<5 seconds
0.1	<5 seconds	0.1	<5 seconds
0.01	20 seconds	0.01	25 seconds
0.001	2 minutes, 20 seconds	0.001	3 minutes, 30 seconds
0.0001	23 minutes	0.0001	33 minutes
0.00001	3 hours, 45 minutes	0.00001	5 hours, 30 minutes
		0.000001	55 hours

4.D. Limiting behavior

With the given choice of initial separation and ending conditions, the expected limit in an infinitely wide pore is 1/3. Figure 9 shows an extended set of data out to a larger gap to show the approach to the limiting value. For spheres (figure 9a), the data for the larger time steps exceeds this slightly with a limiting value between 0.35-0.38; however, the smaller time step shows closer agreement to the expected limit. For circles (figure 9b), none of the time steps used produced a passing probability curve that reached the limiting value in the range of gaps studied. In both cases, the larger time step shows a crossover from underestimating the passing at small gaps to overestimating the value at large gaps.

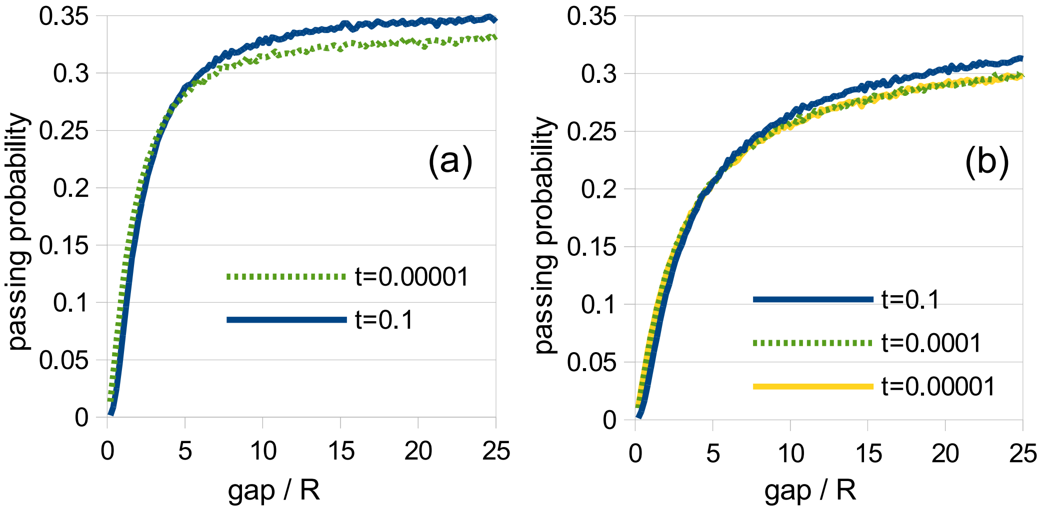

Figure 9: Extended passing probabilities for (a) spheres and (b) circles.

5 Conclusion

A method of calculating the passing parameter, P_{ex}, was created and tested. This data, missing from previous studies, provides an essential connection between experimental results and the reaction-diffusion theory. For example, previous studies have used passing values of P_{ex}=0.125, 0.25, and 0.5. From equation (10), we see that these correspond to a passing rate of P=0.059, 0.11, and 0.2. Using the parameters for spheres from this study, the ratios of pore radius to particle radius for those cases are approximately (using data from figure 7) 2.27, 2.5, and 3.1. A fairly small change in the pore size results in a large change in the passing parameter.

These results are only for circles and spheres. While they yield important information about behavior, may not necessarily represent a given experimental system. An obvious extension to this work would be to use particles that match the size and shape of specific molecules in an actual system. This is much more complicated as it involves rotations for an arbitrary shape particle.

Circles were chosen as they are the most simple case that can be studied. The general behavior of circles and spheres is qualitatively the same, but the scaling with radius ratio is different.

Appendix A: Method Validation

A few simple tests were run on the Langevin program to ensure correct dynamical behavior. The mean square displacement over time for Langevin dynamics is given by:

$$\begin{gathered} \langle x^2 \rangle = 2NDt \\ D = \frac{kT}{m\zeta} \end{gathered} \tag{12}$$

where D is the diffusion coefficient and N is the dimensionality of the diffusion occurring (2 for circles, 3 for spheres). Allowing a particle to diffuse in time should give a linear curve for the mean square displacement. If the dynamics are correct, the slope should match the diffusion coefficient calculated from the input parameters. Figure 10 shows the mean square displacement behavior for circles and spheres. This was calculated for a free particle without a pore. The simulation shows very strong agreement with the expected value from the parameters used.

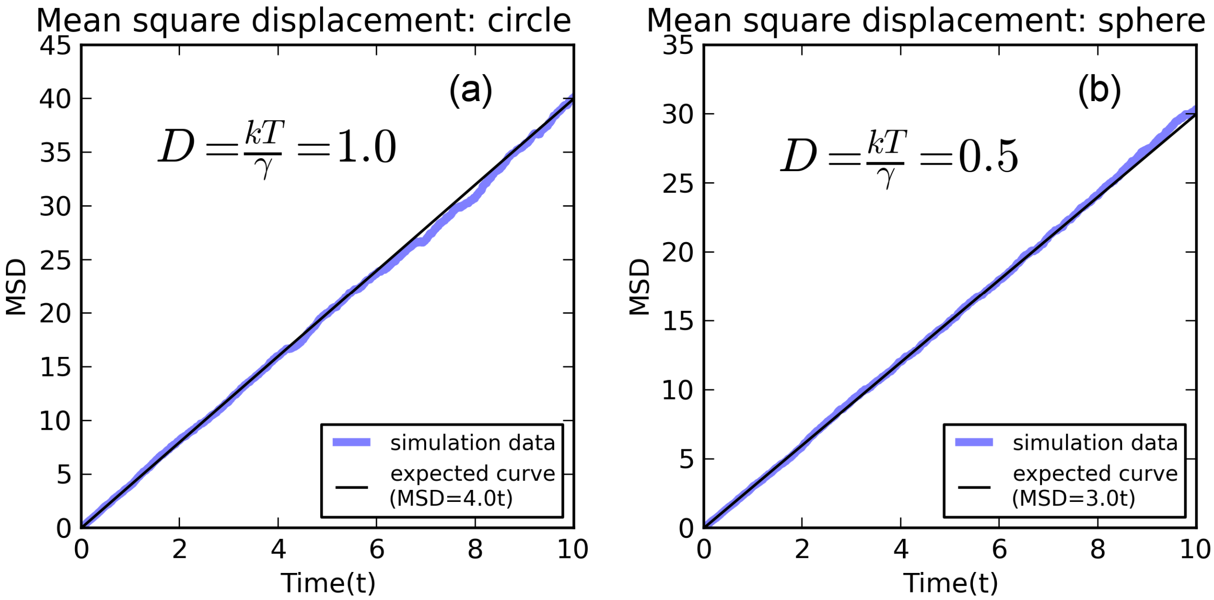

Figure 10: Mean square displacement curves for a lone circle (a) and sphere (b). The black lines show the expected curve.

The time evolution of a particle's probability distribution function is given by a Gaussian distribution [8]:

$$C(x,t)=\frac{1}{\sqrt{2N\pi Dt}}\exp\left(\frac{-x^2}{2NDt}\right) \tag{13}$$

To confirm this behavior, a pair of particles were allowed to move under the Langevin model described above without being confined by a pore. Testing for collisions between particles was turned off which allowed them to pass through each other. Multiple simulations were run with the initial separation fixed at 2. After each move, the separation and time were recorded. A histogram of the results is shown in figure 11. Black lines corresponding to equation (13) are superimposed on the simulation data which show excellent agreement with theory. For these plots, x in equation (13) is Δz, and D is twice the individual diffusion coefficient for a single particle.

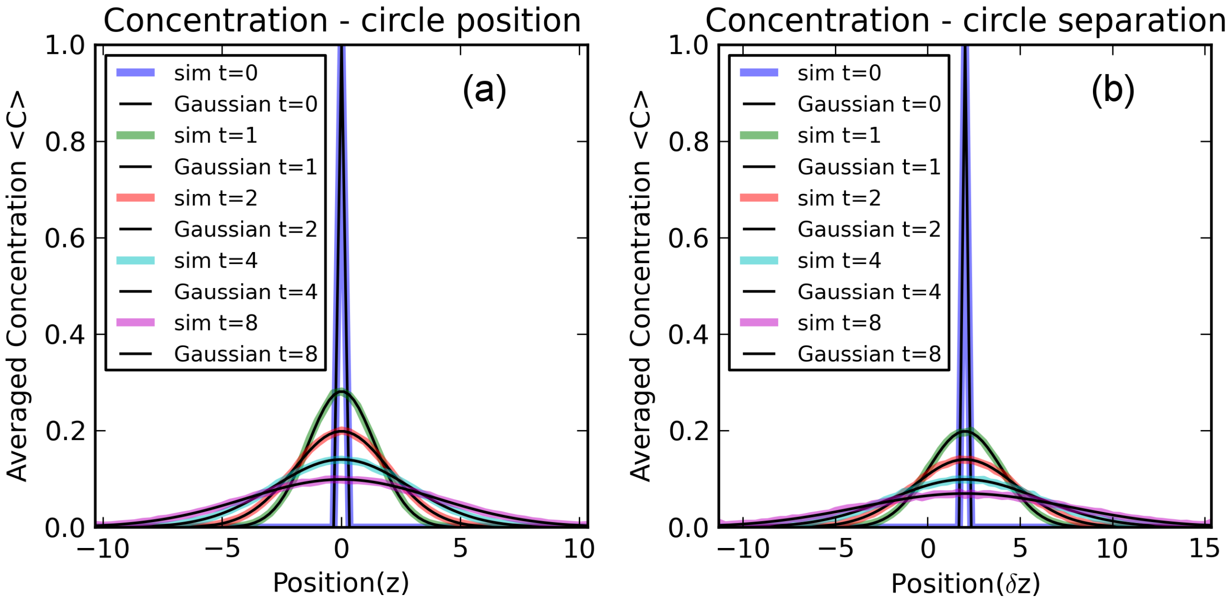

Figure 11: Concentration evolution over time for (a) a circle and (b) a sphere.

Appendix B: Initial Separation

The initial spacing between the particles affects the final passing probability. The expected passing value can be given by:

$$p_{pass}(z_0) = \frac{z_0}{L_{eff} + 3z_0} \tag{14}$$

where L_{eff} is the effective diffusion length for two particles starting in contact to pass by each other. This length will depend on the pore gap and is assumed to be independent of the initial separation. A larger gap will lead to a lower L_{eff} value which represents a lower difficulty in passing. In the limit of large z_0,this goes to 1/3. For the case of unhindered passing (either from an infinitely wide pore or particles that can pass through each other), $L_{eff}=0$, giving a passing rate of 1/3 for all values of z_0. Finally, for the case of no passing, $L_{eff}=\infty$ yielding $P_{pass}=0$.

L_{eff} can be calculated from the case where particles start in contact, $z_0=d$:

$$L_{eff} = d\,\frac{1-p_{pass}(d)}{p_{pass}(d)} \tag{15}$$

The passing value for any initial separation can then be determined from the value for the case where the particles start in contact using the formula:

$$p_{pass}(z_0) = \frac{z_0}{\dfrac{d}{p_{pass}(d)} + 3(z_0 - d)} \tag{16}$$

This dependence on the initial spacing can also be derived using Markov chains with adsorbing states. Consider the general case as shown in figure 12 . The blue particle at 0 is treated as stationary with the red moving. Site D is the initial position, site A is the point at which the particles have passed, and sites B and C are where the red and blue particles are in contact. Finally, site E is the point at which they are considered to have separated. The location of each site along the pore axis is shown below the position with d as the particle's diameter and z_0 as the initial spacing.

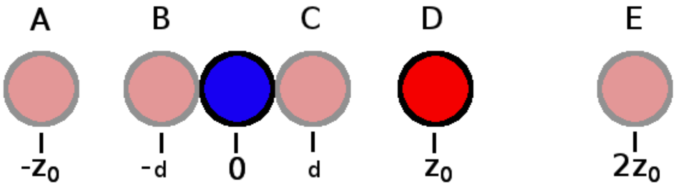

Figure 12: Schematic of initial setup and ending positions.

The probability to go from any site i to site j is given by p_{ij}. Collectively, these are the elements of the transition matrix **P**. The elements in each row must sum to one. As sites A and E are adsorbing states, $p_{AA}=p_{EE}=1$, $p_{AB}=P_{ED}=0$. Non-adjacent sites have zero transition probability. The full matrix is (with the letters labeling the rows and columns for clarity):

$$\boldsymbol{P} = \begin{array}{c} \\ A \\ B \\ C \\ D \\ E \end{array} \begin{array}{c} \begin{array}{ccccc} A & B & C & D & E \end{array} \\ \begin{pmatrix} 1 & 0 & 0 & 0 & 0 \\ p_{BA} & 0 & p_{BC} & 0 & 0 \\ 0 & p_{CB} & 0 & p_{CD} & 0 \\ 0 & 0 & p_{DC} & 0 & p_{DE} \\ 0 & 0 & 0 & 0 & 1 \end{pmatrix} \end{array} \tag{17}$$

For any starting condition, **S**, the configuration, $\mathbf{u}^n$, after n transitions is given by:

$$\boldsymbol{u}^{n}=\boldsymbol{S}\,\boldsymbol{P}^{(n)} \tag{18}$$

The ending distribution after an infinite number of transition steps will have the initial distribution split between the two absorbing states: A and E. To find these values, the matrix P is rearranged to the canonical form (with row and column labels retained to show the changes):

$$\boldsymbol{P}=\begin{array}{cccccc} & D & B & C & A & E \\ D & 0 & 0 & p_{DC} & 0 & p_{DE} \\ B & 0 & 0 & p_{BC} & p_{BA} & 0 \\ C & p_{CD} & p_{CB} & 0 & 0 & 0 \\ A & 0 & 0 & 0 & 1 & 0 \\ E & 0 & 0 & 0 & 0 & 1 \end{array}=\begin{pmatrix} \begin{pmatrix} 0 & 0 & p_{DC} \\ 0 & 0 & p_{BC} \\ p_{CD} & p_{CB} & 0 \end{pmatrix} & \begin{pmatrix} 0 & p_{DE} \\ p_{BA} & 0 \\ 0 & 0 \end{pmatrix} \\ \begin{pmatrix} 0 & 0 & 0 \\ 0 & 0 & 0 \end{pmatrix} & \begin{pmatrix} 1 & 0 \\ 0 & 1 \end{pmatrix} \end{pmatrix}=\begin{pmatrix} \boldsymbol{Q} & \boldsymbol{R} \\ \boldsymbol{0} & \boldsymbol{I} \end{pmatrix} \tag{19}$$

The fundamental matrix N is given by:

$$\boldsymbol{N}=(\boldsymbol{I}-\boldsymbol{Q})^{-1} \tag{20}$$

The probability of a particle ending in state j after starting in state i is given by b_{ij}, defined from:

$$\boldsymbol{B}=\boldsymbol{N}\,\boldsymbol{R} \tag{21}$$

As all particles start at site D and end at either site A or E, only b_{DA} (pass) and b_{DE} (no pass) are relevant:

$$\begin{aligned} b_{DA}&=p_{pass}=\sum_{k} n_{Dk}\,r_{kA}=n_{12}\,p_{BA}=\frac{p_{BA}\,p_{CB}\,p_{DC}}{1-p_{CB}\,p_{BC}-p_{CD}\,p_{DC}} \\ b_{DE}&=p_{nopass}=\sum_{k} n_{Dk}\,r_{kE}=n_{12}\,p_{DE}=\frac{p_{DE}(1-p_{CD}\,p_{BC})}{1-p_{CB}\,p_{BC}-p_{CD}\,p_{DC}} \end{aligned} \tag{22}$$

Recalling that the sum of each row in **P** is one and noting that, by symmetry, $p_{CB}=p_{BC}$ and $p_{CD}=p_{BA}$ gives the simplified expressions:

$$p_{pass}(z_0)=\frac{p_{CB}\,p_{DC}}{1+p_{CB}-p_{DC}}$$
$$p_{nopass}(z_0)=\frac{(1-p_{DC})(1+p_{CB})}{1+p_{CB}-p_{DC}} \tag{23}$$

The problem is now reduced to finding the values of p_{CB} and p_{DC}. The latter is determined from the ratio of the distance between sites D and E to the distance between sites C and E:

$$p_{DC}(z_0)=\frac{z_0}{2z_0-d} \tag{24}$$

The value of p_{CB} can be approximated as:

$$p_{CB}(z_0)=\frac{z_0-d}{L_{eff}+z_0+d} \tag{25}$$

where L_{eff} is the effective diffusion length to pass over the other atom. This length will depend on the ratio of pore radius to particle radius and is assumed to be independent of the initial separation. A greater ratio will lead to a lower L_{eff} value which represents a lower difficulty in passing. Using the definitions from equations (24) and (25), recovers the passing rate given in equation (14).

References

1) Liu, D.-J.; Wang, J.; Ackerman, D. M.; Slowing, I. I.; Pruski, M.; Chen, H.-T.; Lin, V. S.-Y.; Evans, J. W. ACS Catalysis **2011**, 1, 751-763.

2) Wang, J.; Ackerman, D. M.; Kandel, K.; Slowing, I. I.; Pruski, M.; Evans, J. W. Mater. Res. Soc. Symp. Proc. **2012**, 1423.

3) Ackerman, D. M.; Wang J.; Evans, J. W. Physical Review Letters **2012**, 108, 228301.

4) Nedea, S.V.; Jansen, A.P.J.; Lukkien, J.J.; Hilbers, P.A.J.; Phys. Rev. E **2002**, 65, 066701.

5) Nedea, S.V.; Jansen, A.P.J.; Lukkien, J.J.; Hilbers, P.A.J.; Phys. Rev. E **2002**, 66, 066705.

6) Coffery, W. T.; Kalmykov, Yu. P.; Waldron, J. T., *The Langevin Equation* (World

Scientific, Singapore, 2004).

7) Snook, I, T*he Langevin and Generalized Langevin Approach to the Dynamics of Atomic, Polymeric, and Colloidal Systems.* (Elsevier, Amsterdam, 2007)

8) Thornton, J. B.; Thornton, S. T., *Classical Dynamics of Particles and Systems* (Harcount, Orlando, 1995).

CHAPTER 9. LANGEVIN PASSING DYNAMICS OF ASYMMETRIC PARTICLES

1 Introduction

The preceding chapter presented a Langevin dynamics[1,2,3] method of calculating passing probabilities of over-damped molecules within a confined pore. The molecules considered in that treatment were limited in shape to circles and spheres. While valuable information on the general behavior can be determined from these cases, the actual molecules in a pore are usually not spheres. This chapter expands the previous treatment to include non-spherical molecules with the associated complications introduced by the addition of rotations that arise in the motion of these molecules. The approach is general enough to apply to molecules (referred to below as particles) of arbitrary shape.

2 Simulation Description

Except where noted below, the details of the simulation follow those given for the circle and sphere case. The description of the simulation is given in the previous chapter.

2.A. Particle description

Each particle in the system is described by a collection of one or more component spheres joined together to form the desired shape. The spheres represent atoms or collections of atoms in a molecule and together provide an accurate description of the molecule's shape. The particles are rigid and have no internal degrees of freedom, so the relative positions of each component are fixed. This constraint limits the method to cases where the internal motion of the molecules can be neglected. Generalizing beyond this constraint would require internal relaxation during motion. Methods of performing this type of relaxation exist [5,6] but are beyond the scope of this work.

Each of the spheres in the particle has a center position $\mathbf{x}_j$, radius R_j, and mass m_j. From this collection of N spheres, the center of mass position about which rotations are performed, $\mathbf{x}_{com}$, is easily determined:

$$\boldsymbol{x}_{com} = \frac{\sum_j^N \boldsymbol{x}_j m_j}{\sum_j^N m_j} \tag{1}$$

We consider a bounding sphere, centered on the center of mass for the particle, the radius, R_{mol}, of which is determined by the distance of the furthest point in the molecule from the center of mass. This gives the smallest sphere centered on the center of mass of the particle which incorporates the particle. Note that in general, smaller bounding spheres may exist which are not centered on the center of mass. However, this is not the case for the examples considered here.

As in the previous chapter, the pore is an infinite, smooth cylinder of radius R_p, aligned along the z axis, with the origin in the center of the pore (the pore surface is defined by $x^2+y^2 = R_p$ for all z). Since pore length is treated as infinite, there is no possibility of molecules exiting the pore.

2.B. Equations of motion

The system's evolution is described by Langevin equations of motion governing all the system's degrees of freedom. In the most general case, each molecule has six degrees of freedom – three rotational angles (θ_1, θ_2, θ_3) and three translational coordinates r_i for i=(x,y,z). Incremental motion is determined in the body frame of the particle (defined by unit vectors $\mathbf{r_1}$, $\mathbf{r_2}$, and $\mathbf{r_3}$). Furthermore, we will consider only molecular shapes where the friction tensor describing dissipative interaction with the surrounding fluid reduces to a diagonal form in the body frame (thus determined by at most three scalar values for translation and three for rotation). Once determined in the particle's body frame, motions are then converted to the system frame and applied to increment the particle's position in that frame.

At each point in time, the rate off change of the three translational coordinates in the body frame is determined by the over-damped Langevin equations:

$$m\zeta_i \dot{r}_i(t) + \frac{\partial}{\partial r_i} V(r_i, t) = F_i(t) \tag{2}$$

where m is the molecule's mass, ζ_{ri} is the frictional damping coefficient from the surrounding fluid for motion in the $\mathbf{r_i}$ direction (particle frame), V is an external potential (which here is set to zero), and $F_i(t)$ is a Gaussian random force in the $\mathbf{r}_i$ direction (particle frame) with the properties:

$$\begin{gathered}\langle F_i(t)\rangle=0\\ \langle F_i(t)F_i(t')\rangle=2kTm\zeta_i\delta(t-t')\end{gathered} \quad (3)$$

We emphasize that these equations are only applied to determine incremental motion, choosing at each point in time the current body frame of the particle in order to simplify the description of friction. They do not apply globally in a moving body frame.

The evolution of the translational coordinates is given by:

$$r_i(t+\Delta t)=r_i(t)+\dot{r}_i\Delta t \quad (4)$$

At each point in time, the rate of rotation in the body frame is described by the Langevin equations for the angular velocities for this frame, in an over-damped system with no external potential. These are given by [3] (see Appendix A):

$$\begin{gathered}(I_3-I_2)\dot{\theta}_2(t)\dot{\theta}_3(t)+\zeta_{r1}\dot{\theta}_1(t)=\lambda_1(t)\\ (I_1-I_3)\dot{\theta}_1(t)\dot{\theta}_3(t)+\zeta_{r2}\dot{\theta}_2(t)=\lambda_2(t)\\ (I_2-I_1)\dot{\theta}_1(t)\dot{\theta}_2(t)+\zeta_{r3}\dot{\theta}_3(t)=\lambda_3(t)\end{gathered} \quad (5)$$

where I_i is the moment of inertia, ζ_{ri} is the rotational drag, λ_i is a random Gaussian torque term, and the subscript 'i' indicates the axis of rotation. The random torque has the properties:

$$\begin{gathered}\langle \lambda_i(t)\rangle=0\\ \langle \lambda_i(t)\lambda_j(t')\rangle=2kT\zeta_{rij}\delta_{ij}\delta(t-t')\end{gathered} \quad (6)$$

These equations are solved for $\dot{\theta}_i$ which, unlike the translational terms, is, in general, a complicated expression coupling parameters for different rotations. Appendix A gives the formulas for the general case of an arbitrary shape as well as the formulas for a dimer. The values are used to increment the rotational angles of the particle during each configuration change:

$$\theta_i(t+\Delta t)=\theta_i(t)+\dot{\theta}_i\Delta t \quad (7)$$

After each rotation, the vectors defining the frame are updated to the current configuration.

2.C. Configuration changes

As the particle positions evolve, they are restricted to not overlap with each other or with the pore walls. Each trial move is accepted if it results in a configuration where:

- particles A and B do not intersect,
- particle A is entirely within the pore, and
- particle B is entirely within the pore

If any of the above conditions are not true, the trial move is rejected and the system is restored to the previous condition. This acceptance criteria is written as:

$$Acc = Acc_{\text{int}} \wedge Acc_{\text{pore}}^{A} \wedge Acc_{\text{pore}}^{B} \tag{8}$$

where Acc is the overall acceptance function for the trial configuration change (having a value of either true or false), Acc_{int} is the acceptance function for whether the particles do not intersect, and Acc_{pore} is the acceptance function for whether the particles are contained within the pore.

The intersection component is given by:

$$Acc_{\text{int}} = \neg\left(\bigvee_{i,j} I(i,j)\right) \tag{9}$$

where $\vee$ denotes a logical disjunction (yielding true if *any* of the components are true) over all pairs of components i, j formed by taking one component from each particle. I(i, j) is the intersection function for any two components:

$$I(i,j) = \begin{cases} True, \text{if volume of i and j intersect} \\ False, \text{otherwise} \end{cases} \tag{10}$$

The criteria for particle i being within the pore is given by:

$$Acc_{\text{pore}}^{i} = \bigwedge_{j=1}^{n} C_{\text{pore}}(j) \tag{11}$$

where $\wedge$ denotes a logical conjunction over all components of molecule i (yielding true if *all* of the components are true) and $C_{\text{pore}}(j)$ specifies whether component j of the particle is contained within the pore:

$$C_{\text{pore}}(j)=\begin{cases} True\text{, if j is entirely within pore} \\ False\text{, otherwise} \end{cases} \tag{12}$$

Equations (9) - (12) hold for the general case of a particle composed of any type of sub-particles. For the specific case of spherical sub-particles which is considered in this work, equation (10) becomes:

$$I(i,j)=\begin{cases} True\text{, if } \|\mathbf{x}_i-\mathbf{x}_j\|<(R_i+R_j) \\ False\text{, otherwise} \end{cases} \tag{13}$$

and equation (12) becomes:

$$C_{pore}(j)=\begin{cases} True\text{, if } (R_j+\|\mathbf{x}_j\|)\leq R_p \\ False\text{, otherwise} \end{cases} \tag{14}$$

For computational efficiency, the bounding spheres of both particles can be used to exclude cases where the particles are clearly not overlapping each other or the pore. If the condition (R_{mol} + $(x_{com}^2 + y_{com}^2)^{1/2}$) <= R_P holds, all parts of the particle must be within the pore and there is no need to check individual components using equation (11). If it doesn't hold, each component in the particle must be tested individually. Similarly, to check if two particles intersect, the center of mass separation is calculated. If the distance is greater than or equal the sum of the radii of the bounding spheres ($\|\mathbf{x}^A_{com} - \mathbf{x}^B_{com}\| >= R^A_{mol} + R^B_{mol}$), the particles do not overlap. If the distance is less, they may overlap and the separation distance must be calculated for each pair of spheres from different particles using equation (9). These screening tests for overlap can significantly speed up configuration changes for particles with many components.

3 Initial and Final Conditions

In the previous chapter, spheres and circles were started in an “adjacent” configuration where the maximum z value for the left particle equals the minimum z value for the right one. That separation distance, z_0, is equal to their diameter and the simulation is continued until the particles have either moved apart to a separation of $2z_0$ (for no passing) or $-z_0$ (for passing). This choice is desirable because it naturally models the setup in the kinetic Monte Carlo simulations of pores. For particles of arbitrary shape, the initial condition involves choosing an orientation as well as position. In this case, the orientation is chosen at random. This choice leads to a couple options for the initial separation. It is again possible to put them “adjacent” as an initial condition. However, for particles without spherical symmetry, this “adjacent” separation depends on the orientation. Choosing this option requires selecting the initial orientation and then calculating the separation at which particles are adjacent. The particles would then be moved to that separation prior to starting the simulation. While that can be done with little difficulty, this variable initial separation does not match the conceptual model of the pore sites used in the previous KMC studies of particles in pores. It also requires deciding how to handle the ending conditions. Either the ending separations vary with the initial separation or they remain fixed and the distance from the initial position to the ending separations will vary across different simulations.

An alternate approach for the initial separation, and the one used in this work, is to place the particles at a fixed value equal to the sum of the bounding radii of the particles ($z_0 = R^A_{mol} + R^B_{mol}$). This is the smallest distance that guarantees that the randomly oriented particles will not overlap in the initial configuration. Aside from the simplicity of avoiding calculating a different initial condition every simulation, this choice is the conceptual analogue of the choice made for circles and spheres. With this fixed choice of z_0, the ending condition separations are $-z_0$ and $2z_0$ as before.

Given the initial separation z_0, the initial particle positions are selected by choosing orthogonal x,y coordinates inside the pore and random values for θ_1, θ_2, θ_3. The resulting configuration is tested for overlap with the pore wall. Unlike when selecting a separation between particles, the radius of the bounding box is not chosen as the minimum distance between the pore wall and the particle's center of mass. Instead, the intersection is calculated using equation (11).

3.A. Translation and Rotation

In order to perform translations and rotations, the particle's orientation must be tracked. This is done by recording the vectors defining the reference frame of the particle. As rotations are performed, these vectors are rotated as well which increments the body fixed reference frame during the simulation. While the particles change orientation with respect to the frame of the system, they retain the same orientation in their body frame. This removes the need to adjust the friction based on the orientation and converts general off-diagonal friction tensors into diagonal tensors described by a few scalars in our application. All translations occur along the vectors in the molecule's frame and are then projected onto the system's frame.

The axes in the system's frame will be defined as the xyz frame (with axes x,y,z). The particle's frame is the XYZ frame (with axes X, Y, Z). The projections of the X axis into the xyz frame are X_x, X_y, X_z. The other axes have corresponding values.

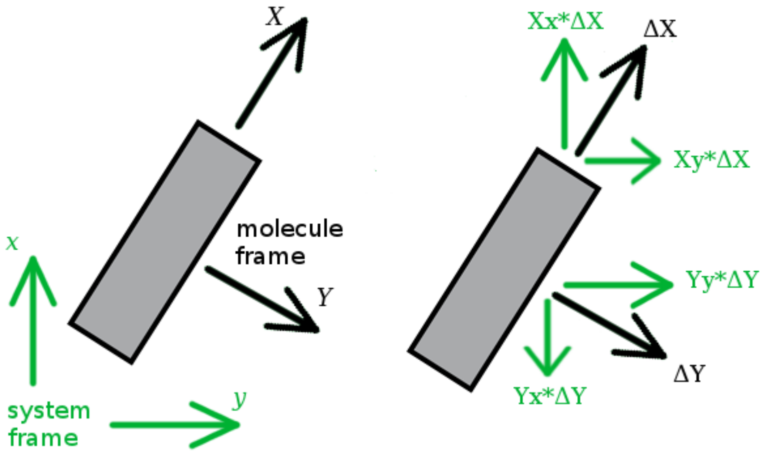

Figure 1: Relation between translation in the system frame and the body frame of the the particle.

All of the Langevin equations govern motion within the XYZ frame. As the friction and force is location independent, translations can be calculated in the XYZ frame and projected into the system frame without the need to keep track of position in both frames.

For a set of translations ΔX, ΔY, ΔZ in the particle's frame, the equivalent translations in the xyz frame are given by:

$$\begin{aligned}\Delta x &= \Delta X * X_x + \Delta Y * Y_x + \Delta Z * Z_x\\ \Delta y &= \Delta X * X_y + \Delta Y * Y_y + \Delta Z * Z_y\\ \Delta z &= \Delta X * X_z + \Delta Y * Y_z + \Delta Z * Z_z\end{aligned} \quad (15)$$

Once these conversions have been made, they are applied to all components of the particles.

Rotation is done using quaternions (see Appendix B). Rotations around each of the three axes are formed into a quaternion. These are multiplied to form the final rotation. This value is converted into a rotation matrix and applied to all the components of the particle. As noted above, the quaternion is also applied to the basis vectors defining the particle's reference frame.

3.B. Frictional terms

The friction coefficients impacting motion can be calculated (or at least estimated) based on the size and shape of the particles (and the properties of the surrounding fluid). For a single sphere, Stoke's law gives a translation friction term of:

$$\zeta_t^1 = 6\pi\eta R \tag{16}$$

where η is the viscosity of the surrounding fluid, R is the sphere radius, and the superscript denotes the single sphere value. The rotational friction term for a single sphere is:

$$\zeta_r^1 = 8\pi\eta R^3 \tag{17}$$

The particles in this study are composed of spherical sub-units. The relevant frictional coefficients for the overall particle can be calculated (or at least estimated) from the structure of the particle and the above results. The method is covered in detail in references [9,10,12].

In general, the scalar friction coefficients will not be the same for different translations and rotations. For motion in the particle frame, there will be at most three distinct translational frictions and three distinct rotational frictions which leads to at most six different coefficients. Particles with higher symmetry may have less than six distinct values. For example, the dimer particle studied here has only two distinct translational frictions and two rotational frictions (see figure 2). For the translation along the dimer axis, the friction is taken to be $\zeta_{t\parallel} = \zeta_t^1$. For translation perpendicular to the dimer axis, the friction is $\zeta_{t\perp} = 2\zeta_t^1$. For the rotation frictions, the dimer results presented in [9, 11] are used. These give a rotational friction along the dimer axis of $\zeta_{r\parallel} = 1.78\zeta_r^1$ and a perpendicular value of $\zeta_{r\perp} = 3.76\zeta_r^1$.

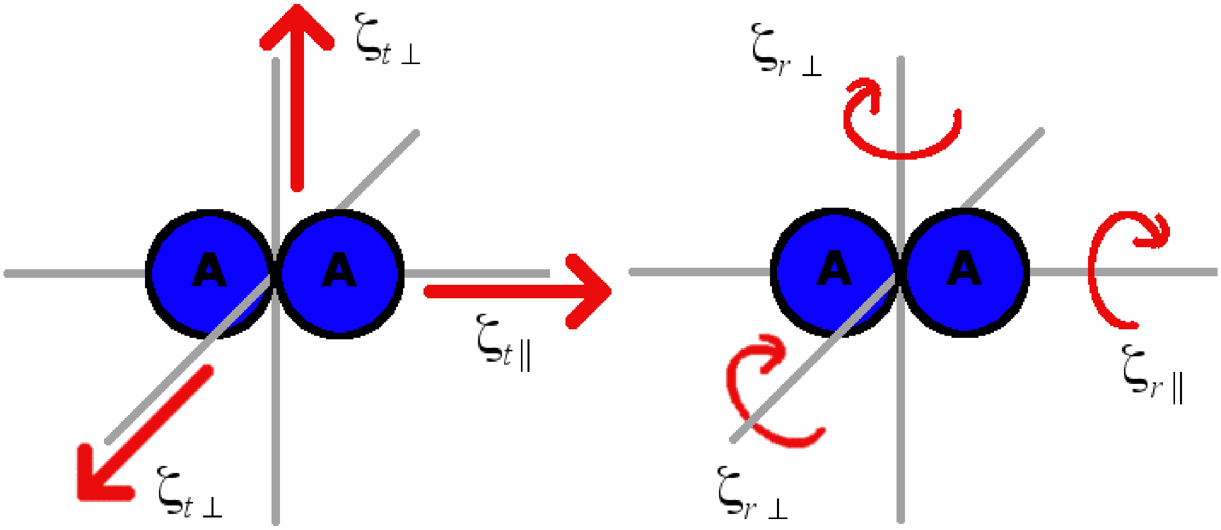

Figure 2: Translation and rotation directions and corresponding friction coefficients for a dimer. The axes are in the frame of the particle.

4 Results: Dimer and Sphere

The case studied was a dimer (composed of two spheres) and a sphere in a pore which adds the rotational effects while maintaining some similarities with the previous case of two spheres. The sphere was chosen to have a radius R, and the dimer is composed of two spheres, each with radius R, in contact with each other (see figure 3). The initial separation is 3R. The separation criteria for passing and non-passing are -3R and 6R, respectively. The pore gap is defined as the diameter of the pore minus twice the the sphere diameter, or 4R. The gap is then $2(R_p – 2R)$.. A gap of zero will be just enough space for the particles to pass but only if the dimer is perfectly aligned with the pore. Any other orientation will not allow passing at that gap size. A gap between 0 and 2R will always require some degree of orientational alignment of the dimer in order for the particles to pass. A gap greater than 2R is wide enough to allow the dimer to pass even when oriented perpendicular to the pore.

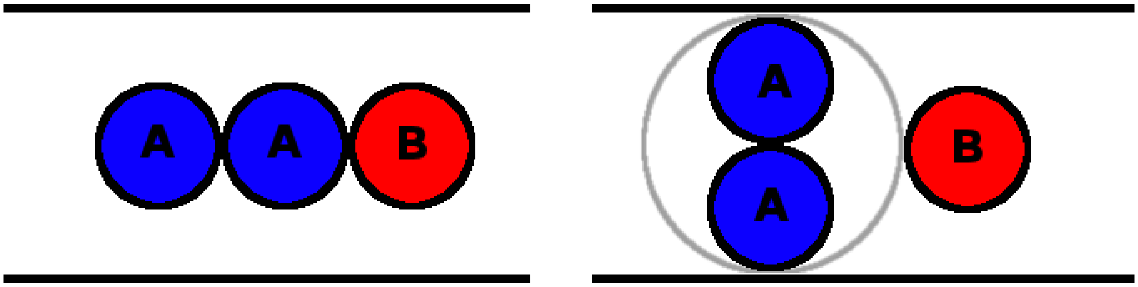

Figure 3: Two examples of the initial configuration. On the left is the dimer aligned with the pore and the particles in contact. On the right, the dimer is perpendicular to the pore axis. The bounding radius is shown to indicate the separation is the same. In both cases, the pore is just wide enough to allow passing if the dimer aligns with the pore.

The z axis (the $\mathbf{r}_3$ direction about which the θ_3 angle is defined) is is treated as the symmetry axis for the dimer. Translation along that axis is performed with a friction coefficient of 1. For translation along the other two axes, the friction coefficient is set to 2.0. The rotation friction is 2.37 when rotating about the dimer axis and 5.0 in the direction perpendicular to the dimer axis based on values from references [9, 11].

A range of time steps between 0.00001 and 1.0 was used for the simulations to determine an appropriate regime for accurate, converged results. Figure 4 shows the passing behavior for these time steps. As seen in the case of two spheres, an insufficiently small time step leads to underestimation of the passing probability. In general, the values monotonically converge to the correct value with decreasing time step. The exception are the values for Δt=1.0. Unlike the system with two spheres, they are close to the correct values. In fact, the data is “better” than data for some of the smaller time steps over most gap sizes. However, these values are erroneous which is evident from the data at very small gaps and very large gaps (not pictured). The data for the dimer-sphere case is noisier than for the sphere-sphere case, but the plot indicates that data from a time step of 0.0001 gives acceptable results. This value agrees with the value found for spheres.

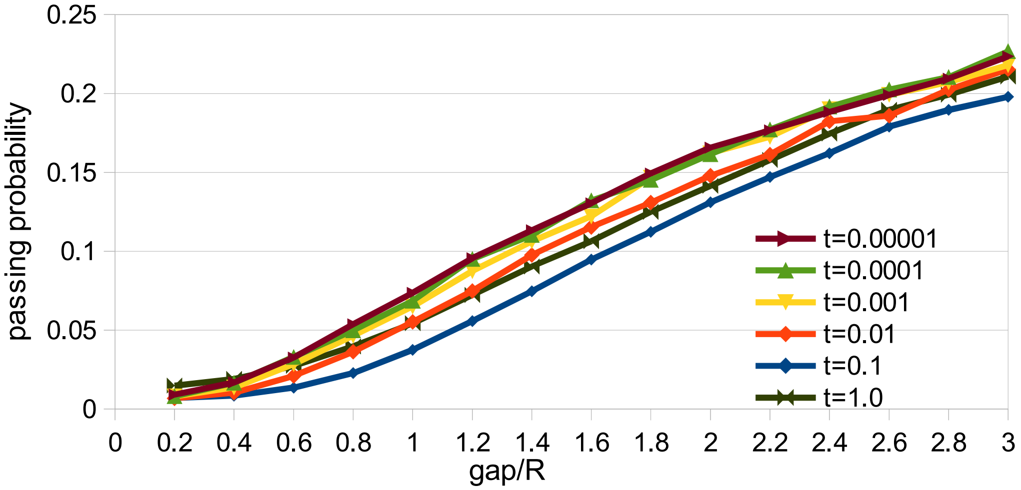

Figure 4: Dimer-sphere passing probability as a function of gap for several time steps

The data for the dimer-sphere case is similar to that from the sphere-sphere case. Comparison is shown in figure 5. For large gaps, the curves converge to the correct limiting passing value and do so at approximately the same rate. For smaller gaps, the sphere-dimer case consistently has a lower passing rate, but the curves are similar in shape. The lower passing rate is attributed to the requirement for alignment of the dimer with the pore axis.

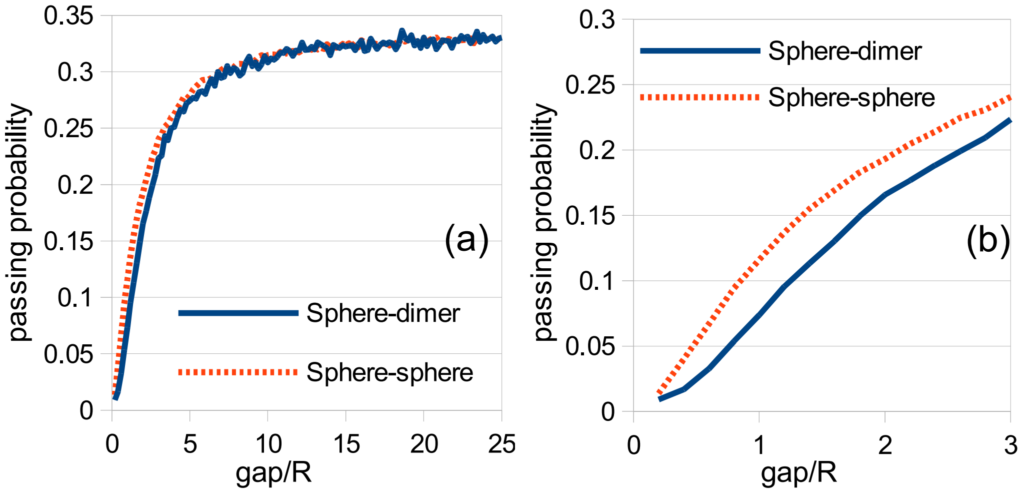

Figure 5: Comparison of passing rates for two spheres to rates for a dimer and a sphere: (a) shows behavior over the full range of the gaps studied and (b) shows the behavior for smaller gap sizes.

5 Conclusion

The method presented here extends the previous approach for passing of pairs of circles and pairs of spheres. Significant additional complication comes from the rotational motion which must be tracked when the spherical symmetry is broken. The method here can be used for particles of arbitrary shape. The general method can be simplified substantially by exploiting symmetry in a specific particle. An example of this process for dimers is presented in Appendix A.

The passing rates for a dimer and sphere were calculated using this method. The time required for the simulation runs increases substantially over the systems with only translational motion. This makes it difficult to get good statistics for the results. Qualitatively, the behavior for a dimer and a sphere shows little difference from the previous case with spheres. The passing rates are lower for all but the largest gap sizes due to the requirement for alignment of the dimer. However, the general behavior of the passing probabilities for different gap sizes is similar to the results for two spheres.

Appendix A: Rotational Langevin Equations

General case

The Newton-Euler [3,4] equation for torque, **τ**, (with the origin at the center of mass) is:

$$\tau = \hat{I}\dot{\boldsymbol{\omega}}(t) + \boldsymbol{\omega}(t) \times \hat{I}\boldsymbol{\omega}(t) \quad , \tag{18}$$

Where $\hat{I}$ is the inertia tensor, and **ω**(t) is the angular velocity (d$\boldsymbol{\theta}$/dt). The inertia tensor, and its components, are:

$$\hat{I} = \begin{bmatrix} I_{11} & I_{12} & I_{13} \\ I_{21} & I_{22} & I_{23} \\ I_{31} & I_{32} & I_{33} \end{bmatrix} \tag{19}$$

$$
\begin{aligned}
I_1 &= I_{11} = \sum_{i=1}^{N} m_i\left(y_i^2+z_i^2\right)\\
I_{12} &= I_{21} = -\sum_{i=1}^{N} m_i\left(x_i y_i\right)\\
I_{13} &= I_{31} = -\sum_{i=1}^{N} m_i\left(x_i z_i\right)\\
I_2 &= I_{22} = \sum_{i=1}^{N} m_i\left(x_i^2+z_i^2\right)\\
I_{23} &= I_{32} = -\sum_{i=1}^{N} m_i\left(y_i z_i\right)\\
I_3 &= I_{33} = \sum_{i=1}^{N} m_i\left(x_i^2+y_i^2\right)
\end{aligned}
\tag{20}
$$

where the sums are over the N subparticles and x_i, y_i, z_i are the distances from the center of subparticle i to the point of rotation.

The Langevin version of equation (18) with no external potential is given by:

$$
\hat{I}\dot{\boldsymbol{\omega}}(t)+\boldsymbol{\omega}(t)\times\hat{I}\,\boldsymbol{\omega}(t)+\hat{\zeta}_r\boldsymbol{\omega}(t)=\boldsymbol{\lambda}(t) \quad , \tag{21}
$$

with $\hat{\zeta}_r$ as the rotational friction drag tensor and $\boldsymbol{\lambda}(t)$ as the random torque vector whose components obey the distribution:

$$
\begin{gathered}
\left\langle \lambda_i(t)\right\rangle = 0\\
\left\langle \lambda_i(t)\lambda_j(t')\right\rangle = 2kT\zeta_{rij}\delta(t-t')
\end{gathered}
\tag{22}
$$

The scalar versions of equation (21) are (with the time dependence implicit):

$$
\begin{gathered}
I_{11}\dot{\omega}_1+I_{12}\dot{\omega}_2+I_{13}\dot{\omega}_3+I_{13}\omega_1\omega_2-I_{12}\omega_1\omega_3+\left(I_{33}-I_{22}\right)\omega_2\omega_3+\\
I_{23}\left(\omega_2^2-\omega_3^2\right)+\zeta_{r11}\omega_1+\zeta_{r12}\omega_2+\zeta_{r13}\omega_3=\lambda_1\\
I_{21}\dot{\omega}_1+I_{22}\dot{\omega}_2+I_{23}\dot{\omega}_3-\omega_1\left(I_{13}\omega_1+I_{23}\omega_2\right)+\left(I_{11}\omega_1-I_{33}\omega_1+I_{13}\omega_2\right)\omega_3+\\
I_{13}\omega_3^2+\zeta_{r21}\omega_1+\zeta_{r22}\omega_2+\zeta_{r23}\omega_3=\lambda_2\\
I_{31}\dot{\omega}_1+I_{32}\dot{\omega}_2+I_{33}\dot{\omega}_3+\left(I_{22}-I_{11}\right)\omega_1\omega_2+I_{12}\left(\omega_1^2-\omega_2^2\right)+\\
I_{23}\omega_1\omega_3-I_{13}\omega_2\omega_3+\zeta_{r31}\omega_1+\zeta_{r32}\omega_2+\zeta_{r33}\omega_3=\lambda_3
\end{gathered}
\tag{23}
$$

These equations are non-linear and complicated by the off diagonal terms in the inertia and friction tensors. To simplify these, we first introduce the frame of the particle where the inertia tensor becomes diagonal. The principle axes are the eigenvectors of equation (19). The principal moments of inertia are the eigenvalues of equation (19) and the inertia tensor becomes a diagonal matrix I' (and defining $I_i \equiv I_{ii}'$) in the particle's frame.

The principal moments of inertia are found by solving for the eigenvalues:

$$0=\begin{vmatrix} I_{11}-X & I_{12} & I_{13} \\ I_{21} & I_{22}-X & I_{23} \\ I_{31} & I_{32} & I_{33}-X \end{vmatrix} \tag{24}$$

Solving for X gives,

$$\begin{gathered} X^3-(I_{11}+I_{22}+I_{33})X^2+(I_{11}I_{22}+I_{11}I_{33}+I_{22}I_{33}-I_{12}^2-I_{13}^2-I_{23}^2)X \\ +(-I_{11}I_{22}I_{33}+I_{11}I_{23}^2+I_{22}I_{13}^2+I_{33}I_{12}^2+2\mathrm{I}_{12}I_{13}I_{23})=0 \end{gathered} \tag{25}$$

The three roots $X=(I_1, I_2, I_3)$ give the diagonal matrix I'. The principal axes (a_{i1}, a_{i2}, a_{i3}) for i=1,2,3 are found by solving for the eigenvectors:

$$0=\begin{bmatrix} I_{11}-I_i & I_{12} & I_{13} \\ I_{21} & I_{22}-I_i & I_{23} \\ I_{31} & I_{32} & I_{33}-I_i \end{bmatrix}\begin{bmatrix} a_{i1} \\ a_{i2} \\ a_{i3} \end{bmatrix} \tag{26}$$

The directions are then found by normalizing the resulting non-unique values such that $a_{i1}^2 + a_{i2}^2 + a_{i3}^2 = 1$.

We evolve the molecules by performing incremental rotations (and translations) in the frame of the particle assuming that the friction tensor is diagonal ($\zeta_{ri} = \zeta_{rii}$) in this frame. In addition, we consider just the over-damped limit and determine instantaneous angular velocities (which are used to increment orientation) via:

$$\begin{gathered} (I_3-I_2)\omega_2(t)\omega_3(t)+\zeta_{r1}\omega_1(t)=\lambda_1(t) \\ (I_1-I_3)\omega_1(t)\omega_3(t)+\zeta_{r2}\omega_2(t)=\lambda_2(t) \\ (I_2-I_1)\omega_1(t)\omega_2(t)+\zeta_{r3}\omega_3(t)=\lambda_3(t) \end{gathered} \tag{27}$$

This set of equations are coupled. However, symmetry or restricted rotation can decouple them for some systems. In the general case, simultaneous solution of these equations must be done numerically. Solving these equations for the rotations is done using the algorithm and code of Skowron & Gould[8].

Dimers

The symmetry of a dimer (figure 2) reduces the complexity of the general rotational equations. Rotation about the z axis (the ω_3 rotation**)** does nothing to change the particle position or alignment. This causes many of the moments of inertia to become zero. Again working in the frame of the particle, the moments are:

$$\begin{gathered} I_1 \equiv I_{11} = 2 m_i R_i^2 \\ I_2 \equiv I_{22} = 2 m_i R_i^2 \\ I_3 \equiv I_{33} = 0 \\ I_{12} = I_{21} = I_{13} = I_{31} = I_{23} = I_{32} = 0 \end{gathered} \tag{28}$$

and the rotational Langevin equations become:

$$\begin{gathered} -I_2 \omega_2(t) \omega_3(t) + \zeta_{r1} \omega_1(t) = \lambda_1(t) \\ I_1 \omega_1(t) \omega_3(t) + \zeta_{r2} \omega_2(t) = \lambda_2(t) \\ \zeta_{r3} \omega_3(t) = \lambda_3(t) \end{gathered} \tag{29}$$

which can be solved analytically (with time dependence implicit):

$$\begin{gathered} \omega_3 = \frac{\lambda_3}{\zeta_{r3}} \\ \omega_1 = \frac{\lambda_1 + \frac{I_2 \lambda_2 \omega_3}{\zeta_2}}{\zeta_1 + \frac{I_1 I_2 \omega_3^2}{\zeta_2}} \\ \omega_2 = \frac{\lambda_2 - I_1 \omega_1 \omega_3}{\zeta_2} \end{gathered} \tag{30}$$

With the generated random torques and the known values of inertia and friction, the angular velocities can be calculated and used to update the rotation angles at each step.

Appendix B: Quaternions

Quaternions [7] provide an alternative method for tracking rotations. The advantage over other methods is greater numeric stability and avoidance of singularities in Euler angles. A quaternion consists of two components, a three dimensional vector (**v**=**i**x+**j**y+**k**z) and a scalar term (w). The real components are tracked as q = [**v**,w]=[(x,y,z),w]. All quaternions used here are normalized: $x^2+y^2+z^2+w^2 = 1$.

Multiplication of two quaternions, q_1 and q_2 is given by

$$q_1 q_2 = [\boldsymbol{v_1} \times \boldsymbol{v_2} + w_1 \boldsymbol{v_2} + w_2 \boldsymbol{v_1}, w_1 w_2 - \boldsymbol{v_1} \cdot \boldsymbol{v_2}] \tag{31}$$

Note that in general $q_1 q_2 \neq q_2 q_1$.

The conjugate of a quaternion (q^{-1}) is simply:

$$q^{-1} = [-\boldsymbol{v}, w] \tag{32}$$

Applying a rotation to a vector **r** is done by treating the vector as a quaternion with zero real part:

$$\begin{pmatrix} \boldsymbol{r}' \\ 0 \end{pmatrix} = q \begin{pmatrix} \boldsymbol{r} \\ 0 \end{pmatrix} q^{-1} \tag{33}$$

A rotation by an angle, α, about an axis defined by the unit vector, **u**, is given by the quaternion:

$$q = \left[\boldsymbol{u} \sin\left(\frac{\alpha}{2}\right), \cos\left(\frac{\alpha}{2}\right) \right] \tag{34}$$

Two rotations (given by quaternions q_1, q_2) can be combined into a third rotation (q_3, which is rotation 1 followed by rotation 2) by multiplying the quaternions:

$$q_3 = q_1 q_2 \tag{35}$$

The quaternion rotation can be written as a rotation matrix and applying it to a vector **r** by treating the vector as a quaternion:

$$M=\begin{bmatrix} w^2+x^2-y^2-z^2 & 2xy-2wz & 2xz+2wy & 0 \\ 2xy+2wz & w^2-x^2+y^2-z^2 & 2yz+2wx & 0 \\ 2xz-2wy & 2yz-2wx & w^2-x^2-y^2+z^2 & 0 \\ 0 & 0 & 0 & 1 \end{bmatrix} \tag{36}$$

$$\begin{pmatrix} \boldsymbol{r}' \\ 0 \end{pmatrix} = M \begin{pmatrix} \boldsymbol{r} \\ 0 \end{pmatrix}$$

References

1) Coffery, W. T.; Kalmykov, Yu. P.; Waldron, J. T., *The Langevin Equation* (World Scientific, Singapore, 2004).

2) Snook, I, *The Langevin and Generalized Langevin Approach to the Dynamics of Atomic, Polymeric, and Colloidal Systems.* (Elsevier, Amsterdam, 2007).

3) McConnell, J. *Rotational Brownian Motion and Dielectric Theory* (Academic Press, London, 1980).

4) Thornton, J. B.; Thornton, S. T., *Classical Dynamics of Particles and Systems* (Harcount, Orlando, 1995).

5) Hess, B; Bekker H, Berendsen HJC, Fraaije JGEM **1997**, 12, 18.

6) Ryckaert, J-P; Ciccotti G, Berendsen HJC J. Comp. Phys. **1977**, 3, 23.

7) Shoemake, K. “Animating rotation with quaternion curves”. SIGGRAPH Proceedings of the 12th annual conference on Computer graphics and interactive techniques. **1985**, p. 245-254.

8) Skowron, J.; Gould, A. **2012** arXiv:1203.1034 [astro-ph.EP]

9) de la Torre, J. G.; Carrasco, B. Eur Biophys J **1998**, 27, 549.

10) Mellado, P.; Iniesta, A. Diaz, F. G.; de la Torre, J.G. Biopolymer **1988**, 27, 1771.

11) Davis, M.H. Chem Eng Sci **1969**, 24, 1766.

12) de la Torre, G. J. (1989). Hydrodynamic properties of macromolecular assemblies. In: Harding SE, Rowe AJ (eds) *Dynamic properties of macromolecular assemblies.* (pp 3–

31). The Royal Society of Chemistry.

CHAPTER 10. GENERAL CONCLUSION

1 Summary and Conclusions

A reaction-diffusion model was developed for particles in a confined pore. This consists of both a discrete kinetic Monte Carlo (KMC) model and a generalized hydrodynamic model. Results of the model were studied in detailed and show strong improvement over other models such as a mean-field approach. The model is general enough to cover a variety of scenarios. Both single file and restricted passing were considered. These deviations from standard diffusion are a key component in systems with narrow pores. Single file restrictions strongly impact the mobility of particles and the resulting concentration profiles within the pore.

The generalized hydrodynamic approach accurately describes both the transient and steady state regimes. This approach requires the input of tracer diffusion values, in this case derived from KMC simulations. Two methods are presented for calculating these diffusion values. The first uses a random walk based approach, while the second uses Fick's law. Characteristic behavior was the same for both methods. Either approach is suitable for generating values for use in the generalized hydrodynamic method.

The Langevin dynamics simulations discussed provide a link between the structure of a particle and the general passing parameter used in the simulations. The method was extensively tested for circular and spherical particles. The results can be used to find pore sizes that correspond to the passing parameters selected in previous chapters.

This method was further generalized to work with molecules of arbitrary shape. The addition of rotations significantly increases the complexity of the model and the time required for simulation. However, using physically realistic shapes gives more accurate results and is necessary for modeling specific experimental systems. Comparison of a dimer and a sphere to the case of two spheres showed that the general behavior of passing was similar but that the actual values were different.

2 Future Work

A number of options exist for expanding on the methods described. The general nature of the work makes it applicable to a variety of specific systems.

The Langevin dynamics approach to passing is designed to mimic real molecules. Using real molecule shapes and the pore sizes from experiments would allow a direct comparison with physical experiments. A challenge here is to select parameters that match the real system. While the passing rate can be calculated via the Langevin simulations, the microscopic reaction rates are not directly known within the pore. A more accurate model would require an appropriate choice of these parameters.

Throughout the study of reaction dynamics within pores, a consistent model has been used. However, the method developed is general enough to apply to other model choices. For example, a topic currently being investigated with this method is modeling reactions with multiple pathways. These reactions produce different products depending on the local conditions under which the reaction occurs. Examples such as this are incremental improvements on the general model that can be added to handle specific cases beyond the ones treated. The flexibility of the models presented allows a variety of these improvements which can build upon the existing approach to form a more comprehensive model of systems, as needed. This modeling should allow for a deeper understanding of behavior of molecules within confined pores.

APPENDIX I. BOUNDARY CONDITIONS FOR BURTON-CABRERA-FRANK TYPE STEP-FLOW MODELS: COARSE-GRAINING OF DISCRETE 2D DEPOSITION-DIFFUSION EQUATIONS

David M. Ackerman[1] and J.W. Evans[2]

A paper published in *Multiscale Modeling & Simulation*

Ames Laboratory – USDOE, and Departments of Chemistry[1], Physics & Astronomy[2], and
Mathematics[2], Iowa State University, Ames, Iowa, 50011

Abstract

We analyze discrete 2D deposition-diffusion equations for the density of adatoms deposited at a periodic array of adsorption sites on a vicinal crystalline surface with kinked steps. Our analysis provides insight into the appropriate boundary conditions (BC) at steps for a coarse-grained Burton-Cabrera-Frank (BCF) type treatment involving continuum 2D deposition-diffusion equations. Such a BCF type treatment should describe step flow on vicinal surfaces under non-equilibrium growth conditions. We focus on cases where there is no activation additional barrier inhibiting to attachment at steps beyond that for terrace diffusion. Then, the classical BCF treatment simply imposes a Dirichlet BC equating the limiting value of the terrace adatom density to its equilibrium value at the step edge. Our analysis replaces this BC with one incorporating finite kinetic coefficients, $K_{\pm}$, measuring inhibited diffusion-limited attachment at kinks. We determine the dependence of $K_{\pm}$ on key parameters such as the kink separation and terrace width, and on the width of nearby terraces. Our formulation provides a framework within which to describe step-pairing phenomena observed on so-called AB-vicinal surfaces without attachment barriers, a feature not captured by the classical BCF treatment.

1 Introduction

Growth, erosion, and relaxation of crystalline surfaces are often characterized in terms of the motion of steps separating adjacent terraces with a height difference of a single atomic layer [1-4]. In a detailed *discrete atomistic picture* of these processes [3,4], atoms are deposited or removed from the surface. The resulting adatoms or advacancies diffuse across terraces on the surface by hopping between adjacent adsorption sites which form a periodic array or lattice. Potentially, there is also transport of these adspecies between different layers. When the adspecies reach and attach to steps, they can typically diffuse along steps and become incorporated into these steps at kink sites. They can also possibly detach from step edges. These processes together induce the motion of steps. It is natural to coarse-grain this detailed atomistic picture to achieve a so-called *continuum step-dynamics picture* in which steps are regarded as continuous curves [1,2,5,6]. Their smooth motion is determined by solving continuum diffusion equations on the terraces including an appropriate deposition or erosion driving term and with suitable boundary conditions (BC) at steps. The local velocity of the step is determined largely from the net diffusive flux of atoms to the step. Such equations are referred to as “deposition-diffusion equations” in this paper. Coarse-graining of atomistic models can potentially enable more efficient computational modeling, and will ideally lead to a deeper or more fundamental understanding of the evolution of surface morphologies. Below, we just use the language of deposition rather than erosion, so that the adspecies are deposited adatoms.

A classic 1951 continuum treatment of Burton, Cabrera, and Frank [7] (BCF) assumed that steps were ideal sources and sinks of adatoms, so that the adatom density on the terraces always approaches its local equilibrium value at these steps. In other words, this treatment imposed a simple Dirichlet BC equating the adatom density at steps to its equilibrium value. Such a situation is generally assumed to apply if there is no additional activation barrier for diffusing adatom to attach to steps beyond that for terrace diffusion. The current contribution focuses on this case of no attachment barrier. Subsequent refinements of this classic treatment initiated by Chernov accounted for inhibited attachment at step edges [8,9], and other extensions incorporated partial transparency or permeability of steps [10]. These various refinements lead to BC’s with a more complex form involving kinetic coefficients, $K_{\pm}$, the magnitude of which reflects the ease of attachment to steps, and also involving a permeability coefficient, P. See Sec.2 for a more detailed description. Within this more general framework, the BC in the classical BCF theory can be regarded as corresponding to the choice $K_{\pm} = \infty$.

Vicinal surfaces present a special, simple terrace-step staircase morphology with an array of parallel steps. This simple morphology provides a natural testing ground to assess various formulations of step dynamics during deposition where the entire step train advances (so-called step flow). Depending on the details of the system, this moving step train can be subject to step pairing, bunching, or meandering instabilities [1-3,6]. Of some relevance here is the existence of a specific sub-class of what have been called AB-vicinal surfaces which present two distinct types of alternating steps [11]. If these surfaces are stable, then the two types of steps have equal chemical potentials and therefore equal equilibrium adatom densities. Thus, the classical BCF treatment (for no attachment barrier) would impose identical Dirichlet BC's at both types of steps implying equal velocities of all steps for a perfect staircase.

Recently, there has been considerable interest in assessing the validity of BCF type BC's, particularly in the far-from-equilibrium regime realized under conditions of "rapid" growth or erosion [12-17]. Our focus is also on the validity of BCF type formulations. Our motivation comes from the observation of step pairing in a simple anisotropic solid-on-solid (SOS) model for AB-vicinal surfaces with no attachment barrier [18], behavior which is not described in the classical BCF treatment (as noted just above). Differing from other recent studies [12-17] described in Sec.2, our strategy is to develop a discrete two-dimensional (2D) deposition-diffusion equation formulation with which to describe and analyze such behavior. The output is effective kinetic coefficients which can provide input to a coarse-grained BCF formulation with generalized Chernov-type BC's (rather than the classical Dirichlet BC). These coefficients are finite despite the absence of an attachment barrier, and depend on kink separation, thereby elucidating the above-mentioned step pairing phenomena. The inadequacy of the classical BCF formulation can be understood since it implicitly assumes high kink densities (i.e., large terrace widths relative to the typical separation between kinks), whereas step pairing behavior considered here only occurs for limited terrace widths (relative to kink separation).

In Sec.2, we review the generalized BCF theory by Chernov et al., and also other theories and strategies for description and analysis of step dynamics. In Sec.3, we briefly describe behavior of an atomistic anisotropic solid-on-solid model with no attachment barriers but which displays step pairing contrasting predictions of the classical BCF theory. Then, in Sec.4, we present our new modeling strategy developing a discrete 2D deposition-diffusion equation model and define relevant kinetic coefficients. Next, in Sec.5, we analyze in detail the case excluding interlayer transport (i.e., with an infinite barrier to attach to descending steps), but no barrier to attach to ascending steps. The case where there is no barrier to attach to either ascending or descending steps is analyzed for uniform vicinal surface in Sec.6. More complex cases with zero attachment barriers are analyzed in Sec.7, and more general cases with finite attachment barriers are discussed in Sec.8. A summary is provided in Sec.9.

2 Step Dynamics

2.A. Traditional (generalized) BCF formulation

The description of step motion during adatom deposition is usually based on quasi-steady-state solutions for the adatom density per unit area, $n(x, t)$ and lateral position x and time t. This density satisfies the continuum deposition-diffusion equation [1,3-7]

$$\partial/\partial t\, n(x, t) = F + D\, \nabla^2 n(x, t) \approx 0. \qquad (1)$$

Here, F is the deposition flux per unit area, and D is the terrace diffusion coefficient for adatoms. The density $n(x, t)$ is taken to satisfy boundary conditions at a step edge of the form [7-10]

$$\pm D\, \nabla_n n|_{\pm} = K_{\pm}(n_{\pm} - n_{eq}) + P(n_{\pm} - n_{\mp}) \; (= J_{\pm}), \qquad (2)$$

ignoring convection terms given that steps move slowly on the time scale of adatom density relaxation. Here, ∇_n denotes the normal derivative to the step edge (in the descending direction), and n_{eq} denotes the equilibrium density of the diffusing species. Also ± indicates the limiting values of various quantities approaching the step edge, where + refers to the lower terrace, and – refers to the upper terrace. See Fig.1. $K_{\pm}$ and P are kinetic coefficients described below.

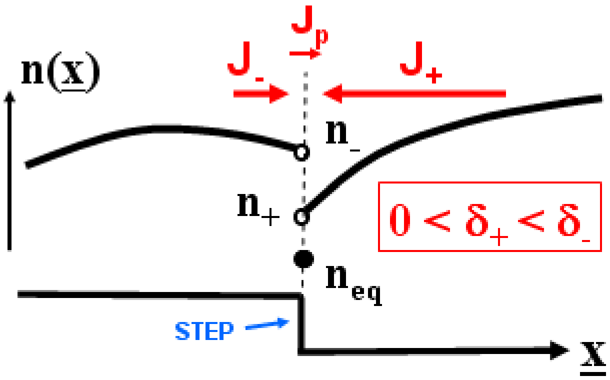

Figure 1: Schematic of the generalized BCF boundary conditions with total diffusion fluxes $J_+ = K_+(n_+ - n_{eq}) + P(n_+ - n_-)$ *and* $J_- = K_-(n_- - n_{eq}) + P(n_- - n_+)$ *reaching the ascending and descending steps, respectively. Also* $J_p = P(n_- - n_+)$ *denotes the flux across the step due to permeability.*

The expressions in (2) represent the *diffusion fluxes*, $J_\pm$, of adatoms reaching the step edge from the lower (+) and upper (-) terrace, and the *step velocity* is given by $V = J_+ + J_-$. The first term on the right hand side corresponds to attachment at steps where $K_\pm$ are the associated kinetic coefficients [8,9]. Thus, K_+ corresponds to intralayer attachment at ascending steps. K_- corresponds to downward interlayer attachment involving transport over descending steps. The second term on the right hand side corresponds to transport across the step where P is the step permeability [10]. Rather than being a relation derived from a class of atomistic models, (2) is usually thought of as a defining relation for the kinetic coefficients.

It is instructive to write $K_\pm = D/L_\pm$ where $L_\pm$ are the corresponding attachment lengths. These reflect any additional energy barriers, $\delta_\pm$, to attachment at step edges, where δ_- corresponds to the Ehrlich-Schwoebel (ES) step-edge barrier inhibiting downward transport over descending steps [3,4,9]. Below, we let ‘a’ denote the surface lattice constant, and $\beta=1/(k_BT)$ denotes the inverse temperature for surface temperature T and Boltzmann constant k_B. Then, traditional formulations typically assign either $L_\pm = a[\exp(\beta\delta_\pm) - 1]$ or $L_\pm = a \exp(\beta\delta_\pm)$ [3,4]. See Appendices A and B. In the case of *facile attachment* at steps (i.e., $\delta_\pm = 0$), the first formulation on which we focus yields $K_\pm/D = \infty$ or $L_\pm = 0$ which recovers classical BCF Dirichlet BC $n = n_{eq}$. The second yields $K_\pm/D = 1/a$ or $L_\pm = a$ for $\delta_\pm = 0$. In the case of an infinite ES barrier precluding, clearly one has that K- =0 and P=0 (i.e., the step is impermeable). With finite $\delta_\pm$, there is no reason to preclude the assignment P>0, and for some systems this seems key to describing observed behavior [19]. For the models considered here when the ES barrier is not finite (and usually zero), one expects physically that the steps are permeable (P>0).

Determination of *step velocities*, V, requires solving the above boundary value problems to determine the fluxes, $J_\pm$. If P>0, then the behavior on all terraces is coupled. The case of most relevance here is where the *permeability term drops out* of (2), either because P=0 or because $n_+ = n_-$. Then, the boundary value problem for each terrace is uncoupled from the rest, and one needs only solve these for terraces adjacent to a step to determine the step velocity. For parallel straight steps, the analysis is simple since the steady-state solution of (1) is a parabolic profile. For a single terrace of width W, let $K_l = D/L_l$ and $K_r = D/L_r$ denote the K-values for the left (ascending) and right (descending) step, respectively, and J_l and J_r the corresponding fluxes. Then, one has that [4]

$$J_l + J_r = FW \text{ and } J_l/(J_l + J_r) = [½ + L_r/W]/[1 + L_l/W + L_r/W] \ (=P_l). \tag{3}$$

The result for the sum of the fluxes follows trivially from mass conservation. We let P_l (P_r) denote the fraction of this flux reaching the left (right) step. Then, the expression for P_r simply follows from that above for P_l after interchanging the labels l and r, and one has that $P_l + P_r = 1$. From (3), it is clear that knowledge of the K-values, or the corresponding attachment lengths, and the terrace width, W, allows evaluation of the fluxes and thus the step velocities. For completeness, we note that the value of excess adatom density, $\delta n = n - n_{eq}$, at the left and right steps can be determined from $K_l\, \delta n_l = J_l$ and $K_r\, \delta n_r = J_r$, respectively.

Finally, we emphasize one consequence of (3): any assignment of attachment lengths far below the terrace widths corresponds to “large” K-values or facile attachment, and yields similar behavior for step dynamics to the classical BCF Dirichlet BC. One should regard $K_\pm/D = O(a)$ as “large”.

2.B. Other established formulations and refinements

A well-established formulation prominent in the liquid-phase crystal growth community is based on the observation that step motion derives from incorporation of atoms at kinks and the resulting motion of those kinks [20,21]. A simple geometric argument implies that the step velocity, V, satisfies $V \propto v_{kink}/L$, where L is the typical kink separation and v_{kink} is the kink velocity along the step. Typically, it is assumed that attachment to kinks is strongly inhibited by a kink attachment barrier, δ_{kink}. Then, one has that $v_{kink} \sim \exp(-\beta\delta_{kink})\ (n-n_{eq})$. This, in turn, implies a step kinetic coefficient of the form $K \sim \exp(-\beta\delta_{kink})/L$. This formulation will not apply to the models of interest here where there are no attachment barriers of any type. However, it is appropriate to note that our analysis will also produce a dependence of K on L (but of a different form).

Within the above picture (which again does not apply for our models), the mean kink separation or density is a key factor in determining step propagation, higher kink densities implying higher propagation velocities. Thus, one is should ask what determines the value of this kink density. For higher temperatures, T, thermal fluctuations of the steps will spontaneously produce a high density of kinks which will presumably be close to its equilibrium value. However, for lower T (or high kink energy), kinks may be rare. Then, the kink density during deposition and step flow may be determined by kinetic factors associated with the 1D nucleation of new rows of atoms on the step. A corresponding kinetic theory has been developed by Voronkov [22] and others [21]. Such kinetic formulations are the precursors of more recent detailed treatments of non-equilibrium step flow described below in Sec.2C.

All of the above formulations apply for the propagation of straight steps. Step evolution in situations with curved steps, e.g., growth of 2D islands, is often analyzed by decomposing the step velocity into two components. One component comes from diffusion-mediated attachment-detachment of atoms from or to the terrace described above by (2), and the second from diffusion along the step edge. In general, the island growth shape [3,4] is determined by interplay between: (i) a Mullins-Sekerka type instability associated with diffusion-limited aggregation of terrace adatoms; and (ii) relaxation of the shape of the growing island due to edge diffusion. Both depend sensitively on the local curvature and the latter on the orientation of the step edge. The edge diffusion flux controlling relaxation can be dominated by a non-equilibrium component (proportional to the local aggregation flux) rather than by the traditional Mullins-type step edge flux which is determined by the gradient in curvature [3,4]. Heuristic forms have been proposed for the non-equilibrium edge flux [23], but rigorous analysis is limited [24].

Finally, we note that the step velocity is given by the net flux of attachment of atoms at the step edge accounting for all attachment pathways. In addition to contributions from diffusion across adjacent terraces and along the step edge, there is the possibility of direct deposition at the step edge. Of course, this contribution will be minor for broad terraces of many lattice constants. Also, relative to traditional atomistic models based on a simple-cubic crystal structure (SOS models), sites at the step edge actually directly capture more depositing atoms than terrace sites for realistic fcc or bcc structures due to “downward funneling” of atoms deposited right at the step edge [25]. One can readily incorporate this effect into step dynamics or discrete models by augmenting the direct deposition flux at step edge sites. Correct accounting for this feature is particularly important for predictions of slope selection during mound formation [26].

2.C. Kinetic terrace-step-kink models

One general strategy utilized in recent analyses of non-equilibrium step dynamics starts with a terrace-step-kink picture of the surface [2,7] and develops separately mean-field diffusion equations for the density of terrace adatoms and for that of edge adatoms, as well as a mean-field convection equation for the density of kinks [12-17]. Constitutive relations are also required for various quantities, e.g., step attachment and detachment fluxes are calculated in terms of the limiting value of the terrace adatom density at the step edge and the actual non-equilibrium edge atom density. Development of this formulation is simplest for step orientations with low kink densities [12], but has been extended to other step orientations [15,16]. The latter development is related to a key component of this paper, i.e., consideration of the dependence of the kinetic coefficient on kink density (noting that kink density is simply related to step orientation).

The focus of these studies has for the most part been in determining key properties of non-trivial non-equilibrium steady-state associated with step flow such as the kink density [12-16]. However, the work of Margetis and Caflisch (MC) [17] also presented results for kinetic coefficients defined by the relation (2), connecting more closely with our focus. MC utilized a perturbation analysis for the regime of small Peclet number (which is inversely proportional to the edge diffusion rate). The study by MC is distinct from but complementary to our own work: MC regards attachment fluxes or adatom densities approaching the step as input parameters and solves for the non-equilibrium steady-state step geometry including kink density. In contrast, we will specify the surface geometry (including the kink distribution along steps) as input and solve the corresponding diffusion-diffusion equation to determine kinetic coefficients.

Interestingly, MC also introduces an effective non-equilibrium stiffness from a perturbation analysis of step flow for slightly curved steps. An analogy is exploited with the equilibrium Gibbs-Thomson relation which relates the equilibrium adatom density for curved steps to step stiffness. Usually stiffness of steps (or more generally of interfaces) is assessed from interface fluctuations. For equilibrated interfaces, the fluctuation amplitude is inversely proportional to stiffness and completely independent of interface mobility [2]. In contrast, the lack of a fluctuation-dissipation relation for general non-equilibrium systems introduces some ambiguity since the mobility no longer factors out of expressions for the fluctuation amplitudes [27]. However, the approach of [17] avoids this ambiguity.

2.D. Discrete lattice-based deposition-diffusion models

An alternative class of strategies to assess appropriate BC's in a BCF formulation for step flow might be based on discrete deposition-diffusion equations describing the adatom density at a discrete periodic array of adsorption sites on stepped crystalline surfaces. A few previous studies have examined the steady-state solutions of the one-dimensional (1D) version of these equations for step flow on vicinal surfaces [3,4,28]. Coarse-graining then allows derivation of BC's of the type (2), as discussed further in Appendix B. However, such 1D models must necessarily describe in an average or effective fashion the complex structure of steps in physical two-dimensional (2D) surface systems where steps have both kink and ledge sites [29].

Thus, in the current study, we are motivated to analyze models based on the steady-state solutions of discrete 2D deposition-diffusion equations which explicitly incorporate the kink and ledge site structure of steps on a vicinal surface. All the details of our model are described in Sec.4A. Certainly our modeling is still somewhat idealized in that it incorporates a simple frozen step geometry. However, it still provides new insights into non-equilibrium step flow, thereby supplementing the alternative modeling strategies of Sec.2C. A goal of these studies is to obtain appropriate boundary conditions for continuum step-dynamics models which are regarded as deriving from coarse-graining of the discrete models over length scales larger than the typical kink separation. A specific aim is to characterize the dependence of the effective kinetic coefficients $K_{\pm}$ on the microscopic parameters in the discrete model, particularly on the mean kink separation.

3 AB-Vicinal Surfaces and Non-Equilibrium Step Pairing

Perhaps the most familiar example of an AB-vicinal surface [11], and one with immense technological significance, is that of vicinal Si(100) [30,31]. A dimer-row reconstruction of the Si(100) surface, together with an alternation of the direction of the dimer rows on adjacent terraces, leads to alternating so-called S_A and S_B type step types. S_B steps have low stiffness and thus meander greatly with a high kink density. S_A steps are stiff and relatively straight with a low kink density. Step pairing has been observed experimentally during deposition on vicinal Si(100) surface with S_B steps initially moving faster than S_A steps. Faster propagation of the more kinked S_B step has been rationalized with the framework of the model for inhibited kink attachment described in Sec.2B, refined by ideas of Voronkov to account for kinetic contributions to the (low) kink density on S_A steps, and also accounting for anisotropic terrace diffusion [21]. It should be emphasized that this is a particularly complex system due to the surface reconstruction. In addition to the features above, attachment and detachment at steps effectively occurs in units larger than atoms (dimers or dimer pairs) [30]. Thus, precise atomistic level modeling is difficult. For this reason, sometimes a heuristic approach is adopted of simply assigning distinct kinetic coefficients to S_A and S_B steps, the latter being higher reflecting higher “accommodation” or “stickiness” at S_B steps [32]. A similar heuristic approach has be adopted in analyses of island formation during Si(100) homoepitaxy [33,34].

Another example of an AB-vicinal surface, structurally equivalent to Si(100), is provided by vicinal Ge(100) surfaces. A rather different realization is provided by surfaces of hcp metal crystals vicinal in the principal direction to the basal plane [11], where close-packed steps alternate between [100]- and [111]-microfaceted structures.

However, our purpose here is to provide a fundamental understanding of step dynamics. Thus, rather than a considering detailed realistic model for a specific system such as Si(100), it is more instructive to consider a simpler generic model. To this end, we consider a simple *anisotropic solid-on-solid (SOS) model* as developed in Ref. [18] which includes random deposition at rate F per site, *isotropic terrace diffusion* with barrier E_d, and *no attachment barriers* at steps. There are attractive *anisotropic interactions* between deposited atoms on nearest-neighbor (NN) adsorption sites. These attractions lead to a thermodynamic preference for aggregation of adatoms with steps or into islands. Specifically, the model incorporates stronger attractive NN interactions $\phi_s>0$ in one direction and weaker NN attractions $\phi_w>0$ in the orthogonal direction. Furthermore, these directions *alternate* between adjacent terraces on a vicinal surface. Activation barriers for either intra- or inter-layer hopping to NN empty sites are chosen to have the form $E_{act} = E_d + n_s\phi_s + n_w\phi_w$ where n_s (n_w) is the number of strongly (weakly) bonded neighbors in the same layer before hopping. Hop rates are given by $h = \upsilon \exp[-\beta E_{act}]$ where again $\beta=1/(k_BT)$. As a result of anisotropic interactions, the vicinal surface displays two types of steps, alternating between straight or stiff (which we denote type-A), and wandering or meandering (which we denote type-B). For B-type meandering steps, the strong bonding is orthogonal to the step, so kink creation is controlled weak bonding which leads to a high density of kinks [2]. For A-type stiff steps, the opposite is true.

Model behavior as determined from Kinetic Monte Carlo simulations is shown in Fig.2. Before deposition on average the two different types of steps are equally spaced. When deposition is initiated, step pairing occurs, the meandering B-type steps initially moving faster than the A-type stiff steps. However, both types of steps have the same equilibrium density, $n_{eq} = \exp[-\beta\phi_b]$ where $\phi_b = \phi_s + \phi_w$, and thus should advance with the same velocity according to the traditional BCF Dirichlet boundary condition. Thus, the observed pairing is a non-equilibrium phenomenon, which has been described previously only qualitatively in terms of differences in “accommodation” or “stickiness” of the two types of steps [18]. The current work will provide a more precise and quantitative formulation.

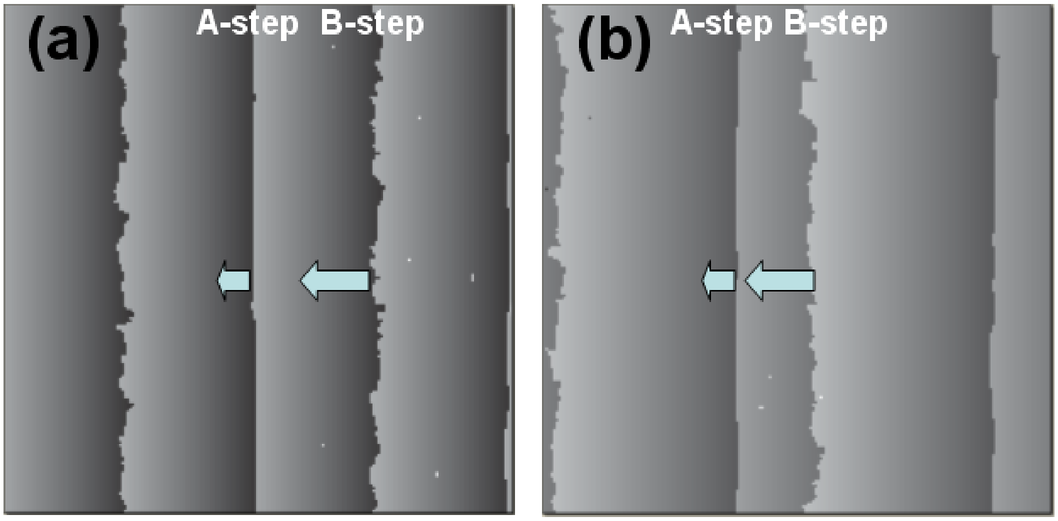

Figure 2: Images (200x200 sites) from our KMC simulation of the anisotropic SOS model for step flow on an AB-vicinal surface with higher terraces on the right: (a) structure of the equilibrated surface (before deposition) with on-average equal spaced terraces and alternating A-type stiff and B-type meandering steps; (b) structure after deposition of ~0.6 layers of atoms. Parameter choices: $\beta\phi_s = 7.25$, $\beta\phi_w = 2.90$, *and* $\upsilon/F = 10^8$.

4 Discrete 2D Deposition-Diffusion Equations for Vicinal Surfaces

4.A. Model specification

Guided by the anisotropic SOS model described in Sec.3, we first consider an idealized 2D deposition-diffusion equation model for deposition on a *perfect vicinal surface* where all terraces have a width of W sites. Kinks are periodically distributed along each step edge with a separation of L lattice constants. Also kinks on different steps are aligned in the direction orthogonal to the steps. Due to periodicity both orthogonal to and parallel to the steps, we need only analyze behavior of the adatom density in an LxW site "rectangular unit cell" on a single terrace between adjacent kink sites. We label sites in this unit cell by (i,j) where $1 \le i \le L$ and $1 \le j \le W$. Step edge sites (i,1) correspond to those at the bottom of an ascending step, where (1,1) is regarded as a kink site which acts as a source and sink for adatoms. Sites (i,W) correspond to those at the upper edge of a descending step. See Fig.3. The adatom density at site (i,j) is denoted by n(i,j), where the density at the kink site is fixed at a constant value of unity, i.e., n(1,1) =1.

Next, we describe the energetics and dynamics of the model also illustrated in Fig.3 where again $\beta=1/(k_BT)$. Atoms are deposited at rate F per site. Given our interest in anisotropic systems, we allow for direction-dependence of the bonding of adatoms to step edge atoms. Edge adatoms at sites (i,1) with $1<i\leq L$ adjacent to the ascending step are regarded as bonded to the step edge atoms via an attractive nearest-neighbor (NN) attraction of strength $\phi_\perp > 0$. In addition, these edge adatoms (with j=1) upon reaching the kink sites are regarded as acquiring additional bonding of strength $\phi_\| > 0$. A terrace atom at site (2,1) upon directly reaching the kink site (1,1) is regarded as acquiring additional bonding of strength $\phi_b = \phi_\perp + \phi_\| > 0$. Thus, the total strength of bonding for adatoms at kink sites is consistently given by ϕ_b. Edge adatoms at sites (i,W) adjacent to the descending step do not have any lateral bonding.

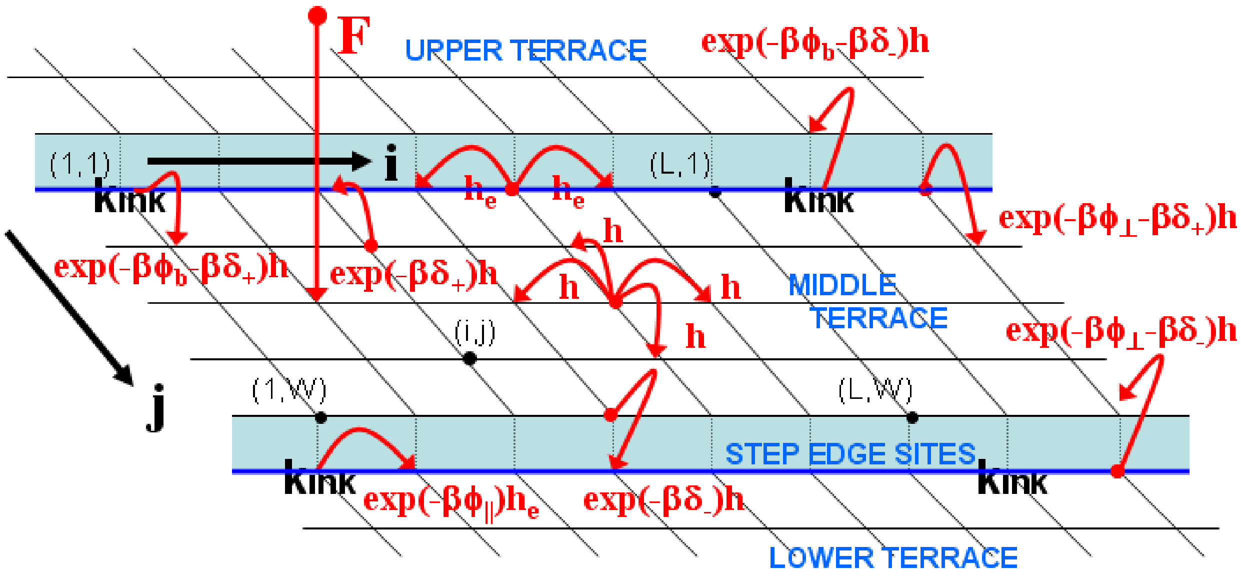

Figure 3: Schematic of discrete 2D deposition-diffusion model for perfect vicinal surface. We show adsorption sites a LxW rectangular unit cell together with nearby surrounding sites, and also indicate kink sites. Rates of various hopping processes (and of deposition) are also indicated.

Hopping of adatoms from terraces sites (i,j) to other sites on the *same* terrace typically occurs at rate h for $2\leq j\leq W$. The only exception is for hopping from site (i,2) to (i,1), which corresponds to attaching to an ascending step, and where the rate may be reduced to $\exp(-\beta\delta_+)h$ in the presence of an additional attachment barrier δ_+. Hopping of edge adatoms already at edge sites (i,1) with $1<i\leq L$ to other edge sites (including the kink site) occurs at rate h_e. According to detailed-balance, a step edge adatom at site (i,1) with $2\leq i\leq L$ hops to terrace site (i,2) on the same terrace with rate $\exp(-\beta\phi_\perp-\beta\delta_+)h$. An adatom at the kink site hops to adjacent step edge sites with

rate $\exp(-\beta\phi_{\|})h_e$, and to the adjacent terrace site (1,2) at rate $\exp(-\beta\phi_b-\beta\delta_+)h$. Consistently, the equilibrium adatom density at the step edge is given by $n_{EQ} = \exp(-\beta\phi_b)n(1,1) = \exp(-\beta\phi_b)$, based on consideration of an equilibrium between terrace and kink adatoms [1-3].

In addition, we must prescribe the details of interlayer adatom hopping between terraces. We allow for the existence of an additional ES step-edge barrier of strength δ_-. This implies that adatoms at sites at an upper step edge (i,M) hop down to adjacent edge or kink sites on the lower terrace at reduced rate $\exp(-\beta\delta_-)h$ relative, which is reduced from that for terrace diffusion. According to detailed-balance, adatoms at the lower step edge sites (i,1) with $1<i\leq L$ can hop to the adjacent upper terrace site with rate $\exp(-\beta\phi_\perp-\beta\delta_-)h$. The atom at the kink site can hop to the adjacent upper terrace site with rate $\exp(-\beta\phi_b-\beta\delta_-)h$. Thus, in the special case of an infinite ES barrier ($\delta_- =\infty$), there is no transport or “communication” between different terraces.

Appendix C presents a refined version of the discrete 1D deposition-diffusion model of Appendices A and B which better captures the features of our discrete 2D model.

4.B. Discrete 2D deposition-diffusion equations

We assume sufficiently low deposition rate that adatom densities are very low and thus adsorption attempts are essentially always successful. Then, the discrete 2D deposition-diffusion equations describing evolution in this model have the steady-state form

$$\begin{aligned} d/dt\, n(i,j) = {} & h^L_{i+1,j}\, n(i+1,j) + h^R_{i-1,j}\, n(i-1,j) + h^U_{i,j-1}\, n(i-1,j) + h^D_{i,j+1}\, n(i,j+1) \\ & - (h^L_{i,j} + h^R_{i,j} + h^U_{i,j} + h^D_{i,j})\, n(i,j) + F \approx 0, \end{aligned} \tag{4}$$

for $1\leq i\leq L$ and $1\leq j\leq W$, except for the kink site (i,j)=(1,1) where n(1,1)=1. Here, $h^X_{i,j}$ denotes the rate for hopping from site (i,j) in a direction X = L (left), R (right), U (up), and D (down) in the (i,j)-plane. Specific values for any (i,j) follow from the description above. The detailed-balance feature of these rates ensures that the *equilibrium solution* for F=0 satisfies $n(i,j) = \exp(-\beta\phi_\perp -\beta\phi_{\|}) = \exp(-\beta\phi_b) = n_{EQ}$ for terrace sites $1<j\leq W$, $n(i,1) = \exp(-\beta\phi_\perp)$ for step edge sites with $1<i\leq L$, and again n(1,1)=1.

There exists a natural rescaling of the above deposition-diffusion equations setting

$$\begin{aligned}&n^*(i,j) = n(i,j) \text{ for terrace sites } 2\le j\le W,\\ &n^*(i,1) = \exp(-\beta\phi_\parallel)\, n(i,1) \text{ for step edge sites with } 2\le i\le L, \text{ and}\\ &n^*(1,1) = \exp(-\beta\phi_\perp-\beta\phi_\parallel)\, n(1,1) = \exp(-\beta\phi_b)\, n(1,1) \text{ for the kink site.}\end{aligned}\tag{5}$$

This rescaling ensures that all terms associated with adatom hopping on the right-hand-side of the rescaled evolution equations can be written in terms of *differences* in n*-values for NN pairs of sites. This, in turn, makes transparent the equilibrium solution $n^*(i,j) = n^*(1,1) = n_{EQ}$ for all (i,j) when F=0. The rescaling also produces more *generic equations* in that rescaled densities for all terrace sites satisfy an equation with exactly the same form for zero attachment barriers, $\delta_\pm=0$, even for sites with j=2 or j=W adjacent to the step edge. This important feature will be exploited below. It is also the case that all edge sites satisfy generic equations (even those adjacent to the kink sites).

Inhomogeneities in the steady-state form of these rescaled equations derive both from deposition terms, and from the coupling to $n^*(1,1)$ of $n^*(i,j)$ with (i,j) neighboring (1,1). It is thus instructive to introduce new variables, $\delta n^*(i,j) = n^*(i,j) - n_{EQ}$ characterizing deviations from equilibrium, so then $\delta n^*(1,1)=0$. Letting δn^* denote a LxW-dimensional vector composed of these quantities, the steady-state form of (3) can be recast in matrix form as

$$\underline{\underline{A}}(h_e/h,\ \phi_\perp)\cdot \delta n^* = (F/h)\ e(\phi_\perp),\tag{6}$$

where the *only* inhomogeneity now comes from the deposition terms on the right-hand-side. The entries of the non-symmetric square (LxW)x(LxW) matrix $\underline{\underline{A}}$ and vector *e* can be readily obtained from comparison with (4). The dependence on h_e/h and on $\phi_\perp$ comes from sites at the step edge. In (6), we leave implicit the dependence on attachment barriers $\delta_\pm$. There is no dependence on $\phi_\parallel$. The form of (6) immediately demonstrates that the equilibrium solution for F=0 satisfies $\delta n^* = 0$, consistent with the above observations. Significantly, it also illustrates basic features of non-equilibrium behavior, e.g., the *exact* proportionality $\delta n^* \propto F$.

The model above was described for a perfect vicinal surface where all terraces have the same width W and kinks are distributed periodically along steps and are aligned in the direction orthogonal to steps. However, the model is readily generalized to treat *more complex vicinal surface geometries*. Our analyses below will often consider bi-periodic systems with alternating broad and narrow terraces, but still with periodically distributed and aligned kinks. In addition, one could consider more complex terrace geometries and arrangements of kinks. In all these cases, there will be a larger rectangular unit cell for which a finite closed set of equations must be analyzed. However, the formulation and structure of the equations is analogous to that above.

4.C. Kinetic coefficients from discrete models

Our focus in this study will be on extracting values for kinetic coefficients, $K_{\pm}$, from analysis of the discrete 2D model for cases where the step permeability term drops out of (2) in the corresponding continuum setting. There, are two situations where this scenario applies. The *first* trivial case is for an infinite ES barrier where naturally P=0. Then, clearly one has $K_- = 0$, and the task is just to determine K_+. The *second* corresponds to cases in a continuum setting where the limiting value of the adatom density is the same approaching any step from either side, i.e., $n_+ = n_-$ in (2) (but these limiting values could differ for different steps). This second situation is realized for a uniform vicinal surface with symmetric attachment barriers, where the adatom density profile is symmetric about the center of the terrace and the same for all terraces. However, to analyze even this case and certainly for more general situations, we must precisely specify a procedure for define these "limiting values" of adatom densities for the discrete picture.

Given the above remarks, we now specify how values of adatom densities at terrace sites, $n(i,2\leq j\leq W)=n^*(i,2\leq j\leq W)$, are smoothly extrapolated or "analytically extended" in a precise and unambiguous way to those at the left step j=1 to determine $n_+^*(i,1)$, or to those at the right step j=W+1 to determine $n_-^*(i,W+1)$. Our basic requirement that the equations for the terrace densities adjacent to the steps (i.e., for j=2 and j=W) can be recast into same generic form as those in the middle of the terraces when incorporating the above extrapolated densities. This formulation is illustrated explicitly in Appendices A and B for a simpler 1D model. An *equivalent* simpler prescription focuses on the diffusion fluxes, $J_+(i,1)$ of adatoms reaching the step j=1 and $J_-(i,W+1)$ of adatoms reaching the step j=W+1, at the left and right of the terrace along column 'i' in the 2D discrete model. We demand that the extrapolated densities $n_+^*(i,1)$ and $n_-^*(i,W+1)$ satisfy

$$J_+(i,1) = \exp(-\beta\delta_+)h\,[n^*(i,2)-n^*(i,1)] = h[n^*(i,2)-n_+^*(i,1)], \text{ and}$$
$$J_-(i,W+1) = \exp(-\beta\delta_-)h\,[n^*(i,W)-n^*(i,W+1)] = h[n^*(i,W)-n_-^*(i,W+1)]. \quad (7)$$

In Sec.4B, we have already noted that for *zero attachment barrier* on a perfect vicinal surface, the equations for rescaled densities have the generic form for j=2 and j=W. This implies that one can make the identification $n_+^*(i) = n_-^*(i) = n^*(i,1) = n^*(i,W+1)$ consistent with (7) above, i.e., in this case of zero attachment barriers, there is no discontinuity at the step edge in extrapolated values of the rescaled adatom density (i.e., one has $n_+^* = n_-^*$). Significantly, the corresponding analysis of the equations for rescaled densities for vicinal surface with non-uniform terrace widths shows that the equality $n_+^* = n_-^*$ is preserved for zero attachment barriers. We exploit this result in our analysis of $K_\pm$ for these cases in Sec.8.

Next, we provide an explicit prescription for the extraction of kinetic coefficients, $K_\pm$, from our discrete 2D model. To this end, we introduce an average along the step edge direction

$$\langle B_i \rangle_i = L^{-1} \Sigma_{1\leq i\leq L}\, B_i. \quad (8)$$

If “a” denotes the lattice constant, then $D = a^2h$ is the terrace diffusion coefficient, and the deposition flux per unit area in (2) satisfies $\mathcal{F} = a^{-2}$ F. Motivated by (2), to define K_+ in the discrete model, we make the replacements

$$a^2(n_+ - n_{eq}) \rightarrow \langle n_+^*(i) - n_{EQ}\rangle_i = \langle \delta n_+^*(i,1)\rangle_i$$
$$= \langle \delta n_+^*{}_{edge}\rangle \text{ (excess edge density)}, \quad (9a)$$

$$a^2\nabla_n n|_+ \rightarrow a^{-1}\langle n^*(i,2) - n_+^*(i,1)\rangle_i = a^{-1}\langle \delta n^*(i,2) - \delta n_+^*(i,1)\rangle_i \text{ (rescaled flux)}, \quad (9b)$$

recalling that $\delta n^*(i,j) = n^*(i,j) - n_{EQ}$. Here, we use that $a^2\, n(x)$ corresponds to a density per site with area a^2, so for example $n_{EQ} = a^2\, n_{eq}$. Then, to define the kinetic coefficients in the discrete model, we make the following replacement

$$K_+/D = (\nabla_n n|_+)/(n_+ - n_{eq}) \text{ in (2)} \quad (10a)$$

$$\rightarrow\ K_+/D = a^{-1} \langle \delta n^*(i,2) - \delta n_+^*(i,1)\rangle_i / \langle \delta n_+^*(i,1)\rangle_i, \quad (10b)$$

to obtain K_+ for the step at j=1. Thus, from (6), one has that $K_+/D = 1/L_+$ depends on h and h_e only through the ratio h_e/h. Perhaps more significantly, K_+ is *independent* of F. (However, K_+/D

does depend on $\beta\phi_\perp$ and $\beta\delta_+$.) A similar analysis applies for K_- and L- for the step at j=W+1. We emphasize that for zero attachment barriers, one has that $n_+^*(i,1) = n^*(i,1)$ and $n_-^*(i,W+1) = n^*(i,W+1)$ making the above types of formulae explicit.

4.D. Selected properties of steady-states and kinetic coefficients

The kinetic coefficients are determined entirely from the steady-state properties of the solutions of the discrete 2D deposition diffusion equations, in particular from the ratio of excess density at the steps to the diffusive flux to the step. In a *continuum setting*, the diffusive flux is constrained by mass conservation, i.e., the amount of material deposited within a region of the terrace must be balanced by the diffusive flux out of that region. This constraint is expressed mathematically by Gauss' Theorem noting that the steady-state form of the continuum deposition-diffusion equations matches that of Poisson's equation. In the continuum setting, it is also common and instructive to introduce the concept of "capture zones" (CZ's) for steps or islands, such that the flux from all points within the capture zone flows to that step or island [4]. Then the CZ area times F gives the total diffusive flux to the step or island.

These basic ideas carry over to a *discrete setting* with some minor modification. The mass conservation constraint described above can be precisely formulated as a discrete version of Gauss' Theorem [37]. One can introduce the concept of CZ's although in general the total diffusion flux will not correspond to an integer number of adsorption sites times F. However, effective CZ boundaries can still be selected to reflect the total diffusion flux. As a simple example, mass conservation for infinite ES barrier and $\delta_+=0$ yields the relation

$$J_+ = \langle J_+(i,1)\rangle = h\langle n^*(i,2) - n^*(i,1)\rangle_i = h\langle \delta n^*(i,2) - \delta n^*(i,1)\rangle_i = F(W-1) \qquad (11)$$

for the total flux reaching the ascending step. As discussed in Sec.2B, the step velocity is determined by the total flux of atoms reaching the step. In addition to the diffusive components, this always includes a component, $J_{dd} = F$, due to direct deposition at the step edge. For a perfect vicinal surface with terraces of width W, mass conservation implies that $J_+ + J_- + J_{dd} = FW$.

Now, we turn to analysis of the dependence of the kinetic coefficients on specific model parameters. First, we remark that the limiting case $h_e \to \infty$ is of special interest since it produces *equilibration of the step edge density*, $n^*(i,1) \rightarrow n_{EQ}$. In fact, the discrete 2D deposition-diffusion equations reduce to the 1D equations of Appendices A and B by virtue of translational invariance along the step direction. Then, simpler "traditional" results for kinetic coefficients immediately follow. In particular, $K_+ = \infty$ with attachment barrier $\delta_+ = 0$, and $K_- = \infty$ with zero ES barrier d- = 0. Thus, an appealing feature of our model is the ability to tune the degree of equilibration (or lack thereof) by adjusting h_e relative to h.

For finite step edge diffusion rates $h_e < \infty$, we will obtain finite values for the effective $K_\pm$ even in the absence of attachment barriers. This is because incorporation at steps inhibited by a "small" kink density, which results in a strictly positive excess edge density $\langle \delta n^*_{edge} \rangle_i$. From this perspective, it is expected that $K_\pm$ should vanish with increasing kink separation $L \rightarrow \infty$. To elucidate this regime and the associated behavior of $K_\pm$, it is natural to introduce a *semi-discrete version* of the fully discrete model described in Sec.4A. Here, the discrete density, n(i,j), in the step direction i for large L is replaced by a semi-continuous quantity, n(x,j), where the continuous position x corresponds to ia. One then analyzes a finite coupled set of continuous deposition-diffusion equations for the n(x,j) for $0<x<aL$ and $1 \leq j \leq W$ where these densities extend periodically to other x. See Appendix D. The resulting analysis indicates that

$$K_\pm(L) \approx A/L^2, \text{ as } L \rightarrow \infty. \tag{12}$$

Furthermore, behavior for a broad range of L should be well described by $K_\pm(L) \approx A/(L^2 + BL + C)$. Since $K_\pm$ are given by the ratio of the attachment flux and the excess step density, the result (12) is understood from the feature that the attachment flux is independent of L [cf. (11)], and the excess step density naturally scales like L^2. As noted in Sec.2B, considerations of kink attachment-limited step flow in liquid-phase crystal growth naturally led to kinetic coefficients which decrease with increasing kink separation. The functional form of $K_\pm$ versus L is different here since we are considering diffusion-limited kink attachment.

Results for $K_\pm$ with finite $h_e < \infty$ will also depend on the width, W, of the terrace on the vicinal surface. Since coarse-grained models are usually applied to situations where the typical kink separation is well below other characteristic lengths (e.g., typical terrace widths), it is natural to examine the behavior of $K_\pm$ in the limit of broad terraces, $W \rightarrow \infty$. For an infinite ES barrier with $\delta_+=0$, using that $h\langle\delta n^*(i,2) - \delta n^*(i,1)\rangle_i = F(W-1)$ from (11). Then, provided that the excess adatom density at steps is roughly proportional to the terrace width $\langle\delta n^*_{edge}\rangle \propto W$, it follows that

$$K_\pm(W) \approx K_\pm(\infty)(W-1)/W. \tag{13}$$

As a sample numerical test of this W-dependence of $\langle\delta n^*_{edge}\rangle$, for L=50, $h=h_e$, and $\beta\phi_\perp=1$, we find that $\langle\delta n^*_{edge}\rangle \approx 0.00305W + 4.2\text{x}10^{-8}$ for W ranging from 50 to 500.

5 Infinite ES Barrier $\delta_- = \infty$ and Zero Attachment Barrier $\delta_+ = 0$

This case of an infinite ES barrier, $\delta_-=0$, has the simplifying feature that atoms cannot attach to a step from the upper terrace, i.e., $K_-=0$, and thus that steps are impermeable, i.e., P=0. Then (2) reduces to the zero-flux boundary condition $D\, \nabla_n\, n|_- = 0$ at descending steps. In such systems, behavior on each terrace is completely independent. We consider in Sec.5 only the case of *zero step attachment barrier* to the step, $\delta_+ = 0$. Our focus is on the determination of the kinetic coefficient, K_+, describing attachment to the ascending step. Here, the *step velocity* is just determined by the width of the associated lower terrace (and by the deposition flux) which constitutes the capture zone (CZ) for the step.

Typical behavior of the rescaled densities $\delta n^*(i,j)$ is shown in Fig.4 for $h=h_e$ and $h/F=10^4$ with L=20, W=20, and $\beta\phi_\perp = 1$. Note the increase in the step edge densities $\delta n^*(i,1)$ between the kink sites above n_{eq}. The traditional view for this case would be that $K_+ = \infty$ forcing the classic BCF boundary condition that $n_+=n_{eq}$. However, as already noted in Sec.4, we find finite values of K_+ due to inhibited incorporation at kinks.

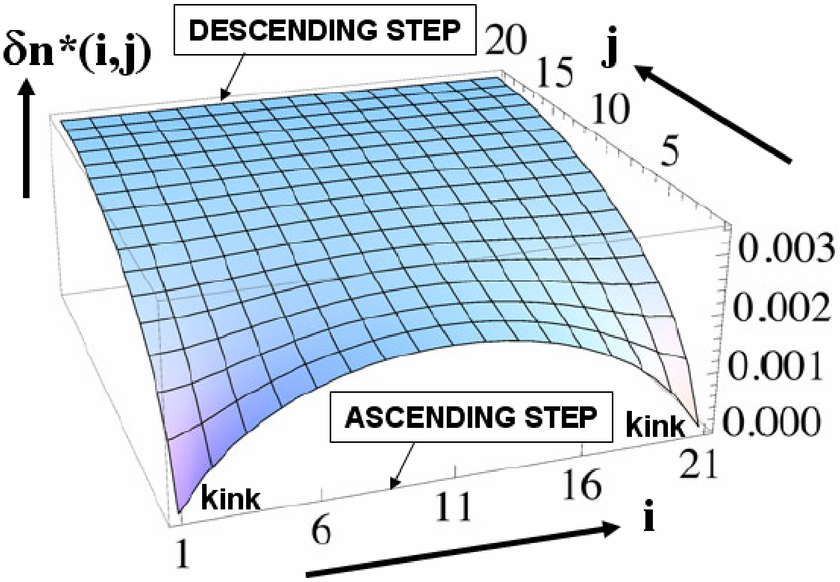

Figure 4: 3D plot of scaled excess adatom density, δn(i,j), for infinite ES barrier, h_e=h, and h/F=10^4 with L=20, W=20, and βϕ⊥ = 1. The foreground of the plot shows the kink sites at i=1 and i=21 where the adatom density is lowest, and also the variation of adatom density along the step edge peaking midway between the kink sites.*

Table 1: $K_\pm(\infty)$ versus kink spacing L for perfect vicinal surfaces with broad terraces. Results are shown for infinite ES barrier ($\delta_-=\infty$) with $\delta_+=0$, and no attachment barriers $\delta_\pm=0$. We have chosen $h_e/h=1$ and βϕ⊥= 1.

Kink spacing, L	$aK_+(\infty)/D$ for $\delta_-=\infty$, $\delta_+=0$	$aK_\pm(\infty)/D$ for $\delta_\pm=0$
20	0.133647	0.088766
40	0.045592	0.032735
60	0.025228	0.018814
80	0.016810	0.012835
100	0.012355	0.009589
150	0.007158	0.005702
200	0.004905	0.003971

Next, we consider the dependence of K_+ on terrace geometry. In Fig.5a, we show results for K_+ versus kink separation L for $h_e/h=1$ with fixed W=100 and βϕ⊥ = 1. It is clear that $K_+\rightarrow 0$ as $L\rightarrow\infty$, and for larger L this decrease is described by (12). Note that for L=1 (an entire step edge composed of kinks), the model reduces to a 1D model with a standard BCF Dirichlet BC so that $K_+ = \infty$. Next, in Fig.5b, we show results for K_+ versus terrace width W for $h_eh/=1$ with fixed

L=40 and $\beta\phi_\perp = 1$. It is clear that K_+ converges to a finite value as $W \to \infty$, and that the functional form is described well by (13) where $aK_+(\infty)/D=0.0455$. See Table I for a list of values of $K_\pm(\infty)$ for various L.

Now, we turn to consideration of the dependence of K_+ on model dynamics and energetics. We have already noted that K_+ depends only on the ratio h_e/h rather than on h and h_e separately. Behavior is shown in Fig.6a for L=30, W=100, and $\beta\phi_\perp = 1$. Apart from some non-linear variation for small $h_e/h<1$, behavior is essentially linear $K_+ \sim c \cdot h_e/h$. This form recovers the classic result $K_+ \to \infty$ as $h_e \to \infty$ in the absence of an attachment barrier. This limiting behavior is due to complete equilibration of the adatom density at the step edge. The asymptotic linear dependence derives from the feature that the flux J_+ converges to a finite value for $h_e = \infty$, and the deviation of step edge densities from equilibrium scales like $\langle \delta n^*_{edge} \rangle \sim h/h_e$.

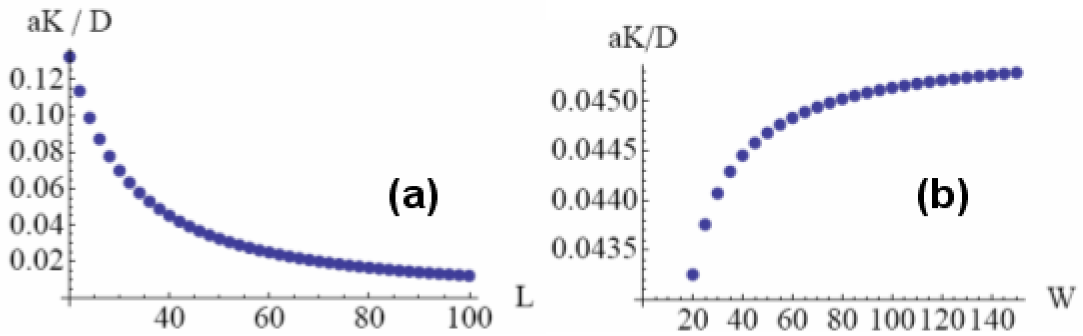

Figure 5: Behavior of $K=K_+$ for an infinite ES barrier and $\delta_+=0$ for $h_e/h=1$ and $\beta\phi_\perp = 1$: (a) K_+ versus L with fixed W=100; (b) K_+ vs W for $h_e/h=1$ with fixed L=40.

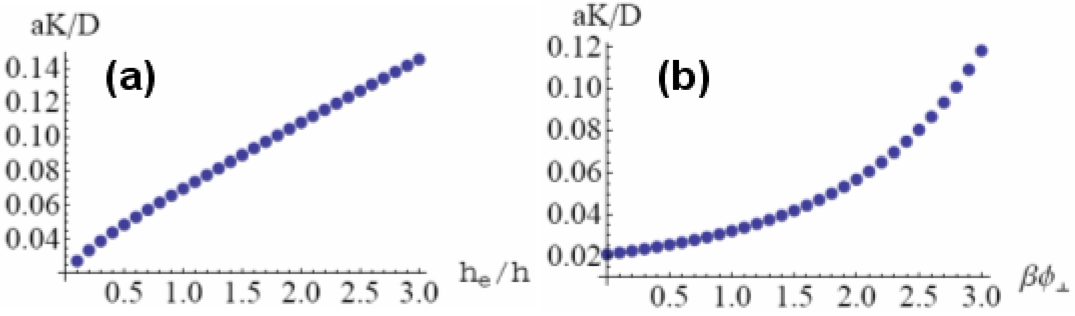

Figure 6: Behavior of $K=K_+$ for an infinite ES barrier and $\delta_+=0$: (a) K_+ versus h_e/h for L=30, W=100, and $\beta\phi_\perp = 1$; (b) K_+ versus $\beta\phi_\perp$ for $h_e/h=1$ and L=W=50.

Finally, we consider the dependence of K_+ on $\beta\phi_\perp$. Intuitively, stronger bonding to the step edge should facilitate capture of diffusing adatoms at kinks. Thus, K_+ should increase with increasing $\beta\phi_\perp$. For $\beta\phi_\perp=0$ where capture is least efficient, K_+ should still retain a finite non-zero value. Numerical results are presented in Fig.6b for L=W=50 and $h=h_e$ (where $aK_+/D = 0.02097$ for $\beta\phi_\perp=0$ and $aK_+/D = 0.03216$ for $\beta\phi_\perp=1$) confirming this behavior. To further elucidate this behavior, we note that as $\beta\phi_\perp \rightarrow \infty$, an exact analysis is possible for the fundamental equations (4) or (5). In this regime, the equations for the rescaled adatom density on the terraces all have the generic form. However, equations for the rescaled adatom densities along the step edge decouple from the terrace densities reducing to a simple 1D discrete diffusion equation (provided that $h_e>0$) with a vanishing deposition source. Thus, the steady-state solution for these edge densities approaches the equilibrium value. Correspondingly, since $<\delta n^*_{edge}> \rightarrow 0$, one has that $K_+ \rightarrow \infty$.

6 Zero Attachment Barriers $\delta_\pm$ =0: Perfect Vicinal Surfaces

We consider here the case of a perfect vicinal surface with terraces of width W and no attachment or ES barriers, $\delta_\pm=0$, where by symmetry one has that $n_+^* = n_-^*$ and that $K_+ = K_-$. In this case, since all steps are equivalent, it is clear that the *step velocities* are the same for all steps and that these are just determined by the single terrace width, W (and the deposition flux). By symmetry together with application of the discrete Gauss' Theorem, the attachment fluxes from both sides of each step are equal, and adopt a value $J_\pm = ½\, F(W-1)$. In the case, the capture zone (CZ) for each step extends symmetrically to the mid-point of the terrace on either side. Since the total flux to each step is the same as for the case of infinite ES barrier, one might expect similar excess step densities, $<\delta n^*_{edge}>$. In fact, we find this density for $\delta_\pm=0$ is larger than that for the case of infinite ES barrier in Sec.5, which implies that the K-value is smaller. See Table I.

First, we consider the dependence of $K_\pm$ on terrace geometry. We find that that $K_\pm \rightarrow 0$ as kink separation $L \rightarrow \infty$. For larger L, the functional form of this decrease is described by (12) as follows from analysis of an appropriate semi-discrete version of the model. For L=1, the 2D model reduces to a 1D model with a standard BCF BC so that $K_\pm = \infty$. As an aside, the value of $K_\pm$ for kink separation L with $\delta_\pm=0$ corresponds closely to the value of K_+ for infinite ES barrier ($\delta_-=\infty$) with $\delta_-=0$ for kink separation 1.25L (with the same W and $\beta\phi_\perp$). In addition, we have examined the convergence of $K_\pm$ to a finite value as $W \rightarrow \infty$, and the functional form is described well by (13) given in Sec.4D just as for the case of infinite ES barrier. See Table I for a list of values of $K_\pm(\infty)$ for various L.

Next, we turn to consideration of the dependence of K_+ on model dynamics and energetics. Apart from some non-linear variation for $h_e/h<1$, one finds an essentially linear variation $K_\pm \sim c \cdot h_e/h$. This follows since $J_\pm$ converge to a finite value for $h_e = \infty$, and one expects that $<\delta n^*_{edge}> \sim h/h_e$, just as for the case on infinite ES barrier. Finally, we consider the dependence of K_+ on $\beta\phi_\perp$. K_+ increases with increasing $\beta\phi_\perp$ from a non-zero value for $\beta\phi_\perp=0$ where capture is least efficient, and $K_+\to\infty$ as $\beta\phi_\perp\to\infty$, i.e., the same behavior for the same reasons as with an infinite ES barrier. For L=W=50 and $h=h_e$, one has $aK_+/D = 0.01666$ for $\beta\phi_\perp=0$ and $aK_+/D = 0.02357$ for $\beta\phi_\perp=1$.

7 Zero Attachment Barriers $\delta_\pm$ =0: Imperfect Vicinal Surfaces

Here, we consider the case of imperfect vicinal surfaces with a distribution of terrace widths. For simplicity, we assume the same density (or separation) of periodically distributed kinks on all steps. Again, kinks on different steps are aligned in the direction orthogonal to the steps. A key feature is that for any distribution of terraces widths in the absence of attachment and ES barriers, the limiting value of the adatom density is the same approaching each step from either side, i.e., n_+ = n- in (2), or $n_+^* = n_-^*$ in the discrete model. Thus, the step permeability term still drops out of (2), and we can determine the (generally different) values of K_+ and K- for each step based on the algorithm described at the end of Sec.4.

7.A. Bi-periodic vicinal surfaces

We consider here the simplest "imperfect case" of a bi-periodic vicinal surface with alternating narrower and broader terraces of widths W_a and W_b. In this case, by reflection symmetry, there is a *single* excess adatom density $<\delta n^*_{edge}>$ at both types of steps. Also, the adatom density profile is symmetric about the middle of each type of terrace. A typical adatom density profile averaged along the steps is shown in Fig.7 for the case of kink spacing L=50, terrace widths W_a=50 and W_b=100, h_e=h, and $\beta\phi_\perp = 1$. In is clear that the capture zone (CZ) for each step extends to the mid-point of the terraces on either side. It is also clear that the velocities of all steps are identical.

In further analysis, we just focus on behavior in the regime of broad terraces. Let $K_\pm^a$ denote the kinetic coefficients for a bi-periodic vicinal surface associated with terraces of widths W_a, and $K_\pm^b$ for the terrace of width W_b. By symmetry, one has that $K_+^a = K_-^a$ and $K_+^b = K_-^b$ since the flux to steps on either side of the same terrace is identical, and since there is a single excess adatom density at steps. Then, it follows that

$$K_\pm^b / K_\pm^a \approx W_b/W_a, \tag{14}$$

In addition, from numerical data, we find that

$$K_\pm^a + K_\pm^b \approx 2\, K_\pm(\infty), \tag{15}$$

where $K_\pm(\infty)$ denotes the value of the kinetic coefficients for a perfect vicinal surface in the limit of broad terraces, and with the same kink density as the bi-periodic case. As an example, for kink separation $L=50$ with $h_e=h$ and $\beta\phi_\perp = 1$ where $2\, aK_\pm(\infty)/D = 0.048158$, we find that for very broad terraces one has $aK_\pm^b/D = 0.032105$ and $aK_\pm^a/D = 0.016053$ for $W_b/W_a = 2$.

The relation (15) can be understood in terms of the behavior of the single excess adatom step density, $<\delta n^*_{edge}>_{BI}$, in the bi-periodic system. Let $<\delta n^*_{edge}>_a \propto W_a$ denote the excess density for a perfect vicinal surface with finite terrace width W_a, etc.. Provided that the excess adatom density is just determined by the average two-dimensional kink density in the system, then it immediately follows that

$$\tfrac{1}{2}(W_a+W_b)/<\delta n^*_{edge}>_{BI} \approx W_a/<\delta n^*_{edge}>_a \approx W_b/<\delta n^*_{edge}>_b. \tag{16}$$

which is equivalent to the sum rule (15). An equivalent perspective comes from the observation that (16) implies that the excess adatom step density $<\delta n^*_{edge}>_{BI}$ in the bi-periodic systems equals that for a perfect vicinal surface with terrace width equal to the average of the terraces in the bi-periodic system.

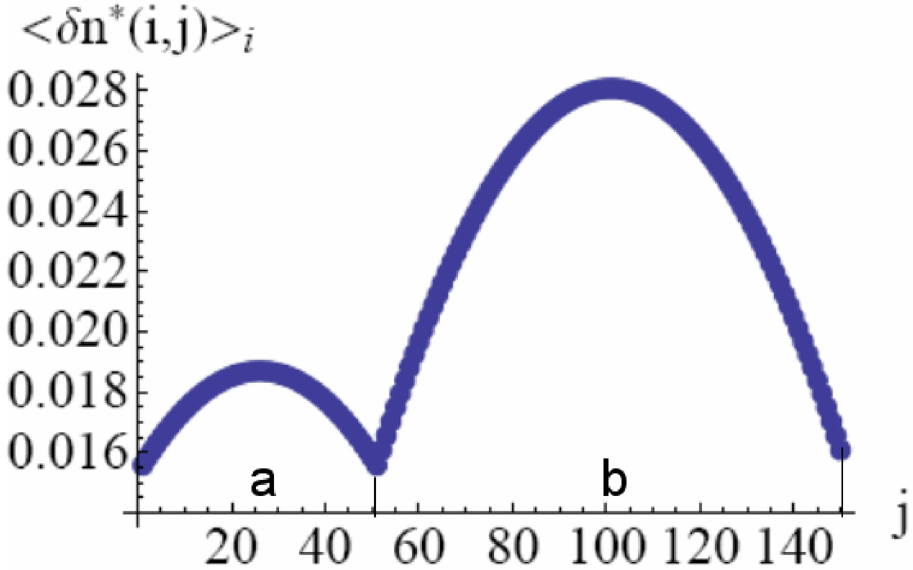

Figure 7: Scaled excess adatom density profile <δn> across the terraces (averaged along steps) for a bi-periodic system with terrace widths* W_a*=50 and* W_b*=100 and zero attachment barriers* $\delta_\pm=0$*. Other parameters are* $h_e=h$*,* $h/F=10^5$*, L=50, and* $\beta\phi_\perp= 1$*. Note the unique excess adatom density at step edges, but the distinct attachment fluxes from different sides of the steps.*

7.B. Tri-periodic and other vicinal surfaces

Consider tri-periodic vicinal surfaces with cyclically alternating terraces of width W_a, W_b, and W_c, but the same kink separation L on all steps. This case is more representative of the general situation. Here, there are three types of steps: S_{ab} separating terraces of width W_a and W_b, and similarly S_{bc}, and S_{ac}. For each step, there are in general two distinct kinetic coefficients $K_\pm^{ab}$ for S_{ab}, etc. No longer is it possible to simply determine diffusive fluxes to steps since the boundaries of the capture zones (CZ's) for each step do not necessarily correspond to the middle of the terraces on either side. Also, in general, each step has a different excess adatom density. However, from numerical analysis for broad terraces, we find analogous to (15) that

$$K_+^{ab} + K_-^{ab} + K_+^{bc} + K_-^{bc} + K_+^{ac} + K_-^{ac} \approx 6\, K_\pm(\infty), \qquad (17)$$

where $K_\pm(\infty)$ denotes the value of the kinetic coefficients for a perfect vicinal surface in the limit of broad terraces, and with the same kink density as the tri-periodic case. For example, in the case where W_a = 22m, W_b = 30m, W_c = 37m, and L=50, we show the adatom density profile in

Fig.8 and give all six K-values in Table II for the case m=5. More generally, we find that the values of the above 6 aK/D-values sum to 0.136766, 0.143657, 0.143983, and 0.144424 for m = 1, 5, 10, and 100, respectively, which should be compared with 6 $aK_{\pm}(\infty)/D$= 0.144473.

Table 2: Values of aK/D for a tri-periodic vicinal surface with terrace widths W_a=22m, W_b=30m, and W_c=37m for m=5, and zero attachment barriers $\delta_{\pm}=0$. Other parameters are $h_e/h=1$, L=50, and $\beta\phi_{\perp} = 1$, so 6 $aK_{\pm}(\infty)/D$= 0.144473. The six aK/D values sum to 0.143657.

aK_+^{ac}/D	aK_-^{ab}/D	aK_+^{ab}/D	aK_-^{bc}/D	aK_+^{bc}/D	aK_-^{ac}/D
0.020269	0.017307	0.021182	0.027904	0.030848	0.026965

In contrast to all the previous examples, in the case of the tri-periodic vicinal surface, the step velocities differ and are non-trivial. According to the general strategy laid out in Sec.2, knowledge of the six K-values (e.g., from Table II for m=5) together with the result (3) allows determination of the diffusive fluxes to each step. Then, adding the simple constant contribution from direct deposition at each step allows determination of the step velocities. It is appropriate to compare the results of our analysis with that from a classical BCF treatment where the adatom densities are symmetric about the center of each terrace. Thus, the diffusive flux to the steps on the left and right side of each terrace are equal (as for any case with equal K-values for the left and right steps). Thus, deviations from classical BCF behavior are due to difference between K-values for the steps at the left and right ends of the different terraces (cf. Table II). The fact that the attachment lengths associated with the K-values are of the order of the terrace widths means that these deviations are significant.

To interpret the sum rule (17) in terms of the excess adatom step densities, let $\langle\delta n^*_{edge}\rangle_a$ denote this density for a perfect vicinal surface with broad terraces of width W_a, etc. For the tri-periodic vicinal surface, let $\langle\delta n^*_{edge}\rangle_{ab}$ denote the excess adatom density at step S_{ab}, and let $W^{\pm}_{ab}$ denote the width of the capture zone (CZ) for this step on the lower (+) and upper (-) terrace. Thus, $W_{ab} = W^+_{ab} + W^-_{ab}$ denotes the full width of the capture zone on both sides of the step. These quantities are defined analogously for other steps. Then, it follows that $W_{ab} + W_{bc} + W_{ac} \approx W_a + W_b + W_c$. See Fig.8. Also since $K_{\pm}^{ab} \propto W^{\pm}_{ab}/\langle\delta n^*_{edge}\rangle_{ab}$ and thus $K_+^{ab} + K_-^{ab} \propto W_{ab}/\langle\delta n^*_{edge}\rangle_{ab}$, etc., (17) is instructively recast as

$$W_{ab}/\langle\delta n^*_{edge}\rangle_{ab} + W_{bc}/\langle\delta n^*_{edge}\rangle_{bc} + W_{ac}/\langle\delta n^*_{edge}\rangle_{ac} = W_a/\langle\delta n^*_{edge}\rangle_a + W_b/\langle\delta n^*_{edge}\rangle_b + W_c/\langle\delta n^*_{edge}\rangle_c. \quad (18)$$

where all three terms on the right-hand-side have the same value. In special cases for tri-periodic systems, e.g., where two of the terraces have equal width, then (18) can be reduced further.

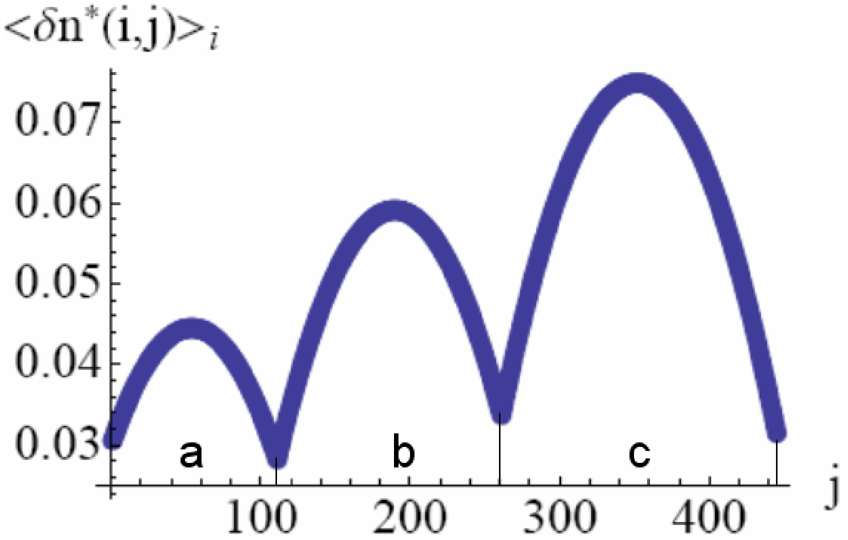

Figure 8: Scaled excess adatom density profile <δn> across the terraces (averaged along steps) for tri-periodic case with terrace widths* $W_a = 22m$, $W_b = 30m$, *and* $W_c = 37m$ *for m=5, and zero attachment barriers* $\delta_\pm=0$. *Excess adatom densities at the steps are* $\langle\delta n^*_{ac}\rangle \approx 0.0305$, $\langle\delta n^*_{ab}\rangle \approx 0.0282$, $\langle\delta n^*_{bc}\rangle \approx 0.0336$. *Other parameters are* $h_e=h$, $h/F=10^5$, $L=50$, *and* $\beta\phi_\perp = 1$. *Note the distinct excess adatom densities at step edges.*

For another perspective leading to a more complete analysis, we note that the K's for the tri-periodic system correspond to those from various bi-periodic systems for suitable choices of terrace widths (and the same kink separation L). For example, $K_\pm^{ab}$ above corresponds to K's in a bi-periodic system with terraces of width $2W^+_{ab}$ and $2W^-_{ab}$, where K_+^{ab} (K_-^{ab}) corresponds to $K_\pm$ for the terrace of width $2W^+_{ab}$ ($2W^-_{ab}$). Then $\langle\delta n^*_{edge}\rangle_{ab}$ corresponds to the unique excess adatom step density in this bi-periodic system. See Fig.9. Thus, $W_{ab}/\langle\delta n^*_{edge}\rangle_{ab} = W/\langle\delta n^*_{edge}\rangle$ for any perfect vicinal surface with terraces of width W and excess adatom step density $\langle\delta n^*_{edge}\rangle$. Extending this analysis for other steps recovers (18).

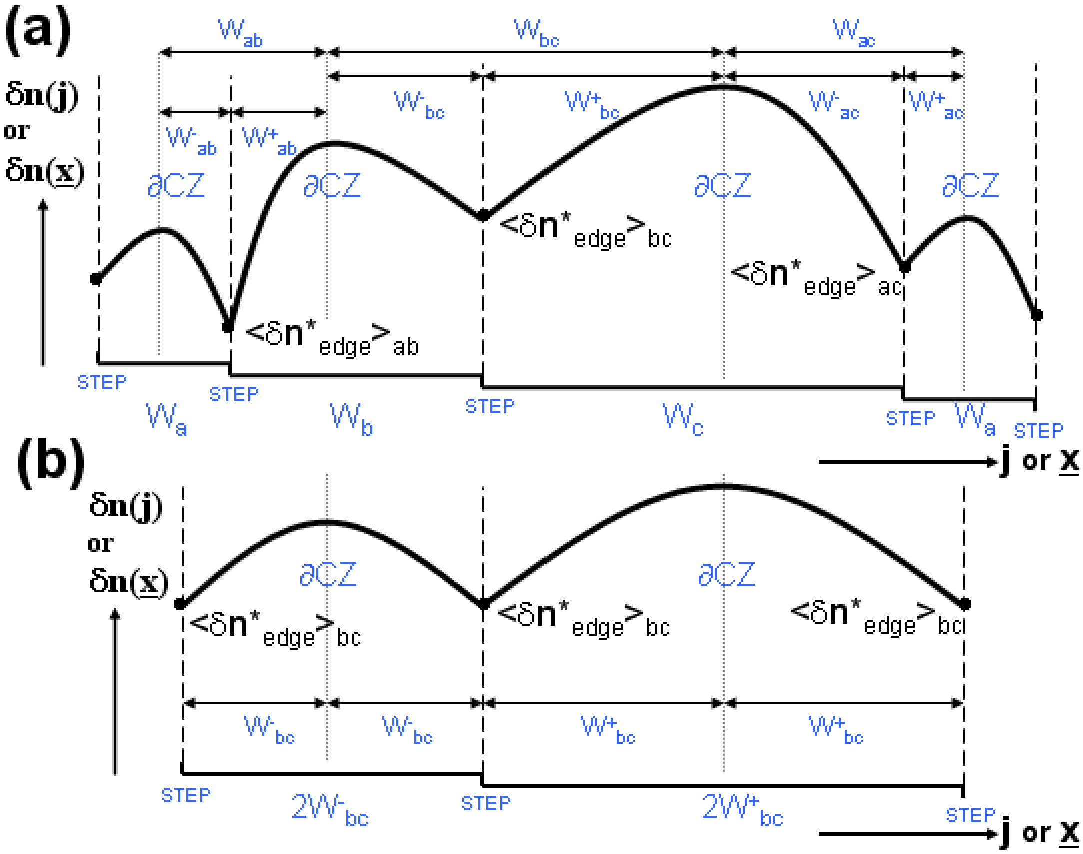

Figure 9: Schematic comparing: (a) scaled excess adatom density profile across the terraces (averaged along steps) for a tri-periodic system; and (b) the profile in one of the "corresponding" bi-periodic systems. Also indicated are the widths of terraces and of various capture zones (CZ), as well as the boundaries of those CZ's (∂CZ).

In more general cases of vicinal surface with higher-order periodicity, one finds a natural generalization of (15) or (17). Broader terraces with smaller neighbors tend to have larger K-values, and the opposite is true for smaller terraces with broader neighbors. The demonstration of these *general K-sum rules* follows from extending the analysis in the previous paragraph.

8 Other Cases Without a Permeability Contribution

In addition to the cases discussed in Sec.5-7, there are other situations (some are discussed here) where the limiting value of the adatom density is the same approaching each step from either side, i.e., $n_+ = n-$ in (2), or $n_+* = n_-*$ in discrete models. Thus, again the step permeability term still drops out of (2), and $K_\pm$ can be determined from the algorithm in Sec.4.

8.A. Finite attachment barriers

For the case of an *infinite ES barrier* where P=0 and behavior on each terrace is isolated from or independent of that on other terraces, we consider the effect of including a *non-zero step attachment barrier* $\delta_+ > 0$ to the ascending step. Intuitively, one expects that the step edge density "behind the attachment barrier" should become more equilibrated and spatially uniform with increasing δ_+. As a result, behavior should reduce to that of the 1D model with an attachment barrier in Appendix A. Consequently, $K_+ = D/L_+$ should asymptote to the 1D result where $L_+ \sim a \exp(\beta\delta_+)$, as $\delta_+ \rightarrow \infty$. This behavior is indeed realized and shown in Fig.10a for $h_e/h=1$, L=50, W=50, and $\beta\phi_\perp = 1$, and $D/(aK_+) \approx \exp(\beta\delta_+) + 77.2$ for large δ_+.

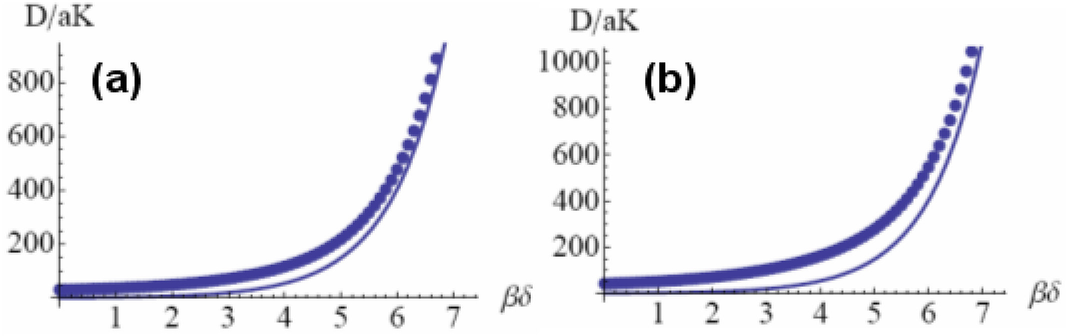

Figure 10: Variation of K-value with finite attachment barrier for $h_e/h=1$, L=50, W=50, and $\beta\phi_\perp = 1$: (a) $D/(aK_+)$ versus $\beta\delta$ with $\delta=\delta_+$ for an infinite ES barrier; (b) $D/(aK_\pm)$ versus $\beta\delta$ for symmetric attachment barrier $\delta_\pm = \delta$. The solid curves show the function $\exp(\beta\delta)$ versus $\beta\delta$.

For a *perfect vicinal surface* with terraces of width W, we consider the case of *symmetric non-zero step attachment barriers* $\delta = \delta_+ = \delta_- > 0$. Here, by symmetry, the limiting value of the adatom density is the same approaching the step from either side, i.e., $n_+^* = n_-^*$, and one also has that $K_+ = K_-$. Again, since the step edge density "behind the attachment barrier" should become more equilibrated with increasing $\delta_\pm$, behavior should reduce to that of the 1D model, so $K_\pm = D/L_\pm$ should asymptote to the 1D result $L_\pm \sim a \exp(\beta\delta)$. This behavior is shown in Fig.10b for $h_e/h=1$, L=50, W=50, and $\beta\phi_\perp = 1$, and $D/(aK_\pm) \approx \exp(\beta\delta) + 155.3$ for large δ. One might anticipate that we could extend consideration of the case of symmetric non-zero step attachment barriers to imperfect vicinal surfaces and still retain the equality $n_+^* = n_-^*$. However, numerical data for a bi-periodic vicinal surface with $W_a \neq W_b$ demonstrates that this is not the case, the adatom density for the broader terraces extrapolating to a higher value at the step edge. In fact, this behavior is consistent with the relations (7) determining extrapolated densities.

8.B. Varying kink separations on AB-vicinal surfaces

Finally, in contrast to all cases considered above in this and previous sections, we consider a situation where the *kink separation differs on different steps*. Motivated by the anisotropic SOS model described in Sec.3 which provides a simple model for an AB-vicinal surface, we specifically analyze the case where the kink separation alternates between L and nL (with $n>1$) on a vicinal surface where all terraces have width W. We choose $L=40$, $n=2$, and $W=15$. Different kink densities on different steps correspond to different attractive interactions between adatoms in the direction of the step edge. Using the terminology of the anisotropic SOS model, we choose $\beta\phi_s = 5.06$ and $\beta\phi_w = 4.36$ to be consistent with our choice of kink separations [30]. Thus, in our discrete 2D deposition–diffusion equation modeling, we choose different values of $\beta\phi_\pm$ for the two types of steps alternating between $\beta\phi_s$ for B-type steps with $L=40$, and $\beta\phi_w$ for A-type steps with $L=80$. A schematic of the steady-state adatom density for this choice of parameters is shown in Fig.11.

Quantitative analysis of the above system yields aK/D-values of 0.589 for the B-type step with higher kink density ($L=40$), and 0.0817 for the A-type step with lower kink density ($L=80$). Then, application of (3) allows determination of the diffusive flux to each step. We find the ratio of diffusive fluxes to A-type and B-type steps is 0.47 (the former being smaller). Accounting for direct deposition at steps on terraces of width $W=15$, one obtains a slightly modified ratio of total fluxes to A-type and B-type steps of 0.49. Thus, if V_A (V_B) denotes the velocity of A-type (B-type) steps for the configuration of Fig.11, it follows that $V_A/V_B = 0.49$. As might be expected given the higher K-value, the B-type step has the higher velocity, consistent with simulation results of Sec.3. An independent way to assess the differing step velocities is provided by Fig.11 where we also show the boundaries (∂CZ) of the capture zones for both steps. Clearly, the B-type step with higher kink density has a significantly larger CZ (quantified below), consistent with the larger velocity. In summary, the different K-values for different steps induce different velocities even starting with a perfect “equilibrium” AB-vicinal surface with uniform terrace widths.

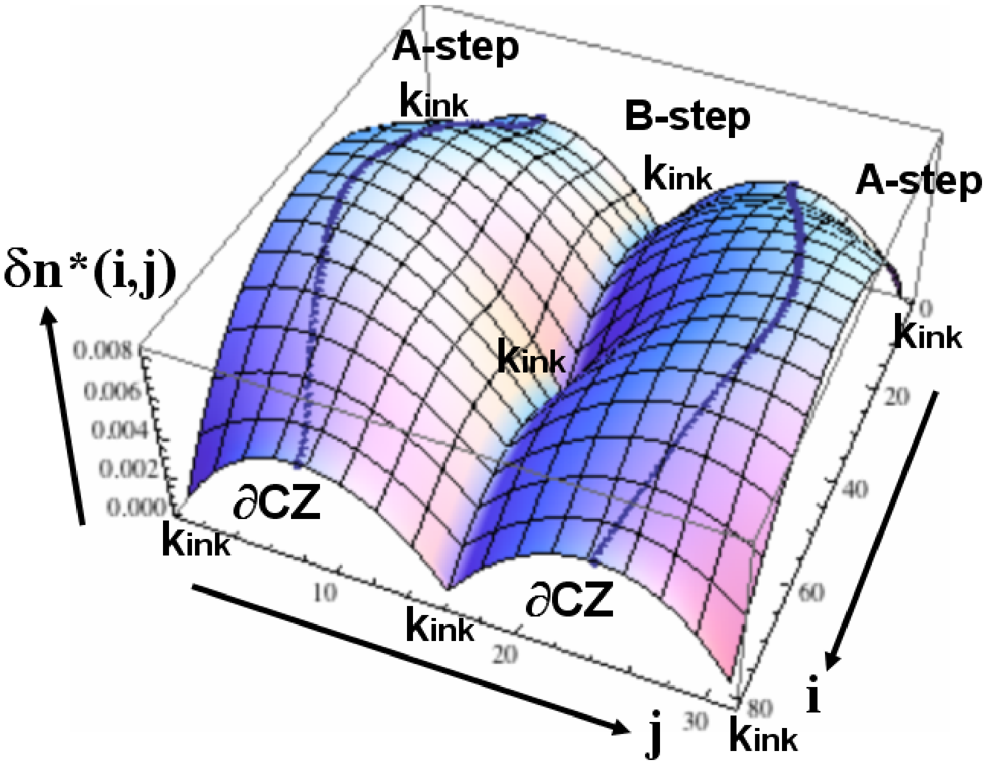

Figure 11: Scaled excess adatom density $\delta n^*(i,j)$ for system with alternating kink density on adjacent steps. We choose kink separations of $L=40$ and $L=80$, a terrace width of $W=15$, and set $h_e=h$, $h/F=10^5$, and $\beta\phi_\perp = 1$. The plot also shows location of the kinks and the non-linear capture zone boundaries (∂CZ).

One might hope that this system could be analyzed in terms of simpler systems with a single kink separation of L and of nL and the appropriate choice of $\beta\phi_\perp$ (cf. our analysis of tri-periodic systems in terms of bi-periodic systems). However, in contrast such analyses above, such an exact analysis is not possible since, e.g., the capture zone boundary between the two steps is not a straight line. See Fig.11. Despite this feature, one can still define an average width, $W_> = 20.3$ ($W_< = 9.7$), of the capture zone for the B-type (A-type) step, where $W_> + W_< = W$. In fact, we note that $W_</W_> = 0.48$ quite consistent with the above estimate of the ratio of step velocities V_A/V_B. Then, to a first approximation, the step edge with kink separation L will have the same $\langle\delta n^*_{edge}\rangle$ as for a perfect vicinal terrace width $2W_>$ with kink separation L and the appropriate value of $\beta\phi_\perp$ and the other parameters (and analogously for the step with fewer kinks). Consequently, $K_\pm$ for the B-type (A-type) step should roughly equal the value of these quantities for a perfect vicinal surface with kink separation of L (nL) and suitable choices of other parameters. The CZ boundaries in Fig.11 are quite bent, limiting the accuracy of the above approximation, but we have checked its validity in other cases with straighter boundaries.

9 Summary

We have implemented a new strategy to obtain insight into the appropriate kinetic coefficients, $K_{\pm}$, for BCF-type boundary conditions for step flow under potentially non-equilibrium conditions. Our approach prescribes as input the geometry of the vicinal surface including the distribution of kinks along step edges. Then, we solve discrete 2D deposition-diffusion equations for this geometry to determine the adatom density distribution, and thus fluxes of attachment at (kinks along) step edges. We obtain explicit values for the $K_{\pm}$ mostly for cases where there is no barrier to attachment to steps and where the step permeability is not relevant. Specifically, we characterize the dependence of the $K_{\pm}$ on the kink density and terrace width, and also obtain a sum rules for these coefficients for imperfect vicinal surfaces with different terrace widths. The systems considered would traditionally be described by the classical BCF picture which equates the adatom density to its equilibrium value at the step edge (corresponding to $K=\infty$). However, this classical treatment fails to capture such phenomena as non-equilibrium step pairing observed in an anisotropic SOS model of an AB-vicinal surface with alternating types of steps [18]. In contrast, our approach is successful.

Our new approach is somewhat complementary to other recent mean-field rate equation modeling based on the terrace-step-kink picture [12-17]. As noted previously, this approach specifies diffusion fluxes or adatom densities at steps as input and determined the dynamic steady-state step structure (in contrast to our specification of step structure and solution of the deposition-diffusion equations). However, both our analysis and that of Margetis and Caflisch (MC) [17] assess kinetic coefficients. We obtain precise numerical values and assess dependence on various geometric parameters for arbitrary energetic and diffusion parameters. MC perform a perturbation analysis to obtained general expressions in the regime of small Peclet number (large edge diffusion). Thus, direct comparison is difficult. However, there is consistency, e.g., between our increase in K-values with increasing kink density and MC's increase with increasing step misalignment.

One perspective on the shortcomings of the classical BCF picture, motivating and highlighted in our work, is that it is geared towards situations with high kink densities and efficient equilibration of the adatom density at step edges. However, for typical kink densities along steps, there is always some inhibition to equilibration (less facile equilibration corresponding to smaller kinetic coefficients). To assess the degree of equilibration, it is instructive to introduce attachment lengths $L_{\pm} = D/K_{\pm}$ (less facile equilibration corresponding to larger attachment lengths). The classical BCF picture does apply in the regime where typical terraces widths far exceed attachment lengths (corresponding to a quantitative characterization of "high kink density"). However, in the case of step pairing described above, this condition is not met. More generally, it is known that traditional continuum near-equilibrium treatments may fail when the relevant characteristic length in the system becomes comparable to natural length scales determined by the microscopic parameters of the model. For example, for diffusion and shape-relaxation of 2D islands on surfaces mediated by edge diffusion, this failure occurs when the linear size of the island becomes comparable to the equilibrium kink separation or to another characteristic length associated with inhibited edge diffusion [35,36].

In our analysis above, with one exception, we have restricted our attention to cases where the limiting value of the adatom density is the same approaching the step from either side, i.e., $n_+ = n-$ in (2), or $n_+^* = n_-^*$ in the discrete model. This means that the permeability term drops out of the traditional BCF BC allowing us to determine the kinetic coefficients $K_{\pm}$ in an unambiguous fashion. It should be emphasized however that except in the case of infinite ES barrier discussed in Sec.5, the steps in our 2D discrete deposition-diffusion equation model should be regarded as permeable. Adatom diffusion across steps is possible without incorporation at kinks. In fact, one would expect permeability to increase with decreasing bond strength $\phi_{\perp}$ and decreasing step edge hop rate h_e. In a more general context, interest in and the importance of step permeability arose in near-equilibrium situations were there were spatial non-uniformities in chemical potential of adatoms causing flow across permeable steps [10,19]. In future work, we will explore various strategies to provide insight into step permeability in our model.

Acknowledgments

This work was supported by the Division of Chemical Sciences (Basic Energy Sciences) of the US Department of Energy (USDOE) through the Ames Laboratory Chemical Physics and PCTC projects. Ames Laboratory is operated for the USDOE by Iowa State University under Contract No. DE-AC02-07CH11358. We thank Da-Jiang Liu for assistance with the atomistic lattice-gas modeling and KMC simulation, and also for valuable discussions.

Appendix A: Discrete 1D Deposition-Diffusion Model for Stepped Surfaces

In this "standard" discrete 1D model, the stepped surface is described by a one-dimensional array of sites labeled j = …, -2, -1, 0, 1, 2,… with positions $x_j = ja$ where 'a' denotes the surface lattice constant. These sites correspond to rows of sites parallel to the step edge in the 2D model. We focus on the region surrounding a step edge or "step site" at j=0, where sites j = -1, -2,.. are on the adjacent upper terrace, and j = 1, 2,.. are on the lower terrace. As in our 2D modeling, we also assume that attachment and detachment from the step edge do not alter the step location from j=0. Thus, we adopt a quasi-static type approximation where step motion is regarded as slow compared to relaxation of the adatom diffusion field. However, one key simplification in this model relative to the 2D case is that we assume that the adatom density right at the step edge is equilibrated. We can allow direct deposition at the step site, but this does not affect analysis of the steady-state adatom density, rather just adding a simple contribution to the step velocity. See Fig.12 for a schematic.

Notation is selected by analogy with our 2D model. We let n(j) denote the adatom density at site j, and set n(0) =1 at the step site. F denotes the deposition flux per site; h denotes the rate of hopping between adjacent terrace sites; $h_{\pm} = \exp(-\beta\delta_{\pm})h$ denote the possibly modified hop rates from the adjacent terrace site j = ±1 to the step site j=0 due to attachment barriers $\delta_{\pm}$; and h_p denotes the rate of direct hopping between sites j= +1 and -1 (reflecting a direct channel for step permeability). Corresponding diffusion coefficients are denoted by $D = a^2h$, $D_{\pm} = a^2h_{\pm}$, and $D_p = a^2h_p$. Finally, we let ϕ_b denote the strength of the bonding of adatoms at step edges (corresponding to bonding at kink sites in a 2D model). As a result, $n_{EQ} = \exp(-\beta\phi_b)n(0) = \exp(-$

$\beta\phi_b$) represents the equilibrium adatom density at the step edge. Also, detailed-balance implies that the rate of hopping from the step edge site j=0 to sites j = ±1 is given by $\exp(-\beta\phi_b)\, h_{\pm}$.

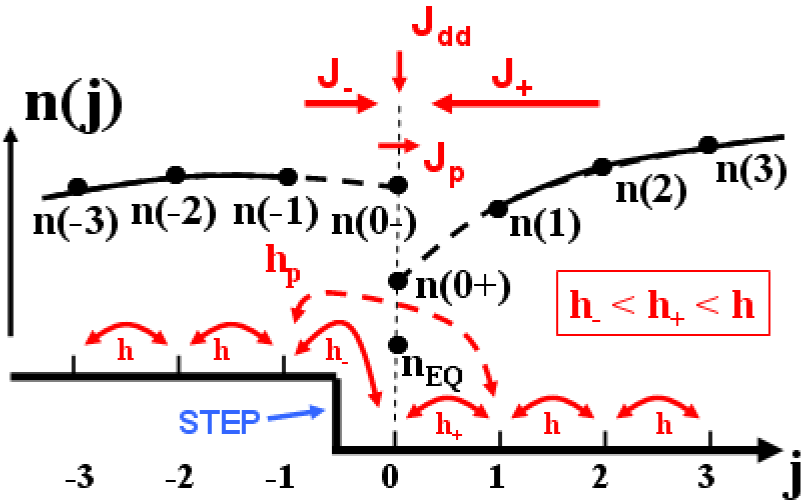

Figure 12: Schematic of adatom density in the standard 1D discrete deposition-diffusion model in the vicinity of a step edge. Also shown are: the adatom hop rates; total diffusion fluxes reaching the step edge, $J_{\pm}$; the flux across the step due to permeability, J_p; and the flux to the step due to "direct deposition", J_{dd}. The latter does not affect the adatom density analysis.

Thus, one has the following discrete steady-state deposition-diffusion equations

$$d/dt\, n(j) = F + h[n(j+1) - 2n(j) - n(j-1)] \approx 0, \text{ for } j>1, \tag{A1}$$

$$d/dt\, n(1) = F + h[n(2) - n(1)] + h_+[n_{EQ} - n(1)] + h_p[n(-1) - n(1)] \approx 0, \tag{A2}$$

with an analogous equations for n(-j).

A particularly important concept is the idea of smoothly extrapolating or "analytically extending" the values n(j) of the adatom densities on lower terrace to the right of the step (j>0) to an extrapolated value n(0+) at the step site. This extrapolated value is obtained from the additional equation [3,4]

$$\begin{aligned} d/dt\, n(1) &= F + h[n(2) - 2n(1) + n(0+)] \\ &= F + h[n(2) - n(1)] + h[n(0+) - n(1)] \approx 0, \end{aligned} \tag{A3}$$

which must be consistent with (A2). The key point here is that by determining n(0+) through a generic equation of the form (A1), one can argue that n(0+) is a natural or analytic extension of n(j) for j>0. Similarly, one can analytically extend those n(j) for the upper terrace on the left of the step (j<0) to n(0-). Another perspective is that we define n(0+) so that the diffusive flux of atoms to the step from the right (J_+) and left (J-) satisfy

$$\begin{aligned} J_+ &= h_+[n(1) - n_{EQ}] + h_p[n(1) - n(-1)] = h[n(1) - n(0+)], \text{ and} \\ J_- &= h_-[n(-1) - n_{EQ}] + h_p[n(-1) - n(1)] = h[n(-1) - n(0-)]. \end{aligned} \tag{A4}$$

Appendix B: Coarse-Graining Discrete 1D Deposition-Diffusion Equations

The above discrete 1D model is connected to a coarse-grained continuum model by assuming that the corresponding smooth continuous adatom density per unit length, n(x), satisfies $n(x_j = ja) = n(j)/a$ at discrete set of spatial points x_j. One then manipulates (A2) and (A3) to extract boundary conditions for n(x) at the step edge x=0. The discrete approximation to the right derivative at x=0 is

$$dn/dx|_{0+} \approx [n(1) - n(0+)]/a^2. \tag{B1}$$

Thus, comparing (A2) and (A3), one obtains

$$D\, dn/dx|_{0+} \approx J_+ \text{ and } -D\, dn/dx|_{0-} \approx J_-. \tag{B2}$$

At this point, one has a choice in formulating BCF-type boundary conditions of the type (2).

In *one simple formulation*, the $n_\pm$ appearing in (2) are identified with $n(\pm1)/a$, and n_{eq} with n_{EQ}/a. Then, by comparison of expressions for $\pm D\, dn/dx|_{0\pm}$ with (2), one has that

$$\begin{aligned} &K_\pm = ah_\pm = D_\pm/a = D/L_\pm \text{ where } L_\pm = a \exp(\beta\delta_\pm), \\ &\text{and } P = ah_p = D_p/a \text{ so } L_p = aD/D_p = ah/h_p. \end{aligned} \tag{B3}$$

However, we argue that a *more appropriate formulation* is to interpret $n_\pm$ as $n(0\pm)/a$ [4]. This formulation corresponds more closely to the 2D model in this paper where $n_\pm$ are interpreted as densities right at the step edge, but no analytic extension is in fact needed in the 2D model when $\delta_\pm = 0$. The difference between these two formulations might be regarded as a different assignment of the step edge position. First, consider the simplest case where $h_p=0$ (no permeability). Then, one can solve (B2) for n(1) in terms of n(0+) to obtain

$$n(1) = [h\, n(0+) – h_+ n_{EQ}]/(h - h_+). \qquad \text{(B4)}$$

Substituting this result for n(1) into the right-hand-side of (B2) yields

$$D\, dn/dx|_{0+} \approx h[n(0+) – n_{EQ}]/(h/h_+ -1). \qquad \text{(B5)}$$

Thus, replacing n(0+) by n_+/a and n_{EQ} with n_{eq}/a, yields an expression for K_+. Together with results of a similar analysis for $D\, dn/dx|_{0-}$, one obtains [4]

$$K_\pm = ah/(h/h_\pm - 1) = D/L_\pm \text{ where } L_\pm = a[\exp(\beta\delta_\pm) – 1] \text{ and } P=0 \text{ (for } h_p=0). \qquad \text{(B6)}$$

For the more general case where $h_p>0$, one might determine both n(±1) in terms of n(0±) and n_{EQ}. However, some complications arise which we will not discuss in this paper.

Appendix C: Refined Discrete 1D Deposition-Diffusion Models

It is instructive to introduce a refined version of the discrete 1D deposition-diffusion equation model of Appendix A which more closely reflects the 2D model analyzed in this paper. Indeed, development of 1D models will generally be most effective if guided by specific 2D models. We retain the geometry of the model described in Appendix A with a 1D array of sites (mimicking rows of sites in 2D) and j=0 denoting the step edge. The key distinction from the standard model is that we now incorporate limited equilibration of the adatom density right at the step edge or “step site”, so that in general $n(0) \neq 1$ and $\exp(-\beta\phi_b)n(0) \neq n_{EQ}$. See Fig.13. More specifically, we introduce a finite rate, R, for decay of n(0) to 1. If we do not include direct hopping across the step (i.e., we set $h_p = 0$), then the revised equations become

$$d/dt\, n(j) = F + h[n(j+1) – 2n(j) – n(j-1)] \approx 0, \text{ for } j>1, \qquad \text{(C1)}$$

$$d/dt\, n(1) = F + h[n(2) – n(1)] + h_+[\exp(-\beta\phi_b)n(0) – n(1)] \approx 0, \qquad \text{(C2)}$$

$$\begin{aligned} d/dt\, n(0) = {} & F + h_+[n(1) – \exp(-\beta\phi_b)n(0)] + h_-[n(-1) – \exp(-\beta\phi_b)n(0)] \\ & + R[1 – n(0)] \approx 0, \end{aligned} \qquad \text{(C3)}$$

with analogous equations for n(-j). Thus $R=\infty$ recovers the standard model of Appendix A. We smoothly extrapolate or “analytically extend” the values n(j) of the adatom densities to the values n(0±) at the step edge or step site via the defining relations

$$\begin{aligned} d/dt\, n(\pm 1) &= F + h[n(\pm 2) - 2n(\pm 1) + n(0\pm)] \\ &= F + h[n(\pm 2) - n(\pm 1)] + h[n(0\pm) - n(\pm 1)] \approx 0. \end{aligned} \tag{C4}$$

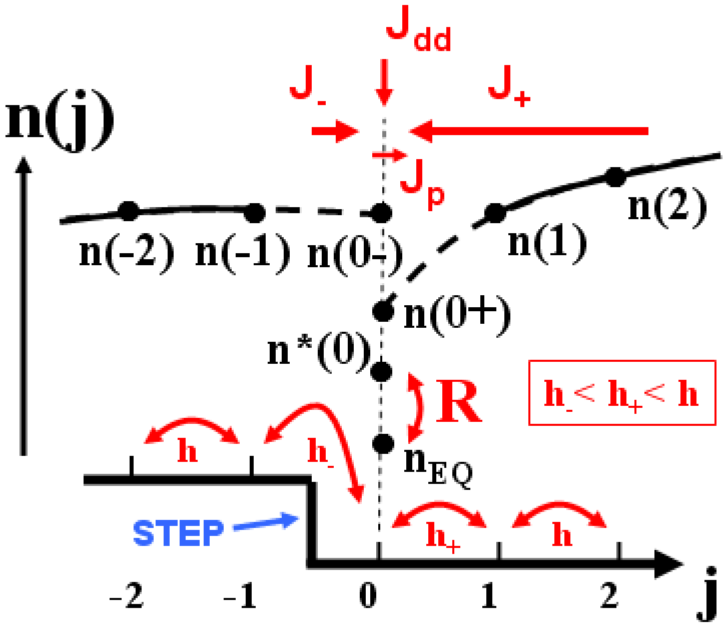

Figure 13: Schematic of adatom density in the refined 1D discrete deposition-diffusion model in the vicinity of a step edge. Also shown are: the adatom hop rates; the relaxation rate at the step edge; total diffusion fluxes reaching the step edge, $J_\pm$; the flux across the step due to permeability, J_p; and the flux to the step due to “direct deposition”, J_{dd}.

To analyze these equations, it is natural to introduce rescaled densities analogous to the 2D discrete model. One sets $n^*(j) = n(j)$ for $j \neq 0$, $n^*(0\pm) = n(0\pm)$, and $n^*(0) = \exp(-\beta\phi_b)n(0)$. One then solves the steady state equations to determine $n^*(\pm 1)$ and $n^*(0)$ in terms of $n^*(0\pm)$ and n_{EQ}. Setting $r = \exp(\beta\phi_b)R$, and using these results to rewrite the expression for the diffusion fluxes approaching the step edge, one obtains

$$K_\pm = ar\,(h/h_\pm - 1)^{-1}[(h/h_+ - 1)^{-1} + (h/h_- - 1)^{-1} + (r/h)]^{-1}, \text{ and} \tag{C5}$$

$$P = ah\,(h/h_{+} -1)^{-1}(h/h_{+} -1)^{-1}[(h/h_{+} - 1)^{-1} + (h/h_{-} -1)^{-1} + (r/h)]^{-1}. \qquad \text{(C6)}$$

Appendix D: Semi-Continuous Deposition-Diffusion Models

Here, we consider the regime where the kink separation, L, is large and regard the terrace width, W, as fixed. It is natural to replace the fully discrete adatom density n(i,j) with a semi-discrete (or semi-continuous) version n(x,j) where n(x=ia,j) = n(i,j)/a denotes the adatom density per unit length along row j. These quantities satisfy a coupled set of continuum deposition-diffusion equations. For an infinite ES barrier, $\delta_{-}=\infty$, and zero attachment barrier $\delta_{+}=0$, these have the form

$$\begin{aligned}
&\partial/\partial t\; n(x,1) = f + D_e\partial^2/\partial x^2\; n(x,1) + h[n(x,2) - \exp(-\beta\phi_{\perp})n(x,1)] \approx 0,\\
&\partial/\partial t\; n(x,j) = f + D\partial^2/\partial x^2\; n(x,j) + h[n(x,j+1)\\
&\qquad\qquad - 2\,n(x,j) + n(x,j-1)] \approx 0 \text{ for } 1<j<W,\\
&\partial/\partial t\; n(x,W) = f + D\partial^2/\partial x^2\; n(x,1) + h[n(x,W-1) - n(x,W)] \approx 0,
\end{aligned} \qquad \text{(D1)}$$

where $D=a^2h$ and $D_e=a^2h_e$ are diffusion coefficients, and $f = a^{-1} F$ is the deposition rate per unit length. For convenience, we set kink positions at $x= \pm aL/2$ and solve these equations for $-aL/2 < x < aL/2$ with boundary conditions $n(\pm aL/2, 1) = \exp(-\beta\phi_{\parallel})/a$ and $\partial/\partial x\; n(\pm aL/2,j) = 0$ for $j>1$.

Just as for the 2D fully discrete model, it is natural to rescale and shift these densities introducing variables $\delta n^*(x,1) = [\exp(-\beta\phi_{\perp})n(x,1)- n_{EQ}]/a$ and $\delta n^*(x,j) = [n(x,j)- n_{EQ}]/a$ for $j>1$, where $n_{EQ} = \exp(-\beta\phi_b)$. Collecting these variables into a W-dimensional vector $\boldsymbol{\delta n}^*(x)$, one obtains a steady-state equation of the form

$$\partial^2/\partial x^2\; \delta n^*(x) - \underline{\underline{B}}(D_e/D,\, \phi_{\perp})\cdot\delta n^*(x) = (f/D)\; e(D_e/D,\, \phi_{\perp}). \qquad \text{(D2)}$$

The entries in the non-symmetric WxW-matrix $\underline{\underline{B}}$ are readily determined from (D1), as are the entries in the W-component vector *e*. Solution of the equations is based on determination of a complete bi-orthonormal set of right- and left-eigenvectors of $\underline{\underline{B}}$ denoted v_k and w_k^T with eigenvalues $\lambda_k \geq 0$ for $0 \leq k \leq W-1$ where $w_k\cdot v_m = \delta_{k,m}$. We will let k=0 denote the “equilibrium eigenstate” where $\lambda_0=0$. By construction of our scaled variables, the right equilibrium eigenvector v_0 has equal components (naturally set to unity). The left equilibrium eigenvector w_0 has a first component equal to $\exp(-\beta\phi_{\perp})D_e/D$ times the rest.

Setting $E_k = (f/D)w_k \cdot e$, the solution to (D2) has the form

$$\delta n^*(x) = \Sigma_{0 \le k \le W-1}\, a_k(x) v_k, \text{ where } \partial^2/\partial x^2\, a_k(x) - \lambda_k\, a_k(x) = E_k. \qquad \text{(D3)}$$

Thus, one has

$$a_0(x) = -\tfrac{1}{2} E_0 x^2 + b_0 \text{ and } a_k(x) = -E_k/\lambda_k + b_k \cosh[(\lambda_k)^{1/2} x] \text{ for } k>0, \qquad \text{(D4)}$$

already accounting for reflection symmetry about $x=0$. The coefficients b_k are determined by satisfying the boundary conditions. While the detailed forms are complex, the key feature is that

$$\begin{aligned} &b_0 = E_0 L^2/8 + \{b_{k>0} \cosh[(\lambda_k)^{1/2} L/2] \text{ terms}\} \text{ and} \\ &b_k \propto L/\sinh[(\lambda_k)^{1/2} L/2] \;\text{ for } k>0. \end{aligned} \qquad \text{(D5)}$$

Finally reconstructing $\delta n^*(x,1)$ yields an expression of the form

$$\begin{aligned} \delta n^*(x,1) = \;& E_0[(L/2)^2 - x^2](v_1)_1 \\ & + L\, \Sigma_{k>0}\, \alpha_k[\cosh[(\lambda_k)^{1/2} L/2] - \cosh[(\lambda_k)^{1/2} x]]/\sinh(\lambda_k)^{1/2} L/2] \,. \end{aligned} \qquad \text{(D6)}$$

Averaging over x reveals an effective scaling of the excess adatom density at the step edge varying roughly like L^2+BL+C, as mentioned after (12). The flux approaching the step edge is independent of L (and is exactly determined as for the fully discrete 2D model). Finally, we mention that the type of analysis and results described here can be readily extended to other cases such as zero attachment barriers, $\delta_\pm = 0$.

References

1) A. Pimpinelli and J. Villain, *Physics of Crystal Growth* (Cambridge UP, Cambridge, 1997).

2) H.C. Jeong and E.D. Williams, *Steps on surfaces: experiment and theory*, Surf. Sci. Rep. 34, 171 (1999).

3) T. Michely and J. Krug, *Islands, Mounds, and Atoms* (Springer, Berlin, 2004).

4) J.W. Evans, P.A. Thiel, and M.C. Bartelt, *Morphological evolution in epitaxial thin film growth: Formation of 2D islands and 3D mounds*, Surf. Sci. Rep. 61, 1 (2006).

5) C. Ratsch, M.F. Gyure, R.E. Caflisch, M. Petersen, M. Kang, J. Garcia, and D.D.

Vvedensky, *Level-set method for island dynamics in epitaxial growth*, Phys. Rev. B 65, 195403 (2002).

6) *Multiscale modeling in Epitaxial Growth*, A. Voigt, ed., Int. Ser. Numer. Math. Vol. 149 (Birkhauser Verlag, Basel, 2005).

7) W.K. Burton, N. Cabrera, and F.C. Frank, *The growth of crystals and the equilibrium structure of their surfaces*, Proc. R. Soc. London, Ser. A 243, 299 (1951).

8) A.A. Chernov, Sov. Phys. Usp. 4, 116 (1961).

9) R.L. Schwoebel, *Step motion on crystal surfaces. II*, J. Appl. Phys. 40, 614 (1969).

10) M. Ozdemir and A. Zangwill, *Morphological evolution of a faceted crystal*, Phys. Rev. B 45, 3718 (1992).

11) J.A. Yancey, H.L. Richards, and T.L. Einstein, *Terrace width distributions for vicinal surface with steps of alternating stiffness*, Surf. Sci. 598, 78 (2005).

12) R.E. Caflisch, W. E, M.F. Gyure, B. Merriman, and C. Ratsch, *A kinetic model for a step edge in epitaxial growth*, Phys. Rev. E 59, 6879 (1999).

13) L.N. Balykov, M. Kitamura, I.L. Maksimov, and K. Nishioka, *Kinetics of non-equilibrium step structure*, Phil. Mag. Lett. 78, 411 (1998).

14) L. Balykov and A. Voigt, *Kinetic model for step flow growth of [100] steps*, Phys. Rev. E 72, 022601 (2005).

15) L. Balykov and A. Voigt, *A 2+1-dimensional terrace-step-kink model for epitaxial growth far from equilibrium*, Multiscale Model. Sim. 5, 45 (2006).

16) L. Balykov and A. Voigt, *A kinetic model for step flow growth in molecular beam epitaxy*, Surf. Sci. 600, 3436 (2006).

17) D. Margetis and R.E. Caflisch, *Anisotropic step stiffness from a kinetic model of epitaxial growth*, Multiscale Model. Sim. 7, 242 (2008).

18) B. Voigtlander, T. Weber, P. Smilauer, and D.E. Wolf, *Transition from island growth to step-flow growth for Si/Si(100) epitaxy*, Phys. Rev. Lett. 78, 2164 (1997).

19) S. Tanaka, N.C. Bartelt, C.C. Umbach, R.M. Tromp, and J.M. Blakeley, *Step permeability and relaxation in biperiodic gratings on Si(100)*, Phys. Rev. Lett. 78, 3342 (1997).

20) *Perspectives on inorganic, organic, and biological crystal growth: From fundamentals to applications*, AIP Conference Proceedings Vol. 916, 13th International Summer School on Crystal Growth, edited by M. Skowronski, J.J. de Yoreo, and C.A. Wang, (AIP, Melville, 2007).

21) I.V. Markov, *Crystal growth for beginners: Fundamentals of nucleation, crystal growth, and epitaxy*, (World Scientific, Singapore, 2003).

22) V.V. Voronkov, Soviet Phys. Crystallogr. 15, 13 (1970).

23) O. Pierre-Louis, M.R. D'Orsogna, and Einstein, *Edge diffusion during growth: The kink-Ehrlich-Schwoebel effect and resulting instabilities*, Phys. Rev. Lett. 82, 3661 (1999).

24) M. Li and J.W. Evans, *Growth coalescence shapes for islands during metal(100) homoepitaxy*, Phys. Rev. B 69, 031410 (2004).

25) J.W. Evans, D.E. Sanders, P.A. Thiel, and A.E. DePristo, *Low temperature epitaxial growth of thin metal films*, Phys. Rev. B 41, 5410 (1990).

26) M. Li and J.W. Evans, *Theoretical analysis of mound slope selection during unstable multilayer growth*, Phys. Rev. Lett. 95, 256101 (2005); 96, 079901E (2006).

27) X. Guo, D.-J. Liu, and J.W. Evans, *Schloegl's second model for autocatalysis with particle diffusion*, J. Chem. Phys. 130, 074106 (2009).

28) T. Zhao, J.D. Weeks, and D. Kandel, *From discrete hopping to continuum modeling on vicinal surface with applications to electromigration*, Phys. Rev. B 71, 155326 (2005).

29) R. Ghez and S.S. Iyer, IBM J. Res. Dev. 32, 804 (1988).

30) H.J.W. Zandvliet, *Energetics of Si(100)*, Rev. Mod. Phys. 72, 593 (2000).

31) B. Voigtlander, *Fundamental processes in Si/Si and Ge/Si epitaxy studied by scanning tunneling microscopy during growth*, Surf. Sci. Rep. 43, 127 (2001).

32) C. Misbah, O. Pierre-Louis, and Y. Saito, *Crystal surfaces in and out of equilibrium: A modern view*, Rev. Mod. Phys. 82, 981 (2010).

33) Y.-W. Mo and M.G. Lagally, *Anisotropy in surface migration of Si and Ge on Si(100)*, Surf. Sci. 248, 313 (1991).

34) C. Pearson, M. Krueger, and E. Ganz, *Direct tests of microscopic growth models using hot scanning tunneling microscopy movies*, Phys. Rev. Lett. 76, 2306 (1996).

35) P. Jensen, N. Combe, H. Larralde, J.L. Barrat, C. Misbah, and A. Pimpinelli, Euro. Phys. J. B 11, 497 (1999).

36) D.-J. Liu and J.W. Evans, *Sintering of 2D nanoclusters in metal(100) homoepitaxial systems: Deviations from predictions of Mullins continuum theory*, Phys. Rev. B 165407 (2002).

37) Consider a region on a terrace including M contiguous sites, such that all hop rates for these and for the adjacent sites are given by h. Then, the steady-state form of the discrete deposition-diffusion equations ensures that the total flux, $J_{TOT} = h\ \Sigma_{B,B'}\ (n_B - n_{B'}) = h\ \Sigma_{B,B'}\ (n^*_B - n^*_{B'})$, out of M equals M·F. In the expression for J_{TOT}, we add all contributions between the boundary sites, B, in M and the adjacent sites, B', outside of M.

APPENDIX II: RING DISTRIBUTION STATISTICS IN AMORPHOUS NETWORKS

1 Introduction

The structure of amorphous silicon and silica has long been a topic of study. The use of mesoporous silica nanospheres (which have an amorphous atomic-scale structure) for catalysis and other applications has led to renewed interest in ways of modeling the amorphous structure. Different methods have been used to form a model of the amorphous network. One conceptual model uses a continuous random network (CRN) which has an interconnected network of bonded atoms. While there are rules governing the number and type of connections, atoms are not required to be in well-defined periodic array of positions as compared to a crystalline structure.

The lack of a well-defined repeating structure makes characterizing the system a non-trivial task. Even confirming that the system has the characteristics of an amorphous structure requires some effort. One approach is to determine the radial distribution function of the atoms in the system. An alternate method is to note that, in both the crystalline and amorphous systems, there is a ring structure defined by the connectivity of the bonds between atoms. The size and distribution of these rings can be characterized and is of interest because it impacts mechanical and electrical properties. Several previous studies have characterized rings [1,2,3,4], the majority having been restricted to analyzing the size distribution of rings. Characterization of arrangement and connectivity of rings gives more information about the structure. The approach taken so far has been an atom-centric study of ring correlations [5,6]. This work instead focuses on a ring-centered approach by presenting a simple and rigorous method of determining ring-ring correlation distributions.

The CRN method and this ring characterization method can be applied to structures other than silica. To provide a simple test case, an amorphous silicon structure is used as an example in this work. The description of the amorphous system used and how it is created is given in section 2. Section 3 gives the description of ring calculation and determining correlations. Section 4 presents results for an example system. Conclusions are given in section 5. Finally, an appendix gives a detailed example using the method described here.

2 Background and Simulation Method

2.A. Ring structures

Within the continuous network, the interconnected bonds form a collection of rings. The size of rings is given by the number of atoms the ring contains. Any given bond will, in general, be part of several different rings which may vary in size.

Rings are considered neighbors if they share one or more sides. This requires that they also share at least two bonded atoms. Only *primitive* rings, defined as those that cannot be reduced into two smaller rings, are considered. Figure 1 shows a primitive ring, a non-primitive ring, and a pair of nearest neighbor rings. Identification of rings from the structure is accomplished using the algorithm described by Yuan and Cormack [7].

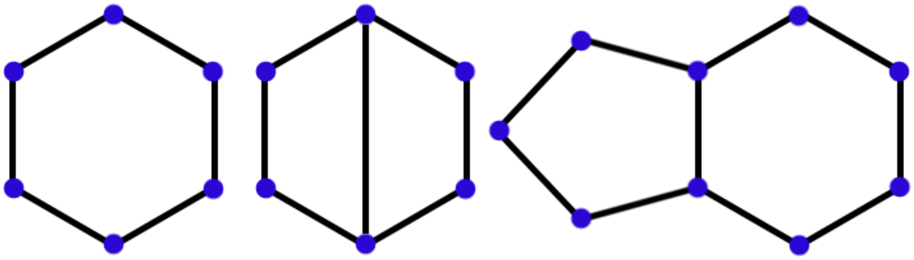

Figure 1: Several rings structures. The leftmost ring is a primitive 6-member ring. The middle 6-member ring is not primitive but is composed of two 4-member, primitive rings. The rightmost pair of primitive rings are nearest neighbors.

2.B. Bond Swapping

Creation of an amorphous structure is accomplished using the bond swapping method described by Wooten *et al* [8,9]. The system studied in this work is amorphous silicon (Si). However, the description below will work for other structures with appropriate modifications to the rules for bonds. Creation of the amorphous network is a three step process. First, an ideal Si crystal structure is built using the known Si crystal structure. Next, bonds are swapped following rules given below to change the connectivity of the system. After each bond-swap, the system is relaxed (by Monte Carlo (MC) methods) while retaining the current network topology. The bond-swap is accepted based on the energy difference before and after the swap according to a Metropolis MC algorithm. The details of each step are given below.

The initial system is derived from the unit cell of a crystal. The size of the system is given by the number of unit cells in each direction. To create the larger crystal, the template atoms are translated an appropriate distance to form a new unit cell. After all the unit cells are created, bonds are constructed based on the bonds in the template structure. Bonds to atoms that are outside of the system box are created using periodic boundary conditions to map them onto corresponding atoms within the box.

The process of creating the random structure is a series of bond swaps. For each swap step, a bond between two atoms is selected at random. The atoms are labeled B and C with the bond labeled B-C. For both atoms B and C, another bonded atom is selected at random to find bonds A-B and C-D, where A≠C and B≠D. To change the configuration, the bonds A-B and C-D are broken and reformed as A-C and B-D, as shown in figure 2. There is no change made to the central bond or the positions which leads to highly strained bond.

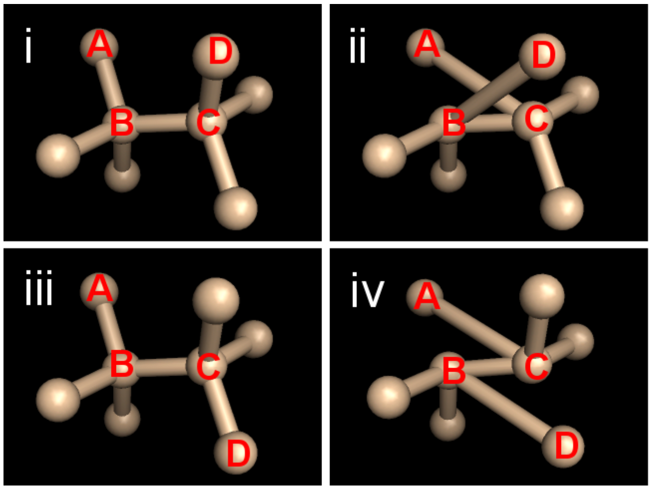

Figure 2: Bond configuration of atoms chosen for bond swap. i) pre-swap ii) post-swap leading to a non parallel configuration iii) pre-swap with alternate selection of atom D. iv) post-swap leading to parallel bond configuration

When selecting bonds to swap, a swap which creates nearly parallel bonds will reduce the strain introduced into the system relative to one which does not create nearly parallel bonds. Identifying these swaps can best be done by ensuring that the bonds are not part of the same 5- or 6- member ring[9]. Figure 2 shows the result of both a non-parallel and a parallel bond swap.

At this stage, all bond swaps are accepted unless they result in the formation of a 3- or 4- member ring. These swaps are always rejected, because in the relaxed state, the angles in a 3- or 4- member ring will always have a significant deviation from the ideal bond angle of 109.5 degrees. The large deviation in angle will lead to a very high strain energy that will be unstable.

Taking the structure from the previous step, another round of bond swapping is performed. This time, after every swap, the region around the bond is relaxed with MC translations of the atoms. Atoms are translated up to a distance Δr_{max} from their location. This distance is a parameter that must be selected. Smaller values will ensure more moves are selected at the cost of a smaller changes per move. The relaxation moves are done at a temperature T_R using a Boltzmann acceptance rule. Typically T_R is very high to ensure the system moves out of potential wells. The energy of the system is calculated using a Keating potential [10] which is given by the following form:

$$E=\sum_{i,j}\frac{3\alpha}{16r_0^2}\left(|\boldsymbol{r}_{i,j}^2|-r_0^2\right)^2+\sum_{i\neq j,k}\frac{3\beta}{8r_0^2}\left(\boldsymbol{r}_{i,j}\cdot\boldsymbol{r}_{i,k}+\frac{1}{3}r_0^2\right)^2 \qquad (1)$$

The first part is a bond interaction, and the second part is an angular interaction. There are no non-bonded interactions. The α and β values are force constants dependent on the type of atoms involved in the bond or angle. Modeling typically emphasizes the value of the ratio β/α, as most properties of the system depend primarily on this parameter [11]. r_0 is the ideal bond length for a perfect crystal. The first sum is over the bonds containing a given atom and the second sum is over the angles formed by three atoms with atom i in the center.

There is no requirement to use a Keating potential; other potentials would be easily substituted. The use of the Keating potential imposes a requirement that the system must be at least 2 unit cells wide in any direction. Using only one unit cell in a given direction can lead to a case where periodic boundary conditions cause an atom to form an angle with itself.

After the system has been relaxed, the swap move is accepted with a Boltzmann probability based on the swapping temperature, T_S. The ΔE used is the difference between the energy before the swap and the energy after the relaxation. The MC relaxation is normally done only in the region of the bond swap for reasons of efficiency. After a number of swaps are performed, a full MC relaxation over the entire system is performed. The structure resulting from this method is used as the amorphous structure for further analysis.

3 Ring Identification and Correlations

The algorithm for finding ring neighbors uses mathematical set objects and operations to identify rings. A brief introduction to the relevant theoretical concepts of sets is given here prior to discussing their usage.

3.A. Sets

In the context of this work, a set is a collection of zero or more unique elements. Sets will be denoted by a list of items enclosed in braces, {}. The order of the elements in the set has no significance. {A,B,C} is a set containing elements A, B, and C. {B,A,C} is the same set. An empty set is denoted as {}.

The following set operations are used (see figure 3 for a schematic description of operations):

- A *union* of two sets, X and Y, will produce a new set, Z, with all elements contained in either X and Y. An element in both X and Y will only appear once in Z. The expression for this union is $Z=X\cup Y$. A union can be taken over many sets at once using notation analogous to a summation:

$$\bigcup_{i=1}^{N} a(i)=a(1)\cup a(2)\cup a(3)\ldots a(N-1)\cup a(N) \tag{2}$$

- The *intersection* of sets X and Y will contain only those elements that appear in both sets. The expression for an intersection is $Z=X\cap Y$.
- The *difference* of set Y from set X will give a set containing all elements in X that are not in Y. The expression for a difference is $Z = X-Y$

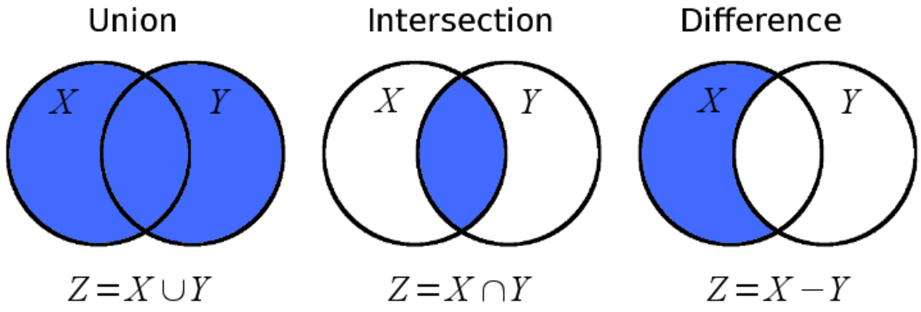

Figure 3: Schematic of three set operations. X and Y sets are indicated by the labeled circles, with the region of overlap being the overlap of the sets. The result, Z, of each operation is indicated by the shaded region.

3.B. Ring Pair Correlations

The procedure for finding ring neighbors is described below. A detailed example is given in the appendix. The appendix example goes step-by-step through the process described here using a simple example system.

In order to determine the distribution of rings, all of the rings in the system are first identified and assigned a unique index. Each ring, once found, is recorded. The ring is stored as the list of atoms in the ring. Those atoms are stored in such an order that adjacent atoms in the list are bonded pairs in the structure with the first and last atoms in the list also being bonded to each other. This creates a list of bonds where each bond is a pair of atom indices.

Additionally, a set of ring pointers, P(j), is maintained for each atom, j. These sets contain references to every ring for which the atom is a member. The neighbors of a ring are denoted as the sets $R_N(i)$ where i is the ring index and N is the order of the nearest neighbor: N=0 is zeroth order neighbor (i.e. the ring itself), N=1 are the first nearest neighbors, N=2 are the second nearest neighbors, etc... The zeroth nearest neighbor set for each ring is trivially determined as a set consisting of only that ring index:

$$R_0(i)=\{i\} \tag{3}$$

In order to find the first nearest neighbor sets, each ring is analyzed separately. From the list of atoms in the ring, a list of all of the bonded pairs of atoms is constructed. This list is b(i) for ring i. For each pair of bonded atoms, j and k, the intersection of ring pointer sets, P(j) and P(k), is found. This gives a set of all rings containing both atoms. The union of these sets from all bonded pairs in a ring gives a set of pointers to all rings that share an edge with the given ring. The ring being analyzed will also be included and must be removed from the set. The remaining rings in the set form the first nearest neighbors. Repeating this for each ring gives the ring neighbor list for all rings. This procedure can be expressed as an equation in set notation:

$$R_1(i)=\left(\bigcup_{(j,k)\in b(i)} P(j)\cap P(k)\right)-R_0(i) \tag{4}$$

Finding further neighbors requires a slightly different procedure. To find the rings a distance of N away from a given ring, we first take the union of all sets of first nearest neighbors for rings at a distance N-1 from the source ring. This gives the set of all rings that can be reached in N steps along the chain of rings. The first N-1 steps are guaranteed to be a shortest path. However, the final step may be to a ring closer (path length N-2), at the same distance (path length N-1), or further away (path length N). To exclude the first two possibilities, take the difference of sets at N-2 and N-1 for this ring from the set of rings that can be reached in N steps. In set notation, the equation for this is:

$$R_N(i)=\left(\bigcup_{m\in R_{N-1}(I)} R_1(m)\right)-R_{N-2}(i)-R_{N-1}(i);\, N\geq 2 \tag{5}$$

Once the ring neighbors have been identified, the neighbor statistics can be found by totaling the number of neighbors of each size for each type of ring in the system.

4 Results for Silicon System

To test the ring correlation method described above, a silicon system was generated using the bond switching method given in section 2. A diamond cubic unit cell (lattice spacing = 0.5427 nm) was used as the basis for the Si system. This cell contains 8 Si atoms with 16 corresponding bonds. The cell was replicated to form a system with six unit cells in each direction. This gives a total of 1728 Si atoms. The parameters for the Keating potential are: $\alpha = 0.1617\text{eV}$, $\beta = 0.046\text{eV}$, and $r_0 = 2.35\text{Å}$. All rings in the perfect crystal are 6-member rings. Clearly, all neighboring rings must also be 6-member rings. Figure 4 shows the correlation search method recovers this distribution.

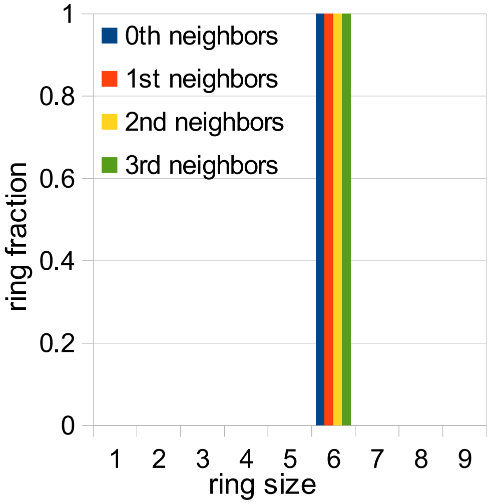

Figure 4: Neighbor ring distributions for 6-member rings in a crystalline structure.

Initially, 100 bonds were swapped with no relaxation. Following that, 1000 swaps were made with a full relaxation of 500 moves after each move swap. Each moves translated an atom a distance of up to 0.5nm. The temperature for both the swap and relaxation was a $1/(k_bT)$ value of 0.4eV. The swap and relaxation were repeated at 0.35eV, 0.3eV, and 0.25eV to cool the system.

After these moves were made, the ring distributions were calculated. Results are shown in figure 5. Specifically, for a specified ring size N=4-9 we determine the distribution of sizes of nearest neighbors, second nearest neighbors, etc. Very little variation is shown in the ring neighbor distributions for different N (i.e. the distributions depend only weakly on N). 6-member rings are the most likely neighbors for all ring sizes. The stability of those rings is evident in that only 6-member rings exist in the crystal structure. Beyond that, there is little deviation from the overall distribution, suggesting there is little correlation between neighbors of different size. It does appear 4-member rings are unlikely to be next to other 4-member rings and more likely to be next to 5- and 6- member rings. However, the small number of 4-member rings present in the system makes it difficult to draw conclusions. Larger rings seem to have a preference to be being closer to similar size rings rather than having them as neighbors further away.

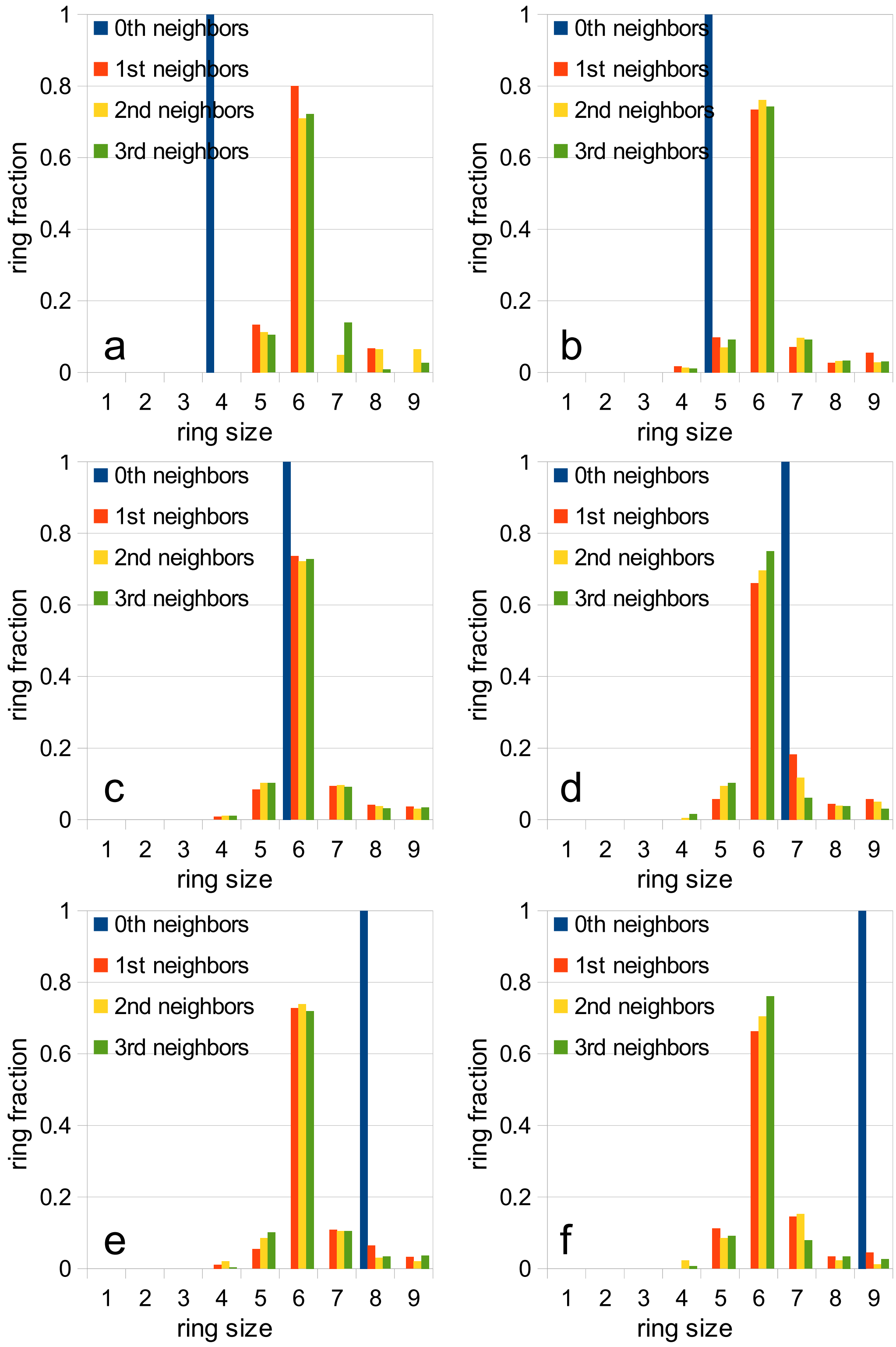

Figure 5: Ring neighbor distributions. (a) N=4,(b) N=5, (c) N=6, (d) N=7, (e)N=8, (f) N=9.

5 Conclusion

The set-based approach to calculating ring correlations provides an efficient way to take an existing structure and calculate the distribution of rings. A significant benefit of this method is the ability to write a few simple, exact equations for calculating the number of rings bounding any given ring (equations 3 - 5). These equations can be easily implemented in code. Some programming languages, such as Python, include built-in support for set operations. Many other languages have libraries available to handle set operations. Using this method and existing code support for sets can reduce the process of finding nearest rings to a handful of lines of code.

Appendix: Correlation Example

For clarity, a complete example of the set-based method of calculating rings is presented here. It shows the steps of the calculations applied to a simple ring system as shown in figure 6. The system shown is two-dimensional, but the procedure is independent of dimension and is unchanged for three-dimensional systems. The atoms in blue are labeled with numbers (1-13), and the rings are labeled with Roman numerals (I - V).

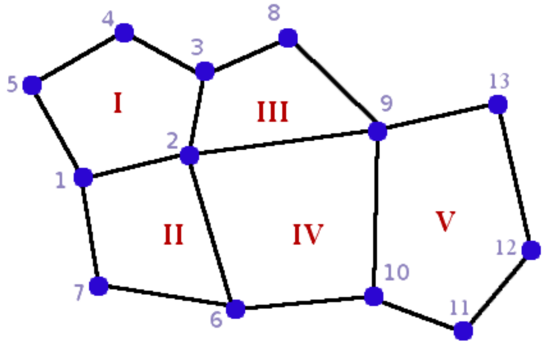

Figure 6: Example ring structure used to illustrate the method

Focusing on ring I, the nearest neighbor rings (i.e. the rings that share a bond with ring I) are II and III. The second nearest neighbor (i.e. a ring that shares a bond with at least one nearest neighbor ring, but does not share a bond with the main ring) is IV. V is a third nearest neighbor. This is clearly seen from the image but not trivial for a computer to determine. Below is the process the algorithm goes through to determine this for ring I. The same procedure would be applied to the other rings as well.

First, the proper lists and sets must be constructed. This only needs to be done once for the system. All correlations are found from this same set of data.

The 5 rings are defined by their atoms as:

- I: [1, 2, 3, 4, 5]
- II: [1, 2, 6, 7]
- III: [2, 3, 8, 9]
- IV: [2, 6, 10, 9]
- V: [9, 10, 11, 12, 13]

The bond lists are:

- b(I) = [(1,2), (2,3), (3,4), (4,5), (5,1)]
- b(II) = [(1,2), (2,6), (6,7), (7,1)]
- b(III) = [(2,3), (3,8), (8,9), (9,2)]
- b(IV) = [(2,6), (6,10), (10,9), (9,2)]
- b(V) = [(9,10), (10,11), (11,12), (12,13), (13,9)]

The ring pointer sets (which rings an atom is in) are:

- P(1) = {I, II}
- P(2) = {I, II, III, IV}
- P(3) = {I, III}
- P(4) = {I}
- P(5) = {I}
- etc. for P(6) through P(13) ...

Now that the data items have been created, the neighboring rings of ring I can be determined. The "zeroth" nearest neighbor (equation 3) is the ring itself and is the only member of the R_0 set for this ring:

$$R_0(I)=\{I\} \tag{6}$$

The first nearest neighbors (equation 4) are generated by first finding the intersection of the pointer sets P(j) and P(k) for each bond (atom pair) in ring I as shown in table 1:

Table 1: Intersection of pointer sets for each atom pair in ring I.

bond atoms: j, k	P(j)	P(k)	$P(j)\cap P(k)$
1, 2	{I, II}	{I, II, III, IV}	{I, II}
2, 3	{I, II, III, IV}	{I, III}	{I, III}
3, 4	{I, III}	{I}	{I}
4, 5	{I}	{I}	{I}
5, 1	{I}	{I, II}	{I}

The union of the values in the last column ($\bigcup_{(j,k)\in b(i)} P(j)\cap P(k)$) is {I, II, III}. Subtracting the zeroth order neighbor (R_0(I) = {I}) gives the the first nearest neighbors: R_1(I) = {II, III}.

The same procedure gives the nearest neighbors for the other rings: R_1(II) = {I, IV}, R_1(III) = {I, IV}, R_1(IV) = {II, III, V}, R_1(V) = {IV}

For the second nearest neighbors of I, equation 5 gives:

$$R_2(I)=\left(\bigcup_{m\in R_1(I)} R_1(m)\right)-R_0(I)-R_1(I) \tag{7}$$

The first term gives all the candidate rings by considering all the nearest neighbors of ring I's nearest neighbors:

$$\bigcup_{m\in\{II,III\}} R_1(m)=R_1(II)\cup R_1(III)=\{I,IV\}\cup\{I,IV\}=\{I,IV\} \tag{8}$$

The second and third terms in equation 7 were previously determined. Subtracting these removes rings that are closer which gives the correct second nearest neighbor ring set. In this case, the set has only one ring:

$$R_2(I)=\{I,IV\}-\{I\}-\{II,III\}=\{IV\} \tag{9}$$

The third nearest neighbor is found using equation 5:

$$R_3(I)=\left(\bigcup_{m\in R_2(I)} R_1(m)\right)-R_1(I)-R_2(I) \tag{10}$$

$$\bigcup_{m\in\{IV\}} R_1(m)=R_1(IV)=\{II\,,III\,,V\} \tag{11}$$

$$R_3(I)=\{II\,,III\,,V\}-\{II\,,III\}-\{IV\}=\{V\} \tag{12}$$

The set of fourth nearest neighbors is empty:

$$R_4(I)=\left(\bigcup_{m\in R_3(I)} R_1(m)\right)-R_2(I)-R_3(I) \tag{13}$$

$$\bigcup_{m\in\{V\}} R_1(m)=R_1(V)=\{IV\} \tag{14}$$

$$R_4(I)=\{IV\}-\{IV\}-\{V\}=\{\} \tag{15}$$

And finally, all higher nearest neighbors are also empty since the first term in equation 5 is an empty set for i>4.

Application of the equations as given above has resulted in the following neighbors for ring I: first nearest neighbors – $R_1(I)=\{II, III\}$, second nearest neighbors – $R_2(I)=\{IV\}$, third nearest neighbors – $R_3(I) = \{V\}$, and all higher nearest neighbor sets are empty. Comparison with figure 6 shows that these are all correct.

References

1) Voyles, P. M. et al. Solar Energy Materials & Solar Cells **2003**, 78, 85.

2) Treacy et al., J of Non-Crystalline Solids **2000**, 266, 150

3) Djordjevic et al., Physical Review B, **1995**, 52, 5685.

4) Vink, R. L. C. et al., Physical Review B **2001**, 64, 245214.

5) Hobbs et al., Philosophical Magazine A **1998**, 78, 679.

6) Marians, C. S. et al., J. of Non-Crystalline Solids **1990**, 124, 242.

7) Yuan, X.; Cormack, A.N. Comp. Mat. Sci. **2002**, 24, 343.

8) Wooten, F.; Winer, K.; Weaire, D. Phys. Rev. Lett. **1985**, 54, 1392.

9) Wooten, F.; Weaire, D. J. Non-Crystalline Solids **1984**, 64, 325.

10) Keating, P. N. Phys. Rev. **1966**, 145, 637.

11) Steinhardt, P.; Alben, R.; Weaire, D. J. Non-Crystalline Solids **1974**, 15, 199.